

**An Integrated Framework for Fabrication, Simulation,  
and Design of Functional Origami**

by

Yi Zhu

A dissertation submitted in partial fulfillment  
of the requirements for the degree of  
Doctor of Philosophy  
(Civil Engineering and Scientific Computing)  
in the University of Michigan  
2022

Doctoral Committee:

Assistant Professor Evgueni T. Filipov, Chair  
Professor Selim Esedoglu  
Professor Karl Grosh  
Professor Kenn Oldham  
Associate Professor Jeff Scruggs

Yi Zhu

yizhu@umich.edu

ORCID: 0000-0001-9667-834X

©Yi Zhu 2022

## **Dedication**

To Curiosity.

## **Acknowledgments**

First, I want to thank my advisor Assistant Professor Evgueni T. Filipov for supporting me throughout the PhD program. The flexible environment within the group, where I can take any class I am interested in and have great flexibility in formulating my own research theme is really significant for me. I also want to thank the committee members, Professor Selim Esedoglu, Professor Karl Grosh, Professor Kenn Oldham, and Associate Professor Jeff Scruggs for their helpful suggestions and discussions through out the PhD program, the proposal presentation, and the final defense. I want to thank all my collaborators, Dr. Mayur Birla, Professor Mark Schenk, Mr. Ziyang Tang, Dr. Yutong Xia, and Mr. Joonyoung Yu for the helpful discussions and their suggestions regarding the work presented in this dissertation.

In addition, I would like to acknowledge the support from all staff members from the Lurie Nanofabrication Facility for helping with the micro-fabrication. Particularly, I want to thank Pilar Herrera-Fierro and Katharine Beach for their training and advice, which greatly helps me to develop my skills in micro-fabrication. I want to thank the faculties, staffs, and students from the Michigan Institute for Computational Discovery and Engineering for the inspiring seminars and interactions.

Finally, I want to thank the support from my family, my group mates, my friends, and especially my parents Bo Wang and Da Zhu.

## Table of Contents

<b>Dedication</b> .....	<b>ii</b>
<b>Acknowledgments</b> .....	<b>iii</b>
<b>List of Figures</b> .....	<b>viii</b>
<b>List of Tables</b> .....	<b>xii</b>
<b>Abstract</b> .....	<b>xiii</b>
<b>Chapter 1 Introduction</b> .....	<b>1</b>
1.1 Applications of Functional Origami . . . . .	2
1.2 Current Fabrication Methods for Functional Micro-Origami . . . . .	3
1.3 Current Simulation Methods for Functional Origami . . . . .	5
1.4 Current Design Methods for Functional Origami . . . . .	8
1.5 Novel Fabrication, Simulation, and Design of Functional Origami . . . . .	9
1.6 Simulation Codes and Databases . . . . .	10
<b>Chapter 2 Electro-Thermal Micro-Origami</b> .....	<b>12</b>
2.1 MEMS and Micro-Origami . . . . .	12
2.2 Electro-Thermal Actuator for Functional Origami . . . . .	13
2.2.1 Design of electro-thermal actuator . . . . .	13
2.2.2 Customizable micro-fabrication for electro-thermal origami . . . . .	16
2.3 Folding Performance of Electro-Thermal Actuator . . . . .	19
2.3.1 Static elastic folding . . . . .	19
2.3.2 Dynamic elastic folding . . . . .	20
2.3.3 Quasi-static plastic folding . . . . .	24
2.4 Achieving Complex Functions with Micro-Origami . . . . .	26
2.4.1 Controllable multi-degree-of-freedom shape morphing . . . . .	27
2.4.2 Combining elastic and plastic folding for complex functions . . . . .	29
2.5 Concluding Remarks . . . . .	33
<b>Chapter 3 Compliant Crease Bar and Hinge Model</b> .....	<b>34</b>
3.1 Bar and Hinge Models . . . . .	34

3.2	Derivation of Model Stiffness Parameters . . . . .	35
3.2.1	Derivation of bar areas . . . . .	36
3.2.2	Derivation of rotational spring stiffness . . . . .	39
3.2.3	Modeling of panels . . . . .	40
3.3	Model Verification . . . . .	41
3.3.1	Infinitesimal stiffness verification . . . . .	41
3.3.2	Large deformation stiffness verification . . . . .	44
3.4	Simulation Examples . . . . .	45
3.4.1	Self-Folding of a plate pattern . . . . .	45
3.4.2	Self-folding of a flower pattern . . . . .	46
3.4.3	A bistable four-fold vertex . . . . .	49
3.4.4	Bistable Miura-ori beams . . . . .	50
3.5	Concluding Remarks . . . . .	52
<b>Chapter 4</b>	<b>Global Self-Contact Model . . . . .</b>	<b>54</b>
4.1	Contact Models for Origami and for FE Methods . . . . .	54
4.2	Formulation of the Global Panel Contact Model . . . . .	57
4.2.1	Methodology: principle of stationary potential energy and barrier functions	57
4.2.2	Contact potential, force vector, and stiffness matrix . . . . .	58
4.2.3	Definition of the point to triangle distance $d$ . . . . .	60
4.2.4	Calculation of gradient and Hessian of $d$ . . . . .	63
4.3	Numerical verification . . . . .	68
4.4	Implementation and Behaviors of the Contact Model . . . . .	70
4.4.1	Implementation scheme . . . . .	70
4.4.2	Behavior of global panel contact simulation . . . . .	72
4.5	Numerical Examples . . . . .	75
4.5.1	Self-folding of a box . . . . .	76
4.5.2	Loading of an inter-locking box corner . . . . .	77
4.5.3	Folding sequence of a box corner . . . . .	78
4.5.4	Loading of an inter-locking origami . . . . .	80
4.6	Concluding Remarks . . . . .	81
<b>Chapter 5</b>	<b>Multi-Physics Electro-Thermal Actuation Model . . . . .</b>	<b>83</b>
5.1	Active Origami and Multi-Physical Simulation . . . . .	83
5.2	A Simulation Framework for Functional Origami . . . . .	85
5.2.1	Step 1: Solving the heat transfer problem . . . . .	85
5.2.2	Step 2: Solving the stress-free angle . . . . .	89

5.2.3	Step 3: Solving the equilibrium position . . . . .	90
5.3	Calibration and Parameter Selection . . . . .	90
5.3.1	Heat transfer within origami structures . . . . .	90
5.3.2	Heat transfer between origami structures and surrounding environments . . . . .	92
5.4	Experimental Verification . . . . .	94
5.4.1	Single-crease origami with a folding threshold . . . . .	95
5.4.2	Double-crease origami with thermo-mechanical coupling . . . . .	97
5.5	Application Examples . . . . .	98
5.5.1	Simulation of a crane pattern . . . . .	98
5.5.2	Folding of a Miura beam lifter . . . . .	99
5.5.3	Optimization of origami gripper . . . . .	100
5.6	Concluding Remarks . . . . .	103
<b>Chapter 6</b>	<b>Origami Inverse Design with Interpretable Machine Learning . . . . .</b>	<b>105</b>
6.1	Introduction of Machine Learning . . . . .	105
6.1.1	Machine learning as surrogate models . . . . .	106
6.1.2	Interpretable machine learning and decision trees . . . . .	108
6.2	Computing Inverse Design Rules with the Tree Method . . . . .	110
6.2.1	Generate origami performance database . . . . .	112
6.2.2	Train decision trees to obtain design rules . . . . .	112
6.2.3	Select design rules with better precision . . . . .	113
6.2.4	Hold out testing and hyperparameter selection . . . . .	114
6.3	Handling Categorical Features for Comparing Different Patterns . . . . .	117
6.4	Solving Multi-Objective Problems for Multi-Physical Performances . . . . .	121
6.5	Enabling Holistic Origami Inverse Design . . . . .	125
6.6	Concluding Remarks . . . . .	129
<b>Chapter 7</b>	<b>Conclusion and Future Challenges . . . . .</b>	<b>131</b>
7.1	Major Contributions . . . . .	131
7.2	Future Challenges . . . . .	132
<b>Appendix A</b>	<b>A Review on Origami Simulation . . . . .</b>	<b>134</b>
A.1	Introduction, History, and Organization . . . . .	134
A.2	Scope and Terminology . . . . .	135
A.3	Kinematics-Based Simulations . . . . .	138
A.3.1	Developable and flat-foldable origami and reflection based simulations . . . . .	142
A.3.2	Spherical Trigonometry and analytical methods . . . . .	144
A.3.3	Trigonometry and analytical methods . . . . .	148

A.3.4	Loop closure condition and numerical methods . . . . .	149
A.3.5	Other simulations of thin and rigid origami . . . . .	153
A.3.6	Openings and compliant creases . . . . .	154
A.3.7	Thick origami . . . . .	156
A.4	Mechanics-Based Simulations . . . . .	158
A.4.1	Rigid panel models . . . . .	162
A.4.2	Bar and hinge models . . . . .	164
A.4.3	Plate theory based simulations . . . . .	168
A.4.4	Finite element simulations . . . . .	169
A.4.5	Rethinking reduced order mechanical models: Hybrid formulations . . .	172
A.4.6	Capturing panel contact . . . . .	174
A.5	Multi-Physics Based Simulations . . . . .	176
A.6	Available Simulation Packages . . . . .	179
A.7	Selecting and Developing Appropriate Origami Simulations . . . . .	184
A.8	Future Challenges and Concluding Remarks . . . . .	189
	<b>Bibliography . . . . .</b>	<b>192</b>



## List of Figures

1.1	Functional origami applications at different length scales. . . . .	2
1.2	Fabrication methods for small-scale functional origami and challenges in the field. . .	4
1.3	Simulations methods for functional origami and challenges in the field. . . . .	6
1.4	Design methods for functional origami and challenges in the field. . . . .	8
2.1	Design of the electro-thermal actuator for the active micro-origami. . . . .	14
2.2	Residual stress and curvature of released systems. . . . .	15
2.3	Beam rotation of a 400 $\mu\text{m}$ long actuator beam with varying gold thickness. . . . .	16
2.4	Fabrication flow chart of the electro-thermal micro-origami system. . . . .	17
2.5	Devices for testing the performance of a single-crease origami. . . . .	18
2.6	Elastic static folding performance of a single-crease origami system. . . . .	20
2.7	Elastic dynamic folding performance of a single-crease origami system. . . . .	21
2.8	A 1-DOF model to estimate the resonance frequency. . . . .	22
2.9	Relationship between the blocking moment and elevated temperature. . . . .	24
2.10	Degradation of the folding range is minor after 99000 cycles of folding and unfolding.	25
2.11	Plastic folding behavior of the micro-origami. . . . .	26
2.12	Proof-of-concept experiment of the plastic folding behavior of the micro-origami. . .	27
2.13	The hysteretic folding behavior of a single-crease origami with 200 $\mu\text{m}$ beams under different loading cycles. . . . .	28
2.14	A micro-origami gripper with a large gripping range. . . . .	29
2.15	A micro-origami gripper that can first assemble into the 3D configuration using lock- ing devices then achieve gripping motion. . . . .	30
2.16	Combining elastic active folds and passive folds for origami with both mountain and valley folds. (a-c) A single-unit Miura micro-origami; (d-e) A multi-unit Miura beam.	31
2.17	Creating complex origami crane that can first assemble then flaps its wings using a combination of elastic folds and plastic folds. . . . .	32
3.1	(a) Conventional bar and hinge models; (b) Compliant crease bar and hinge models; (c-e) Rotational springs added to capture richer mechanical deformation. . . . .	36
3.2	Derivation of bar areas for the compliant crease bar and hinge model . . . . .	37
3.3	Derivation of rotational spring stiffness for compliant crease bar and hinge model. . .	38
3.4	Infinitesimal tensile stiffness verification. (a-b) Tensile loading of compliant crease bar and hinge model and the FE model; (c-e) Comparison between the compliant crease bar and hinge model and the FE model for different $\alpha$ and $\beta$ values. . . . .	41

3.5	Infinitesimal shear stiffness verifications. (a-b) Shear loading of the compliant crease bar and hinge model and the FE model; (c-e) Comparison between the compliant crease bar and hinge model and the FE model for different $\alpha$ and $\beta$ values. . . . .	42
3.6	Infinitesimal bending stiffness verification. . . . .	43
3.7	Infinitesimal torsional stiffness verification. . . . .	43
3.8	Comparison between the bar and hinge model and FE simulation for large deformation bending. . . . .	45
3.9	Comparison between the bar and hinge model and FE simulation for large deformation loading with combined bending and torsion. . . . .	46
3.10	Comparing the compliant crease bar and hinge model, the smooth fold model, and the FE model. Figure (a) and (b) are reprinted from [Hernandez et al., 2016b]. Copyright (2016), with permission from Elsevier. . . . .	47
3.11	Self-folding of a flower like pattern with different strain energy profile. The reference crease is displayed in the black circle. . . . .	48
3.12	Loading of a bistable four-fold vertex. Energy curves plotted for a case with missing angle of $7.5^\circ$ . . . . .	50
3.13	Bistable Miura beams. The physical models are made with polymer creases and cardboard paper panels (The left edge is fixed at $\theta = 20^\circ$ ). . . . .	51
4.1	Origami folding is difficult to simulate because of the existence of global panel contact. . . . .	56
4.2	Panel penetration prevention is achieved by creating an imaginary repulsive force field around the triangle, and the magnitude of the forces can be calculated based on the closest distance from the point to the triangle $d$ . . . . .	59
4.3	Calculation of the point to triangle distance. . . . .	61
4.4	(a-c) Numerical verification of penetration prevention and contact initiation (requirements 2 and 3); (d-f) Numerical verification for continuity of internal forces (requirement 1). . . . .	69
4.5	Intentional and unintentional omissions of contact. . . . .	71
4.6	Influence of potential scaling factor and using the model to simulate thick panels in origami. . . . .	73
4.7	The panel contact model can capture the internal forces and reaction forces accurately. . . . .	74
4.8	Self-folding of an origami box pattern with inter-panel contact. . . . .	76
4.9	Self-folding and loading of the locking box corner. . . . .	77
4.10	Studying the correct folding sequence to build an origami box corner using inter-panel contact. . . . .	79
4.11	Studying the stiffness jumps in origami assemblages under the influence of global panel contact. . . . .	80
5.1	Simulating of electro-thermal actuation with a bar and hinge model. . . . .	84
5.2	Flowchart for the rapid simulation framework for electro-thermally actuated origami systems. . . . .	86
5.3	Simulating heat transfer using a bar and hinge model. . . . .	87
5.4	Capping $t_{env}$ to simulate thermal boundaries. . . . .	88
5.5	Verification of the proposed simulation for heat transfer within the origami structure. . . . .	91
5.6	Calibration of the heat transfer between the origami and the surrounding environment. . . . .	93

5.7	Checking the model accuracy for capturing the heat transfer between the origami and the surrounding environment with different material thermal conductivity. . . . .	94
5.8	Comparison between the predicted folding behavior from simulation method and the measured folding behavior of electro-thermal one-panel micro origami. . . . .	95
5.9	Comparison between the predicted folding behavior from simulation method and the measured folding behavior of electro-thermal two-panel micro origami. . . . .	96
5.10	Simulation of the self-folding of an origami crane. (a) Folding the crane pattern with applied heating to all active creases. (b) Folding the crane pattern with two creases deactivated. . . . .	98
5.11	Simulation of a Miura-ori pattern lifting device. . . . .	100
5.12	Optimizing the power consumption of a micro-origami 3-D gripper. . . . .	101
5.13	Verifying the results of optimization with experiments. . . . .	102
6.1	Using machine learning as surrogate models for physical simulations. . . . .	107
6.2	Training process of machine learning methods. . . . .	108
6.3	Decision tree method for solving supervised learning problems. . . . .	109
6.4	Using interpretable machine learning to compute design rules from origami design. . . . .	110
6.5	A detailed framework for pattern selection and feature design of origami. . . . .	111
6.6	(a) Introduction of decision tree method. (b) Training a decision tree. (c) Using the one-hot encoder to convert categorical data. (d) Hold out testing setup. . . . .	115
6.7	Gird search results for the canopy database. . . . .	116
6.8	Gird search results for the gripper database. . . . .	117
6.9	Gird search results for the arch database. . . . .	118
6.10	Building the origami canopy database. . . . .	119
6.11	Design rules computed for the canopy database. . . . .	120
6.12	Building the origami gripper database. . . . .	122
6.13	Design rules computed for the origami gripper database. . . . .	124
6.14	Populating the origami arch database using an origami shape fitting algorithm. . . . .	126
6.15	Design rules computed for the origami arch database. . . . .	128
A.1	The history of simulation of origami systems in a broad brush stroke (left) and related simulations and analyses from other engineering disciplines (right). . . . .	135
A.2	Definitions of common origami terminologies. . . . .	137
A.3	An introduction to kinematics-based simulations. . . . .	141
A.4	Developability and flat-foldability of an origami with a single vertex. . . . .	143
A.5	Simulating origami folding using spherical trigonometry. . . . .	145
A.6	Applying the fold angle multiplier to analyze the folding motion of an Miura origami pattern. . . . .	147
A.7	Geometry of Miura-ori using standard trigonometry. . . . .	148
A.8	Simulating “thin and rigid” origami vertex as spherical linkage. (a) An origami system. The $n_1, n_2, n_3$ denotes a local coordinates for the first panel (corresponds to $\theta_1$ ), where we have $n_1 \parallel e_1$ and $n_3$ perpendicular to the panel. (b) The corresponding spherical linkage model. . . . .	150
A.9	Loop closure based simulation techniques cannot capture situations where panels intersect. . . . .	153

A.10	Origami with openings (a), and those with compliant creases (b,c) can be modeled similar to spherical linkages, but with additional constraints. . . . .	154
A.11	Design and modeling techniques for thick origami systems. . . . .	156
A.12	An introduction to mechanics-based simulations of physical systems. . . . .	158
A.13	Using kinematic simulations to capture simple mechanical responses. . . . .	162
A.14	Rigid panel models for kinematic studies. (a) Rigid bar models; (b) Rigid truss model for thick origami; (c) Rigid frame models. . . . .	163
A.15	(a) The bar element and the rotational spring element; (b) standard bar and hinge model for simulating origami; (c) compliant crease bar and hinge model for simulating origami. . . . .	165
A.16	Using plate theory based models to simulate origami systems. (a) from [Zhang et al., 2021], (b) right from [Hu et al., 2021]. . . . .	168
A.17	Different types of FE models used for simulation of origami structures. The lower figures of (a) to (d) are from [Filipov et al., 2016], [Heimbs et al., 2007], [Hernandez et al., 2016a], and [Fang et al., 2016] respectively. . . . .	170
A.18	Different types of mechanical models for origami panels and creases. . . . .	172
A.19	Panel contact and prevention of panel penetration in origami simulation. Figure (a) from [Liu and Paulino, 2017a], figure (b) from [Gillman et al., 2018], figures (c) and (d) from [Zhu and Filipov, 2019a], and figure (e) from [Dong and Yu, 2021]. . . . .	175
A.20	Multi-physics simulation of active origami. Figure (b) from [An et al., 2018], figure (c) from [Zhu and Filipov, 2021a], figure (d) from [Hathcock et al., 2021], figure (e) from [Nauroze et al., 2018]. . . . .	177
A.21	A universal origami simulation approach is not achievable; instead, there is an exponential growth in tailored models that can capture distinct properties and characteristics for individual origami problems. . . . .	185
A.22	Considerations for selecting and developing simulation techniques for origami systems.	187

## List of Tables

1.1	Existing challenges and the proposed solution methods in each chapter. . . . .	9
3.1	Nomenclature used in Chapter 3 . . . . .	35
4.1	Nomenclature used in Chapter 4 . . . . .	55
4.2	Pseudo-code for Implementation of Panel Contact . . . . .	70
A.1	A summary of kinematics-based simulations for thin and rigid origami. . . . .	139
A.2	A summary of kinematics-based simulations for compliant crease origami systems and thick origami systems. . . . .	140
A.3	A summary of rigid panel-based models and bar and hinge models for origami. . . . .	159
A.4	A summary of plate theory based simulations and FE simulations for origami. . . . .	160
A.5	A summary of available kinematic simulation packages for origami structures. . . . .	180
A.6	A summary of available mechanical simulation packages for origami structures. . . . .	181
A.7	A summary of adds-on packages and commercial packages for origami structures. . . . .	182

## **Abstract**

The elegant and simple idea of using origami to create 3D structures from 2D surfaces is suitable for designing engineering systems like soft robots, programmable metamaterials, smart facades, shareable infrastructures, and many more. This dissertation proposes an integrated framework on fabrication, simulation, and design of functional origami systems to overcome the limitations of state-of-the-art methods. This new framework can be used to build functional origami structures with superior and versatile functionalities for applications where programmability, 3D assembly, and dense packaging are desirable.

First, this dissertation introduces a versatile fabrication method for an electro-thermal micro-origami system that can accomplish superior controllability and complex functionality that is beyond the capability of existing micro-origami structures. A high-performance actuator, which can fold both elastically and plastically, is designed and integrated into these micro-origami structures to achieve multi-degree-of-freedom actuation and versatile shape morphing motion for complex functionality. The work in this chapter greatly extends the motion versatility and functional complexity of existing micro-origami systems. This electro-thermal micro-origami can be used for building functional micro-robots, surgery tools, transducers, and many other MEMS devices.

Next, this work introduces a simulation framework developed for functional origami structures, where three new models are created to capture complex behaviors within functional origami systems. The framework can simulate more realistic geometries

of origami compliant creases, global panel contact between origami assemblages, and the multi-physical actuation in active origami. In addition, an open-access simulation package is developed to implement this framework and the package is published on GitHub. Together, the three models and the simulation package provide the much needed tools for capturing the behaviors of functional origami structures and pave the ground for future researches on optimization and inverse design of functional origami. The Appendix of this dissertation gives a thorough review of different origami simulation techniques. For the first time, this work systematically analyzes and categorizes different simulation techniques for origami-inspired systems so that future researchers can better select and develop origami simulations for their specific applications.

Finally, this dissertation harnesses an interpretable machine learning method to establish a holistic inverse design procedure of functional origami structures. This method can handle categorical features for comparing different origami patterns and tackles multi-objective problems for considering multi-physics performance targets. Moreover, the method enables existing geometry-based origami inverse design algorithms to further consider non-geometrical performance. The proposed method provides a holistic inverse design procedure for building superior functional origami systems.

In summary, this work provides novel methods for fabrication, simulation, and design of origami structures. The established methods in this dissertation complement existing tools of origami engineering and allow future researchers to build better functional origami systems for resolving practical engineering challenges.

## Chapter 1. Introduction

Folding, a concentration of curving within a thin film or a narrow rod of material, has generated various inspiring phenomena in nature and in our daily lives. For example, some insects have wings with folded edges to resist the load from flying [Wootton, 1981] and proteins require accurately folded 3D configurations to function properly [Dobson, 2003]. Seeing artist transforming a thin piece of paper into origami insects, fishes, and birds must have inspired engineers and scientists to think about the vast potential of utilizing folding techniques to build structural systems for engineering applications. Over the past decades, various origami inspired structures have been proposed for different applications, including deployable architectural structures [Filipov et al., 2015, Filipov et al., 2019, Cai et al., 2019], reconfigurable space structures [Lang et al., 2016, Cai et al., 2017b, Hernandez et al., 2017b], functional robots [An et al., 2018, Felton et al., 2014, Kamrava et al., 2018], actuators and sensors [Martinez et al., 2012, Nauroze et al., 2018], small-scale responsive systems [Yoon et al., 2014, Rogers et al., 2016, Na et al., 2015, Breger et al., 2015, Bassik et al., 2009], medical devices [Jager et al., 2000, Leong et al., 2008, Leong et al., 2009], metamaterials [Fang et al., 2018, Lv et al., 2014, Ma et al., 2018b, Silverberg et al., 2014, Silverberg et al., 2015, Kamrava et al., 2017] and more [Yasuda et al., 2017, Faber et al., 2018, Hur et al., 2017]. There are several advantages of using origami inspired assemblages for building engineering structures. For example, origami structures provide methods to densely pack engineering systems, saving storage space and maximizing the functionality [Lang et al., 2016, Hernandez et al., 2017b]. In addition, many origami structures can be used to create metamaterials with tunable mechanical, thermal, electro-magnetic, and other properties [Fang et al., 2018, Lv et al., 2014, Ma et al., 2018b, Liu et al., 2019, Overvelde et al., 2016, Hanna et al., 2014, Schenk and Guest, 2013]. Moreover, origami principles provide a fabrication method to convert 2D surfaces into 3D systems with intricate geometries, especially when it is difficult to build 3D structures directly [Rogers et al., 2016, Na et al., 2015, Breger et al., 2015, Bassik et al., 2009, Leong et al., 2010].

In the following sections, we will give an overview of the application, fabrication, simulation, and design of functional origami. We will discuss the capabilities and limitations of the existing methods. Furthermore, the limitations within existing fabrication, simulation, and design methods for origami will lead us to five unresolved challenges in the field of origami engineering. These five challenges include: (1) How to build functional origami to achieve complex functions? (2) How to simulate functional origami with compliant creases? (3) How to simulate global panel contact



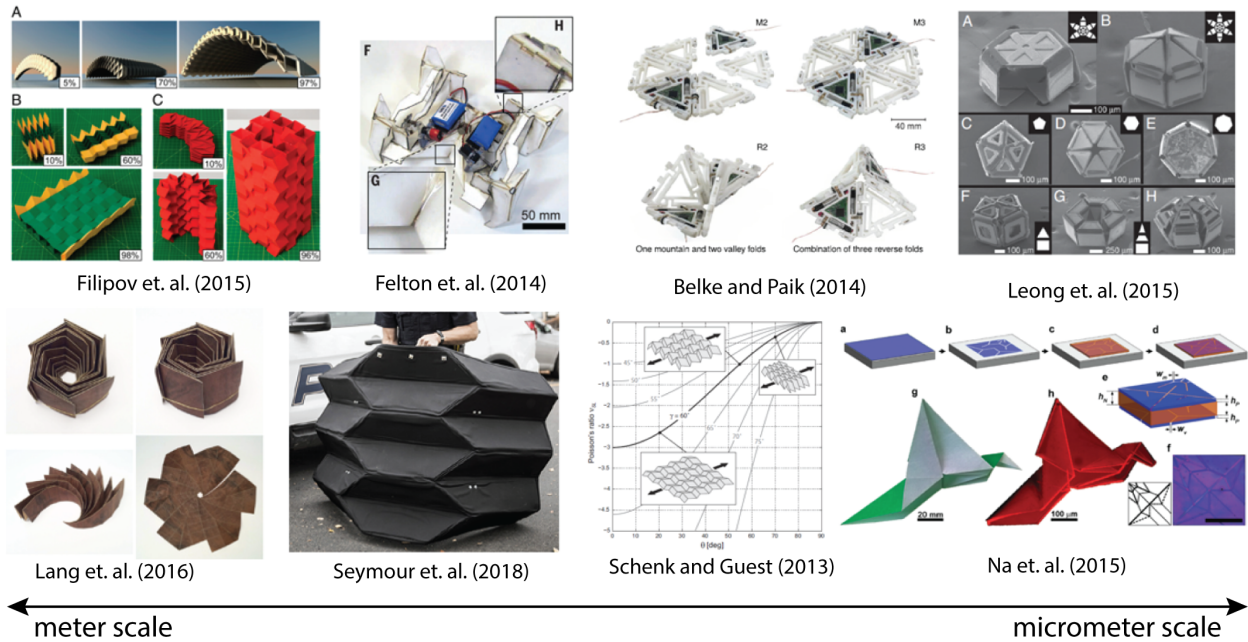


Figure 1.1: Functional origami applications at different length scales.

in functional origami? (4) How to simulate multi-physics actuation in functional origami? and (5) How to design functional origami with categorical features and multi-objective performance targets? Finally, to address these five challenges, this chapter will introduce a novel integrated framework for fabrication, simulation, and design of functional origami that is proposed in this dissertation.

## 1.1 Applications of Functional Origami

Functional origami is a type of engineered origami structure that can achieve designated functions that is beyond the aesthetic purpose of origami art. Functional origami structures can be used for engineering applications at different length scales (see Fig. 1.1). At greater-than-meter scales, these origami systems can be used to design deployable structures for packaging applications or for adaptive purpose. Architectural structures like adaptive facades can be made with functional origami [Babilio et al., 2019], and space structures like solar panels and antennas can be densely packed using the appropriate origami patterns [Lang et al., 2016, Hernandez et al., 2017b]. Other slightly smaller structures like packageable ballistic shields can also be made with origami assemblies [Seymour et al., 2018].

At meter-to-centimeter scales, functional origami structures provide novel methods to build various reconfigurable robots and programmable mechanical systems. Using the concepts of origami, engineers have successfully transformed flat surfaces to 3D robots [An et al., 2018] for

achieving functions like walking [Felton et al., 2014] and gripping [Butler et al., 2020]. Other robotic components, like actuator and sensor systems, can also be made with origami structures [Li et al., 2017, Kamrava et al., 2017, Nauroze et al., 2018]. In addition, origami systems can also be used to build metamaterials for programmable properties. For example, various mechanical metamaterials have been built using origami assemblages [Fang et al., 2018, Schenk and Guest, 2013, Lv et al., 2014, Silverberg et al., 2014, Silverberg et al., 2015]. Electro-magnetic systems like programmable frequency selective surfaces (FSS) can also be built using origami structures [Fuchi et al., 2016, Fuchi et al., 2012, Nauroze and Tentzeris, 2019, Biswas et al., 2020].

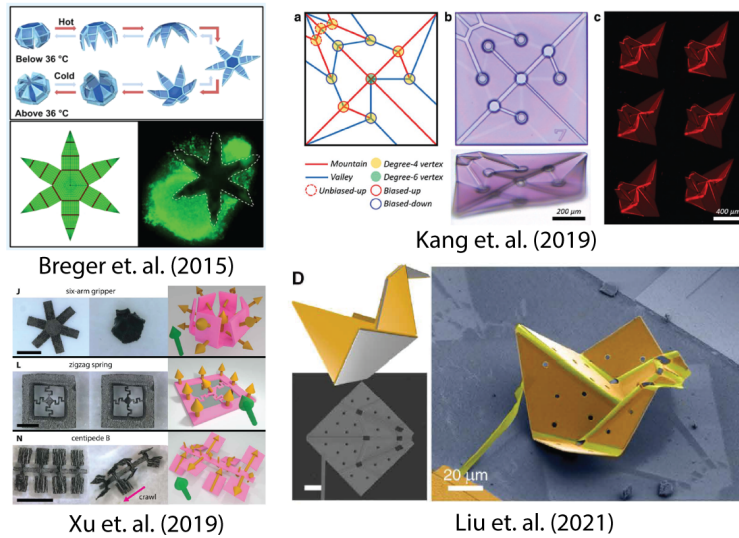
At sub-centimeter scales, functional origami are more often used as fabrication techniques to build 3D systems. This is because conventional small scale fabrication methods like photolithography based micro-fabrication have difficulties to build complex 3D structures directly [Rogers et al., 2016, Na et al., 2015]. Through forming 3D systems using origami principles, these small-scale structures can achieve superior functions. For example, micro-origami can accomplish non-invasive surgery [Leong et al., 2009, Yoon et al., 2014], complex robotic motions [Liu et al., 2021, Na et al., 2015], cell manipulation [Jager et al., 2000], and drug delivery [Leong et al., 2008].

## **1.2 Current Fabrication Methods for Functional Micro-Origami**

The fabrication of functional origami is different at different scales. In general, there are more fabrication methods and actuation methods available at larger scales. For example, at decimeter scale, origami systems can be made with broadly available materials like flat plastic sheet, cardboard, and electric motors [Felton et al., 2014, Belke and Paik, 2017]. In addition, active materials (such as thermally active polymers or SMAs) can also be used to fold origami systems to form different 3D geometries at centimeter scales [An et al., 2018, Hawkes et al., 2010]. Finally, other fabrication methods like the PCB based monolithic fabrication [Sreetharan et al., 2012, Wood et al., 2008] and the 3D printing technology [Mao et al., 2015] can also be used to build origami systems at this scale.

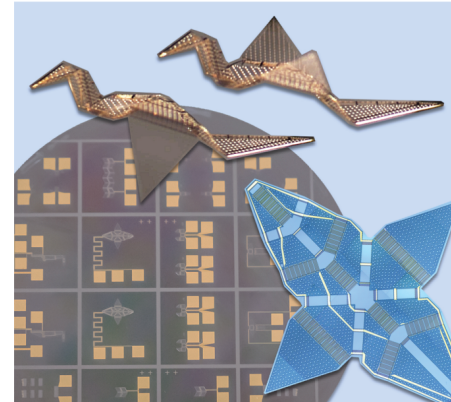
However, less methods are available to build functional origami systems at sub-millimeter scale because it is difficult to build small electric motors and integrate heterogeneous components into micro-scale systems. In general, engineering structures at sub-millimeter scale are built with photolithography based micro-fabrication processes. These processes are used to create microelectromechanical system (MEMS), which is the technology that is behind the accelerometers, gyroscopes, RF-switches, and many other micro-devices we use in our daily lives [Senturia, 2001]. This photolithography based micro-fabrication process has an inherent 2D nature [Rogers et al., 2016, Leong et al., 2010] and has difficulties to build complex 3D geometries directly. There-

### Current Micro-Origami Achieves Simple Fold-Unfold Motions



### Existing Challenge:

How to build micro-origami to achieve complex motions and functions?



➔ Chapter 2

Figure 1.2: Fabrication methods for small-scale functional origami and challenges in the field.

fore, it is beneficial to combine origami designs and the photolithography based fabrication so that we can convert 2D micro-surfaces to complex 3D micro-structures for superior performance and functionality (see Fig. 1.2).

Folding actuation at micro-scale is usually achieved using bi-material morphs created with active materials [Kang et al., 2019, Na et al., 2015, Silverberg et al., 2015, Yoon et al., 2014]. These bimorph designs usually have two layers: one made with an active material and the other made with a passive material. When a certain stimulus is applied, the active material will experience expansion or contraction and the other material will stay passive, which forces the bimorph system to generate bending motion. Unlike the discrete hinges used in larger origami structures, these bi-material morphs bend with distributed curvatures and the widths of these actuating creases are usually not negligible. Pragmatic solutions for creating small-scale functional origami structures include using passive hinges with magnetically active panels [Shaar et al., 2015, Iwase and Shimoyama, 2005, Yi and Liu, 1999, Zou et al., 2001, Kim et al., 2011], thermally active materials [Kang et al., 2019, Na et al., 2015, Silverberg et al., 2015, Yoon et al., 2014], bimetallic morphs [Randhawa et al., 2010, Bassik et al., 2009], and several others [Liu et al., 2011, Fu et al., 2018, Ning et al., 2018].

Despite the advancements in designing and building functional micro-origami structures, the current functional micro-origami systems usually have one or more limitations. For example, existing micro-origami systems tend to have limited motion complexity and can only achieve simple fold and unfold motions because these systems require applying environmental stimuli for actuation, where the folding or unfolding motions are correlated to applying or removing the stimuli [Na

et al., 2015]. In addition, these active micro-origami systems tend to have slow folding speed either because they use actuation materials with relatively slow response speed [Liu et al., 2011] or because it takes time to apply environmental stimuli (such as heating up water [Na et al., 2015, Kang et al., 2019]). Moreover, existing actuator creases can either fold elastically (reversibly) or plastically (irreversibly) but not both, which limits the programmability of current micro-origami systems. These limitations lead us to the first challenge we will tackle in this dissertation and it is:

*Challenge 1: How to build functional micro-origami to achieve complex functions?*

### **1.3 Current Simulation Methods for Functional Origami**

There has been a number of simulation methods developed for analyzing the folding motions and properties of functional origami structures in the past decades. The Appendix of this dissertation gives a thorough review on origami simulations. Here, we will briefly go over these existing methods, explain their formulations, point out their limitations, and identify three challenges to be resolved in this dissertation. In general, we can broadly split origami simulation methods into three categories and they are: kinematic models, simplified mechanical models, and finite element models (see Fig. 1.3).

Early origami simulation methods were mostly kinematics based. For example, the rigid folding algorithm developed by Tachi is one successful kinematic simulation method for origami structures [Tachi, 2009c, Tachi, 2009a]. The method assumes the origami panels are rigid so all the deformations are concentrated in the folding creases [Tachi, 2009c, Tachi, 2009a], and these folding creases are simplified as 1D rotating hinge lines for simplicity. The algorithm tracks the viable folding motions complying with the geometrical constraints imposed by the pattern with numerical methods such as the Euler’s method [Tachi, 2009c, Belcastro and Hull, 2002]. Similar and mathematically equivalent kinematic simulations for origami structures can also be found in other studies [Evans et al., 2015b, Feng et al., 2020a, Wu and You, 2010]. Although this type of methods is successful and is widely used in the origami engineering community, it cannot capture the deformable panels and compliant creases (folding creases with distributed width) in functional origami structures. To extend kinematical simulations to capture compliant creases, the “smooth fold” model is developed [Hernandez et al., 2016b, Hernandez et al., 2017c]. This model uses the rigid panel assumption but can consider the compliant crease geometries explicitly.

More recently, simplified mechanical models, such as the bar and hinge model, are proposed to capture deformable panels in origami structures. These models treat the entire origami structure as a deformable body with flexibility in both the panels and the creases [Liu and Paulino, 2017a]. A number of different variations of bar and hinge models were developed in the past decades [Filipov et al., 2017, Liu and Paulino, 2018a, Zhu and Filipov, 2020, Zhu and Filipov, 2019b, Zhu and Filipov,

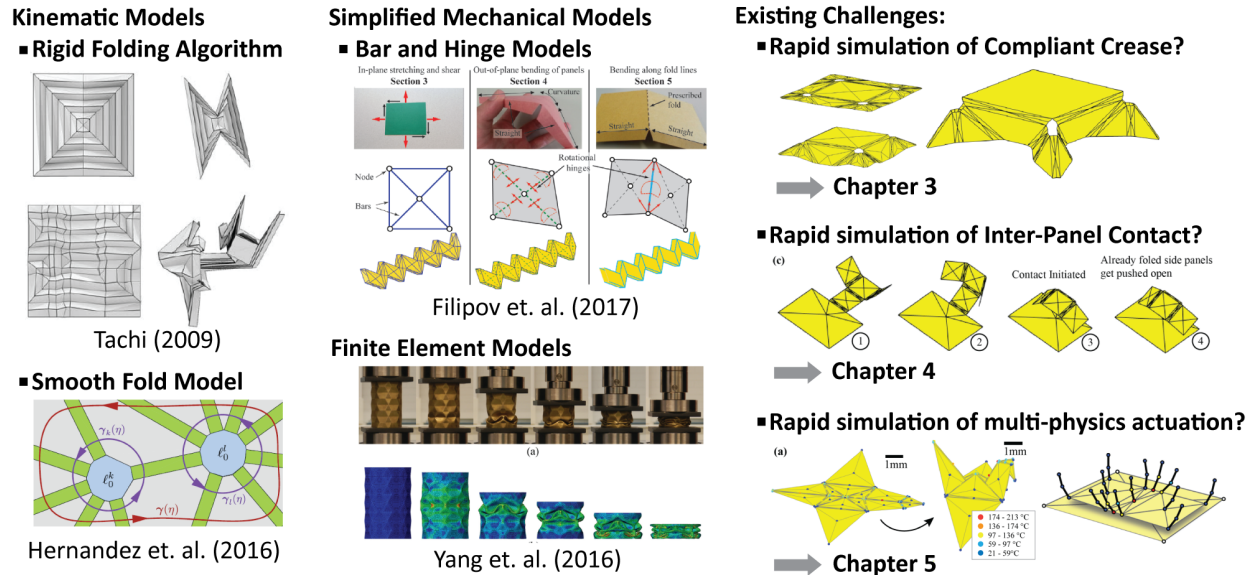


Figure 1.3: Simulations methods for functional origami and challenges in the field.

2019a], and a detailed comparative study is available in [Filipov et al., 2017]. In addition to the bar and hinge models, plate theory based models were also created to capture the behaviors of functional origami systems [Hu et al., 2021, Zhang et al., 2021, Soleimani et al., 2021]. These plate theory based models can be seen as coarse-meshed versions of FE simulations where the model fidelity is traded for faster simulation run time.

Finally, we can use finite element (FE) models to simulate the behaviors of functional origami structures. These FE simulations are used widely in origami engineering community because they produce high fidelity results [Ma and You, 2014, Ma et al., 2018a, Mukhopadhyay et al., 2020, Na et al., 2015]. These simulations are usually implemented using plate elements and can capture the local deformations in both origami panels and origami creases [Ma and You, 2014, Ma et al., 2018a, Mukhopadhyay et al., 2020, Na et al., 2015]. Although these FE simulations can produce high fidelity results, it usually takes tremendous efforts to build and run them to obtain usable results. Moreover, FE simulations can behave like “black boxes”, which makes them not suitable for some scientific explorations.

This dissertation will focus on the bar and hinge model, which is the most widely used simplified mechanical model for origami structures. This model is popular among the origami engineering community because it can capture the global mechanical behaviors in origami systems and is computationally efficient [Wei et al., 2013, Grey et al., 2020, Liu et al., 2020, Filipov and Redouty, 2018, Masana and Daqaq, 2019, Gillman et al., 2019]. The bar and hinge model simulates an origami pattern using extensional bar elements and rotational spring elements. The bar elements are extensional springs in 3D that can capture the in-plane behaviors such as panel stretching and

shearing, and the rotational spring elements are folding hinge lines with stiffness that can capture the out-of-plane behaviors such as panel bending and crease folding [Liu and Paulino, 2016, Liu and Paulino, 2017a].

One limitation of existing bar and hinge models is that they use simplified 1D creases and thus, cannot simulate compliant crease origami structures. Capturing compliant creases is important because most functional origami systems do not have localized hinges and instead, they have thin shell like regions to serve as creases [Jager et al., 2000, Bassik et al., 2009, Wheeler and Culpeper, 2016, Leong et al., 2009, Yoon et al., 2014]. Capturing these compliant creases is also important for studying advanced mechanical behaviors such as bistability and multi-stability in origami assemblies [Faber et al., 2018] and allows better representation of origami contact and panel thickness accommodation [Zhu and Filipov, 2019a, Butler et al., 2020]. This limitation leads us to the second challenge of this dissertation:

*Challenge 2: How to simulate functional origami with compliant creases?*

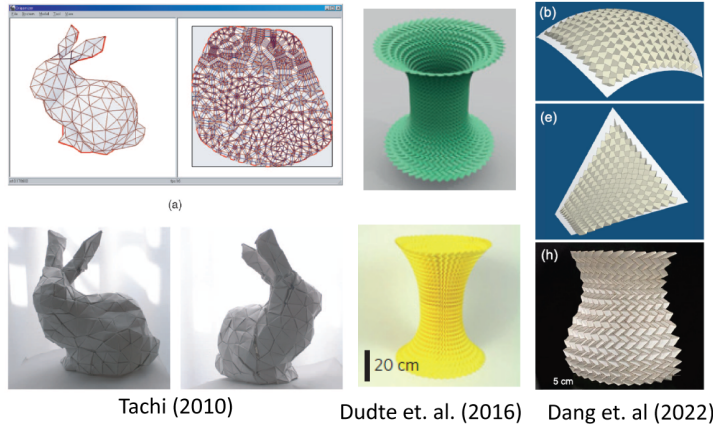
Another major limitation of these existing bar and hinge models is that they cannot capture the global panel contact induced behaviors within functional origami structures [Liu and Paulino, 2017a, Liu and Paulino, 2016]. In fact, this limitation is not unique to the bar and hinge models. Prior to this work, both existing simplified mechanical simulations and kinematic simulations could not capture global panel contact [Schenk and Guest, 2013, Wei et al., 2013, Belcastro and Hull, 2002, Tachi, 2009c]. Although FE simulations tend to provide an alternative method, the computation time required to run a contact simulation with FE approaches tends to be long. This leads us to the third challenge of this dissertation:

*Challenge 3: How to simulate global panel contact in functional origami?*

Finally, existing bar and hinge models cannot capture multi-physics actuation mechanisms within functional origami structures. Similar to the global contact, integrating multi-physics actuation into other simplified mechanical simulations or kinematic simulations is also challenging. Without resolving this issue, the design of functional origami systems can only be based on trial and error approaches, which are not effective. For example, thermally active folding creases are used to fold origami structures at small scales with only sub-optimal performance because these functional origami structures are designed using trial and error approaches [Zhu et al., 2020, Na et al., 2015, Kang et al., 2019, Breger et al., 2015]. To address this limitation, this dissertation also aims to resolve the following Challenge 4:

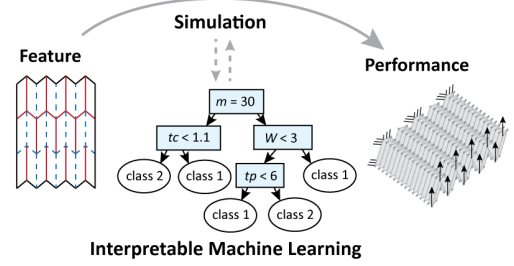
*Challenge 4: How to simulate multi-physics actuation in functional origami?*

### Current Origami Design Methods Focus on Shape Fitting



### Existing Challenge:

How to build active origami with categorical features, multi-physics behaviors, and multi-dimensional performance target ?



Chapter 6

Figure 1.4: Design methods for functional origami and challenges in the field.

## 1.4 Current Design Methods for Functional Origami

The advancement in origami simulation techniques makes it possible to develop inverse design algorithms of functional origami structures. So far, most of these existing inverse design methods focus on addressing the shape fitting problem [Dang et al., 2022, Dudte et al., 2016, Tachi, 2010d] (see Fig. 1.4). For example, Tachi’s Origamizer [Tachi, 2010d] provides an algorithmic solution to fit an origami to arbitrary 3D geometries using tuck-folding techniques. The work by Dudte et al. demonstrates an optimization based method to build Miura-ori patterns to fit arbitrary surfaces [Dudte et al., 2016]. In addition to the shape fitting, other kinematic based inverse design problems were also studied by the origami community. For example, the TreeMaker proposed by Lang [Lang, 1997, Lang, 2009] provides an algorithm to compute the base pattern design for complex origami. The work by Chen et al. [Chen et al., 2020] demonstrates that it is possible to use mixed integer programs to determine the mountain-valley assignment of origami patterns.

Despite the advancements introduced above, designing functional origami structures is still a challenging task. This is because the majority of existing inverse design methods for origami structures do not consider multi-physical behaviors and are only tailored for specific patterns. These methods cannot tackle categorical features needed for comparing different origami patterns and cannot resolve multi-objective problems needed for simultaneously considering multiple multi-physical performance targets. Without the capability of comparing different patterns and addressing multi-physical performance targets, a holistic origami inverse design methodology cannot be established. These limitations in existing origami design methods lead us to the Challenge 5:

*Challenge 5: How to design functional origami structures with categorical features and multi-objective performance targets?*

Table 1.1: Existing challenges and the proposed solution methods in each chapter.

<b>Topics</b>	<b>Existing challenges</b>	<b>Solution</b>
Fabrication	How to build functional micro-origami to achieve complex functions?	Chapter 2
Simulation	How to simulate functional origami with compliant creases?	Chapter 3
	How to simulate global panel contact in functional origami?	Chapter 4
	How to simulate multi-physics actuation in functional origami?	Chapter 5
Design	How to design functional origami with categorical features and multi-objective performance targets?	Chapter 6

## 1.5 Novel Fabrication, Simulation, and Design of Functional Origami

The work in this dissertation establishes a novel framework for fabrication, simulation, and design of functional origami systems. Each chapter in this dissertation aims to resolve one of the challenges introduced previously. Table 1.1 summarizes these unresolved challenges and the proposed solutions in this dissertation.

First, a versatile micro-fabrication process is established in Chapter 2 to resolve the first challenge. With this novel micro-fabrication process, an electro-thermal actuator that can fold both elastically and plastically can be integrated into functional micro-origami systems to achieve complex motions and functions. The folding capability of this actuator array is tested to demonstrate its superior performance. Multiple micro-origami devices, including a micro-crane that can fold and flap its wings and a inter locked micro-origami gripper, are built and tested in this chapter to highlight the superior performance and functionality.

In addition, a multi-physics based reduced order simulation framework is established to resolve Challenges 2, 3, and 4. This simulation framework is based on bar and hinge models but drastically expands the capabilities of existing formulations. Chapter 3 introduces an improved bar and hinge model to capture the existence of compliant creases. Additional bar elements and rotational spring elements are used to capture the distributed width of compliant creases explicitly. The bar area and rotational spring stiffness are derived by matching the stiffness of the bar and hinge model to that of a theoretical plate system. After the derivation, finite element simulations are used to verify the accuracy of the model. Computational examples show that this model is crucial for simulating bistable behaviors in functional origami systems. Chapter 4 establishes the first global panel contact model for simplified origami simulations. This model introduces a barrier function into the total potential of the origami system to address the potential panel contact. This contact potential function can generate large forces between contacting panels so that the panel penetration is prevented. Application examples show that the model is efficient and can capture the accurate



contact geometry within an origami pattern. This model allows us to study the stiffness jumps and interlocking behaviors associated with global panel contact in functional origami assemblages that cannot be captured with previous simplified origami simulations. Chapter 5 introduces a multi-physics based model to capture the folding behaviors in electro-thermal micro-origami systems. In this chapter, a reduced order heat transfer simulation is established for functional origami systems. A 1-D conduction model is established to capture the heat transfer between the origami and the surrounding environment and a standard linear triangle thermal element is used for simulating the heat transfer within the origami structure. This model is verified against both finite element simulations and experiments to demonstrate its accuracy and effectiveness. More significantly, this chapter uses application examples to show that this actuation model can be used to optimize the performance of electro-thermal functional origami structures. In addition to the three models demonstrated in Chapter 3, Chapter 4, and Chapter 5, an open-access simulation package that implements all three models is coded and published on GitHub [Zhu and Filipov, 2021c]. Finally, a thorough review on origami simulations can be found in the Appendix. For the first time, this review systematically categorizes existing simulation techniques for origami structures, introduces their formulations, and analyzes their pros and cons. The work will enable future researchers to develop better simulation techniques for origami structures.

Finally, Chapter 6 introduces an interpretable machine learning based inverse design method for functional origami structures to address Challenge 5. When using the proposed methodology, an origami performance database is built using the simulation package developed in Chapters 3 to 5 and a decision tree-random forest machine learning method is trained to learn the underlying structures in this database. We demonstrate that identifying the more informative tree branches in the decision tree-random forest method can provide us useful design rules to build superior functional origami structures. This machine learning based inverse-design method is particularly suitable for origami systems because it can capture the interaction between categorical and continuous features and can tackle the multi-objective problems needed for designing functional origami with multi-physics performance targets. We also demonstrate that this methodology can enhance other origami shape fitting algorithms to design for non-geometrical performance targets such as mechanical stiffness.

## **1.6 Simulation Codes and Databases**

In addition to developing the simulation models from Chapter 3 to 5, a simulation code package is developed for implementing these three models. Moreover, the origami performance databases used in Chapter 7 are also published and made open-access online. Here, we introduce the simulation code package and the origami performance databases built for this thesis.

**SWOMPS** An open access software package that implements all the origami models from Chapter 3 to Chapter 5 is coded and made open-access on GitHub. This package is called SWOMPS and it stands for Sequentially Working Origami Multi-Physics Simulator. The following link can be used to find the package <https://github.com/zzhuyii/OrigamiSimulator>. A tutorial paper associated with this simulation package can be found in [Zhu and Filipov, 2021c].

**Database codes** Three origami performance databases used in Chapter 6 and the corresponding simulation codes for building the three databases are also provided as supplementary materials. These three databases are:

- Data S1: Database on origami canopy;
- Data S2: Database on active origami gripper;
- Data S3: Database on origami shape fitting;

The codes used for generating the databases are available on GitHub: <https://github.com/zzhuyii/GenerateOrigamiDataSet>

**Machine learning codes** The implementation codes for the decision tree based inverse design method introduced in Chapter 6 are also published on GitHub: <https://github.com/zzhuyii/TreeForOrigami>. This code package is built in Python.

## **Chapter 2. Elctro-Thermal Micro-Origami**

This chapter introduces an electro-thermal micro-origami system that can fold elastically and plastically to resolve Challenge 1 of this dissertation. A versatile and powerful MEMS actuator is designed and integrated into micro-origami systems to achieve complex motions and functions. More specifically, this actuator crease can fold elastically and rapidly at different atmospheric temperatures and can achieve plastic folding to permanently change the fold configuration. The highly versatile motions enabled by these actuator creases allow the micro-origami to achieve sophisticated shape morphing for self-assembly and superior functionality.

This chapter is arranged as the following. First, we will discuss existing MEMS (microelectromechanical systems) and micro-origami systems in Section 2.1. We will echo with Challenge 1 proposed in the Introduction, and give a more detailed discussion on MEMS based actuators. After that, Section 2.2 introduces the design and fabrication of the proposed electro-thermal actuator system, and Section 2.3 uses a single-crease origami device to test the folding capability of the proposed electro-thermal actuator. The results show that the proposed system can achieve large folding angle elastically and rapidly, can function at various atmospheric temperatures, and can fold plastically to reprogram the zero current rest angle. Moreover, a long term deterioration test is performed to demonstrate the robustness of the actuator. After testing the folding behaviors, Section 2.4 shows a number of samples to highlight the capabilities of the proposed micro-origami systems. These micro-origami examples show that the proposed system can achieve complex functions and motions, like folding a crane with flapping wings and building inter-locked origami gripper systems, by combining elastic folds, plastic folds, and individually controllable folding circuits.

### **2.1 MEMS and Micro-Origami**

MEMS stands for microelectromechanical systems and is the technology behind most of the sensors and micro-systems, including the accelerometers, gyroscopes, ink-jet printing heads, RF-switches, and many more, that we use in our daily lives. Despite being a robust field, most MEMS devices are limited to a 2D plane because traditional photolithography fabrication for MEMS has difficulties building 3D systems directly. Combining origami principles with MEMS is beneficial because it overcomes the limitation of traditional MEMS and enables the fabrication of complex

3D micro-systems [Na et al., 2015, Bassik et al., 2009, Leong et al., 2010]. However, as discussed in Chapter 1 Introduction, existing micro-origami systems tend to have limitations that prevent them from achieving complex motions and functions, including the slow response speed, reliance on external stimuli, and limited motion versatility.

To resolve the challenge, this chapter designs and integrates a novel MEMS based actuator, which is more powerful and versatile than the existing actuators for micro-origami, into a functional origami structure. More specifically, this chapter uses an electro-thermal bimorph micro-actuator. To give a rationale of choosing this particular actuator, we will first give an introduction of different MEMS actuators.

Traditional MEMS actuators can be roughly divided into electro-static actuators, piezoelectric actuators, and electro-thermal actuators [Wootton, 1981, Suh et al., 1999, Todd et al., 2006, Chronis and Lee, 2005, Oldham et al., 2007, Choi et al., 2017]. The electro-static actuator tends to have a finger-capacitor structure that can accumulate electric charge when applying voltage. This accumulated electric charge can generate electro-static forces to produce actuator motions. Because electro-static force decays drastically with distance, these electro-static actuators cannot generate large deformations. The piezoelectric actuators use piezoelectric materials, which produce strain when applying voltage, to generate the designated motions. Similarly, these piezoelectric actuators also cannot produce large motions because the output strains are small.

Unlike the previous two forms of MEMS actuators, the electro-thermal actuators can achieve larger motion range. These electro-thermal actuators generate motions using Joule heating and thermal expansion. A number of different designs can be used to convert the thermal expansion in materials to useful actuator motions. These electro-thermal actuators can be further divided into three types: hot and cold arm systems, Chevron-type systems, and bimorph systems [Potekhina and Wang, 2019]. For origami applications, the bimorph electro-thermal actuators are most relevant because they can produce out-of-plane folding motions [Todd et al., 2006, Suh et al., 1999, Ataka et al., 1993, Zhang et al., 2015, Luo et al., 2005, Luo et al., 2006], whereas the rest two types are only capable of providing in-plane motions. Therefore, it is possible to design a powerful electro-thermal bimorph actuator and use it to fold micro-origami for complex motions and functions.

## **2.2 Electro-Thermal Actuator for Functional Origami**

### **2.2.1 Design of electro-thermal actuator**

In this section, we introduce the design of the electro-thermal actuator system. Figure 2.1 shows the design of the bi-layer electro-thermal actuator used to drive the micro-origami. This electro-thermal micro-actuator has a patterned gold heater layer and a SU-8 polymer layer. The actuator

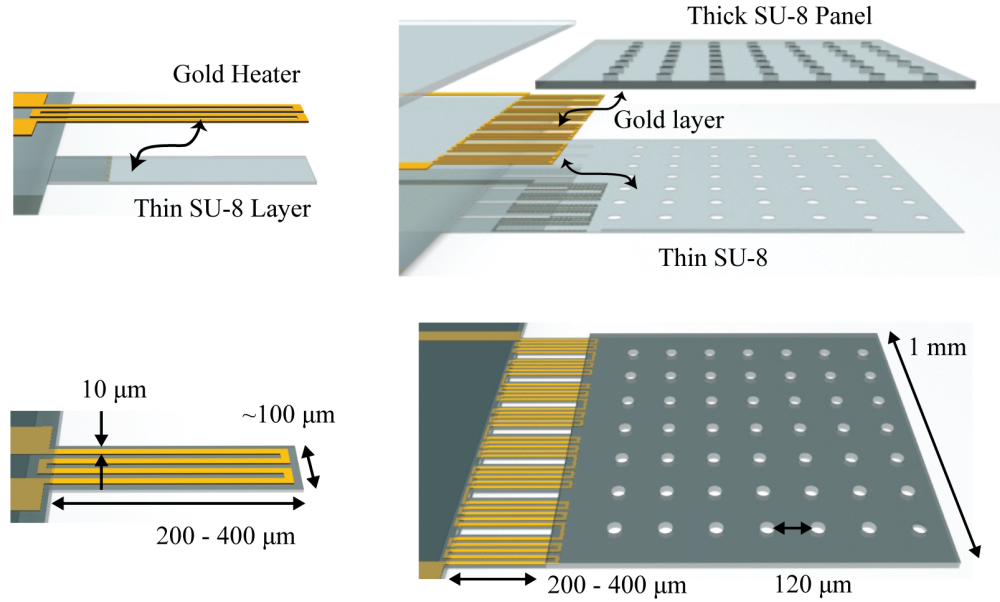


Figure 2.1: Design of the electro-thermal actuator for the active micro-origami.

system can produce large bending motion in two steps. First, Joule heating is generated by applying current through the gold heater to elevate the temperature of the actuator. Next, because the polymer layer has a larger thermal expansion coefficient than the gold, this bi-material actuator can bend towards the gold side. When operating at a low temperature, the folding motion from this actuator array is elastic, so the motion is fully recovered upon removal of the applied current. We choose gold and SU-8 for their relatively large difference in thermal expansion coefficient (TEC) [Chronis and Lee, 2005], which allows the actuators to achieve large folding angles ( $\alpha_{Au} = 14 \text{ ppm/K}$ ,  $\alpha_{SU-8} = 52 \text{ ppm/K}$ ).

The gold layer integrates multiple functions in this micro-origami design, which include: (1) Strengthening the surfaces of the thin film SU-8 to prevent the upwards bending triggered by the residual stress (see Figure 2.2); (2) Heating up the actuators locally; (3) Acting as an electronic circuit to control folding creases separately; (4) Serving as the passive layer for the large difference in TEC. With this high level of integration, the fabrication process is greatly simplified and only needs three masks. The proposed fabrication cannot create actuators that actively bend downwards because putting gold film under the thin film SU-8 triggers unwanted residual stress profile (see Figure 2.2). However, as will be demonstrated later, it is possible to bypass this problem by putting actuators only at upward folding creases while leaving downward folding creases as elastic springs. By arranging these actuators into arrays and connecting them with thick SU-8 panels (see Fig. 2.1), a single-crease origami is made. Figure 2.1 also shows the detailed dimensions of the benchmark

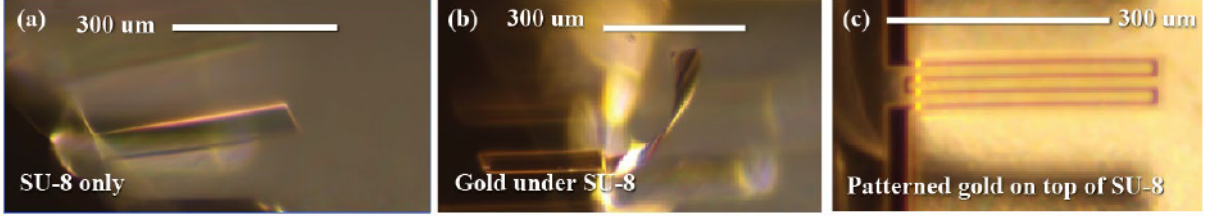


Figure 2.2: Residual stress and curvature of released systems.

single-crease origami tested in this article. Although this work only fabricates and tests designs in the range of 1 mm for a panel, the origami system can be scaled up and down without changing the principle of design.

Here, we introduce the bi-material beam model proposed by Timoshenko [Timoshenko, 1925] that can be used to estimate the folding behavior of this bi-material actuator system. The curvature of the bi-material beam under elevated temperature can be calculated as:

$$\kappa = \frac{6(\alpha_g - \alpha_s)\delta T(1+m)^2}{h(3(1+m)^2 + (1+mn)(m^2 + \frac{1}{mn}))}, \quad (2.1)$$

where the notations used are defined as the follows:  $\alpha_s$  and  $\alpha_g$  are the thermal expansion coefficient of the SU-8 layer and the gold layer;  $m = t_s/t_g$ , where  $t_s$  and  $t_g$  are the thickness of SU-8 layer and the gold layer;  $n = E_s/E_g$ , gives the ratio of Young's modulus of the two material;  $h$  is the total thickness of the bimorph and  $h = t_s + t_g$ ;  $\delta T$  is the elevated temperature of the bimorph actuator.

To optimize the thickness of gold, we fix the thickness of the SU-8 layer to be  $0.8 \mu\text{m}$  and vary the thickness of gold to find a thickness that gives the largest curvature. The Young's modulus of gold is assumed to be  $E_g = 79 \text{ GPa}$  and the thermal expansion coefficient is  $\alpha_g = 14 \text{ ppm/K}$ . We manually reduce the Young's modulus of gold by half because gold only covers about half of the actuator area. The material properties of SU-8 are assumed as the following: Young's modulus of  $E_s = 2 \text{ GPa}$  and thermal expansion coefficient of  $\alpha_s = 52 \text{ ppm/K}$ . The elevated temperature used is set as  $80 \text{ K}$  and the results are given in the Figure 2.3. The curvature is converted into the rotation of a  $400 \mu\text{m}$  beam for more intuitive understanding. The conversion between rotation and curvature is:  $rotation = l \cdot \kappa$ , where  $l = 400 \mu\text{m}$  is the beam length. As shown in Figure 2.3, a gold layer of around  $0.1 \mu\text{m}$  thickness can give the maximum rotation. For the final design, a  $0.2 \mu\text{m}$  thick layer of gold is selected for better robustness without significantly changing the folding behavior.

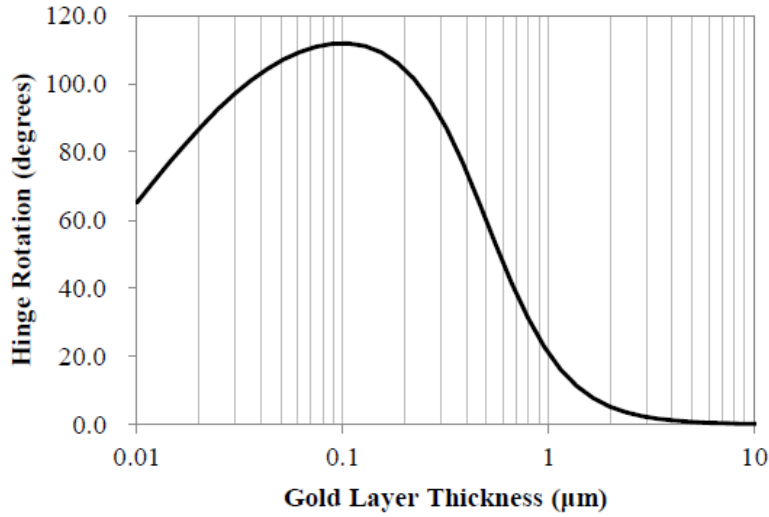


Figure 2.3: Beam rotation of a 400  $\mu\text{m}$  long actuator beam with varying gold thickness.

### 2.2.2 Customizable micro-fabrication for electro-thermal origami

This subsection introduces the fabrication method for building the proposed electro-thermal micro-origami and demonstrate the versatility and simplicity of the process. Figure 2.4 shows the fabrication flow chart of the proposed micro-origami. This process starts with spinning a thin film SU-8 2000.5 resin (0.8  $\mu\text{m}$ ) on top of a bare Si wafer. Because the SU-8 2000.5 resin is a very fine and thin solution, it is difficult to maintain a nice and even film directly on top of the bare Si wafer. Thus, mild oxidization is recommended to improve the film condition. We use 20 sec of  $\text{O}_2$  plasma etch to promote the adhesion and this allows us to obtain an even SU-8 thin film. Next the SU-8 thin film is soft baked for one minute and patterned with standard mask aligner. The exposure time can be calculated according to the datasheet provided by the manufacturer. Hard contact mode or equivalent is recommended for better pattern transfer. Adding an extra dosage of exposure in addition to the recommended time from the data sheet is also recommended to further improve the adhesion. After the exposure, one minute of post exposure baking and 90 sec of developing is used to remove the unexposed SU-8.

A thorough hard bake is necessary to ensure that the SU-8 is fully cross-linked. However, overheating the thin film SU-8 can change its residual stress profile and results in unwanted residual curvatures. Based on the results of this work, a long hard bake at relatively low temperature produces a better result. For the structures fabricated and tested in this work, we performed an overnight hard bake at 70 degree centigrade.

Next, a 0.2  $\mu\text{m}$  gold layer is deposited on top of the thin film SU-8 using e-beam evaporation.

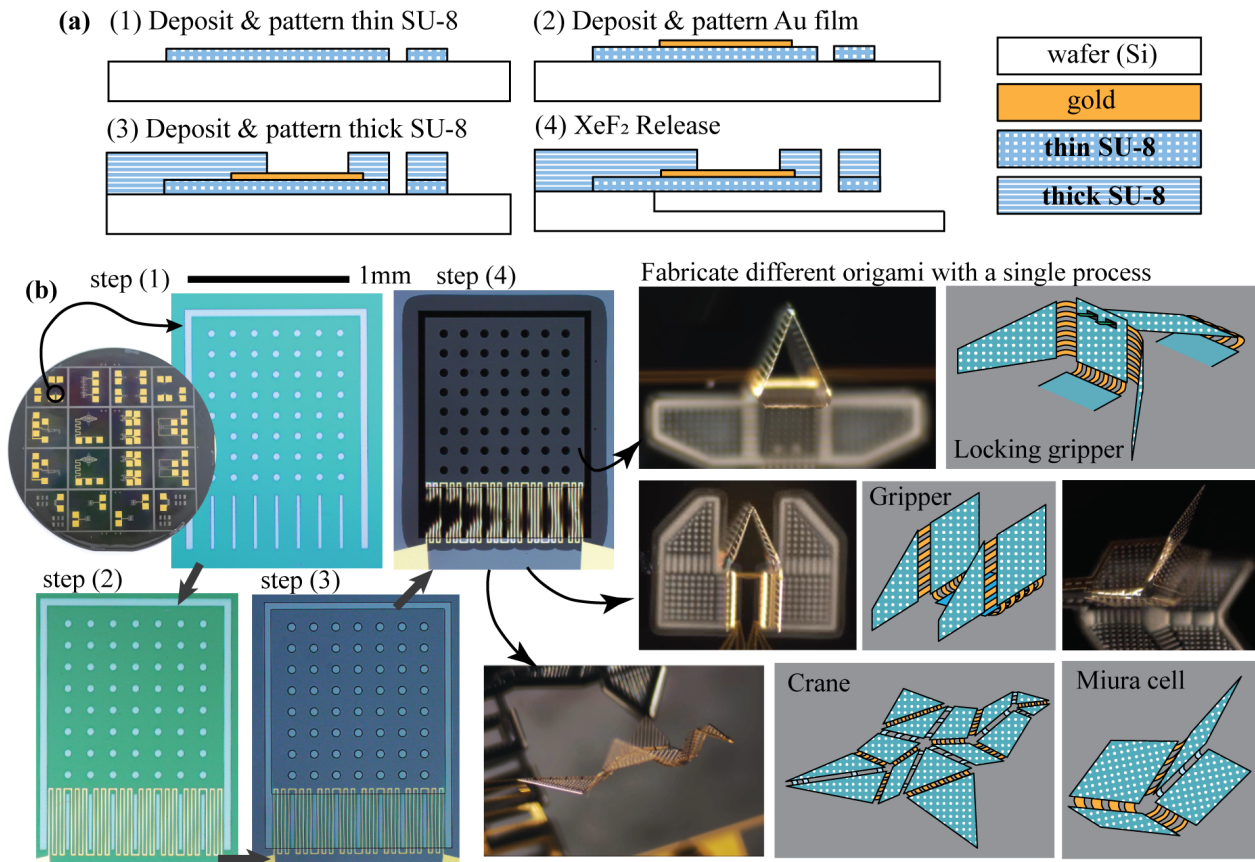


Figure 2.4: Fabrication flow chart of the electro-thermal micro-origami system.

To promote the adhesion between the gold and the SU-8, a 0.01  $\mu\text{m}$  layer of chrome adhesion layer is added under the gold. The gold layer is masked by common photoresists, such as SPR 220, and patterned with standard wet etch. It is necessary to perform a short O<sub>2</sub> plasma etch immediately before the wet etch to promote the quality of etching. After the wet etch, the masking photoresists can be removed with IPA and Acetone. This will not damage the thin film SU-8 because SU-8 is not dissolvable by IPA or Acetone.

After patterning the gold, a thicker SU-8 layer is deposited and patterned to fabricate the panel. A 20  $\mu\text{m}$  thick layer of SU-8 2010 is spin coated onto the wafer. The spread and spin speed is determined according to the data sheet provided by the manufacturer. Similar to the thin film, this thick SU-8 is patterned with standard photo-lithography equipment using a hard contact mode. To ensure good adhesion between the thick SU-8 layer and the existing layers, slightly extending the exposure time is recommended. This extra time helps to resist the peeling off during the developing of SU-8. Moreover, it is recommended not to use IPA for rinsing to further avoid peeling off. Finally, the structure is released with a xenon difluoride etch machine. A number of 40  $\mu\text{m}$  wide



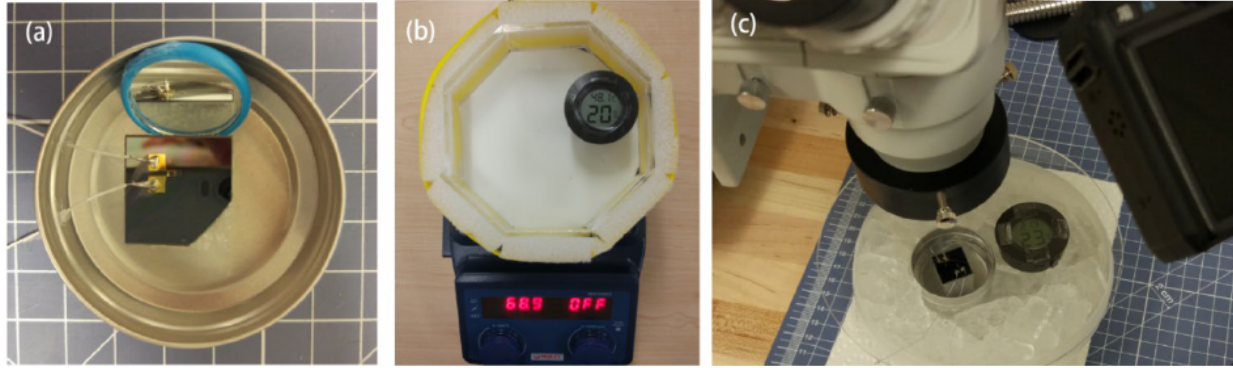


Figure 2.5: Devices for testing the performance of a single-crease origami.

etch holes in a square grid at  $120\ \mu\text{m}$  spacing is added to the origami panel for releasing the system from the silicon substrate.

One of the major concerns when fabricating small-scale structures is to control and mitigate the influence of residual stresses. In the proposed method, the gold layer also serves to control the residual stresses that can cause initial curvature as shown in Figure 2.2. The thin film SU-8 has a tendency to bend upward after release due to the gradient residual stress across thickness. Thus, by putting the patterned gold layer on top of the SU-8, it is possible to strengthen the SU-8 surface and prevent this initial curvature from happening. On the other hand, putting the gold layer under the thin SU-8 can trigger unwanted residual stress as shown in Figure 2.2 (b). This unwanted residual stress makes it more challenging to create actuators that bends downward.

Next, Fig. 2.5 shows how to package these small-scale origami systems for testing. Relatively large ( $3\ \text{mm} \times 3\ \text{mm}$ ) gold pads, which make it possible to directly solder thin electric wires for connection, are added into the micro-origami designs. However, using large connection pads is not the most efficient way of packing, despite being the simplest. In real practice, it is possible to use much smaller pads ( $100\ \mu\text{m} \times 100\ \mu\text{m}$ ) and wire bonding machines to connect and power these origami devices. With the wire bonding technique, it is possible to pack many more small-scale origami onto a single wafer to reduce the fabrication price of a single origami device.

Before the micro-origami structures are released, the silicon wafer is diced into smaller pieces and placed within metal boxes (Figure 2.5 (a)). A small mirror is used to provide a side view of the single-crease origami samples (Figure 2.5 (a)). This mirror allows us to directly measure the folding angle of the single-crease origami using the microscope camera pictures taken during the tests. The electric wires are connected to a DC source meter (or an AC source meter) to apply and measure the input voltage and current.

Figure 2.5 (b) and (c) show the devices we used to change the environmental temperature. A

hot plate is used to generate temperature that is higher than the room temperature and an ice bath is used to generate the temperature that is lower than the room temperature. Foam walls are used to build an insulated compartment for testing. A circular lid is built from transparent acrylic sheet to cover the compartment so that an enclosed and stable thermal environment is obtained.

## 2.3 Folding Performance of Eletro-Thermal Actuator

The folding performance of individual origami crease controls the global performance of the functional origami structures, so it is important to test the capability of the proposed micro-actuator. In this section, a single-crease origami system is tested in detail to highlight the four most attractive capabilities of the proposed micro-actuator: (1) to achieve large folding (forming an acute interior angle with greater than  $90^\circ$  folding from the initial orientation) displacements reversibly; (2) to function in atmospheric environments with different temperatures; (3) to fold rapidly; (4) to have the zero current rest angle reprogrammed. The first three capabilities highlight the good elastic folding capability, while the last capability enables the plastic folding to reprogram the shape of the micro-origami.

### 2.3.1 Static elastic folding

We first study the static elastic folding of these single crease micro-origami (see Fig. 2.6). Figure 2.6 (b) shows the relationship between the folding angle and applied current for single-crease origami systems with different actuator lengths and Fig. 2.6 (c) shows the measured current-voltage relationships. As shown in the measurements, longer actuators can achieve higher folding angles at the same current level but also require higher voltage input. It takes about 3.0 V of voltage and 20 mW of power to fold these single-crease origami to a right angle, which is reasonable for the ability to achieve large and rapid folding. Because the panels in these structures are thick and heavy (20 times thicker than the actuator), these single-crease origami structures tend to rest at negative folding angles under the influence of gravity. A threshold current is required to overcome gravity for lifting the panel off from the silicon wafer. However, this threshold current is difficult to determine because the negative folding region cannot be visually observed. This threshold effects will be studied with greater details in Chapter 5, when introducing a new simulation method for the multi-physics electro-thermal actuation.

The single-crease origami system can fold elastically in common atmospheric temperatures (see Fig. 2.6 (a)). Results for actuation at  $1^\circ\text{C}$  to  $49^\circ\text{C}$  show that, although the systems are affected by the environmental temperature, it is possible to offset the influence by changing the current and the voltage input (Fig. 2.6 (d)). This temperature range is selected because it represents common temperature range of outdoor atmospheric environments. The systems can function around

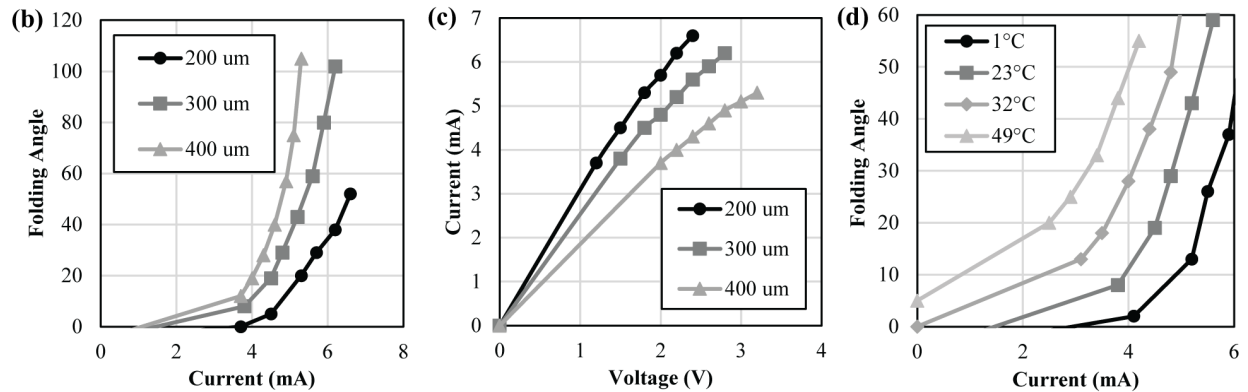
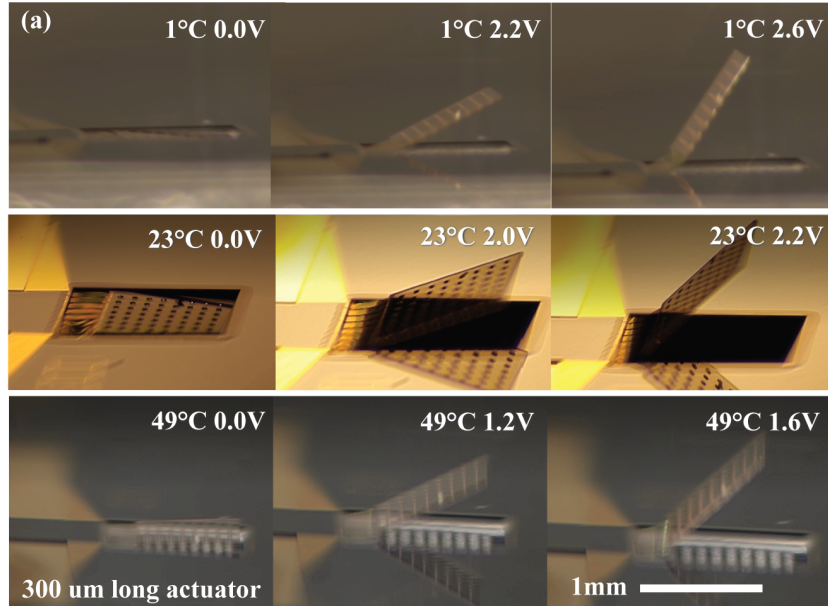


Figure 2.6: Elastic static folding performance of a single-crease origami system.

and below freezing temperature. However the zero current rest angle is negative under this low temperature, which is restricted by the wafer below and cannot be observed (Fig. 2.6 (d)).

### 2.3.2 Dynamic elastic folding

This single-crease system can also achieve rapid elastic folding up to and slightly beyond resonance. We demonstrate this behavior using sine wave sweeping tests (from 1 Hz to 200 Hz) with three different input voltage setups (see Figure 2.7). The folding motion is mostly quasi-static when the frequency is low. However, as the input frequency increases, the response becomes dynamic: the motion range decreases gradually until 20 to 40 Hz and then increases to a peak at the resonance frequency. The single-crease origami can oscillate with a folding range of  $65^\circ$  at

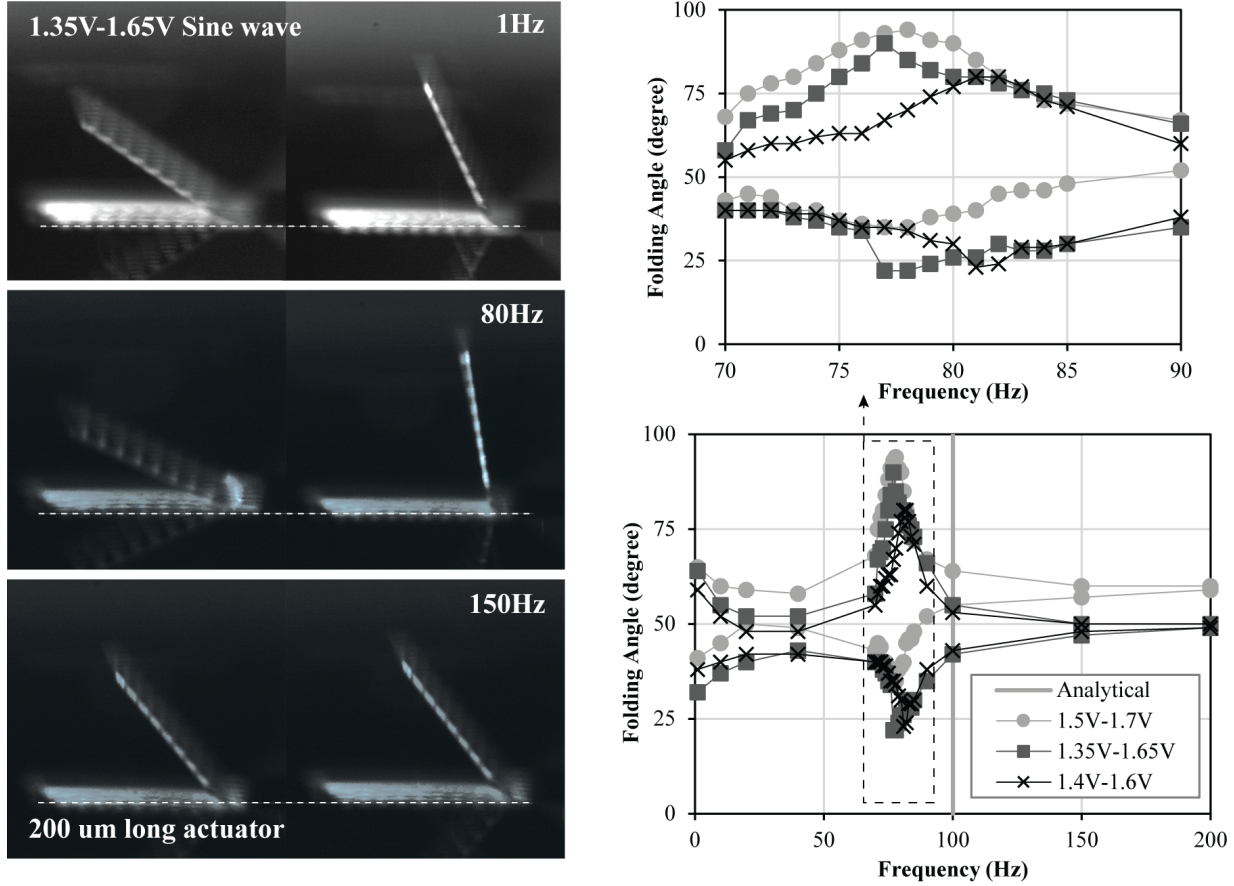


Figure 2.7: Elastic dynamic folding performance of a single-crease origami system.

resonance when applying a 77 Hz AC voltage input (peak to peak voltage is 1.35V to 1.65V). This folding performance achieves an average speed of about  $10000^\circ \text{ sec}^{-1}$ . At a higher frequency of 150 Hz, the sample only oscillates locally with small motion because the actuators cannot heat and cool fast enough at higher frequencies. The single-crease origami system shows a longer fundamental period when increasing the AC voltage amplitude or increasing the DC voltage offset. This period elongation occurs because the actuator is working at higher temperature when the voltage is higher, which in turn causes the material to become softer. The rapid folding capability of the proposed system is far beyond what is offered by most existing micro-origami systems that require more than several seconds to fold [Na et al., 2015, Silverberg et al., 2015, Liu et al., 2021]. The high folding speed of the proposed micro-origami offers an unprecedented ability to achieve rapid and responsive shape morphing systems at the micro-scale.

A one-degree-of-freedom analytical model can be used to estimate the resonance frequency of the single-crease origami. The single-crease origami system is simplified as a rotational spring of stiffness  $K_{spr}$  connected to a panel with the moment of inertia about the spring as  $J_p$  (see Fig. 2.8).

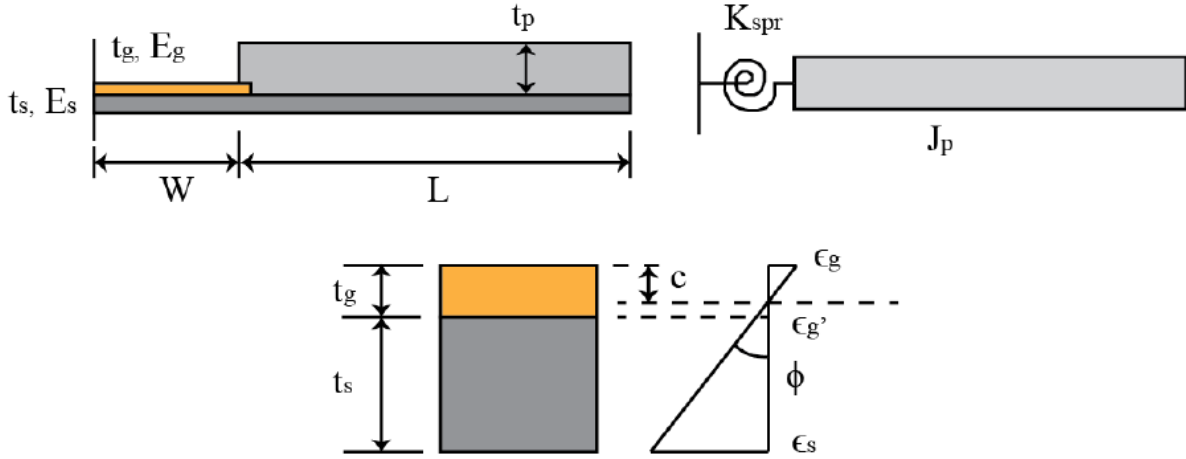


Figure 2.8: A 1-DOF model to estimate the resonance frequency.

Geometries and material properties used to calculate the stiffness and the moment of inertia are:  $t_g = 0.2 \mu\text{m}$ ,  $E_g = 79 \text{ GPa}$ ,  $t_s = 0.8 \mu\text{m}$ ,  $E_s = 2 \text{ GPa}$ ,  $W = 200 \mu\text{m}$ ,  $t_p = 20 \mu\text{m}$ ,  $L = 1 \text{ mm}$ . To simplify the calculation, it is possible to assume that the depth of the system is 1 (dimension perpendicular to the page). The density of SU-8 is assumed to be  $\rho_s = 1200 \text{ kg/m}^3$ , which will be used to calculate the moment of inertia of the panel.

First, the bending rigidity of the bimorph actuator is calculated. We assume that the neutral axis (the term  $c$ ) is in the gold layer and assume that the material response is linear elastic. Because the heaters only cover about half the area of actuator, the Young's modulus of gold is reduced by a factor of two. The equilibrium of forces requires:

$$\frac{1}{2}\epsilon_g c E_g = \frac{1}{2}\epsilon_g'(t_g - c)E_g + \frac{1}{2}(\epsilon_s + \epsilon_g')t_s E_s, \quad (2.2)$$

$$\epsilon_g = \phi c, \quad (2.3)$$

$$\epsilon_g' = \phi(t_g - c), \quad (2.4)$$

$$\epsilon_s = \phi(t_g + t_s - c). \quad (2.5)$$

Solving the above equations gives the location of the neutral axis  $c = 0.184 \mu\text{m}$ . Thus, the neutral axis is indeed in the gold layer and the above calculation is valid. The bending rigidity can then be calculated as:

$$\begin{aligned}
EI_{comp} &= \frac{1}{3}E_g c^3 + \frac{1}{3}E_g(t_g - c)^3 + (c + \frac{1}{2}t_s)E_s(t_g - c)t_s + \frac{1}{2}(c + \frac{2}{3}t_s)E_s t_s^2 \\
&= 5.56 \times 10^{-10} \text{ N} \cdot \text{m}.
\end{aligned} \tag{2.6}$$

The bending rigidity of beam can then be converted to the stiffness of the rotational spring with the pseudo-rigid-body model as:

$$K_{spr} = \frac{EI_{comp}}{W}. \tag{2.7}$$

The moment of inertia of the panel is:

$$\begin{aligned}
J_p &= \frac{1}{12}\rho_s(t_p + t_s)L^3 + \rho_s(t_p + t_s)L(W + \frac{1}{2}L)^2 \\
&= 1.43 \times 10^{-11} \text{ kg} \cdot \text{m}.
\end{aligned} \tag{2.8}$$

In addition, because half of the area of the actuator crease region is occupied by the releasing holes, it is necessary to further reduce the spring stiffness by half to consider the reduction in stiffness. Finally, the fundamental frequency of this 1-DOF system is calculated as follows:

$$\omega = \sqrt{\frac{K_{spr}}{2J_p}} = 311.8 \text{ rad/sec}, \tag{2.9}$$

$$f = \frac{\omega}{\pi} = 99 \text{ Hz}. \tag{2.10}$$

Despite the simplicity of this 1-DOF model, this analytical prediction is close to the 80 Hz resonance frequency recorded in the experiment. The fundamental frequency is overestimated because (1) the 1-DOF model can overestimate the stiffness of the structure and (2) the damping effect is neglected.

This analytical model can also be used to study the blocking moment of the single-crease origami. The blocking moment is defined as the moment that prevents the bimorph actuators from folding (no deformation) at a given elevated temperature. With the calculated  $EI_{comp}$  the blocking moment for a given elevated temperature is:

$$M_{block}(\delta T) = EI_{comp}\kappa(\delta T). \tag{2.11}$$

where the term  $\kappa(\delta T)$  is calculated using Eqn. (2.1). The relationship between the elevated temperature and the blocking moment is shown in Figure 2.9, and the gravity induced moment acting on the structure is also plotted for reference. As shown in the result, the actuator system needs to first overcome the gravity induced negative folding before producing the positive upward folding.

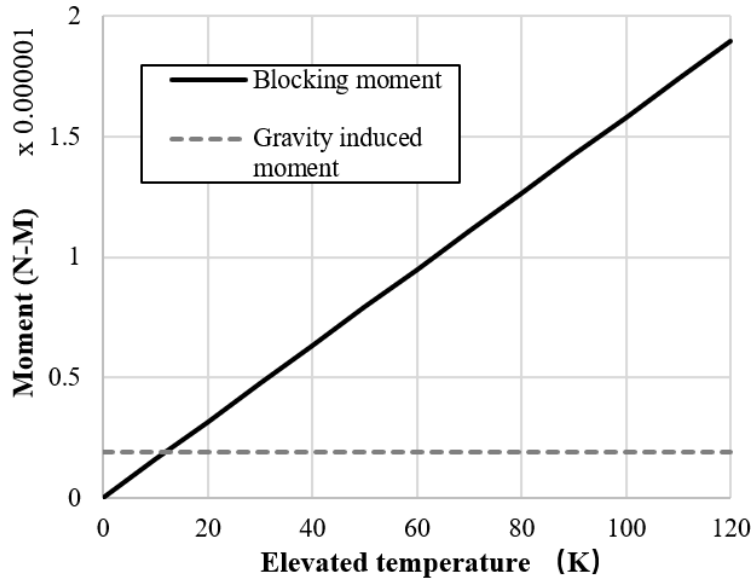


Figure 2.9: Relationship between the blocking moment and elevated temperature.

More advanced simulation methods are required to fully understand these complex behaviors, and the simulation model proposed in Chapter 5 will address these concerns.

Finally, the dynamic loading is used to investigate the durability of these electro-thermal actuators. In Fig. 2.10, a single-crease micro origami with 300  $\mu\text{m}$  long actuators is set to be oscillating at its resonance frequency of 55 Hz for 30 minutes. During the experiment, the minimum fold angle and the maximum fold is recorded to check if any obvious degradation happens. Figure 2.10 shows the measured results, and we can see that these micro-actuators display limited degradation. The minimum fold angle remains unchanged throughout the testing and the maximum fold angle increases by only a few degrees (from  $\approx 83^\circ$  to  $\approx 86^\circ$ ). Overall, this slight increase in maximum fold angle is minor compared to the total range of the actuator. During this 30 minutes long experiment, this single-crease origami sample has experienced 99000 cycles of folding and unfolding, highlighting the superior durability of the proposed design.

### 2.3.3 Quasi-static plastic folding

In addition to the superior elastic folding capabilities, this electro-thermal actuator can also fold plastically. This plastic folding ability greatly enhances the versatility and functionality of the micro-origami system and allows for controlled programming and reprogramming of the folded shape. Figure 2.11 shows how to achieve this plastic folding by overheating the actuator to high temperatures and applying forces simultaneously. Because the thin SU-8 layer will display visco-

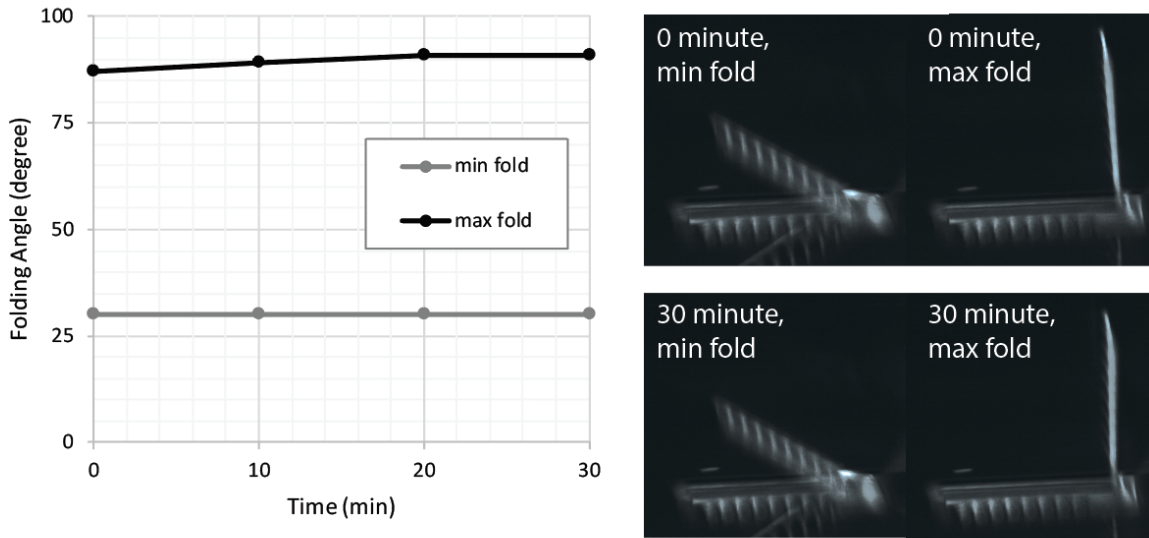


Figure 2.10: Degradation of the folding range is minor after 99000 cycles of folding and unfolding.

elasto-plastic deformation at high temperature, the stress free angle of the creases can be reprogrammed permanently.

Figure 2.12 demonstrates a proof-of-concept experiment to reprogram the folding state of a single-crease origami with 200  $\mu\text{m}$  long actuator beams. At the beginning, the zero current rest angle of this single-crease origami is zero degrees. The crease folds and unfolds reversibly, when applying and removing the 2.4 V of input, and no obvious plastic deformation is observed for multiple cycles of loading. However, when 3.0 V are applied across the circuit, the crease folds beyond 90° and the SU-8 polymer starts to experience a visco-elasto-plastic material behavior. At this state, the influence of gravity further deforms the crease (as an external load), and the zero current rest angle is reprogrammed. After removing the applied current, this single-crease origami develops ten degrees of plastic deformation, and its reversible motion from 0V to 2.4 V is also offset by the same amount. Next, we can recover the original zero current rest angle by directly pressing down on the panel and reapplying 3.0 V to overheat the crease again.

Figure 2.13 show the measured hysteretic folding curves of the single-crease micro-origami, where two loading cycles are applied to systems with 200  $\mu\text{m}$  and 400  $\mu\text{m}$  long actuator beams. First, a sequence of loading cycle A, cycle B, and cycle A is applied onto the single-crease origami with 200  $\mu\text{m}$  beams and the recorded motion is plotted in Fig. 2.13 (c). During the first cycle A loading, no plastic folding is observed because the voltage is low, so the unloading curve falls directly on top of the loading curve. However, plastic folding is observed during the cycle B loading, where the applied voltage is high enough to cause the SU-8 material to deform visco-



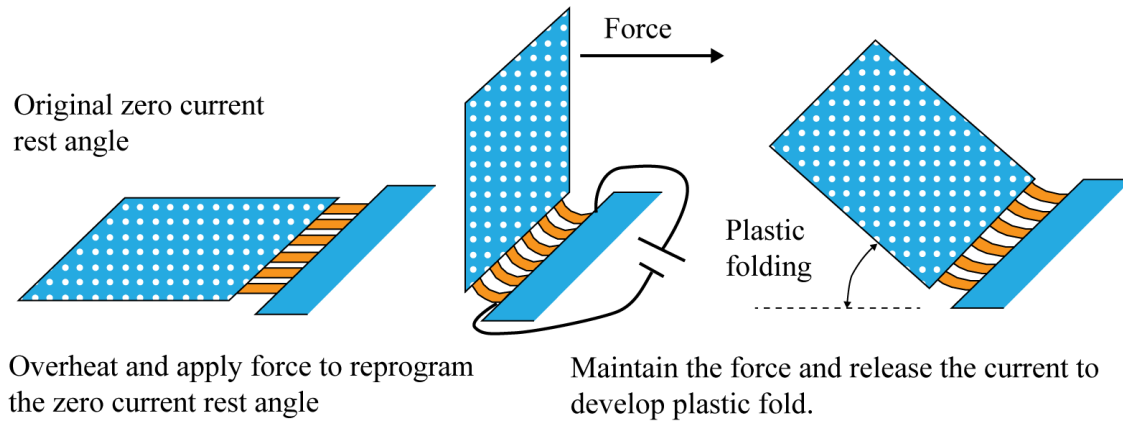


Figure 2.11: Plastic folding behavior of the micro-origami.

elasto-plastically. At the end of the loading cycle B, the zero current rest angle is changed to 10 degrees from the perfectly flat state. When a second loading cycle A is applied, the plastic folding does not occur. The loading and unloading curves coincide but are offset by the new zero current rest angle. Next a loading cycle B is applied onto a single-crease origami with 400  $\mu\text{m}$  actuator beams, and the loading curve shows that no plastic folding or hysteresis is developed during the process. This is because longer actuators have higher resistance and thus generate lower temperatures when the same voltage is applied. Because this plastic folding technique does not require continuous power input after reprogramming the zero current rest angle, it provides an energy efficient solution for creating 3D origami systems that do not need to recover their original flat configurations. When this reprogramming method is used to permanently change the shape of these micro-origami, passive folds that act like elastic springs can be integrated into the system to generate this external force.

## 2.4 Achieving Complex Functions with Micro-Origami

Now that we have demonstrated the superior folding capabilities of the proposed micro-actuator, the next goal is to show how micro-origami structures, equipped with these powerful micro-actuators, can accomplish complex motions and functions. In the following part of this section, five micro-origami systems will be demonstrated to highlight the versatility, preciseness, controllability, and functionality of the proposed micro-origami systems.

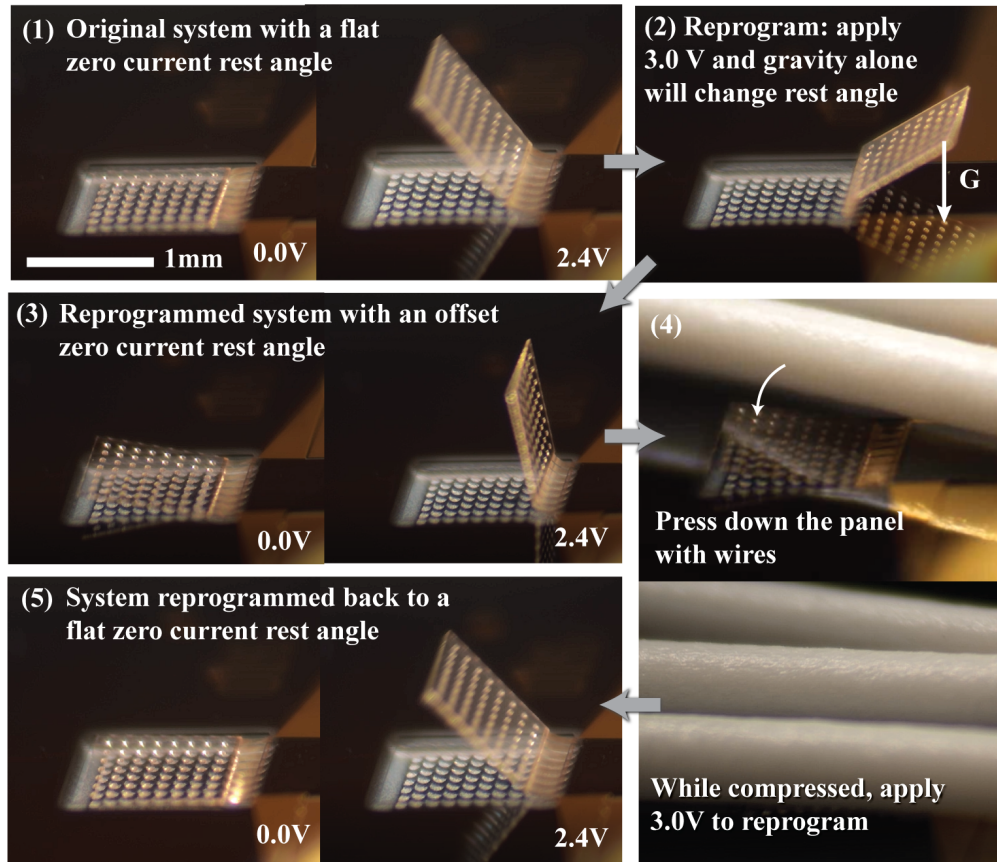


Figure 2.12: Proof-of-concept experiment of the plastic folding behavior of the micro-origami.

### 2.4.1 Controllable multi-degree-of-freedom shape morphing

First, we demonstrate that the proposed micro-origami systems can accomplish complex functions using separately controllable folding creases with two origami gripper examples. Because of the inherent 2D nature of photolithography based micro-fabrication, it is difficult to create gripper type mechanisms with a large motion range [Chronis and Lee, 2005, Choi et al., 2017]. However, with the principles of origami, it is possible to fold 3D systems that can achieve large gripping motion. In this section, we demonstrate two designs of origami grippers that have different characteristics. Figure 2.14 shows one design of the origami gripper that can achieve a large gripping range and can survive a wet environment where it is sprinkled with water. This micro-origami has two side panels for 3D assembly and two gripper panels acting as gripping arms. First, a voltage is applied across the assembly circuit (1) to fold the gripper into its functional state; next, we apply a voltage across the function circuit (2) to grip; finally, the origami gripper can return to its original flat position after usage by releasing the applied voltage. The same gripper is next subjected to a wet environment where the origami is sprinkled with water (Fig. 2.14 (c) right). The cooling effects

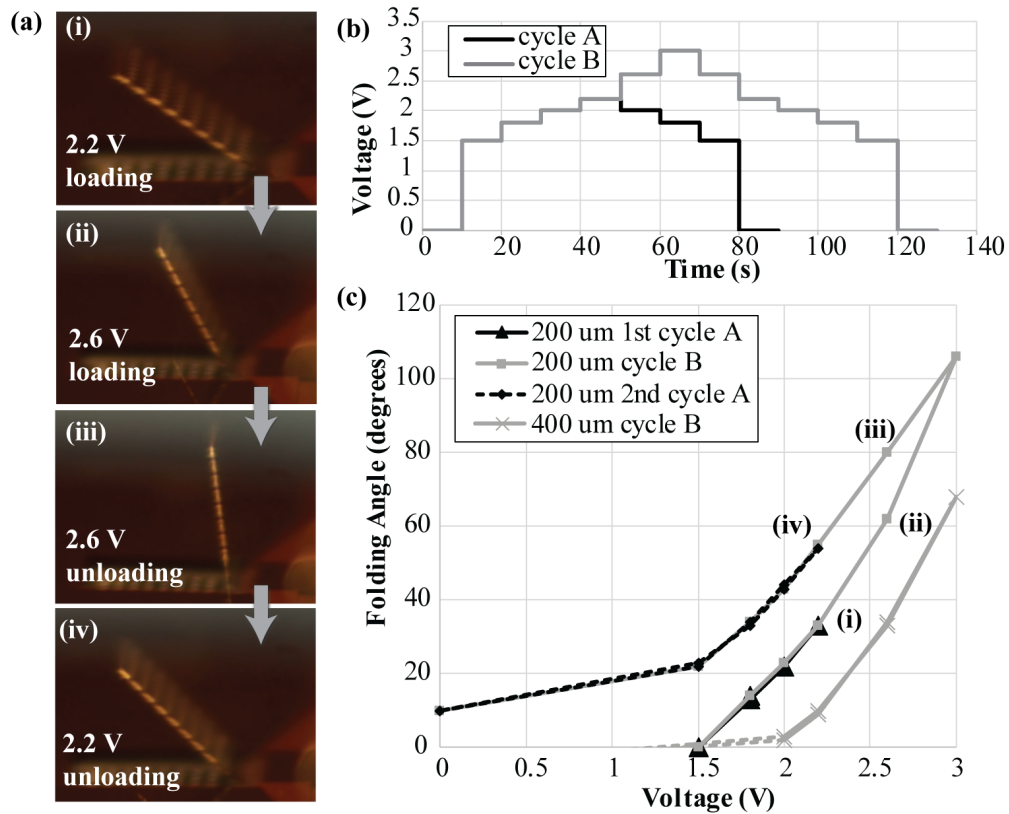


Figure 2.13: The hysteretic folding behavior of a single-crease origami with 200  $\mu\text{m}$  beams under different loading cycles.

of water evaporation dramatically changes the local thermal environment and leads to unwanted folding at points where water is sprayed. However, as the water dries, the origami recovers its capability to fold and grip.

The second gripper design can lock into a functional 3D state, where it can remain without additional input of current (see Fig. 2.15). This origami design has two pins and two corresponding holes that can lock the system into a 3D shape. The 3D assembly requires controlling two separate heater circuits, and a third circuit is later used to actuate the gripper. Because these actuator systems do not rely on using environmental stimulus, this micro origami can achieve individual crease control needed for the complex assembly, where the two 20  $\mu\text{m}$  thick pins are aligned precisely with the two 60  $\mu\text{m}$  wide holes. After the locking, the system can remain assembled even when the current in the circuits is removed. This gripper can be more energy efficient for extended usage, because it requires no continuous heating for maintaining the functioning state after the locking assembly. Moreover, the locking device makes the origami gripper mechanically more robust, because the gripping functionality now only depends on two actuated creases rather

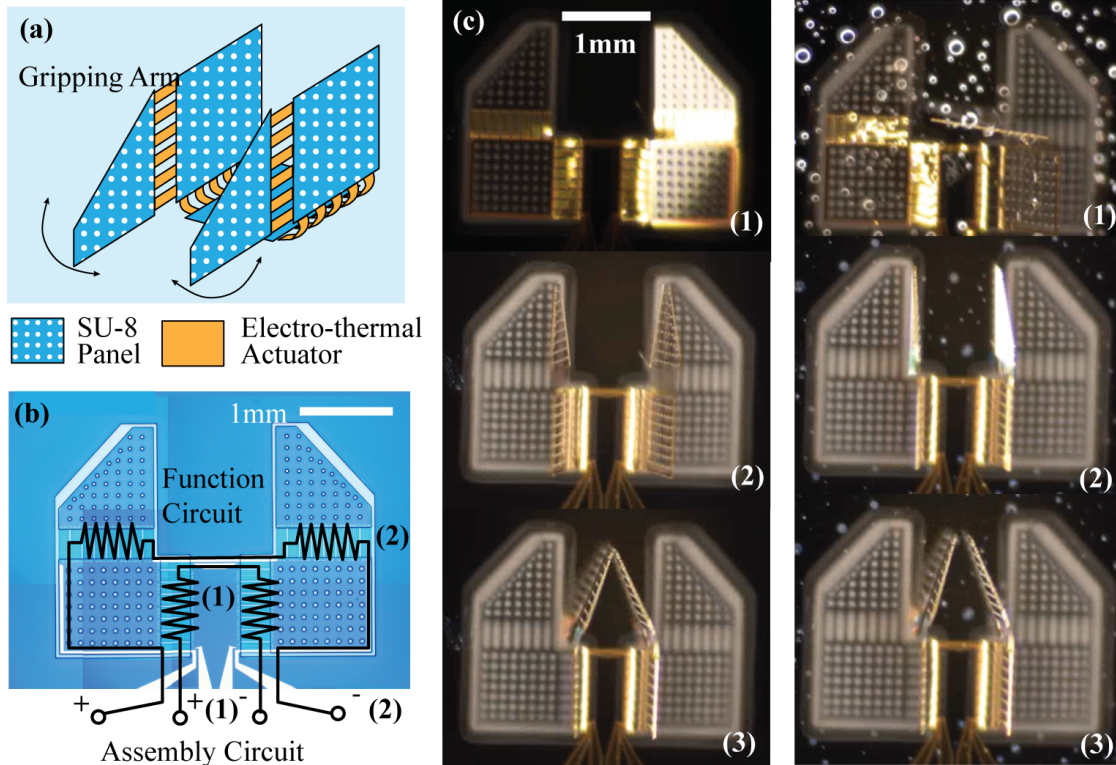


Figure 2.14: A micro-origami gripper with a large gripping range.

than the four creases used in the first design.

## 2.4.2 Combining elastic and plastic folding for complex functions

Next, we introduce two techniques to create complex origami systems: one by combining active folds and passive folds, and the other by combining the elastic folding and the plastic folding. Together, the two techniques open up new potentials to create complex origami systems for functional shape-morphing and reprogrammable 3D systems at smaller scales.

We first show how to fold origami systems with both mountain and valley folds using a combination of active and passive folds. To that end, we had to overcome an inherent limitation of the fabrication approach, which allows only upward bending of creases due to residual stress (see Figure 2.2). Instead of actively folding all creases simultaneously, we use the active folds to generate the upward folding, and let those creases that fold downward remain passive and behave like elastic rotational springs. If the pattern is designed to have one degree-of-freedom kinematics, accurate folding can potentially be achieved by only actuating the upward folding creases. The first example is a single Miura-ori unit made up of three active folding creases that bend upwards and

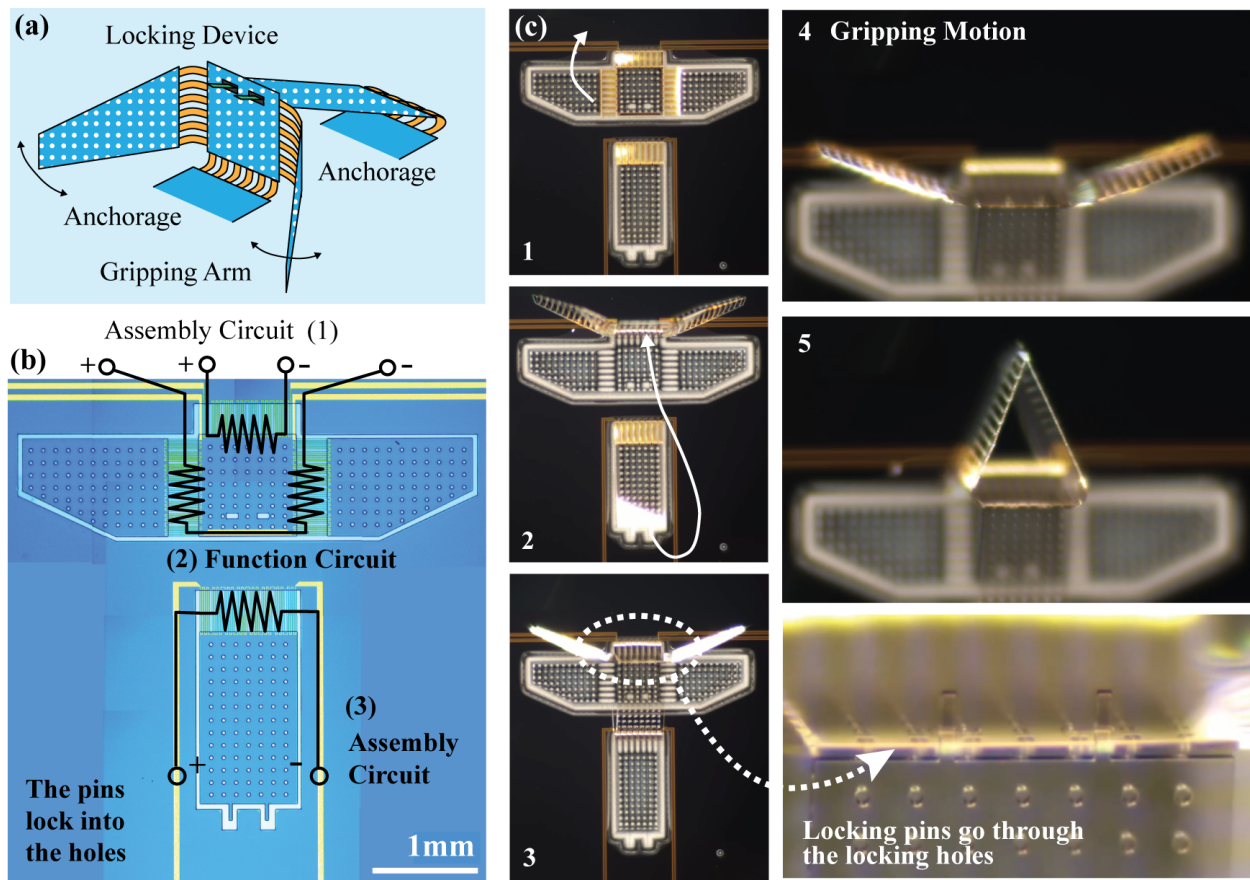


Figure 2.15: A micro-origami gripper that can first assemble into the 3D configuration using locking devices then achieve gripping motion.

one passive crease that deforms like an elastic rotational spring (Figure 2.16 (a-c)). The second example is a Miura-ori system with three units that all fold together when actuated (Figure 2.16 (d-f)). Micro-origami structures like these provide a basic building block for micro-actuators or metamaterials [Fang et al., 2016, Kamrava et al., 2018]. The Miura-ori pattern is known to have one degree-of-freedom kinematics, which is needed for the proposed design approach. Generic origami patterns can also be designed to have the 1-DOF kinematics using origami simulation methods [Tachi, 2010d, Tachi, 2009c]. For more complicated patterns, kinematic analysis alone may not be sufficient to determine if the system can be folded accurately and the placement of actuators will play a significant role [Stern et al., 2017]. For these more complicated systems, bar and hinge models [Liu and Paulino, 2017a, Zhu and Filipov, 2020, Zhu and Filipov, 2019a], which can consider the mechanical properties of an origami, can be used to study if the system can fold accurately. These micro-origami can alter between the unfolded and the folded 3D shape swiftly, which is superior to many existing systems and allows them to be used for various applications in

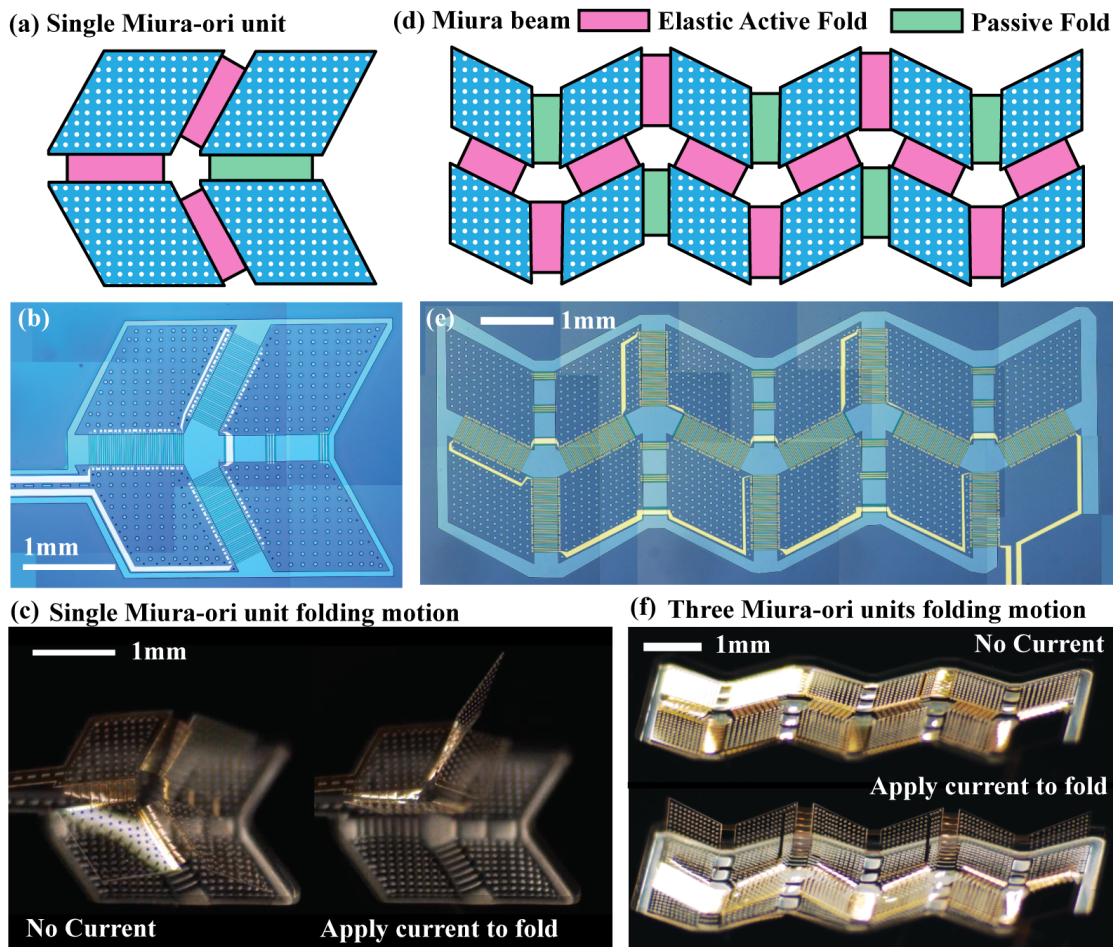


Figure 2.16: Combining elastic active folds and passive folds for origami with both mountain and valley folds. (a-c) A single-unit Miura micro-origami; (d-e) A multi-unit Miura beam.

robotics and metamaterials, where fast folding is needed.

Next, we show that by combining the elastic folding and the plastic folding, we can create programmable 3D micro-origami systems to achieve functions that were not realizable previously. For example, although origami cranes have been folded at smaller scales [Na et al., 2015], those systems cannot achieve active functions such as flapping the wings after the initial 3D assembly. In this section an origami crane pattern that can fold and subsequently flap its wings is shown (Figure 2.17 (a)). The plastic folding is used to reprogram the origami shape into a static 3D crane geometry and the elastic folding is subsequently used to flap the wings of this crane. We first apply a current across the folding circuit, to overheat the creases and to develop plastic folding using the forces generated by gravity and the passive folds that tend to revert the pattern back to a flat state (Figure 2.17 (b)). When we release the applied current, the plastic folding occurs in the reverse direction, and the crane pattern reaches a static folded configuration. After the

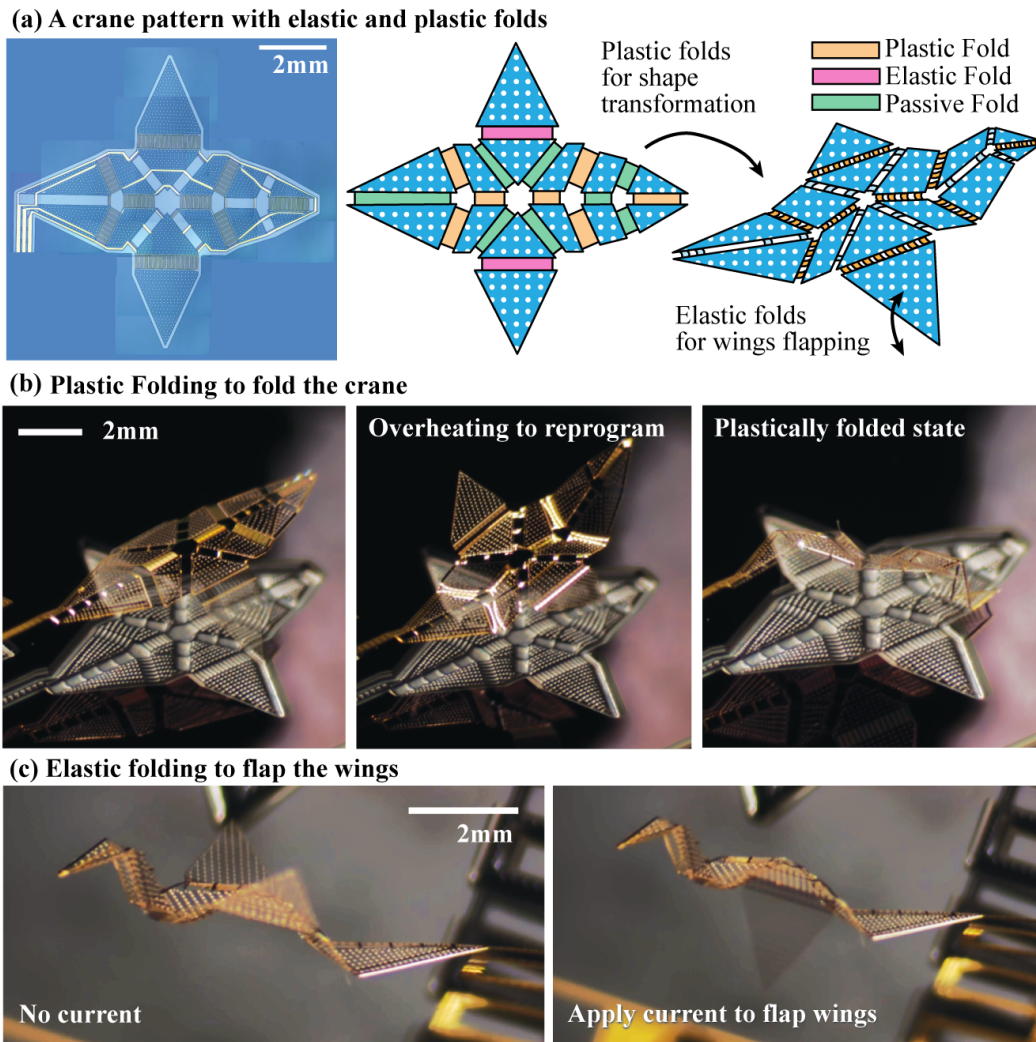


Figure 2.17: Creating complex origami crane that can first assemble then flaps its wings using a combination of elastic folds and plastic folds.

crane is successfully folded, we can apply current through the wing circuit to elastically flap the wings as shown on Figure 2.17 (c). With the multiple active degrees-of-freedom provided with the proposed system, the micro-origami can first fold permanently to a desired 3D geometry with one set of plastic folds and then achieve functions with another set of elastic folds. The combination of elastic, plastic, and passive folds allows us to create high performance shape morphing origami systems at smaller scales that were not achievable previously. In practice, designers can use longer actuators to achieve elastic folding at lower functioning temperature or use shorter actuators to achieve higher crease temperature for plastic folding.

## 2.5 Concluding Remarks

In this chapter, a new fabrication and actuation methodology for electro-thermal micro-origami systems is introduced and tested in detail. The fabrication of the system is simple and only requires a three masks process, because we integrate multiple functions into a single gold layer. Unlike most existing origami systems, the proposed electro-thermal micro-origami can fold without relying on an environmental stimulus, which allows these micro-origami to achieve rapid and large elastic folding in common atmospheric environments with temperatures ranging from 1°C to 49°C. The proposed origami systems can have the folded state of creases (zero current rest angle of creases) to be reprogrammed by overheating, which provides a method to generate permanently and plastically folded 3D geometries. Experiments show that, in addition to having relatively good folding performance, the folding creases of the proposed micro-origami have reasonable power consumption and require low voltage input. Moreover, because these micro-origami systems do not need environmental stimulus for actuation, they can have multiple active degrees-of-freedom and thus can achieve shape morphing with complex motion paths and a higher level of functional versatility. For example, we present a micro-origami gripper that can align locking pins to locking holes to assemble a mechanically robust interlocked structure and can subsequently perform large displacement gripping motion after locking. Finally, we introduce two methods to create complex origami systems from unidirectional electro-thermal actuators. The first method combines active and passive folds to create origami patterns with both valley (upward) and mountain (downward) folding directions. Two Miura-ori patterns demonstrate the rapid shape morphing between folded and flat states achieved with the proposed system. The second method uses plastic folding to reprogram the 3D shape of the micro-origami then uses elastic folding to achieve functional motions. An origami crane pattern is presented to demonstrate this method. The crane can first permanently change its 3D geometry using the plastically folded creases and then flaps its wings with another set of creases that folds elastically.

We believe future research can enhance the capabilities of the proposed systems and overcome limitations presented in the current work. New active polymers can be used to improve the efficiency, folding capability, and control of the residual stress to achieve simultaneous upward and downward actuation. Batteries and on-board sensors can also be integrated into these micro-origami systems to create fully autonomous functional micro-robots. The integrated fabrication and actuation methodologies demonstrated in this chapter provide a customizable framework for future work in micro-scale functional origami systems.



## Chapter 3. Compliant Crease Bar and Hinge Model

This chapter introduces a compliant crease bar and hinge model to resolve the Challenge 2 proposed in Chapter 1 Introduction. More specifically, existing standard bar and hinge models are modified to capture the compliant creases explicitly. This modification allows the new bar and hinge model to better capture the geometry and mechanics of functional origami systems.

This chapter is arranged as the following. First, we will give a brief introduction of the standard bar and hinge models to motivate and illustrate the development of the compliant crease bar and hinge model. After that, Section 3.2 derives the stiffness parameters of the compliant crease bar and hinge model by matching the model stiffness to that obtained from fundamental plate theories and pseudo-rigid-body models. Next, in Section 3.3, a thorough verification study is performed by comparing the proposed model against FE simulations for both small strain stiffness and large strain stiffness. Finally, Section 3.4 presents simulation examples to show the efficiency and capability of the proposed model. Moreover, the presented examples show that this new bar and hinge model can capture the bistability in compliant crease origami accurately. The nomenclatures used in this Chapter are summarized in Table 3.1.

### 3.1 Bar and Hinge Models

In a bar and hinge model, the *bars* are extensional elements that can capture in-plane stretching and shearing, and the *rotational springs* (hinges) are rotational hinge like elements with stiffness that can capture out-of-plane bending and torsion. Detailed formulation of the bar elements and the rotational spring elements can be found in [Liu and Paulino, 2017a, Filipov et al., 2017]. Figure 3.1 (a) gives an illustration of a standard bar and hinge model. In this standard model, a folding crease within an origami is represented as a single rotational spring. This formulation is widely used to study the mechanical behaviors of origami systems [Filipov and Redoutey, 2018, Dong and Yu, 2021] and works well for paper-based origami systems [Liu and Paulino, 2017a, Liu et al., 2020, Masana and Daqaq, 2019], which indeed have narrow fold lines. However, this standard model is not suitable for functional origami structures that have compliant creases for thickness accommodation [Butler et al., 2020] and actuation [Na et al., 2015, Zhu et al., 2020, Breger et al., 2015].

To better simulate the geometry and mechanics of compliant creases, a new compliant crease

Table 3.1: Nomenclature used in Chapter 3

Symbols	Definition
$L, W$	Length and width of creases
$t_{crease}, t_{panel}$	Thickness of creases and panels
$A_0, A_1, A_2, A_3$	Areas of bars for crease region
$\nu_{crease}, \nu_{panel}$	Poisson's ratio for creases and panels
$E_{crease}, E_{panel}$	Young's modulus for creases and panels
$k_{a,pl}, k_{a,BH}$	Axial stiffness of crease from plate theory and bar and hinge model
$k_{s,pl}, k_{s,BH}$	Shear stiffness of crease from plate theory and bar and hinge model
$K_{spr1}, K_{spr2}$	Rotational spring stiffness for crease region
$f$	Torsional stiffness scaling factor
$A_{panel}, K_{panel}$	Area and rotational spring stiffness for panels
$\alpha$	Crease Aspect Ratio
$\beta$	Thickness Ratio

bar and hinge model is developed here as shown in Fig. 3.1 (b). This new model is developed based on the observed behaviors of an origami assemblage with compliant creases. When a compliant crease is folded by applying pure moment on it, the curvature of the crease is evenly distributed across the width (Fig. 3.1 (c)). The proposed model captures this more even distribution of curvature and the three-dimensional geometry using three lines of rotational springs instead of just one. Two rotational springs connect the panels to the crease area, and two half-length rotational springs are located along the center of the crease region. When relative torsion occurs between two panels, the connecting crease deforms diagonally as indicated in the Fig. 3.1 (d). This behavior is captured with the four additional rotational springs placed diagonally within the crease region. Notably, this meshing technique also captures the extensional stiffness of creases, which can play a significant role in analyzing bistable and multistable behaviors of origami [Faber et al., 2018].

### 3.2 Derivation of Model Stiffness Parameters

The compliant crease bar and hinge model can be defined based on the following geometric parameters: the crease width  $W$ , crease length  $L$ , crease thickness  $t_{crease}$ , and panel thickness  $t_{panel}$  (Fig. 3.2 (a)). Two indexes, *Crease Aspect Ratio* and *Thickness Ratio*, are defined to quantify the geometrical characteristics of compliant creases. The *Crease Aspect Ratio* is defined as:  $\alpha = W/L$ , where  $W$  and  $L$  are crease width and crease length respectively (see Fig. 3.2 (a)). The *Thickness Ratio* is defined as:  $\beta = t_{panel}/t_{crease}$ , where  $t_{panel}$  and  $t_{crease}$  are the thickness of panels and creases respectively. These two indexes describe geometric properties of compliant crease origami that affect the local and global stiffness of the system. Common origami designs with compliant creases typically have a Crease Aspect Ratio  $\alpha \approx 0.1$  and a Thickness Ratio  $\beta \approx 3.0$  [Yoon

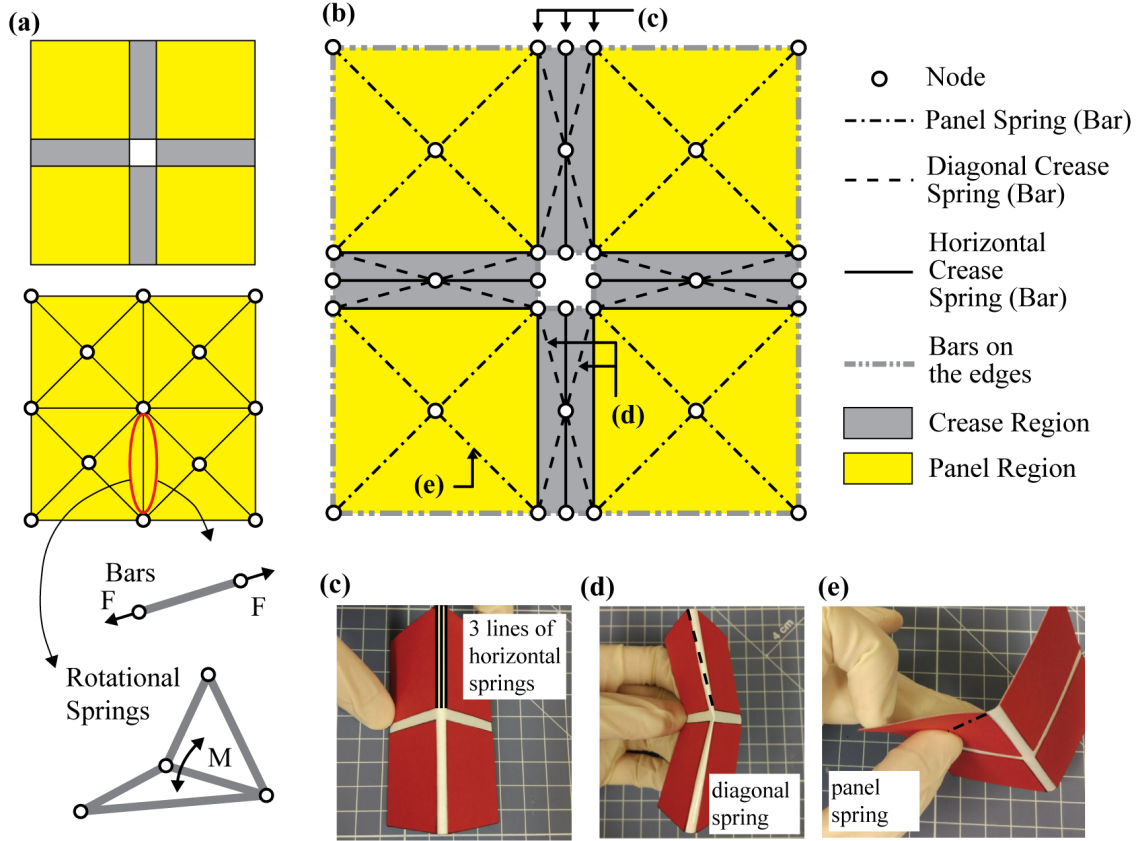


Figure 3.1: (a) Conventional bar and hinge models; (b) Compliant crease bar and hinge models; (c-e) Rotational springs added to capture richer mechanical deformation.

et al., 2014, Bassik et al., 2009]. Deriving the bar and hinge model requires solving the bar area ( $A_0, A_1, A_2, A_3$ ) and the rotational spring stiffness ( $K_{spr1}$  and  $K_{spr2}$ ). We will start with the bar areas first.

### 3.2.1 Derivation of bar areas

Bar areas of the model are determined by matching the stiffness of the bar and hinge model to that from a theoretical plate model of the same bulk material. The bars within a crease region are divided into four different groups as shown in the Fig. 3.2 (b). The area of  $A_0$  bars is later determined in the panel modeling section and is temporarily assumed to be infinite in this section. This assumption generally works well because panels are usually much thicker and stiffer than creases.

The area of  $A_1$  bars is calculated such that they produce the same stiffness as a plane-stress plate under a uniform tensile loading (Fig. 3.2(c)). The stiffness of the plate is calculated by applying a

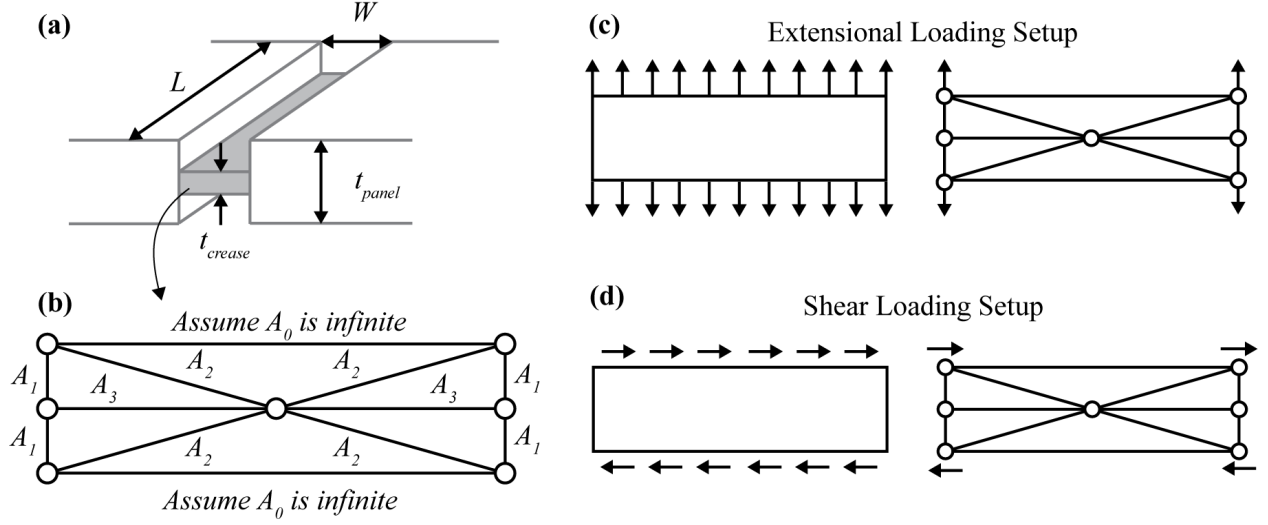


Figure 3.2: Derivation of bar areas for the compliant crease bar and hinge model

unit normal strain field  $\vec{\epsilon} = [1 \ 0 \ 0]^T$  and the total extensional stiffness of the plate model is obtained as:

$$k_{a,pl} = \frac{\frac{E_{crease} t_{crease} L}{1 - \nu_{crease}^2}}{W}, \quad (3.1)$$

where the  $E_{crease}$  and  $\nu_{crease}$  are the Young's modulus and Poisson's ratio of the crease region respectively. The axial stiffness of the compliant crease in the bar and hinge model is calculated with one additional assumption: the contribution of diagonal bars ( $A_2$  bars) is neglected because of their large inclination. This assumption tends to be valid because the crease length  $L$  is typically much larger than its width  $W$ . With this additional assumption, only four  $A_1$  bars are contributing to the axial stiffness and thus the stiffness of the bar and hinge model is calculated as:

$$k_{a,BH} = \frac{2EA_1}{W}. \quad (3.2)$$

By setting  $k_{a,BH} = k_{a,pl}$ , we solve the assigned area for  $A_1$  bars as:

$$A_1 = \frac{Lt_{crease}}{2(1 - \nu_{crease}^2)}. \quad (3.3)$$

Similarly, the area of diagonal bars ( $A_2$  bars) is set such that they produce the same shear stiffness as a plate with the same bulk material. A unit shear strain field  $\vec{\epsilon} = [0 \ 0 \ 1]^T$  is applied and the shear stiffness of the plate is calculated as:

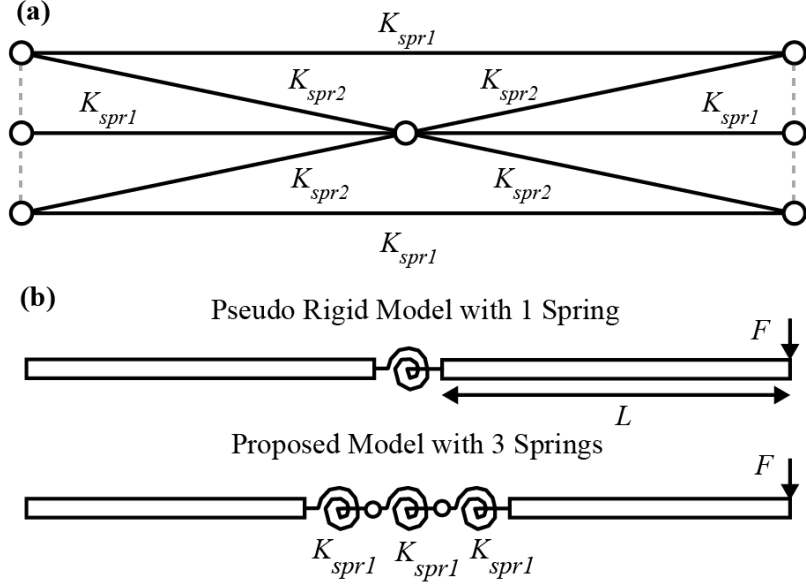


Figure 3.3: Derivation of rotational spring stiffness for compliant crease bar and hinge model.

$$k_{s,pl} = \frac{E_{crease}t_{crease}L}{2W(1 + \nu_{crease})}. \quad (3.4)$$

Because  $A_0$  bars are assumed to have infinite area, only the diagonal bars are contributing to the shear deformation in the bar and hinge model. Therefore, the shear stiffness of the bar and hinge model can be calculated as:

$$k_{s,BH} = \frac{2E_{crease}A_2}{(W^2 + L^2)^{1.5}} L^2. \quad (3.5)$$

By setting  $k_{s,BH} = k_{s,pl}$ , we can solve the assigned areas for  $A_2$  bars. It is further assumed that  $A_3$  bars have the same area as the  $A_2$  bars. Overall, the  $A_3$  bars do not contribute significantly either to tensile or shear behaviors, because they are orthogonal to the edge of the crease region. Although this assumption is somewhat crude, it greatly simplifies the formulation and gives results that match FE simulations relatively well as will be demonstrated in following sections. The areas of  $A_2$  and  $A_3$  bars are thus calculated as:

$$A_3 = A_2 = \frac{(L^2 + W^2)^{1.5}}{4(1 + \nu_{crease})} \frac{t_{crease}}{LW}. \quad (3.6)$$

### 3.2.2 Derivation of rotational spring stiffness

In this section, upper case  $K_{spr}$  denotes the length-normalized spring stiffness, and the lower case  $k_{spr}$  is the total stiffness of the rotational spring, which is calculated as:

$$k_{spr} = K_{spr}L_{spr}, \quad (3.7)$$

where  $L_{spr}$  is the length of the rotational spring. A compliant crease within an origami structure can be treated as a compliant mechanism and modeled as a single rotational spring using the pseudo-rigid-body model described in [Howell, 2001] (Fig. 3.3 (a)). The rotational stiffness of the corresponding pseudo-rigid-body crease model is given as:

$$k_{crease} = \frac{E_{crease}I}{W} = \frac{E_{crease}Lt_{crease}^3}{12W}. \quad (3.8)$$

In the proposed model, this single rotational spring is further divided into three lines of springs (The four  $K_{spr1}$  in Fig. 3.3 (a) and (b)) to better match the distributed curvature observed in real compliant creases. Because one spring is split into three lines of springs, the rotational stiffness of each spring should be increased by a factor of three such that it produces the same global stiffness as the one-spring pseudo-rigid-body model. Thus the normalized rotational spring stiffness for these four  $K_{spr1}$  springs is given as:

$$K_{spr1} = \frac{3E_{crease}I}{WL} = \frac{E_{crease}t_{crease}^3}{4W}. \quad (3.9)$$

All above mentioned model parameters are derived analytically. However, it is difficult to solve the stiffness of the four diagonal rotational springs  $K_{spr2}$  using the previous strategies and thus their stiffness is obtained by matching the results from FE simulations of compliant creases for a specific scenario. A factor  $f$  is used to scale the stiffness of  $K_{spr2}$  with respect to  $K_{spr1}$  as shown in Eqn. 3.10. By matching the infinitesimal torsional stiffness of the bar and hinge model with the FE simulation for the  $\alpha = 0.1$  and  $\beta = 3.0$  case,  $f = 4$  is obtained and  $K_{spr2}$  is calculated as:

$$K_{spr2} = fK_{spr1} = \frac{4 \times 3E_{crease}I}{WL} = \frac{E_{crease}t_{crease}^3}{W}. \quad (3.10)$$

It makes sense that this factor  $f$  should be greater than one, because the corresponding diagonal deformations have more concentrated curvatures as shown on Fig. 3.1 (c), and thus the diagonal springs should be stiffer. Details on the performance of this assigned  $f = 4$  when other values of  $\alpha$  and  $\beta$  are encountered will be demonstrated in the following verification section.

To sum up, the model parameters representing the crease stretching, shearing, and bending

behaviors are derived analytically using the pseudo-rigid-body model and theoretical plate model. However, because of the simplicity of a bar and hinge representation, we were not able to derive the model parameters related with torsional behaviors of a crease analytically. Thus an additional parameter  $f$  is used to match the torsional behavior of the proposed model to FE simulation result of a specific geometric set up with  $\alpha = 0.1$  and  $\beta = 3.0$ . These values are selected because they are representative of common origami structures [Yoon et al., 2014, Bassik et al., 2009]. This additional  $f$  factor only affects the stiffness of the rotational spring  $K_{spr2}$  and thus does not influence the model behavior for crease stretching (controlled mainly by  $A_1$ ), crease shearing (controlled mainly by  $A_2$ ), and crease bending (controlled mainly by  $K_{spr1}$ ). Generally speaking, we find the suggested value  $f = 4$  gives relatively good results over a large range of  $\alpha$  and  $\beta$  values as will be demonstrated in the following verification section.

### 3.2.3 Modeling of panels

The area of the bars within panels is calculated using the generalized N5B8 model derived in [Liu and Paulino, 2018a] as shown in Eqn. (3.11). The equation is formulated with the panel area  $S$  and total length of the bars  $L_i$  within the panel, and is derived such that the strain energy is preserved when the panel undergoes uniform in-plane dilation.

$$A_{panel} = \frac{2St_{panel}}{(1-\nu)\sum_{i=1}L_i} \quad (3.11)$$

The rotational spring stiffness within the panel is derived based on the knowledge that bending stiffness scales with the cubic of thickness and the material stiffness [Timoshenko and Krieger, 1959]. The cubic of the ratio between panel thickness and crease thickness and the ratio of Young's modulus are used to scale the normalized crease stiffness to obtain the stiffness for panel springs as:

$$K_{panel} = \frac{E_{panel}t_{panel}^3}{E_{crease}t_{crease}^3}K_{crease}. \quad (3.12)$$

More robust models for bar and hinge formulations of origami panels as those in [Filipov et al., 2017] could be used, but they are derived based on fully restrained panel edges. For the purpose of this article, these two simple equations work relatively well because the deformation of panels is usually not the controlling factor that governs the global behavior of compliant crease origami as will be shown in the example section.

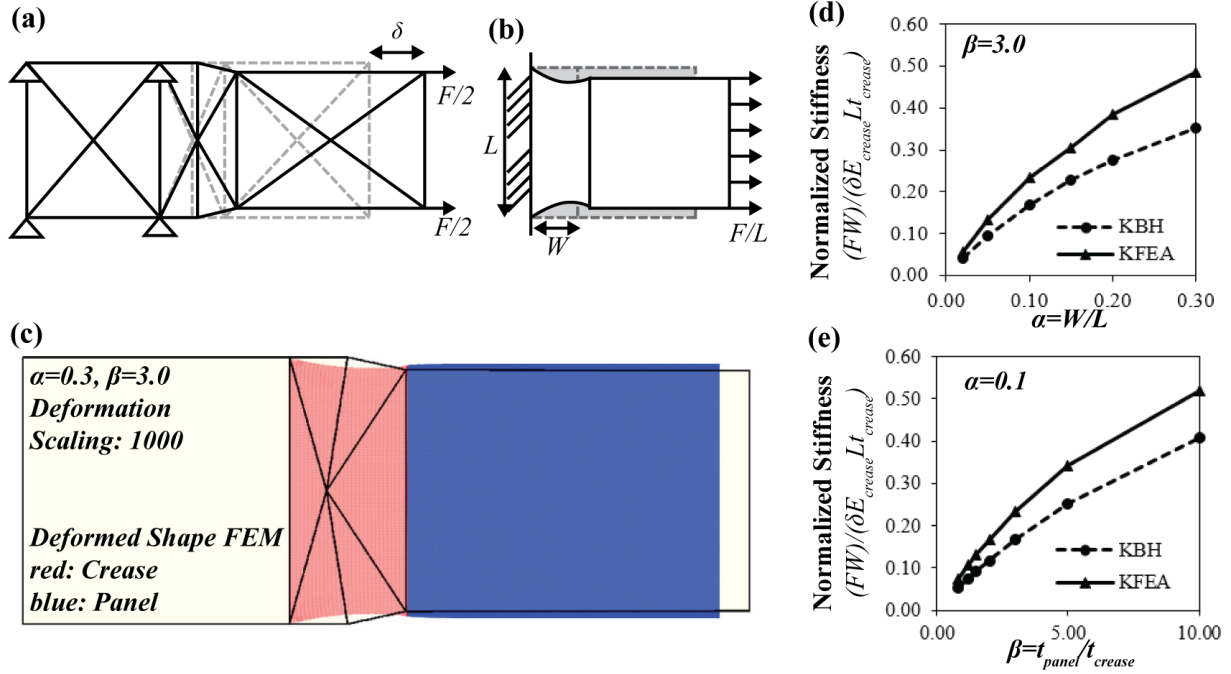


Figure 3.4: Infinitesimal tensile stiffness verification. (a-b) Tensile loading of compliant crease bar and hinge model and the FE model; (c-e) Comparison between the compliant crease bar and hinge model and the FE model for different  $\alpha$  and  $\beta$  values.

### 3.3 Model Verification

In this section, the proposed compliant crease bar and hinge model is compared against FE simulations to verify its performance. This verification is divided into two parts: infinitesimal stiffness and large deformation stiffness. In the following verification sections, the elastic moduli of creases and panels are set to be  $E_{crease} = E_{panel} = 2GPa$ , while the Poisson's ratios of both creases and panels are set as  $\nu_{crease} = \nu_{panel} = 0.3$ , which are realistic values of soft crease origami assemblages.

#### 3.3.1 Infinitesimal stiffness verification

Four types of loading are checked in the infinitesimal stiffness verification. They are tensile, shear, bending, and torsional loading. Stiffness predictions from the compliant crease bar and hinge model are compared against FE simulations when varying  $\alpha$  values or  $\beta$  values (defined at the start of model derivation section). The value of  $\alpha$  is changed by varying  $W$  while fixing  $L = 2.0cm$ , and the value of  $\beta$  is changed by varying  $t_{panel}$  while fixing  $t_{crease} = 0.1mm$ . These values were selected because they represent realistic small-scale origami structures.

The tensile verification for the bar and hinge model with respect to the FE simulation is shown



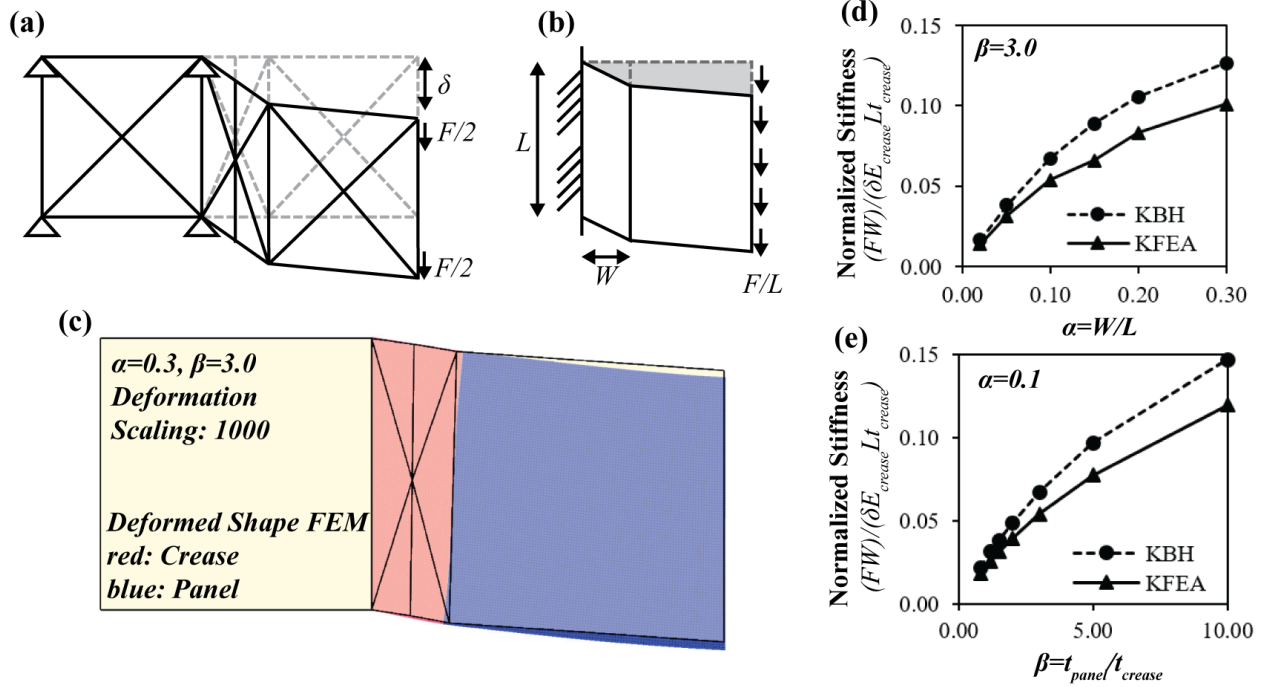


Figure 3.5: Infinitesimal shear stiffness verifications. (a-b) Shear loading of the compliant crease bar and hinge model and the FE model; (c-e) Comparison between the compliant crease bar and hinge model and the FE model for different  $\alpha$  and  $\beta$  values.

in Fig. 3.4. Infinitesimal stiffness of both models is normalized by  $E_{crease}Lt_{crease}/W$  to give a dimensionless result. The proposed bar and hinge model is about 10 – 25% softer than the FE simulation for all explored geometric variations of the structure. This difference is attributed to the error in the panel region rather than the crease region as demonstrated in the Fig. 3.4 (c). The generalized N5B8 panel model as defined in Eqn. (3.11) does not capture the Poisson's effect correctly and underestimates the stiffness because it only matches the strain energy under uniform dilation. The total amount of deformation  $\delta$  in the compliant crease region appears appropriate, however the deformed shape does not match the FE simulation exactly.

The results of shear verification are summarized in Fig. 3.5. Similar to the tension case, the stiffness plotted is normalized by  $E_{crease}Lt_{crease}/W$  to give dimensionless results. Figure 3.5 (c) and (d) show that the mismatch between the bar and hinge model and FE simulation is around 10 – 15%, with the bar and hinge model predicting stiffer responses. This difference is most likely due to the error in the model formulation of panels rather than of creases (see Fig. 3.5 (e)) due to the same reason discussed in the tensile verification.

Figure 3.6 (a) and (b) illustrate the loading set up for infinitesimal bending verification and the results are plotted in Fig. 3.6 (c) and (d). The stiffness predictions from the two models match well

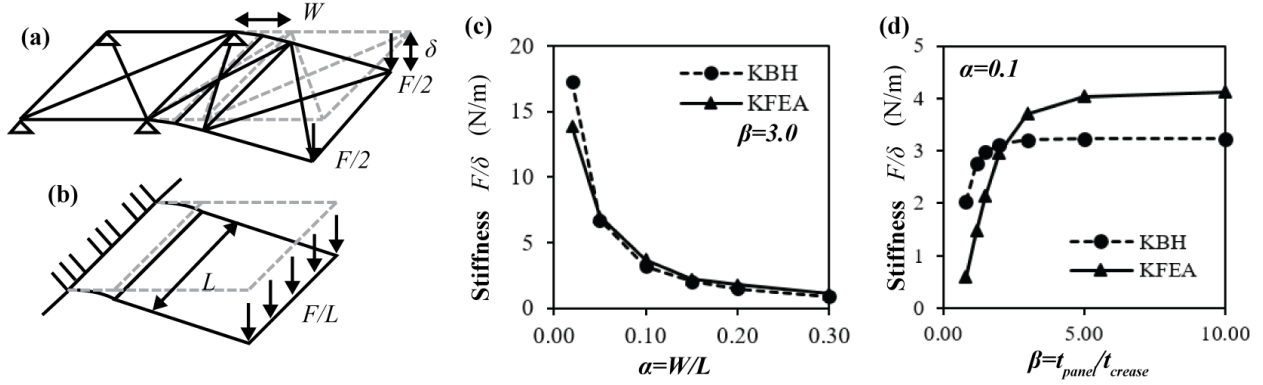


Figure 3.6: Infinitesimal bending stiffness verification.

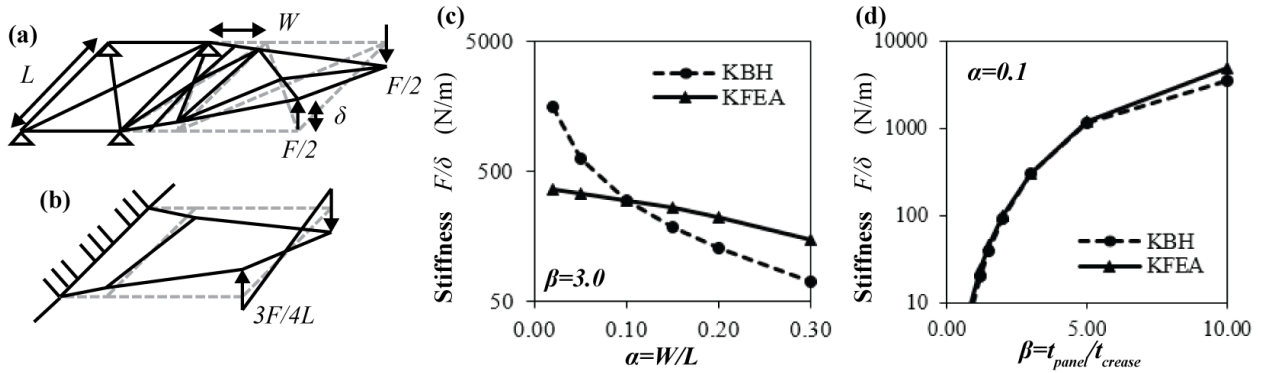


Figure 3.7: Infinitesimal torsional stiffness verification.

for different  $\alpha$  values when  $\beta \approx 3.0$  as illustrated in Fig. 3.6 (c). When  $\beta$  becomes large ( $\beta > 5$ ), the stiffness mismatch between the two models reaches an asymptotic value of about 25%. This mismatch is due to the additional diagonal rotational springs  $K_{spr2}$  that are introduced to capture torsional deformations of the crease. These diagonal springs soften the bending stiffness of the crease by introducing additional degrees of freedom. The softening is much less apparent at larger strains, as will be demonstrated in the following section. When  $\beta$  is small, the mismatch is larger because bending of panels is significant in the global deformation and it is not captured by the bar and hinge model.

The verification of torsional stiffness is summarized in Fig. 3.7. The results only match well when  $\alpha \approx 0.1$  and differ significantly otherwise. When  $\alpha$  is small, the contribution of torsional deformation from the panel is large, while when  $\alpha$  is large the pseudo-rigid-body model proposed in Eqn. (3.8) does not hold. The bar and hinge model is not well suited for capturing these torsional deformations over a wide range of  $\alpha$  values, and thus, we tune the factor  $f$  in Eqn. (3.10) such that

realistic results are obtained for a typical compliant crease region with  $\alpha \approx 0.1$ . The torsion results match well for different values of  $\beta$  when  $\alpha = 0.1$  as shown in Fig. 3.7 (d).

Overall, the proposed bar and hinge model can predict infinitesimal stiffness of origami assemblages relatively well. The proposed model matches FE simulation well when  $\alpha \approx 0.1$  and  $\beta \approx 3.0$ , which are typical values found in real origami inspired engineering structures. Exceeding these ranges tends to create errors in the simulations, but these errors are often still within acceptable ranges. Considering that the proposed compliant crease bar and hinge model only has about one tenth of the degrees of freedom when compared with a coarsely meshed FE simulation, this accuracy is acceptable.

### 3.3.2 Large deformation stiffness verification

For the verification of large deformation stiffness, only pure bending and combined bending and torsion are studied because shear and tensile deformations are substantially smaller. Two methods are used to compare compliant crease bar and hinge model with the FE simulation: (1) *Relative error* is used to measure the influence of  $\beta$  on the difference in response between the two models because force displacement curves generally overlaps for different values of  $\beta$ ; (2) Force displacement curves are used to demonstrate the influence of the  $\alpha$  value, because relative error did not show clear correlation as  $\alpha$  changes. The relative error is defined as:

$$Error = \frac{1}{N} \sum_{i=1}^N \frac{\sqrt{(\delta_i^{FEA} - \delta_i^{BH})^2}}{\delta_i^{FEA}}, \quad (3.13)$$

where  $N$  is the total number of load increments, and  $\delta_i^*$  is the predicted deformation of the  $i^{th}$  load increment from the different models. The loading was set-up such that the two models have the same force increment sequence. In the following verifications,  $\alpha$  is varied by fixing  $L = 2.0cm$  while changing  $W$ , and  $\beta$  is varied by fixing  $t_{crease} = 0.1mm$  while changing  $t_{panel}$ .

Figure 3.8 (a) illustrates the loading set up for the verification of large deformation bending. Figure 3.8 (b) shows that the bar and hinge model matches the FE model well when  $\beta$  is around 2 to 3. The error reaches an asymptotic value of 20% as  $\beta$  becomes large. This mismatch is also due to the additional diagonal springs  $K_{spr2}$ , which add additional flexibility as described in the infinitesimal bending section. When  $\beta < 1.2$ , the results from the bar and hinge model become highly offset from the FE model. This offset is because the proposed bar and hinge model is not able to capture the bending behavior of the relatively thin panels. The large error when  $\beta < 1.2$  is not of a concern because realistic origami inspired structures with compliant creases usually have a larger  $\beta$ . Our verification indicates that the relative error is less affected by the  $\alpha$  index and is around 5% to 10% for all  $\alpha$  tested. Thus, the force displacement curves are plotted to better

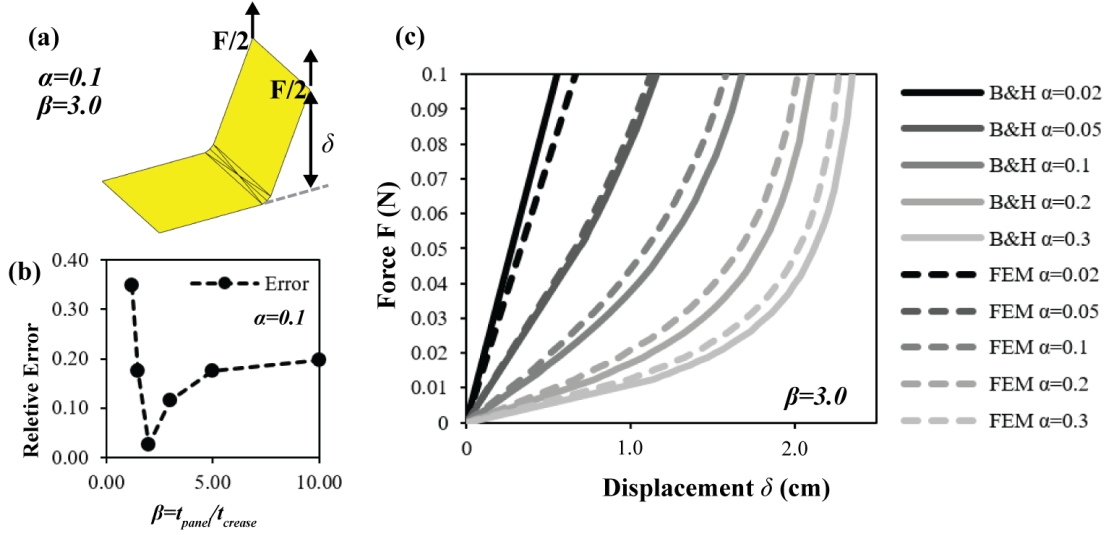


Figure 3.8: Comparison between the bar and hinge model and FE simulation for large deformation bending.

illustrate the influence of the  $\alpha$  value. Figure 3.8 (c) shows that the compliant crease bar and hinge model matches the FE simulation relatively well for all  $\alpha$  values tested when  $\beta = 3.0$ .

Figure 3.9 shows the results for the verification of combined torsional and bending loading case. The trends found in the combined torsion and bending case are similar to those found in the pure bending case with large strain. When  $\beta > 2.0$ , the relative error between the FE simulation and the proposed bar and hinge model varies between 5% to 10%. Larger errors are observed as the panels become very thin ( $\beta < 1.2$ ). Similarly, the force displacement curves are plotted for various  $\alpha$  values and the relative errors for these curves are between 5% to 10%.

## 3.4 Simulation Examples

### 3.4.1 Self-Folding of a plate pattern

To demonstrate the capability and efficiency of the proposed model, we simulate the folding of a plate pattern with four vertexes by applying external loads on the origami structure as demonstrated in [Hernandez et al., 2016b]. The equilibrium is traced with a modified general displacement controlled method used in [Liu and Paulino, 2017a]. Because the detailed dimensions of structure were not provided in the reference, the dimensions used in the bar and hinge model are assumed such that they provide a similar shape. The thickness of panels is assumed to be five times the thickness of creases, so that the structure behaves like a rigid panel origami. Although the bar and hinge model cannot recreate the exact smooth curvature at the folds, it provides the same global

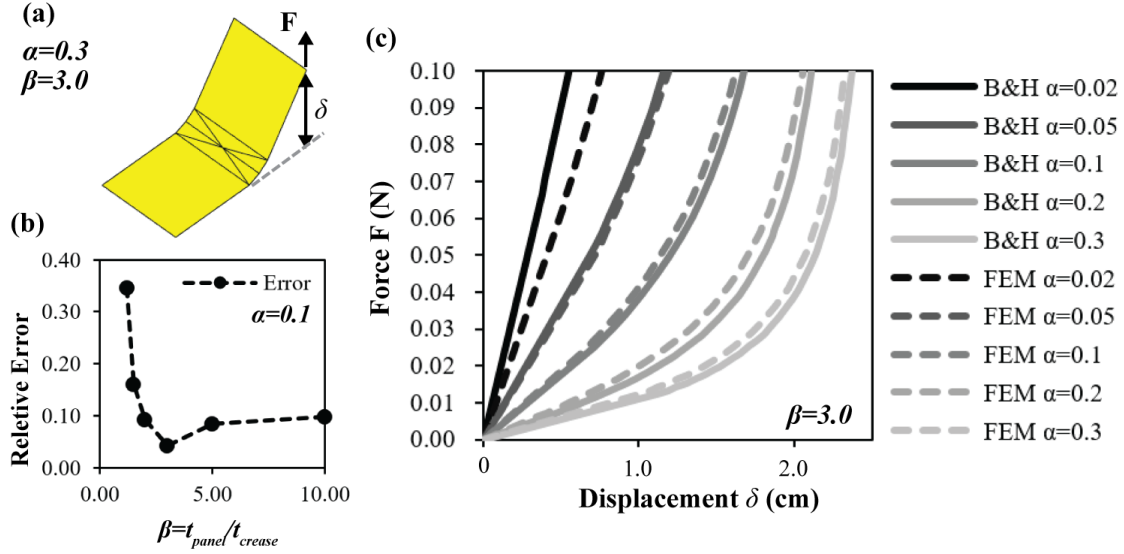


Figure 3.9: Comparison between the bar and hinge model and FE simulation for large deformation loading with combined bending and torsion.

shape for the origami (Fig. 3.10 (c)).

Simulation results and the computation time of the smooth fold model and FE simulation are obtained directly from [Hernandez et al., 2016b]. The 20 second run-time for the bar and hinge model was recorded on a modern (2018) desktop computer with an i7-7700 processor. The proposed model was able to fold the structure with only about 5% of computation time needed for the smooth fold model. If only the global response and the geometry of the structure are of interest, using the proposed model can save a large amount of computational effort. However, the proposed model does not have a high resolution of the local response, so the smooth fold model or the FE simulation would be more suitable if the local response is of interest.

### 3.4.2 Self-folding of a flower pattern

Generally speaking, the folding speed of each crease within a rigid origami is different due to the geometrical constraints imposed by the pattern. However, real self-folding functional origami usually actuate all creases simultaneously at similar rates and thus require special design of the pattern [Na et al., 2015]. Here, we demonstrate how the proposed model can be used to approach this problem.

In this example, a flower-like pattern with 48 creases is used (see Fig. 3.11). This flower pattern has a diameter that is about 10cm and its creases can be self-folded to different angles and with different mountain or valley assignments. The panels have a Young's modulus that is assumed to be

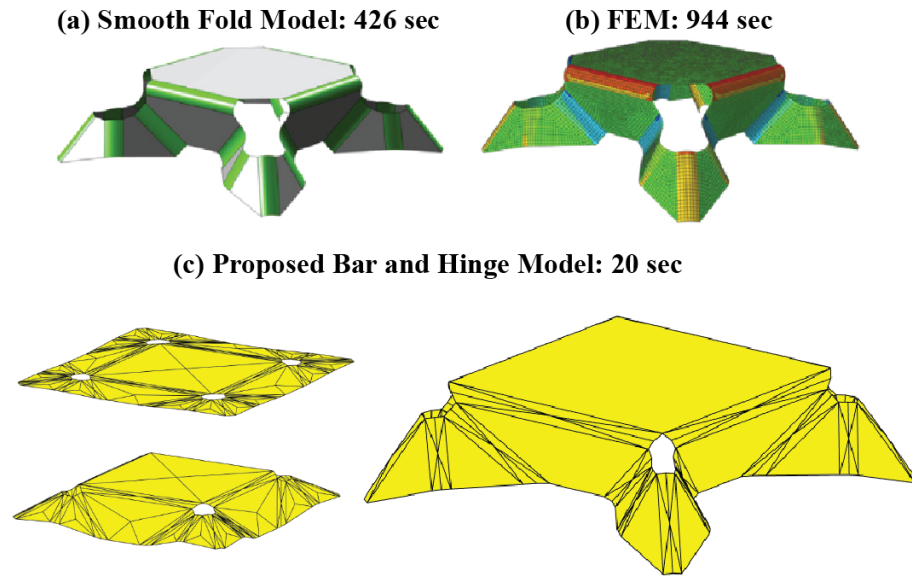


Figure 3.10: Comparing the compliant crease bar and hinge model, the smooth fold model, and the FE model. Figure (a) and (b) are reprinted from [Hernandez et al., 2016b]. Copyright (2016), with permission from Elsevier.

2000MPa and the creases have a modulus that is 20MPa. The thickness of creases are 0.3mm and the thickness of panels are 1mm. These dimensions are selected such that they represent realistic functional origami structures. The self-folding is accomplished by changing the stress-free angle of each crease incrementally and tracing the equilibrium with a Newton-Raphson iteration method.

Both Fig. 3.11 (a) and (b) attempt to fold the same structure into an umbrella-like configuration by assigning an alternating mountain-valley crease arrangement around the center vertex. These mountain-valley assignments give us a water bomb base. In the folding sequence presented in Fig.3.11 (b), the stress free angle of all mountain folds is gradually changed to  $0.5\pi$  and the stress free angle of all valley folds is gradually changed to  $\pi$ . This self-folding path meets the rigid folding requirements relatively well, and thus the real folding angle follows the assigned stress free angle closely. This folding path allows the structure to be successfully folded to the desired umbrella configuration with minimum strain energy developed as demonstrated in Fig. 3.11 (d). However, if all creases are folded at the same rate, this pattern does not fold to the umbrella shape correctly (see Fig. 3.11 (b)). In this folding path, the stress free angles for both mountain folds and valley folds are gradually changed to  $0.7\pi$  and thus have the same speed of folding. Because the folding path does not match well with the rigid folding constraints imposed by the pattern, the structure becomes trapped at an undesired configuration and the real folding angles diverge from the assigned stress free angles extensively. This divergence generates a large amount of

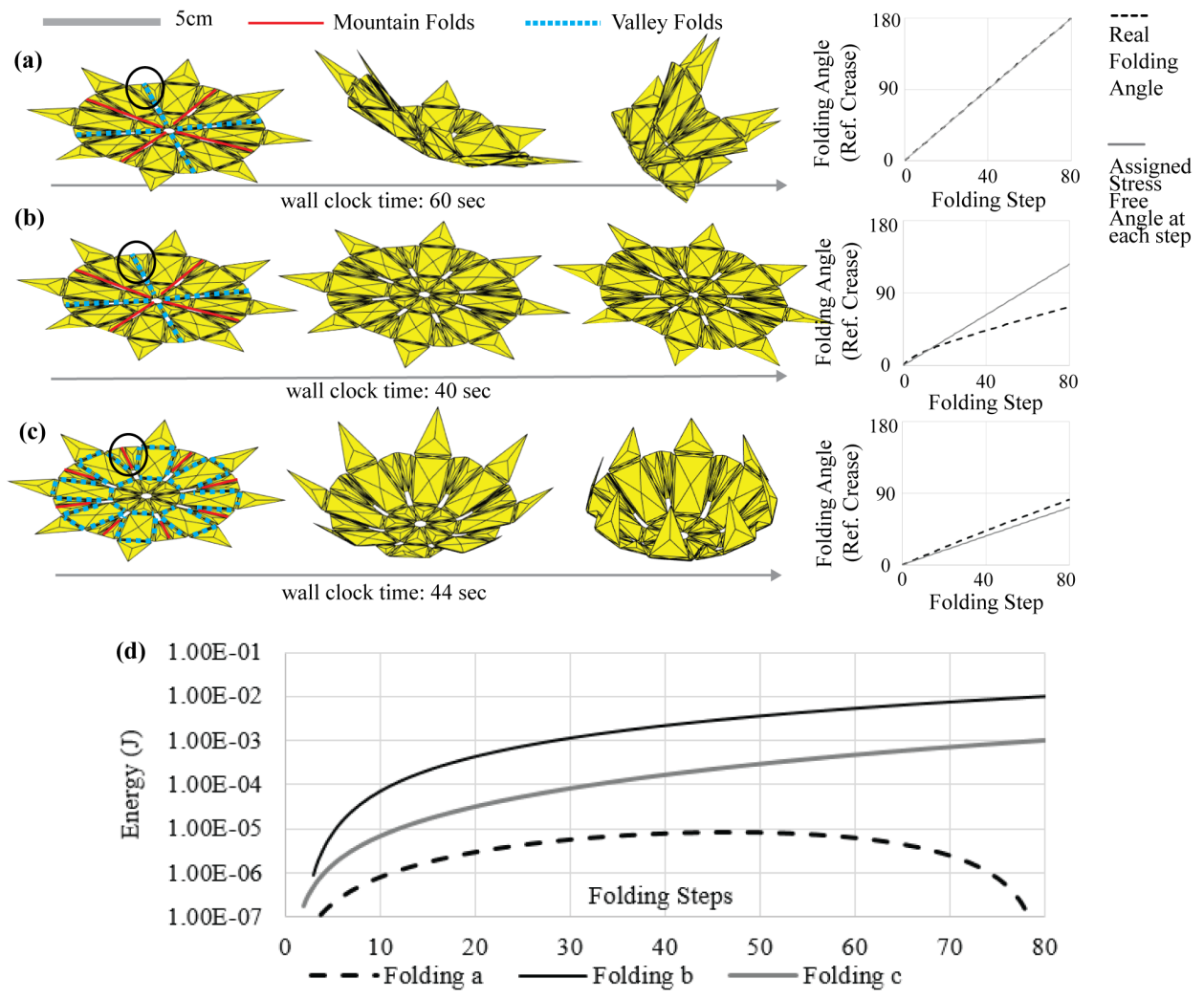


Figure 3.11: Self-folding of a flower like pattern with different strain energy profile. The reference crease is displayed in the black circle.

strain energy that is stored within the structure (Fig. 3.11 (d)). In real practice, one can solve this problem by (i) adjusting the folding rate of each crease, or (ii) by assigning different folding sequence of each crease.

Figure 3.11 (c) shows another possible folding path of the structure where each crease is folded such that the final geometry looks like a bowl. In this case, all active compliant creases are folded simultaneously and their folding rates are the same. Because all creases are folded with the same rate, the folding path does not follow rigid folding requirements exactly. However, because the assigned folding path does not diverge from the rigid folding path significantly, the structure folds to its final configuration successfully despite building up strain energy in the system.

Although the pattern studied here has 48 creases and is a relatively complex problem, all simulations of the self-folding are finished within one minute. This example further demonstrates the efficiency of the proposed model and shows that the model is suitable to study the self-folding process of compliant origami systems. The model allows researchers to investigate the possible design space rapidly and to learn about the global behaviors of the system before building more detailed FE models.

### 3.4.3 A bistable four-fold vertex

Next, in Fig. 3.12 we study the bistable behavior of a four-fold vertex presented in [Faber et al., 2018]. This four-fold origami vertex is a cone-like structure that experiences bistable snap-through behavior when loaded. Figure 3.12 (a) shows the loading set up of the structure, where four nodes in the center are fixed in space while the loads are applied at the center of each panel. From the top view, these panels appear as  $5 \times 5 \text{ cm}^2$  squares, and all compliant creases have the same  $6 \text{ mm}$  width. The cone shape is generated by moving the shared center nodes upward and the four outer free corners downward, which skews the square panel to form the missing angle as shown in Fig. 3.12 (a). Thus the actual panels are not square but are rhombus if flattened onto a plane. The thickness of the creases is  $1 \text{ mm}$  and the thickness of the panels is  $2.2 \text{ mm}$ . These geometries are selected such that they represent the structure presented in [Faber et al., 2018]. The Young's modulus of the crease material is set as  $25 \text{ MPa}$  and the panel material is set as  $2852 \text{ MPa}$ . We directly use these values from [Faber et al., 2018] without altering them to recreate the test response recorded from [Faber et al., 2018] with our model. In principle, changing the material properties could eventually change the bistable behavior of these systems as well.

Figure 3.12 (b) shows the force displacement curves recorded during the loading process and Fig. 3.12 (c) records the energy landscape. The force-displacement results obtained from the analyses are in good agreement with the experimental findings presented in [Faber et al., 2018], when comparing the initial peak force in the bistable snap-through. Furthermore, the plots show that



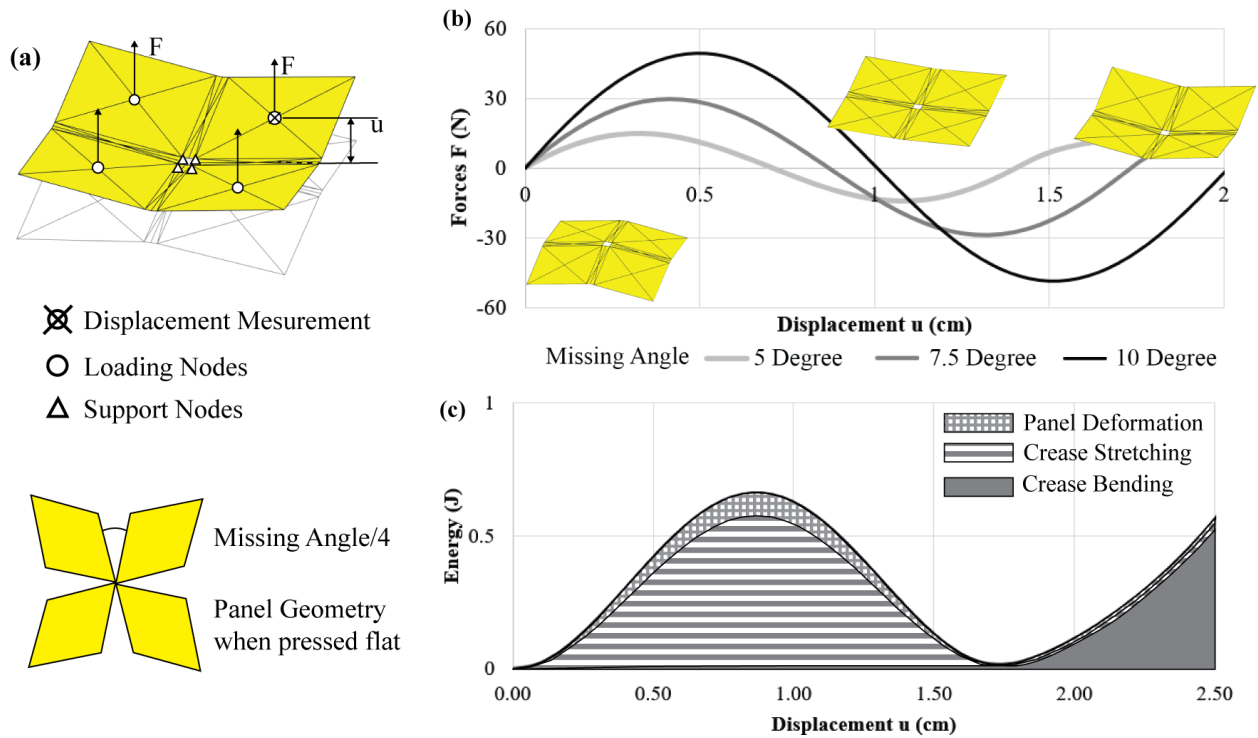


Figure 3.12: Loading of a bistable four-fold vertex. Energy curves plotted for a case with missing angle of  $7.5^\circ$ .

the crease stretching energy dominates the energy barrier that forms the bistable snap-through behavior, again matching the observations presented in [Faber et al., 2018] well. Because conventional origami modeling techniques simplify the compliant creases as rotational hinges that have no width, they cannot capture the creases extensional deformations and thus cannot capture this type of bistable behavior. This example demonstrates that the proposed model provides a relatively fast and accurate simulation method to study bistable behaviors of origami where the bistability occurs due to the presence of compliant creases.

### 3.4.4 Bistable Miura-ori beams

In this section, the bistable behavior of a Miura-ori beam with three units will be studied. The Miura-ori pattern is developable, and can become bistable, for example if (1) there is differential stiffnesses and rest angles in the fold lines [Waitukaitis et al., 2015], or (2) if applied constraints and loads cause reorientation of the geometry. Here, we explore the second case where a simple Miura-ori sheet is loaded to invert one of its vertices. To demonstrate this bistable behavior, we use a physical model with flexible polymer sheet creases and cardboard paper to serve as the panels

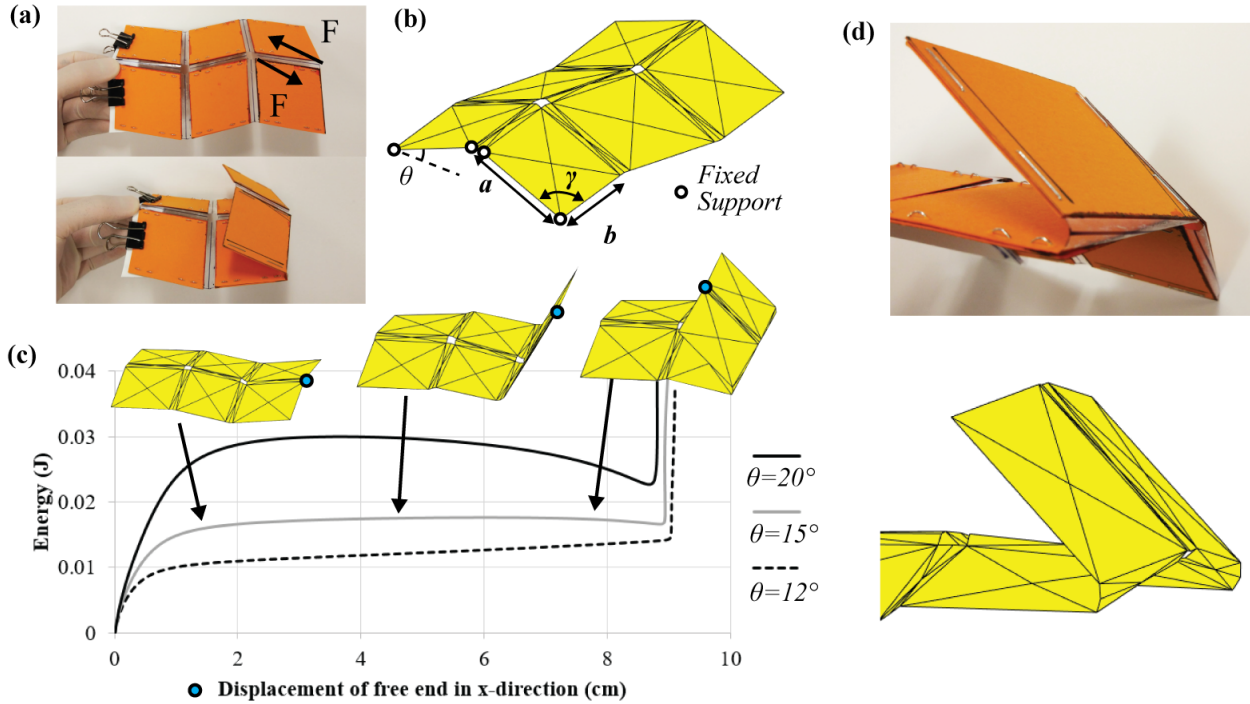


Figure 3.13: Bistable Miura beams. The physical models are made with polymer creases and cardboard paper panels (The left edge is fixed at  $\theta = 20^\circ$ ).

(Fig. 3.13 (a)). The geometry of the Miura-ori system is set as illustrated in Fig. 3.13 (b), with  $a = b = 5\text{cm}$  and  $\gamma = 80^\circ$ . The thickness of the creases is  $0.1\text{mm}$  and the thickness of the panels is  $1\text{mm}$ . The width of the creases is  $6\text{mm}$  for all compliant creases. We assume the panels have a Young's modulus of  $1\text{GPa}$  and the creases have a Young's modulus of  $2\text{GPa}$ . When a pair of loads is applied to the outermost unit of the Miura cantilever (forces  $F$  in Fig. 3.13(a)), the outermost two panels bend over and reach another stable state. The left edge of the physical model is restrained to keep the angle  $\theta = 20^\circ$  fixed throughout the simulation.

We perform numerical simulations for the same Miura beam folded to three different  $\theta$  values. Figure 3.13 (c) shows that by decreasing the folding angle  $\theta$  we can obtain less obvious bistable behaviors, and at  $\theta = 12^\circ$ , we obtain a monostable structure. This behavior is expected because when the  $\theta$  value is approaching zero, the Miura cantilever is not folded and is mostly flat. Thus, loading the structure using the pair of forces displayed in Fig. 3.13 (a) is only bending the two creases elastically, which gives a monostable response. When the  $\theta$  value becomes larger, the geometry of the folded Miura cantilever gives rise to the second stable configuration, where the last vertex has to be inverted into a new state that is not compatible with the initial rigid folding kinematics.

This is another example that demonstrates the benefits of having compliant creases modeled explicitly, especially when studying bistable behaviors in origami structures. Besides the previously mentioned stretching deformation of creases, this example demonstrates that relative torsional deformations between adjacent panels is also important for capturing the correct geometry of these bistable origami. Figure 3.13 (d) shows how the proposed model captures this relative torsion between adjacent panels by including the additional diagonal  $K_{spr2}$  springs ( $A_2$  bars) into the creases region.

### 3.5 Concluding Remarks

This chapter proposes an improved formulation for a bar and hinge model to study the behavior of origami assemblages with flexible compliant creases. Equations for assigning bar areas and spring stiffness are derived by matching the stiffness of the bar and hinge model to that from the theoretical plate model and the pseudo-rigid-body model for crease stretching, shearing, and bending behaviors. However, due to the simplicity of the proposed model, one spring stiffness  $K_{spr2}$  for crease torsion cannot be obtained analytically. Thus a factor  $f$  is used to scale it so that the torsional stiffness of our model matches the FE simulation for  $\alpha = 0.1$  and  $\beta = 3.0$  case. We latter confirm that this selected  $f = 4$  factor performs relatively well for a much wider range of  $\alpha$  and  $\beta$  values in the verification section.

The proposed model is checked against FE simulations and the results match generally well under tensile, shear, bending, and torsion for infinitesimal deformation. The proposed model produces the best estimate of structural stiffness when the crease aspect ratio is  $\alpha \approx 0.1$  and the panel thickness ratio is  $\beta \approx 3.0$ . These ratios are representative of real origami systems with compliant creases. At large deformations, the behavior of the proposed model is not sensitive to the  $\alpha$  value and is able to give closely matched predictions when  $\beta > 1.2$ .

Simulation examples were used to further demonstrate the capabilities and efficiency of the model. The model can capture the crease bending for three dimensional folding simulations and can approximate self-assembly where folds are actuated. In self-assembly simulations, the model can predict if the desired shape will be reached with simultaneous actuation of all folds, or if the folds will need to be actuated separately to successfully complete the folding process. Furthermore, the proposed model captures the contribution from torsional and extensional behaviors of creases, which are of great significance when studying the bistable or multi-stable behaviors of origami inspired assemblages with non-negligible crease width. Many origami patterns that are traditionally considered monostable are in fact multistable when the added flexibility of compliant hinges is taken into account. The proposed model can be used as a fast and relatively accurate modeling technique for preliminary exploration of origami inspired assemblages with compliant

creases.

## Chapter 4. Global Self-Contact Model

This chapter introduces a novel method to capture the global panel contact within functional origami systems to tackle Challenge 3 proposed in the Introduction. This contact model is derived by adding an additional contact potential to the total potential of the bar and hinge models. Moreover, this proposed contact simulation method is computationally efficient and can capture the internal forces, the contact configuration, and the thickness of origami panels accurately.

The organization of this chapter is as the following. First, we give a brief introduction of contact simulations for origami models and for FE models. This section focuses on highlighting the differences between the two problems and motivates the development of the inter-panel contact model. Then, Section 4.2 derives the formulation of the proposed contact model in detail, which is followed by a numerical verification in Section 4.3. Next, Section 4.4 introduces an implementation scheme for including the proposed model within a bar and hinge simulation framework. This scheme is next tested to verify its continuity, penetration prevention, and contact initiation needed to build a well-performing contact model. Moreover, we showed that the proposed model can be used to simulate thickness of panels in an origami by tuning the model parameters accordingly. In the end, computational examples are provided in Section 4.5 to demonstrate the validity and efficiency of the proposed model. The nomenclatures used in this chapter is summarized in Table 4.1.

### 4.1 Contact Models for Origami and for FE Methods

Simulation of global panel contact is difficult and crucial for modeling functional origami systems. Although many existing origami simulation techniques have included the local contact prevention: the folding is stopped when a crease is folded by 180 degree [Tachi, 2009c, Liu and Paulino, 2017a], there is currently no method to capture the global panel contact in functional origami systems.

The existence of global panel contact can add substantial difficulties to determine if an origami pattern can be folded or not even for a simple single vertex. Figure 4.1 demonstrate this using a comparison of a spherical linkage problem and a single vertex folding problem. The spherical linkage problem can be seen as a reduced single vertex foldability problem where panel contact does not need to be considered. For this reduced problem, the loop closure condition provides a necessary and sufficient condition for the rotated linkage to be in a valid configuration. In fact,

Table 4.1: Nomenclature used in Chapter 4

Symbols	Definition
$\mathbf{I}_{3 \times 3}$	$3 \times 3$ identity matrix
$\mathbf{0}_{3 \times 3}$	$3 \times 3$ zero matrix
$E$	Young's modulus of material
$A$	Cross section area of a simple bar element
$L_0$	Length of a simple bar element
$\Pi$	Potential energy (strain energy)
$\mathbf{f}$	Internal force vector
$\mathbf{K}$	Stiffness matrix
$\mathbf{x}$	Deformed nodal coordinate (generic)
$\mathbf{X}$	Reference nodal coordinate (generic)
$\mathbf{u}$	Deformation vector (generic)
$\mathbf{x}_0, \mathbf{x}_1, \mathbf{x}_2, \mathbf{x}_3$	Deformed nodal coordinates of the four nodes
$\mathbf{X}_0, \mathbf{X}_1, \mathbf{X}_2, \mathbf{X}_3$	Reference nodal coordinates of the four nodes
$\mathbf{u}_0, \mathbf{u}_1, \mathbf{u}_2, \mathbf{u}_3$	Deformation vectors of the four nodes
$d$	Distance between the point and the triangle
$d_0, d_0c, d_0e$	Initiation thresholds for panel contact
$k_e$	Potential scaling factor
$V$	Volume of the parallelepiped (with a sign)
$A_{s0}$	Area square of the parallelogram in zone 0
$A_{s2}$	Area square of the parallelogram in zone 2
$L_s$	Length square of the distance between two nodes in zone 2
$\mathbf{x}_{z0}, \mathbf{x}_{z1}, \mathbf{x}_{z2}$	Deformed nodal coordinates for three zones

this loop closure equation is the basis of many existing kinematic simulation methods for origami systems [Tachi, 2009c, Tachi, 2009a]. To further consider the foldability problem of a single vertex, potential interaction between different origami panels must be considered. In this case, the loop closure condition no longer guarantees the validity of a folded condition and it only states a necessary condition, because of the potential panel contact indicated in Fig. 4.1 (b).

On top of the above foldability problem, there is an even more challenging question to ask: How do the mechanical properties of an origami pattern change once the global panel contact is initiated? The inter panel contact within an origami pattern usually induces changes in the mechanical behaviors, such as the sudden stiffness jump studied in [Fang et al., 2016, Fang et al., 2018]. In addition, the inter-panel contact also allows engineers to build various inter locking origami that can sustains forces without adhesion [Mao et al., 2015, Kamrava et al., 2017]. Such behaviors can be utilized to design metamaterials and locking devices for various engineering applications. Unfortunately, limited works have done to address this issue in the field of origami simulation.

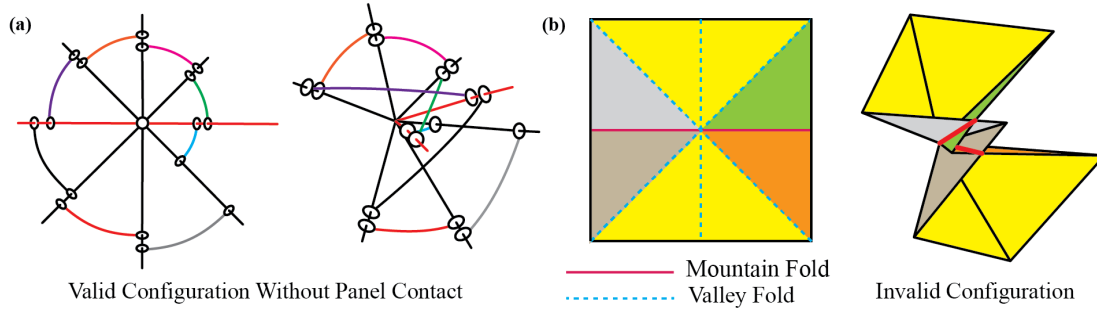


Figure 4.1: Origami folding is difficult to simulate because of the existence of global panel contact.

Although modeling of global panel contact in origami is rarely studied, contact modeling in FE models (often in combination with discrete element (DE) models) is a more robust field of research. It is not our focus to introduce the field in a detailed manner, but we focus more on how the origami contact problem is different from conventional contact simulation within a FE framework.

The contact simulations in FE analysis can be roughly split into two major topics: contact detection and contact mechanics [Dahlstrom and Lindkvist, 2007, Vorobiev, 2012]. The contact detection mostly focuses on determining the geometrical relationship between different bodies and searching for contacting elements. A variety of methods can be selected based on the geometrical characteristics or other special properties of the system for optimal efficiency [Zhong and Nilsson, 1989, Oldenburg and Nilsson, 1994, Zheng et al., 2017, Munjiza and Andrews, 1998, Perkins and Williams, 2001]. FE simulation usually requires a fine mesh for useful results, and thus the number of degrees of freedom involved in contact detection is typically large. Because of the large number of degrees of freedom, a key objective in the implementation of contact detection is to find ways that will bring down the overall computational cost. For example, in many modern software programs contact is only tracked on user pre-specified surfaces, and not over the entire model domain. However, only a sparse mesh is needed to capture the geometry, kinematics, and global mechanics for origami simulations, and thus much fewer degrees of freedom are required for simulating an origami than performing typical FE simulations (such as those in [Hirota, 2002]). Therefore, the key issue in origami contact is not how to reduce the number of areas for contact detection, but instead how to capture the contacting geometry correctly even when the contacting nodes are sparsely spaced. The field of contact mechanics focuses on the force law used to obtain the correct model response. Reference [Adams and Nosonovsky, 2000] gives a thorough review of various models for contact mechanics. So far, no significant exploration has been performed on the contact force laws for origami structures and how the force laws can influence the foldability or other mechanical behaviors of an origami.

Although finite element (FE) simulations provide one option for studying the influence of global panel contact on the mechanical behavior of an origami pattern and is indeed used to study related problems, such as those in [Mukhopadhyay et al., 2020], it requires tremendous modeling efforts and long computation time to obtain useful results. In many situations, it is difficult to have the desired computing resources or the time schedule to analyze the foldability and eventually the mechanics of origami structures under the influence of panel contact with FE simulations.

Because of the above mentioned problems, it is difficult to design a foldable structure and eventually analyze its mechanical properties if panel contact were to happen. One way to bypass such problem is to use a thoroughly studied base pattern for the design. For example, with the Miura-ori pattern, a large number of engineering devices were designed, such as deployable tubes with high out-of-plane stiffness [Filipov et al., 2015, Filipov et al., 2019], origami grippers [Kamrava et al., 2018], frequency selective surface [Nauroze et al., 2018], and metamaterials [Schenk and Guest, 2013, Ma et al., 2018b, Lv et al., 2014]. Because the design is based on the Miura-ori, the foldability is preserved and thus the structure is guaranteed to be foldable. However, using pre-exist patterns provides limited geometries for engineering applications, where more generalized patterns are desired. To address the issue, the following sections formulated a contact simulation method for origami model to capture the global contact induced mechanical behaviors within an origami effectively.

## 4.2 Formulation of the Global Panel Contact Model

### 4.2.1 Methodology: principle of stationary potential energy and barrier functions

The panel contact model proposed in this chapter is constructed under the framework of the principle of stationary potential energy with the help of barrier functions. Within the framework of principle of stationary potential energy, the equilibrium position of a deformable body is a configuration that gives a stationary potential energy (gradient of potential vanishes). To prevent the panels from penetrating each other, a set of barrier functions are added into the total potential of the system such that the potential goes to infinite as the distances between the contacting panel and the contacting node approaches zero. This is similar to the interior point method for linear programs where barrier functions in the form of  $\ln(x_i)$  can be added into the total cost function to replace the constraint  $x_i \geq 0$  [Bertsimas and Tsitsiklis, 1997].

We start with a brief review of the principle of stationary potential energy. We will use the principle to derive the internal force vector and the stiffness matrix of a 1-D extensional bar element. To simplify our derivation, it is further assumed that the bar has a constant stiffness  $\frac{EA}{L_0}$ , where  $E$



is the Young's modulus,  $A$  is the area of the bar section, and  $L_0$  is the original length of the bar. The total Lagrangian approach is used to formulate the equations, and the potential energy of a bar element can be written as:

$$\Pi_{bar} = \frac{EA}{2L_0} (\sqrt{(x_1 - x_2)^2} - L_0)^2, \quad (4.1)$$

where the  $x_1$  and  $x_2$  are the current (deformed) configuration of the two nodes on the 1-D axis, and the term  $\sqrt{(x_1 - x_2)^2} - L_0$  measures the elongation of the spring. By taking the gradient of the potential, the internal force vector  $\mathbf{f}_{bar}$  is obtained as:

$$\mathbf{f}_{bar} = \frac{\partial \Pi_{bar}}{\partial \mathbf{u}} = \frac{\partial \Pi_{bar}}{\partial \mathbf{x}} = \frac{EA}{L_0} \frac{(\sqrt{(x_1 - x_2)^2} - L_0)}{\sqrt{(x_1 - x_2)^2}} \begin{bmatrix} x_1 - x_2 \\ x_2 - x_1 \end{bmatrix}, \quad (4.2)$$

where  $\mathbf{x} = [x_1, x_2]^T$  are the current nodal coordinates represented as a  $2 \times 1$  vector. The displacement vector  $\mathbf{u}$  is defined as  $\mathbf{u} = \mathbf{x} - \mathbf{X}$  where upper-case  $\mathbf{X} = [X_1, X_2]^T$  is the reference (undeformed) nodal coordinate vector. Because the reference configuration is constant we have  $\frac{\partial \Pi_{bar}}{\partial \mathbf{u}} = \frac{\partial \Pi_{bar}}{\partial \mathbf{x}}$ . By further taking the Hessian of the potential, we obtain the stiffness matrix  $\mathbf{K}_{bar}$  of the spring:

$$\mathbf{K}_{bar} = \frac{\partial^2 \Pi_{bar}}{\partial \mathbf{u}^2} = \frac{\partial^2 \Pi_{bar}}{\partial \mathbf{x}^2} = \frac{EA}{L_0} \begin{bmatrix} 1 & -1 \\ -1 & 1 \end{bmatrix}, \quad (4.3)$$

which gives back the constant spring stiffness that we assumed. In the formulation of panel contact, the same procedure of using the principle of stationary potential energy will be followed, except that the calculations involve more nodes and are thus lengthier.

#### 4.2.2 Contact potential, force vector, and stiffness matrix

To simulate the contact between panels, a repulsive force field is added around each triangulated panel (referred to as *triangle* in the following text). This force field acts on three nodes of the triangle and another node (referred to as the *point* in the following text) from another triangle. Figure 4.2 illustrates the concept with the red node referring the point. In the proposed model, the repulsive forces grow to infinity as the distance between the point and the triangle approaches zero such that panel penetration is prevented.

We assume that the contact force is conservative so that we can derive it by prescribing a potential function that acts as a barrier function using the principal of stationary potential energy. This assumption of conservation generally works well when our goal is to prevent panel penetrations and capture phenomena such as a sudden stiffness jump studied in [Fang et al., 2016, Fang et al.,

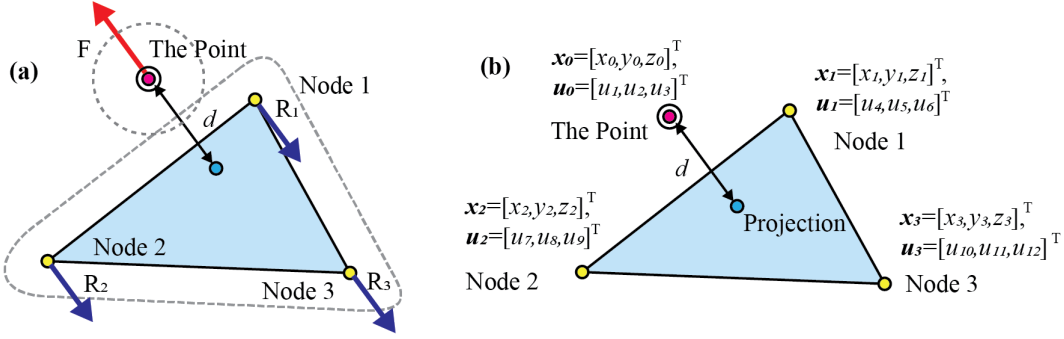


Figure 4.2: Panel penetration prevention is achieved by creating an imaginary repulsive force field around the triangle, and the magnitude of the forces can be calculated based on the closest distance from the point to the triangle  $d$ .

2018], sequential folding induced self-locking [Mao et al., 2015], or an inter-locking behaviors that sustains forces without adhesion [Kamrava et al., 2017]. Generally speaking, the frictional forces do not comply with the principle of stationary potential energy, and requires solving initial value problems with dynamics mechanics solvers. The proposed model could potentially be extended to capture those behaviors, but the work is beyond the scope of this chapter.

We set three requirements in selecting a proper potential function: (1) the function should produce a continuous force field (continuity); (2) the function should give infinite forces and stiffness as the distance between the point and the triangle approaches zero (penetration prevention); and (3) the function should have a piecewise formulation such that the repulsive forces are only triggered when the point is close to the panel and are zero otherwise (contact initiation/disengagement). To achieve these three requirements, the contact potential is constructed using the closest distance  $d$  (Fig. 4.2) between the triangle and the point and is expressed as:

$$\Pi(d(\mathbf{x})) = \begin{cases} k_e \left\{ \ln \left[ \sec \left( \frac{\pi}{2} - \frac{\pi d}{2d_0} \right) \right] - \frac{1}{2} \left( \frac{\pi}{2} - \frac{\pi d}{2d_0} \right)^2 \right\} & (d \leq d_0) \\ 0 & (d > d_0), \end{cases} \quad (4.4)$$

where  $d_0$  is the threshold when the repulsive force is triggered and  $k_e$  is a constant used to scale the magnitude of the potential. When  $d > d_0$  the potential is zero so that there is no repulsive forces and no additional stiffness. In the most general situation, the point to triangle distance  $d$  is a function of all four deformed nodal coordinates  $\mathbf{x}_0, \mathbf{x}_1, \mathbf{x}_2,$  and  $\mathbf{x}_3$  (Fig. 4.2 (b)). The form of this contact potential equation is inspired from the interior point method for linear programs, where the constraint  $x > 0$  can be represented as  $-\ln(x)$  in the objective function. Other origami simulation packages like the MERLIN [Liu and Paulino, 2017a], also uses similar strategies to capture local panel contact. With the potential equation formulated, we can obtain the corresponding internal

force vector by taking the gradient of the contact potential as:

$$\mathbf{f} = \frac{\partial \Pi}{\partial \mathbf{u}} = \frac{\partial \Pi}{\partial \mathbf{x}} = \begin{cases} k_e \left\{ \frac{\pi}{2d_0} \left( \frac{\pi}{2} - \frac{\pi d}{2d_0} - \tan \left( \frac{\pi}{2} - \frac{\pi d}{2d_0} \right) \right) \frac{\partial d}{\partial \mathbf{x}} \right\} & (d \leq d_0) \\ 0 & (d > d_0), \end{cases} \quad (4.5)$$

where  $\mathbf{u}$  is the corresponding nodal displacement vector of the four nodes and is defined as  $\mathbf{u} = \mathbf{x} - \mathbf{X}$ , following the convention of using lowercase  $\mathbf{x}$  for deformed configuration and uppercase  $\mathbf{X}$  for undeformed (reference) configuration. Because the nodal coordinate vector of the undeformed configuration  $\mathbf{X}$  is constant, we have  $\frac{\partial \Pi}{\partial \mathbf{x}} = \frac{\partial \Pi}{\partial \mathbf{u}}$ . Similarly, the stiffness matrix can be constructed by taking the Hessian of the potential as:

$$\mathbf{K} = \frac{\partial^2 \Pi}{\partial \mathbf{u}^2} = \frac{\partial^2 \Pi}{\partial \mathbf{x}^2} = \begin{cases} k_e \left\{ \frac{\pi}{2d_0} \left( \frac{\pi}{2} - \frac{\pi d}{2d_0} - \tan \left( \frac{\pi}{2} - \frac{\pi d}{2d_0} \right) \right) \frac{\partial^2 d}{\partial \mathbf{x}^2} \right. \\ \left. + \left( \frac{\pi}{2d_0} \right)^2 \left[ \sec^2 \left( \frac{\pi}{2} - \frac{\pi d}{2d_0} \right) - 1 \right] \left( \frac{\partial d}{\partial \mathbf{x}} \right) \left( \frac{\partial d}{\partial \mathbf{x}} \right)^T \right\} & (d \leq d_0) \\ 0 & (d > d_0) \end{cases} \quad (4.6)$$

### 4.2.3 Definition of the point to triangle distance $d$

Fully calculating the internal forces and stiffness associated with the contact potential requires calculating the closest distance between the contacting triangle and the point. To calculate the closest distance, we need to first determine the relative location between the point and the triangle. There are three different cases for defining the point to triangle distance  $d$  as demonstrated in Fig. 4.3 (a). The problem of determining the contact zones can be done by linear decomposition or projection. Figure 4.3 (a) shows the vectors that will be used to achieve this goal. Vectors  $\mathbf{p}_1$ ,  $\mathbf{p}_2$ , and  $\mathbf{p}_3$  point from node 1, node 2, and node 3 to the projection of the point respectively. Vectors  $\mathbf{E}_1$  and  $\mathbf{E}_2$  point from node 1 to node 2 and node 1 to node 3 respectively.

For zone 0, we use vectors  $\mathbf{E}_1$  and  $\mathbf{E}_2$  to form a basis and linearly decompose  $\mathbf{p}_1$  within the basis. (By saying linear decomposition, we mean writing  $\mathbf{p}_1 = a\mathbf{E}_1 + b\mathbf{E}_2$ ). If both results ( $a$  and  $b$ ) are positive and are less than one, then the point falls in zone 0.

For zone 1, without loss of generality, we assume that the point is closest to node 1. We then linearly decompose the vector  $\mathbf{p}_1$  within the basis formed by vectors  $\mathbf{v}_{11}$  and  $\mathbf{v}_{12}$ . If both results are positive, the point is within zone 1 and is closest to node 1.

For zone 2, we assume that the point is closest to the line segment formed by node 1 and node 2. We project vector  $\mathbf{p}_1$  onto vectors  $\mathbf{E}_1$  and  $\mathbf{v}_{11}$ , and next project vector  $\mathbf{p}_2$  onto  $-\mathbf{E}_1$ . If all three results are positive, the point falls within zone 2 and is closet to the line segment formed by node 1 and node 2.

Practically, there is no need to differentiate the cases when the point falls on the edge where

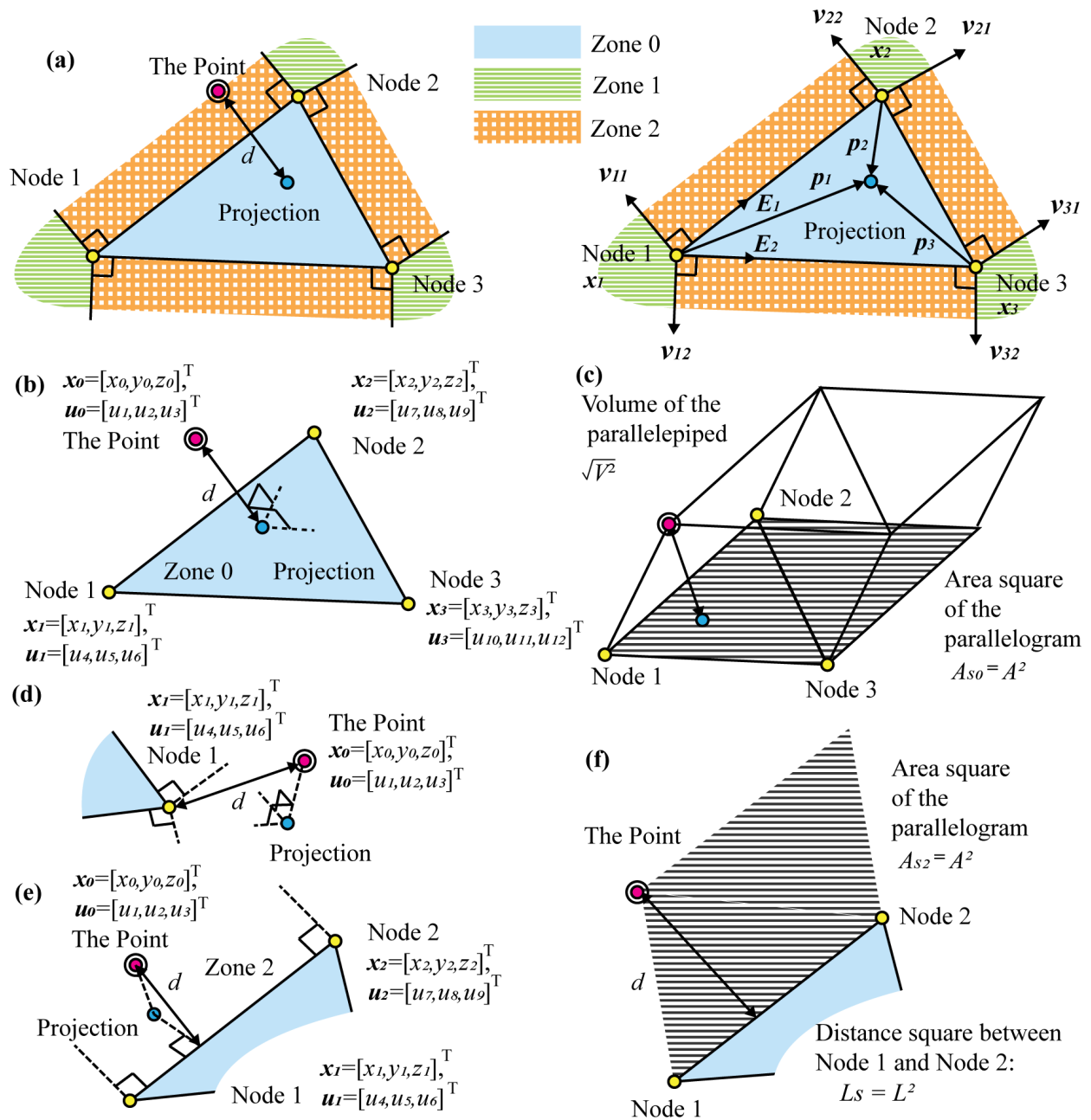


Figure 4.3: Calculation of the point to triangle distance.

two or three separate zones meet. Because the contact potential has continuity over the three zones, using equations from different zones yields the same answer on the edges. Therefore, we can always use ' $\geq$ ' and ' $\leq$ ' rather than ' $>$ ' and ' $<$ ' for judging the zones when coding the implementation package, and the problem is solved automatically.

If the projection is located within zone 0, then the point to triangle distance is a node to plane distance, which can be calculated as:

$$d = \frac{\sqrt{V^2}}{\sqrt{A_{s0}}} = \frac{\sqrt{\{(\mathbf{x}_0 - \mathbf{x}_1)^T [(\mathbf{x}_2 - \mathbf{x}_1) \times (\mathbf{x}_3 - \mathbf{x}_1)]\}^2}}{\sqrt{[(\mathbf{x}_2 - \mathbf{x}_1) \times (\mathbf{x}_3 - \mathbf{x}_1)]^2}}. \quad (4.7)$$

Equation 4.7 calculates the distance  $d$  by dividing the volume of the parallelepiped by the area of the parallelogram (Fig. 4.3 (c)), which is in the form of a triple product of three vectors over the value of a cross product of two vectors. Square-root-of-square is used to obtain an absolute value of point to triangle distance  $d$ .  $A_{s0}$  is defined to represent the square of the area of the parallelogram in zone 0 formed by the three nodes of the triangle as in Fig. 4.3 (c). In zone 0, the nodal coordinate vector and nodal displacement vector are both  $12 \times 1$  vectors and can be written as  $\mathbf{x}_{z0} = [\mathbf{x}_0^T, \mathbf{x}_1^T, \mathbf{x}_2^T, \mathbf{x}_3^T]^T$ , and  $\mathbf{u}_{z0} = [\mathbf{u}_0^T, \mathbf{u}_1^T, \mathbf{u}_2^T, \mathbf{u}_3^T]^T$  respectively, where the individual nodal quantities  $\mathbf{x}_0, \mathbf{x}_1, \mathbf{x}_2, \mathbf{x}_3, \mathbf{u}_0, \mathbf{u}_1, \mathbf{u}_2$ , and  $\mathbf{u}_3$  are defined according to Fig. 4.3 (b).

If the projection is located within zone 1, the point to panel distance is calculated as a node to node distance, which can be expressed as:

$$d = \sqrt{(\mathbf{x}_1 - \mathbf{x}_0)^T (\mathbf{x}_1 - \mathbf{x}_0)}. \quad (4.8)$$

Without loss of generality, we assume that node 1 is closest to the point. This case is relatively simple and is demonstrated on Fig. 4.3 (d). In this zone, because only two nodes are used to construct the point to triangle distance, the nodal coordinates vector and nodal displacement vector are both  $6 \times 1$  vectors and are defined as  $\mathbf{x}_{z1} = [\mathbf{x}_0^T, \mathbf{x}_1^T]^T$ , and  $\mathbf{u}_{z1} = [\mathbf{u}_0^T, \mathbf{u}_1^T]^T$  respectively (Fig. 4.3 (d)).

If the projection is located within zone 2, the point to triangle distance  $d$  is the point to line distance as illustrated on Fig. 4.3 (e). It is assumed that the point is closest to the line segment formed by node 1 and node 2, and the point to triangle distance is calculated using:

$$d = \frac{\sqrt{A_{s2}}}{\sqrt{L_s}} = \frac{\sqrt{[(\mathbf{x}_0 - \mathbf{x}_1) \times (\mathbf{x}_2 - \mathbf{x}_1)]^2}}{\sqrt{(\mathbf{x}_2 - \mathbf{x}_1)^T (\mathbf{x}_2 - \mathbf{x}_1)}}, \quad (4.9)$$

which is in the form of an area of a parallelogram over the length between the two nodes (see Fig. 4.3 (f)).  $A_{s2}$  represents the square of area of the parallelogram formed with the three nodal coordinates in zone 2 and  $L_s$  represents the square of length between node 1 and node 2. In zone 2, because three nodes are used to construct the point to triangle distance, the corresponding

nodal coordinate vector and nodal displacement vector are both  $9 \times 1$  vectors and are written as:  $\mathbf{x}_{z2} = [\mathbf{x}_0^T, \mathbf{x}_1^T, \mathbf{x}_2^T]^T$ , and  $\mathbf{u}_{z2} = [\mathbf{u}_0^T, \mathbf{u}_1^T, \mathbf{u}_2^T]^T$  respectively (Fig. 4.3 (e)).

#### 4.2.4 Calculation of gradient and Hessian of $d$

After computing the point to triangle distance  $d$ , its gradient and Hessian need to be calculated so that Eqn.4.5 and Eqn.4.6 can be used to calculate the contact force vector and the stiffness matrix. Because the point to triangle distance has different formulations in the different zones, the gradient and Hessian of  $d$  also need to be calculated separately.

In zone 0, the point to triangle distance is calculated using Eqn.4.7. Based on this formulation, the gradient of  $d$  can be calculated using:

$$\frac{\partial d}{\partial \mathbf{x}} = \frac{\partial d}{\partial \mathbf{x}_{z0}} = \frac{\eta}{\sqrt{A_{s0}}} \frac{\partial V}{\partial \mathbf{x}_{z0}} - \frac{1}{2} \frac{\eta V}{\sqrt{A_{s0}^3}} \frac{\partial A_{s0}}{\partial \mathbf{x}_{z0}}, \quad (4.10)$$

where  $\eta = \text{sign}(V)$  is the sign of  $V$ . The Hessian of  $d$  is:

$$\begin{aligned} \frac{\partial^2 d}{\partial \mathbf{x}^2} = \frac{\partial^2 d}{\partial \mathbf{x}_{z0}^2} = & \frac{\eta}{\sqrt{A_{s0}}} \frac{\partial^2 V}{\partial \mathbf{x}_{z0}^2} - \frac{1}{2} \frac{\eta}{\sqrt{A_{s0}^3}} \left( \frac{\partial V}{\partial \mathbf{x}_{z0}} \right) \left( \frac{\partial A_{s0}}{\partial \mathbf{x}_{z0}} \right)^T - \frac{1}{2} \frac{\eta V}{\sqrt{A_{s0}^3}} \frac{\partial^2 A_{s0}}{\partial \mathbf{x}_{z0}^2} \\ & - \frac{1}{2} \frac{\eta}{\sqrt{A_{s0}^3}} \left( \frac{\partial A_{s0}}{\partial \mathbf{x}_{z0}} \right) \left( \frac{\partial V}{\partial \mathbf{x}_{z0}} \right)^T + \frac{3}{4} \frac{\eta V}{\sqrt{A_{s0}^5}} \left( \frac{\partial A_{s0}}{\partial \mathbf{x}_{z0}} \right) \left( \frac{\partial A_{s0}}{\partial \mathbf{x}_{z0}} \right)^T. \end{aligned} \quad (4.11)$$

As defined in the previous section,  $A_{s0}$  is the square of the area of the parallelogram formed by the three nodes of the triangle, and  $V$  is the volume of the parallelepiped (Fig. 4.3 (c)). Because four nodal coordinates are used to define the point to panel distance  $d$  in zone 0, the gradient of  $d$  in zone 0 is a  $12 \times 1$  vector while the Hessian of  $d$  will give a  $12 \times 12$  matrix.

In zone 1, the point to triangle distance is calculated using Eqn.4.8, so the gradient can be calculated using:

$$\frac{\partial d}{\partial \mathbf{x}} = \frac{\partial d}{\partial \mathbf{x}_{z1}} = \left[ \left( \frac{\partial d}{\partial \mathbf{x}_0} \right)^T, \left( \frac{\partial d}{\partial \mathbf{x}_1} \right)^T \right]^T = \left[ \frac{1}{d} (\mathbf{x}_0 - \mathbf{x}_1)^T, \frac{1}{d} (\mathbf{x}_1 - \mathbf{x}_0)^T \right]^T, \quad (4.12)$$

and the Hessian can be calculated using:

$$\frac{\partial^2 d}{\partial \mathbf{x}^2} = \frac{\partial^2 d}{\partial \mathbf{x}_{z1}^2} = \begin{bmatrix} \frac{\partial^2 d}{\partial \mathbf{x}_0 \partial \mathbf{x}_0} & \frac{\partial^2 d}{\partial \mathbf{x}_0 \partial \mathbf{x}_1} \\ \frac{\partial^2 d}{\partial \mathbf{x}_1 \partial \mathbf{x}_0} & \frac{\partial^2 d}{\partial \mathbf{x}_1 \partial \mathbf{x}_1} \end{bmatrix} = \begin{bmatrix} \frac{1}{d} \mathbf{I}_{3 \times 3} - \frac{1}{d^3} (\mathbf{x}_0 - \mathbf{x}_1)(\mathbf{x}_0 - \mathbf{x}_1)^T & -\frac{1}{d} \mathbf{I}_{3 \times 3} + \frac{1}{d^3} (\mathbf{x}_0 - \mathbf{x}_1)(\mathbf{x}_0 - \mathbf{x}_1)^T \\ -\frac{1}{d} \mathbf{I}_{3 \times 3} + \frac{1}{d^3} (\mathbf{x}_0 - \mathbf{x}_1)(\mathbf{x}_0 - \mathbf{x}_1)^T & \frac{1}{d} \mathbf{I}_{3 \times 3} - \frac{1}{d^3} (\mathbf{x}_0 - \mathbf{x}_1)(\mathbf{x}_0 - \mathbf{x}_1)^T \end{bmatrix}. \quad (4.13)$$

The symbol  $\mathbf{I}_{3 \times 3}$  represents a  $3 \times 3$  identity matrix. Because only two nodal coordinates are used to construct the point to panel distance in zone 1,  $\frac{\partial d}{\partial \mathbf{x}_{z1}}$  is a  $6 \times 1$  vector and  $\frac{\partial^2 d}{\partial \mathbf{x}_{z1}^2}$  is a  $6 \times 6$  matrix.

In zone 2, the point to panel distance is calculated using Eqn.4.9. The gradient is calculated using the following equation:

$$\frac{\partial d}{\partial \mathbf{x}} = \frac{\partial d}{\partial \mathbf{x}_{z2}} = \frac{1}{2} \frac{1}{\sqrt{A_{s2} L_s}} \frac{\partial A_{s2}}{\partial \mathbf{x}_{z2}} - \frac{1}{2} \frac{\sqrt{A_{s2}}}{\sqrt{L_s^3}} \frac{\partial L_s}{\partial \mathbf{x}_{z2}}, \quad (4.14)$$

and the Hessian is calculated as:

$$\begin{aligned} \frac{\partial^2 d}{\partial \mathbf{x}^2} = \frac{\partial^2 d}{\partial \mathbf{x}_{z2}^2} &= \frac{1}{2} \frac{1}{\sqrt{A_{s2} L_s}} \frac{\partial^2 A_{s2}}{\partial \mathbf{x}_{z2}^2} - \frac{1}{4} \frac{1}{\sqrt{A_{s2}^3 L_s}} \left( \frac{\partial A_{s2}}{\partial \mathbf{x}_{z2}} \right) \left( \frac{\partial A_{s2}}{\partial \mathbf{x}_{z2}} \right)^T \\ &\quad - \frac{1}{4} \frac{1}{\sqrt{A_{s2} L_s^3}} \left( \frac{\partial A_{s2}}{\partial \mathbf{x}_{z2}} \right) \left( \frac{\partial L_s}{\partial \mathbf{x}_{z2}} \right) - \frac{1}{2} \frac{\sqrt{A_{s2}}}{\sqrt{L_s^3}} \frac{\partial^2 L_s}{\partial \mathbf{x}_{z2}^2} \\ &\quad - \frac{1}{4} \frac{1}{\sqrt{A_{s2} L_s^3}} \left( \frac{\partial L_s}{\partial \mathbf{x}_{z2}} \right) \left( \frac{\partial A_{s2}}{\partial \mathbf{x}_{z2}} \right)^T + \frac{3}{4} \frac{\sqrt{A_{s2}}}{\sqrt{L_s^5}} \left( \frac{\partial L_s}{\partial \mathbf{x}_{z2}} \right) \left( \frac{\partial L_s}{\partial \mathbf{x}_{z2}} \right)^T. \end{aligned} \quad (4.15)$$

Because three nodal coordinates are used to construct the distance  $d$ , the gradient of  $d$  is a  $9 \times 1$  vector and the Hessian is a  $9 \times 9$  matrix.

To finish the above calculations, it is necessary to calculate the gradients and Hessians of  $V$ ,  $A_{s0}$ ,  $A_{s2}$  and  $L_s$ . The gradients and Hessians of  $V$ ,  $A_{s0}$ ,  $A_{s2}$  and  $L_s$  need to be solved separately for different zones because the number of nodal coordinate needed for calculation is different. We use  $\mathbf{x}_{z0}$ ,  $\mathbf{x}_{z1}$ , and  $\mathbf{x}_{z2}$  to denote the nodal coordinate vectors for zone 0, zone 1, and zone 2 respectively, just as the notations used in the previous formulation section.

The volume of parallelepiped formed by four nodes  $\mathbf{x}_0$ ,  $\mathbf{x}_1$ ,  $\mathbf{x}_2$ , and  $\mathbf{x}_3$  can be calculated using the following:

$$V = (\mathbf{x}_0 - \mathbf{x}_1) \cdot [(\mathbf{x}_2 - \mathbf{x}_1) \times (\mathbf{x}_3 - \mathbf{x}_1)]. \quad (4.16)$$

This value is used in the Eqn.4.7, Eqn.4.10, and Eqn.4.11, and the gradient of the volume  $V$  is a  $12 \times 1$  vector as:

$$\begin{aligned} \frac{\partial V}{\partial \mathbf{x}_{z0}} &= \left[ \left( \frac{\partial V}{\partial \mathbf{x}_0} \right)^T, \left( \frac{\partial V}{\partial \mathbf{x}_1} \right)^T, \left( \frac{\partial V}{\partial \mathbf{x}_2} \right)^T, \left( \frac{\partial V}{\partial \mathbf{x}_3} \right)^T \right]^T \\ &= \begin{bmatrix} [a, b, c]^T \\ (\mathbf{x}_2 - \mathbf{x}_3) \times (\mathbf{x}_0 - \mathbf{x}_1) - [a, b, c]^T \\ (\mathbf{x}_3 - \mathbf{x}_1) \times (\mathbf{x}_0 - \mathbf{x}_1) \\ (\mathbf{x}_1 - \mathbf{x}_2) \times (\mathbf{x}_0 - \mathbf{x}_1) \end{bmatrix}, \end{aligned} \quad (4.17)$$

where the  $[a, b, c]^T$  vector is calculated using:

$$[a, b, c]^T = (\mathbf{x}_2 - \mathbf{x}_1) \times (\mathbf{x}_3 - \mathbf{x}_1). \quad (4.18)$$

The Hessian of the volume  $V$  is a  $12 \times 12$  matrix and can be calculated as:

$$\begin{aligned} \frac{\partial^2 V}{\partial \mathbf{x}_{z0}^2} &= \begin{bmatrix} \mathbf{0}_{3 \times 3} & \frac{\partial^2 V}{\partial \mathbf{x}_0 \partial \mathbf{x}_1} & \frac{\partial^2 V}{\partial \mathbf{x}_0 \partial \mathbf{x}_2} & \frac{\partial^2 V}{\partial \mathbf{x}_0 \partial \mathbf{x}_3} \\ \frac{\partial^2 V}{\partial \mathbf{x}_1 \partial \mathbf{x}_0} & \mathbf{0}_{3 \times 3} & \frac{\partial^2 V}{\partial \mathbf{x}_1 \partial \mathbf{x}_2} & \frac{\partial^2 V}{\partial \mathbf{x}_1 \partial \mathbf{x}_3} \\ \frac{\partial^2 V}{\partial \mathbf{x}_2 \partial \mathbf{x}_0} & \frac{\partial^2 V}{\partial \mathbf{x}_2 \partial \mathbf{x}_1} & \mathbf{0}_{3 \times 3} & \frac{\partial^2 V}{\partial \mathbf{x}_2 \partial \mathbf{x}_3} \\ \frac{\partial^2 V}{\partial \mathbf{x}_3 \partial \mathbf{x}_0} & \frac{\partial^2 V}{\partial \mathbf{x}_3 \partial \mathbf{x}_1} & \frac{\partial^2 V}{\partial \mathbf{x}_3 \partial \mathbf{x}_2} & \mathbf{0}_{3 \times 3} \end{bmatrix} \\ &= \begin{bmatrix} \mathbf{0}_{3 \times 3} & -skew(\mathbf{x}_2 - \mathbf{x}_3) & -skew(\mathbf{x}_3 - \mathbf{x}_1) & -skew(\mathbf{x}_1 - \mathbf{x}_2) \\ skew(\mathbf{x}_2 - \mathbf{x}_3) & \mathbf{0}_{3 \times 3} & -skew(\mathbf{x}_3 - \mathbf{x}_0) & -skew(\mathbf{x}_2 - \mathbf{x}_0) \\ skew(\mathbf{x}_3 - \mathbf{x}_1) & skew(\mathbf{x}_3 - \mathbf{x}_0) & \mathbf{0}_{3 \times 3} & -skew(\mathbf{x}_1 - \mathbf{x}_0) \\ skew(\mathbf{x}_1 - \mathbf{x}_2) & skew(\mathbf{x}_2 - \mathbf{x}_0) & skew(\mathbf{x}_1 - \mathbf{x}_0) & \mathbf{0}_{3 \times 3} \end{bmatrix} \end{aligned} \quad (4.19)$$

where the symbol  $\mathbf{0}_{3 \times 3}$  is a  $3 \times 3$  zero matrix, and the  $skew()$  operator is defined as the following:

$$skew([u, v, w]^T) = \begin{bmatrix} 0 & -w & v \\ w & 0 & -u \\ -v & u & 0 \end{bmatrix}. \quad (4.20)$$



This skew() operator basically back calculates the skew tensor from its axial vector.

The area of a parallelogram in zone 0 formed by three nodes  $\mathbf{x}_1$ ,  $\mathbf{x}_2$ , and  $\mathbf{x}_3$  of the triangle can be calculated using:

$$A = \sqrt{A_{s0}} = \sqrt{[(\mathbf{x}_2 - \mathbf{x}_1) \times (\mathbf{x}_3 - \mathbf{x}_1)]^2}. \quad (4.21)$$

The gradient of  $A_{s0}$  with respect to  $\mathbf{x}_{z0}$  is a  $12 \times 1$  vector in zone 0, and the Hessian is a  $12 \times 12$  matrix. The gradient of  $A_{s0}$  can be calculated using:

$$\frac{\partial A_{s0}}{\partial \mathbf{x}_{z0}} = \left[ \left( \frac{\partial A_{s0}}{\partial \mathbf{x}_0} \right)^T, \left( \frac{\partial A_{s0}}{\partial \mathbf{x}_1} \right)^T, \left( \frac{\partial A_{s0}}{\partial \mathbf{x}_2} \right)^T, \left( \frac{\partial A_{s0}}{\partial \mathbf{x}_3} \right)^T \right]^T = \begin{bmatrix} \mathbf{0}_{3 \times 1} \\ 2(\mathbf{x}_2 - \mathbf{x}_3) \times [a, b, c]^T \\ 2(\mathbf{x}_3 - \mathbf{x}_1) \times [a, b, c]^T \\ 2(\mathbf{x}_1 - \mathbf{x}_2) \times [a, b, c]^T \end{bmatrix}, \quad (4.22)$$

and the Hessian of  $A_{s0}$  can be calculated using:

$$\frac{\partial^2 A_{s0}}{\partial \mathbf{x}_{z0}^2} = \begin{bmatrix} \mathbf{0}_{3 \times 3} & \mathbf{0}_{3 \times 3} & \mathbf{0}_{3 \times 3} & \mathbf{0}_{3 \times 3} \\ \mathbf{0}_{3 \times 3} & \frac{\partial^2 A_{s0}}{\partial \mathbf{x}_1^2} & \frac{\partial^2 A_{s0}}{\partial \mathbf{x}_1 \partial \mathbf{x}_2} & \frac{\partial^2 A_{s0}}{\partial \mathbf{x}_1 \partial \mathbf{x}_3} \\ \mathbf{0}_{3 \times 3} & \frac{\partial^2 A_{s0}}{\partial \mathbf{x}_2 \partial \mathbf{x}_1} & \frac{\partial^2 A_{s0}}{\partial \mathbf{x}_2^2} & \frac{\partial^2 A_{s0}}{\partial \mathbf{x}_2 \partial \mathbf{x}_3} \\ \mathbf{0}_{3 \times 3} & \frac{\partial^2 A_{s0}}{\partial \mathbf{x}_3 \partial \mathbf{x}_1} & \frac{\partial^2 A_{s0}}{\partial \mathbf{x}_3 \partial \mathbf{x}_2} & \frac{\partial^2 A_{s0}}{\partial \mathbf{x}_3^2} \end{bmatrix}. \quad (4.23)$$

The three diagonal terms are calculated using:

$$\frac{\partial^2 A_{s0}}{\partial \mathbf{x}_1^2} = 2\{[(\mathbf{x}_2 - \mathbf{x}_3)^T (\mathbf{x}_2 - \mathbf{x}_3)] \mathbf{I}_{3 \times 3} + (\mathbf{x}_2 - \mathbf{x}_3)(\mathbf{x}_3 - \mathbf{x}_2)^T\}, \quad (4.24)$$

$$\frac{\partial^2 A_{s0}}{\partial \mathbf{x}_2^2} = 2\{[(\mathbf{x}_3 - \mathbf{x}_1)^T (\mathbf{x}_3 - \mathbf{x}_1)] \mathbf{I}_{3 \times 3} + (\mathbf{x}_3 - \mathbf{x}_1)(\mathbf{x}_1 - \mathbf{x}_3)^T\}, \quad (4.25)$$

$$\frac{\partial^2 A_{s0}}{\partial \mathbf{x}_3^2} = 2\{[(\mathbf{x}_1 - \mathbf{x}_2)^T (\mathbf{x}_1 - \mathbf{x}_2)] \mathbf{I}_{3 \times 3} + (\mathbf{x}_1 - \mathbf{x}_2)(\mathbf{x}_2 - \mathbf{x}_1)^T\}. \quad (4.26)$$

Because of the symmetry, only three off-diagonal terms need to be calculated and the remaining three can be obtained by transposing the matrix. The off-diagonal terms can be calculated using:

$$\begin{aligned} \frac{\partial^2 A_{s0}}{\partial \mathbf{x}_1 \partial \mathbf{x}_2} &= \left( \frac{\partial^2 A_{s0}}{\partial \mathbf{x}_2 \partial \mathbf{x}_1} \right)^T = 2[(\mathbf{x}_3 - \mathbf{x}_1)^T (\mathbf{x}_2 - \mathbf{x}_3)] \mathbf{I}_{3 \times 3} \\ &\quad - 2(\mathbf{x}_3 - \mathbf{x}_1)(\mathbf{x}_2 - \mathbf{x}_3)^T - 2 \text{skew}([a, b, c]^T), \end{aligned} \quad (4.27)$$

$$\begin{aligned} \frac{\partial^2 A_{s0}}{\partial \mathbf{x}_2 \partial \mathbf{x}_3} &= \left( \frac{\partial^2 A_{s0}}{\partial \mathbf{x}_3 \partial \mathbf{x}_2} \right)^T = 2[(\mathbf{x}_1 - \mathbf{x}_2)^T (\mathbf{x}_3 - \mathbf{x}_1)] \mathbf{I}_{3 \times 3} \\ &\quad - 2(\mathbf{x}_1 - \mathbf{x}_2)(\mathbf{x}_3 - \mathbf{x}_1)^T - 2 \text{skew}([a, b, c]^T), \end{aligned} \quad (4.28)$$

$$\begin{aligned} \frac{\partial^2 A_{s0}}{\partial \mathbf{x}_3 \partial \mathbf{x}_1} &= \left( \frac{\partial^2 A_{s0}}{\partial \mathbf{x}_1 \partial \mathbf{x}_3} \right)^T = 2[(\mathbf{x}_2 - \mathbf{x}_3)^T (\mathbf{x}_1 - \mathbf{x}_2)] \mathbf{I}_{3 \times 3} \\ &\quad - 2(\mathbf{x}_2 - \mathbf{x}_3)(\mathbf{x}_1 - \mathbf{x}_2)^T - 2 \text{skew}([a, b, c]^T). \end{aligned} \quad (4.29)$$

The area of a parallelogram in zone 2 formed by three nodes  $\mathbf{x}_1$  and  $\mathbf{x}_2$  of the triangle and the point  $\mathbf{x}_0$  can be calculated using:

$$A = \sqrt{A_{s2}} = \sqrt{[(\mathbf{x}_2 - \mathbf{x}_1) \times (\mathbf{x}_0 - \mathbf{x}_1)]^2}. \quad (4.30)$$

The gradient of  $A_{s2}$  with respect to  $\mathbf{x}_{z2}$  is a  $9 \times 1$  vector in zone 2, and the Hessian is a  $9 \times 9$  matrix. The gradient of  $A_{s2}$  can be calculated using:

$$\frac{\partial A_{s2}}{\partial \mathbf{x}_{z2}} = \left[ \left( \frac{\partial A_{s2}}{\partial \mathbf{x}_0} \right)^T, \left( \frac{\partial A_{s2}}{\partial \mathbf{x}_1} \right)^T, \left( \frac{\partial A_{s2}}{\partial \mathbf{x}_2} \right)^T \right]^T = \begin{bmatrix} 2(\mathbf{x}_1 - \mathbf{x}_2) \times [a, b, c]^T \\ 2(\mathbf{x}_2 - \mathbf{x}_0) \times [a, b, c]^T \\ 2(\mathbf{x}_0 - \mathbf{x}_1) \times [a, b, c]^T \end{bmatrix}, \quad (4.31)$$

where  $[a, b, c]^T = (\mathbf{x}_2 - \mathbf{x}_1) \times (\mathbf{x}_0 - \mathbf{x}_1)$  and Hessian of  $A_{s2}$  can be calculated using:

$$\frac{\partial^2 A_{s2}}{\partial \mathbf{x}_{z2}^2} = \begin{bmatrix} \frac{\partial^2 A_{s2}}{\partial \mathbf{x}_0^2} & \frac{\partial^2 A_{s2}}{\partial \mathbf{x}_0 \partial \mathbf{x}_1} & \frac{\partial^2 A_{s2}}{\partial \mathbf{x}_0 \partial \mathbf{x}_2} \\ \frac{\partial^2 A_{s2}}{\partial \mathbf{x}_1 \partial \mathbf{x}_0} & \frac{\partial^2 A_{s2}}{\partial \mathbf{x}_1^2} & \frac{\partial^2 A_{s2}}{\partial \mathbf{x}_1 \partial \mathbf{x}_2} \\ \frac{\partial^2 A_{s2}}{\partial \mathbf{x}_2 \partial \mathbf{x}_0} & \frac{\partial^2 A_{s2}}{\partial \mathbf{x}_2 \partial \mathbf{x}_1} & \frac{\partial^2 A_{s2}}{\partial \mathbf{x}_2^2} \end{bmatrix}. \quad (4.32)$$

The three diagonal terms are calculated using:

$$\frac{\partial^2 A_{s2}}{\partial \mathbf{x}_0^2} = 2\{[(\mathbf{x}_1 - \mathbf{x}_2)^T (\mathbf{x}_1 - \mathbf{x}_2)] \mathbf{I}_{3 \times 3} + (\mathbf{x}_1 - \mathbf{x}_2)(\mathbf{x}_2 - \mathbf{x}_1)^T\}, \quad (4.33)$$

$$\frac{\partial^2 A_{s2}}{\partial \mathbf{x}_1^2} = 2\{[(\mathbf{x}_2 - \mathbf{x}_0)^T (\mathbf{x}_2 - \mathbf{x}_0)] \mathbf{I}_{3 \times 3} + (\mathbf{x}_2 - \mathbf{x}_0)(\mathbf{x}_0 - \mathbf{x}_2)^T\}, \quad (4.34)$$

$$\frac{\partial^2 A_{s2}}{\partial \mathbf{x}_2^2} = 2\{[(\mathbf{x}_0 - \mathbf{x}_1)^T(\mathbf{x}_0 - \mathbf{x}_1)]\mathbf{I}_{3 \times 3} + (\mathbf{x}_0 - \mathbf{x}_1)(\mathbf{x}_1 - \mathbf{x}_0)^T\}. \quad (4.35)$$

Similarly, because of the symmetry, only three off-diagonal terms need to be calculated and the remaining three can be obtained by transposing the matrix:

$$\begin{aligned} \frac{\partial^2 A_{s2}}{\partial \mathbf{x}_1 \partial \mathbf{x}_2} &= \left(\frac{\partial^2 A_{s2}}{\partial \mathbf{x}_2 \partial \mathbf{x}_1}\right)^T = 2[(\mathbf{x}_0 - \mathbf{x}_1)^T(\mathbf{x}_2 - \mathbf{x}_0)]\mathbf{I}_{3 \times 3} \\ &\quad - 2(\mathbf{x}_0 - \mathbf{x}_1)(\mathbf{x}_2 - \mathbf{x}_0)^T - 2\text{skew}([a, b, c]^T), \end{aligned} \quad (4.36)$$

$$\begin{aligned} \frac{\partial^2 A_{s2}}{\partial \mathbf{x}_2 \partial \mathbf{x}_0} &= \left(\frac{\partial^2 A_{s2}}{\partial \mathbf{x}_0 \partial \mathbf{x}_2}\right)^T = 2[(\mathbf{x}_1 - \mathbf{x}_2)^T(\mathbf{x}_0 - \mathbf{x}_1)]\mathbf{I}_{3 \times 3} \\ &\quad - 2(\mathbf{x}_1 - \mathbf{x}_2)(\mathbf{x}_0 - \mathbf{x}_1)^T - 2\text{skew}([a, b, c]^T), \end{aligned} \quad (4.37)$$

$$\begin{aligned} \frac{\partial^2 A_{s2}}{\partial \mathbf{x}_0 \partial \mathbf{x}_1} &= \left(\frac{\partial^2 A_{s2}}{\partial \mathbf{x}_1 \partial \mathbf{x}_0}\right)^T = 2[(\mathbf{x}_2 - \mathbf{x}_0)^T(\mathbf{x}_1 - \mathbf{x}_2)]\mathbf{I}_{3 \times 3} \\ &\quad - 2(\mathbf{x}_2 - \mathbf{x}_0)(\mathbf{x}_1 - \mathbf{x}_2)^T - 2\text{skew}([a, b, c]^T). \end{aligned} \quad (4.38)$$

$L_s$  is defined as the square of Length between two nodes  $\mathbf{x}_1$  and  $\mathbf{x}_2$  as:

$$L_s = (\mathbf{x}_1 - \mathbf{x}_2) \cdot (\mathbf{x}_1 - \mathbf{x}_2). \quad (4.39)$$

In zone 2, the nodal coordinate vector is a  $9 \times 1$  vector so the gradient is also a  $9 \times 1$  vector and the Hessian is  $9 \times 9$  matrix. The gradient and Hessian of  $L_s$  can be calculated using:

$$\frac{\partial L_s}{\partial \mathbf{x}_z} = \left[ \left(\frac{\partial L_s}{\partial \mathbf{x}_0}\right)^T, \left(\frac{\partial L_s}{\partial \mathbf{x}_1}\right)^T, \left(\frac{\partial L_s}{\partial \mathbf{x}_2}\right)^T \right]^T = \begin{bmatrix} \mathbf{0}_{3 \times 1} \\ 2(\mathbf{x}_1 - \mathbf{x}_2) \\ 2(\mathbf{x}_2 - \mathbf{x}_1) \end{bmatrix}, \quad (4.40)$$

$$\frac{\partial^2 L_s}{\partial \mathbf{x}_z^2} = \begin{bmatrix} \mathbf{0}_{3 \times 3} & \mathbf{0}_{3 \times 3} & \mathbf{0}_{3 \times 3} \\ \mathbf{0}_{3 \times 3} & 2\mathbf{I}_{3 \times 3} & -2\mathbf{I}_{3 \times 3} \\ \mathbf{0}_{3 \times 3} & -2\mathbf{I}_{3 \times 3} & 2\mathbf{I}_{3 \times 3} \end{bmatrix}. \quad (4.41)$$

### 4.3 Numerical verification

In this section, the three requirements previously proposed for the formulation will be verified numerically. These three requirements are: (1) continuity; (2) penetration prevention; and (3)

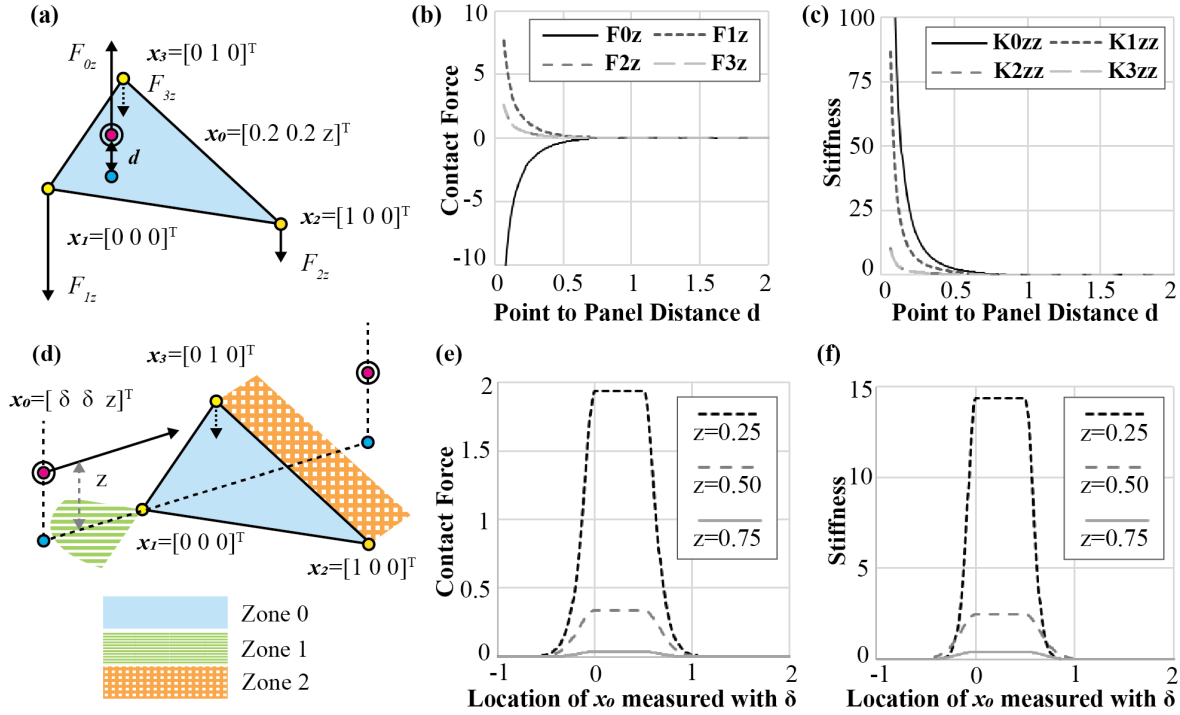


Figure 4.4: (a-c) Numerical verification of penetration prevention and contact initiation (requirements 2 and 3); (d-f) Numerical verification for continuity of internal forces (requirement 1).

contact initiation/disengagement.

To test the requirements (2) and (3), a triangular panel is set still in space by defining three nodal coordinates as:  $\mathbf{x}_1 = [0, 0, 0]^T$ ,  $\mathbf{x}_2 = [1, 0, 0]^T$ , and  $\mathbf{x}_3 = [0, 1, 0]^T$ . The initiation threshold is set as  $d_0 = 1$ . The coordinates of the point are set to be  $\mathbf{x}_0 = [0.2, 0.2, z]^T$ , where  $z$  is the height of the point. The value of  $z$  is changed from two gradually to zero, representing the situation when the point gradually approaches the panel. As the point to panel distance goes to zero, both the reacting internal forces and the stiffness are approaching infinity (see Fig. 4.4 (b) and (c)). Figure 4.4 (b) and (c) also demonstrate that the proposed model will not generate any additional internal forces or stiffness unless the point approaches the panel closer than the contact initiation threshold ( $d < d_0$ ). This simulation shows that the formulation satisfies requirements (2) and (3).

Because the point to panel distance is defined for three zones separately, it is necessary to test the requirement (1) to ensure that the internal forces are indeed continuous when the point crosses between different zones. This test is performed by moving the point across the panel and recording the internal forces and stiffness (see Fig. 4.4 (d)). A variable  $\delta$  is used to control the location of the point, and the test is performed for three different values of height  $z$ . Figure 4.4 (e) and (f) show the internal forces and stiffness with respect to the location of the point when it moves across the panel. The recorded internal forces are indeed continuous when the point moves across the

Table 4.2: Pseudo-code for Implementation of Panel Contact

---

Insert this loop when calculating internal forces and stiffness of bar and hinge model

---

```

1:  for each Triangle(j) in Panel(i)
2:      for each Node(p) in Panel(q)
3:          if q!=i
4:              Check which zones Node(p) falls in
5:              Compute distance  $d$  between Node(p) and Triangle(j) with Eqn. 4.7 to 4.9
6:              if distance  $d \leq d_0$ 
7:                  Calculate derivatives of  $V$ ,  $A_{s0}$ ,  $A_{s2}$  and  $L_s$  (section 4.2.4)
8:                  Assemble  $\frac{\partial d}{\partial x}$  and  $\frac{\partial^2 d}{\partial x^2}$  with Eqn. 4.10 to 4.15 with previous results
9:                  Assemble internal force vector Eqn. 4.5
10:                 Assemble stiffness matrix with Eqn. 4.6
11:             end if
12:         end if
13:     end for
14: end for

```

---

three zones, thereby numerically demonstrating a satisfactory performance for requirement (1) on continuity. Although z-direction stiffness is continuous for this particular test, it is not continuous for general situations. To ensure the compliance with the principle of stationary potential energy, the stiffness does not need to be continuous but only needs to be integrable.

## 4.4 Implementation and Behaviors of the Contact Model

### 4.4.1 Implementation scheme

Table 4.2 summarizes the procedure to include the proposed panel contact formulation into any bar and hinge model. The loops in the pseudo code are set to cycle through different combinations of the points and the triangles. Once a combination is selected, we will check the relative position between the point and the triangle to determine the correct zone, and calculate the point to triangle distance with Eqn. 4.7 to 4.9. If this distance is small enough to initiate the contact process, the additional internal forces vector and stiffness matrix will be computed based on Eqn. 4.5, Eqn. 4.6. With the calculation of internal force vector and stiffness matrix established, the equilibrium path of the folding structure can be traced with various increment-iterative methods (such as the Modified Generalized Displacement Controlled Method). Readers may refer to [Liu and Paulino, 2017a] for the use of the Modified Generalized Displacement Controlled Method in analyzing nonlinear origami, and to [Leon et al., 2011, Leon et al., 2014] for details about nonlinear solution schemes.

The implementation scheme in Table 4.2 includes a double-loop through all the panels, which

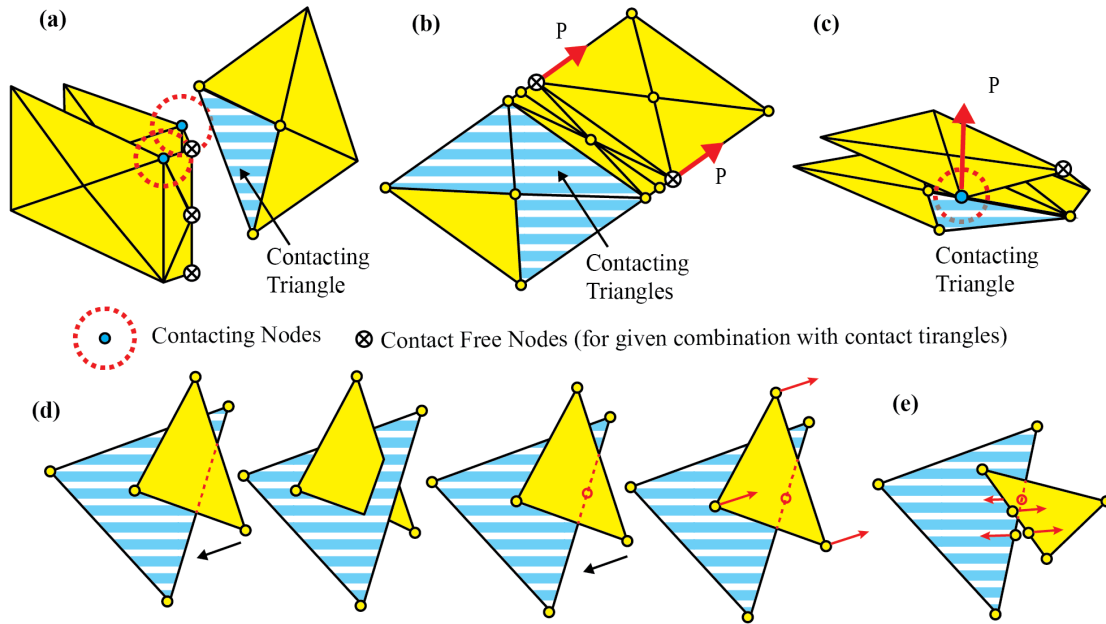


Figure 4.5: Intentional and unintentional omissions of contact.

makes it quadratically more expensive than the computation of assembling the stiffness matrix. This additional computational cost is expected when solving the foldability problem of a unknown new origami patterns, because it is necessary to check all possible panel contact combinations. If we need to exhaust all combinations for new patterns, it is not wise to use a finely meshed FE model to simulate folding because the computation cost would be enormous. The proposed bar and hinge implementation provides a lower cost alternative to FE models, because the folding sequence and contact can be captured using a sparse distribution of nodes. If more accurate estimation of the structure and associated contact mechanics are required, FE models would be used next. Additionally, because the nature of the origami contact would be already known (from the sparse global simulation), the FE models could be built to only detect and capture contact where it is expected to occur. This two model approach for simulating folding and contact in origami would be drastically more efficient than using FE models for the entire process.

When implementing the proposed model, it is possible to omit checking for contact between some combinations of the points and the triangles. Such omissions can save a considerable amount of computational time without introducing large errors into the simulation. When contact is implemented in the bar and hinge model with compliant creases [Zhu and Filipov, 2019b], it is possible to make two types of such omissions. First, nodes in the center line of the creases (three crossed nodes in Fig. 4.5 (a)) can be neglected for panel contact. This simplification will not introduce large errors into the simulation because the creases are usually narrow compared with the panels.

Therefore, when a triangle is approaching the nodes at the center of a crease, the nodes on the adjacent panels (two blue nodes in Fig. 4.5 (a)) are enough to stop the movement of the triangle. Second, it is not necessary to check for contact between nodes sharing the same crease from adjacent panels (see Fig. 4.5 (b)). This rule is introduced so that the tensile repulsive force within a crease is avoided if the initiation threshold  $d_0$  is larger than the width of the crease  $W$ . This simplification generally works well because the only possibility that these combinations will contact is to fold the crease to 180 degrees, which is already captured by other nodes as shown in Fig. 4.5 (c). If these two type of omitted contact are deemed as necessary for a particular origami pattern, it is not hard to check them because the compliant creases are triangulated and thus the same contact model applies.

Figure 4.5 (d) shows one limitation of the proposed implementation scheme. Because of the sparsity of nodes in a bar and hinge representation of an origami structure, sometimes direct panel to panel contact cannot be captured. Fortunately, most of the origami patterns do not encounter this problem, but if it were to happen, it could be solved by sub-discretizing the triangular panel and adding additional nodes to the edges of the origami as illustrated in Fig. 4.5 (d). Similarly, the edge to edge contact cannot be captured by the proposed model without adding more nodes to the edges (see Fig. 4.5 (e)).

#### 4.4.2 Behavior of global panel contact simulation

In this section, we study how the proposed panel contact formulation behaves when implemented within a bar and hinge model with compliant creases. A simulation example with a single compliant crease is used to demonstrate the behavior of the proposed model. The single fold origami is simply supported as shown in Fig. 4.6 (a), and the loading set-up is illustrated in Fig. 4.6 (b). Three model parameters can be used to adjust the behavior of the panel contact simulation for origami structures. These parameters include: (i) the potential scaling factor  $k_e$ , (ii) the contact initiation threshold  $d_{0e}$  for nodes at the edge of the panel, and (iii) the contact initiation threshold  $d_{0c}$  for nodes at the center of the panel.

The influence of the potential scaling factor  $k_e$  is first studied. In this test, the length of the upper panel is set to be  $x = 1.6$  cm while the length of the lower panel is set to be  $L = 2$  cm. The width of the crease is set as  $W = 4$  mm, which represents realistic origami structures with compliant creases. The panel contact initiation threshold is set as  $d_0 = d_{0e} = d_{0c} = 2$  mm and different values of  $k_e$  are used to form a group of simulations. The upper panel is first self-folded to  $\theta_0 = 0.1\pi$  before the nonlinear loading starts. The height of the node on the outer edge of the upper panel is denoted as  $z$  and is used to measure the deformation. Figure 4.6 (c) shows that the potential scaling factor  $k_e$  can be used to control the smoothness of transition when panel contact is initiated. When

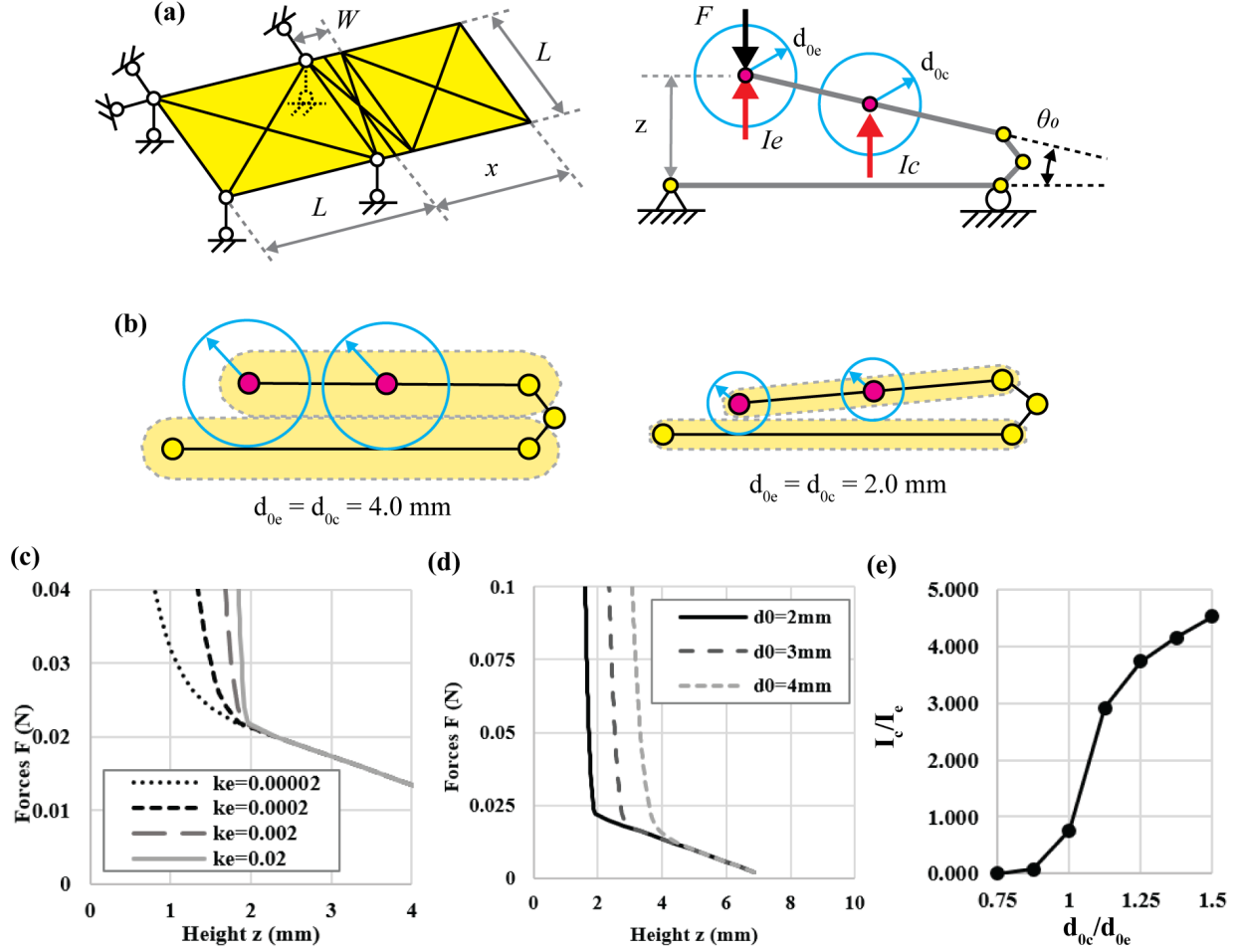


Figure 4.6: Influence of potential scaling factor and using the model to simulate thick panels in origami.

a larger  $k_e$  is used, a larger contact force vector and a stiffness matrix is obtained which results in a sharper transition after the triggering of panel contact. By controlling the value of  $k_e$ , it is possible to tune the behavior of the model such that it simulates the existence of thickness in origami. When  $k_e = 0.02$  or higher for this case, a sharp transition occurs such that the height of the node on the outer edge practically stops at  $z = 2 \text{ mm}$ , which mimics the loaded configuration of having a 2 mm thick panel (1 mm on each side). If only general contact is of interest a lower  $k_e$  can be used for a smoother transition, which would be beneficial for faster model convergence.

Both the absolute magnitude of  $d_{0e}$  and  $d_{0c}$  and the relative ratio between them can affect the deformed configuration and contact forces of the structure. In order to simulate thickness in origami, the potential scaling factor is set as  $k_e = 0.05$  so that a sharp initiation of panel contact is obtained. By setting  $d_0 = d_{0e} = d_{0c}$ , we can study the influence of the absolute values of  $d_{0c}$  and  $d_{0e}$  on the behavior of the model. Figure 4.6 (b) show how the deformed configuration changes



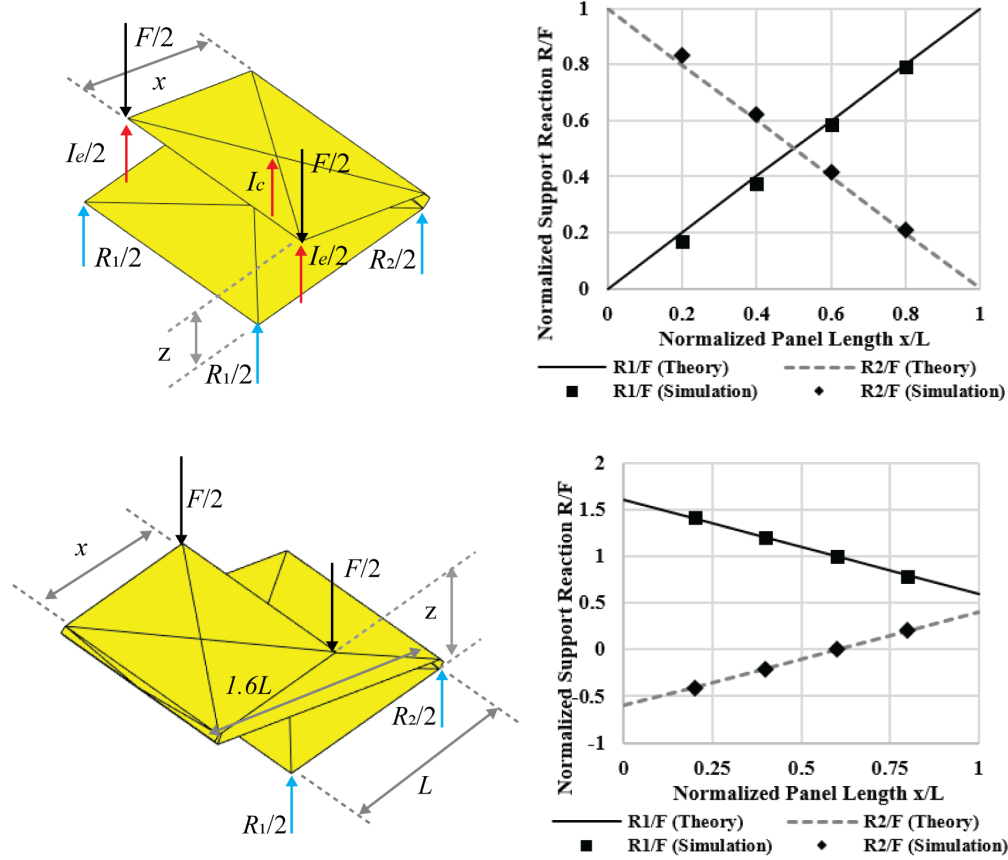


Figure 4.7: The panel contact model can capture the internal forces and reaction forces accurately.

when different values of  $d_0$  are used, and Fig. 4.6 (d) shows the corresponding force displacement curves. A larger value of  $d_0$  leads to earlier initiation of contact and thus larger contact forces. When the same load is applied, the model with larger  $d_0$  has larger separation between panels, and the separation (measured with  $z$ ) is exactly around the value of  $d_0$ , which represents the behavior including panel thickness in simulating origami.

Figure 4.6 (e) shows that by varying the ratio between  $d_{0c}$  to  $d_{0e}$ , different contact force distributions can be obtained. The symbol  $I_c$  and  $I_e$  refer to the contact forces of nodes at the center and nodes at the edge of panels respectively (see Fig. 4.6 (a)). If the panels are relatively thin compared to the width of the crease  $W$ , the edge of the panels will contact first and thus the internal contact forces should be centered at the edges. This behavior can be simulated by setting  $d_{0c}/d_{0e}$  to be a relatively small value ( $< 0.7$ ) as shown in Fig. 4.6 (e). On the other hand, if the panels are relatively thick compared to the widths of the creases or if there are extruded parts in the center of the panels (e.g. motors, sensors, or batteries in some mechanical origami devices), a larger  $d_{0c}/d_{0e}$  value can be used such that the contact forces are concentrated at the center node of the panel.

Next, we check if the proposed model can capture the reaction forces correctly for both the

single fold origami and another double fold origami (Fig. 4.7). This test is performed by varying the length of the upper panel  $x$  and comparing the simulated support reactions with the theoretical solutions. In these particular tests, the panel length is set as  $L = 2$  cm and the width of the crease is set as  $W = 1.5$  mm. The potential scaling factor is set as  $k_e = 0.0002$  and the two initiation thresholds are set as  $d_{0e} = 1.5$  mm and  $d_{0c} = 1.05$  mm such that contact forces concentrate on the node at the outer edge. Figure 4.7 shows how the support reactions change as  $x/L$  varies. It is found that the proposed panel contact model can simulate the support reactions correctly, which further confirms the model's compliance with the principal of stationary potential energy.

In general, we recommend selecting the  $d_0$  to be relatively close to the real panel thickness such that the simulation has a similar geometry as the real structure. When the real thickness of the panel is small, however, we recommend select the  $d_0$  to be larger than the real thickness to avoid numerical instability. Values around 2% to 5% of the panel length can be a good initial guess. The selected  $k_e$  value should scale the contact potential such that it is comparable to strain energy (potential energy) stored within the structure under elastic deformation. If the contact potential is much larger than the strain energy in the structure or vice versa, adding the two energy terms can results in numerical instability. Unfortunately, selecting the proper  $k_e$  is largely based on trial-and-error method (e.g. similar to picking a load step in a Newton-Raphson method).

One limitation of the current simulation code is that the contact forces can grow to infinite without considering the material failure within the structure. The material model used in this bar and hinge model assumes elasticity and cannot capture yielding, softening, or brittle failures in the material. This indicates that the stiffness and forces jump is credible but only to a point when the material stress and strain are not large enough to trigger failure. When material failure does happen, the stiffness and forces should drop and should not go to infinity. More realistic responses can be obtained if we adjust the bar model and the rotational spring model such that they can mimic material failure, but these topics are beyond the scope of this work and are seen as potential future research directions.

## 4.5 Numerical Examples

In this section, four simulations are performed to demonstrate the efficiency and capability of the the proposed model. These simulations are designed to test the proposed model with more complicated patterns beyond those in the previous sections. Both self-folding simulation and loading simulation are tested within the four examples.

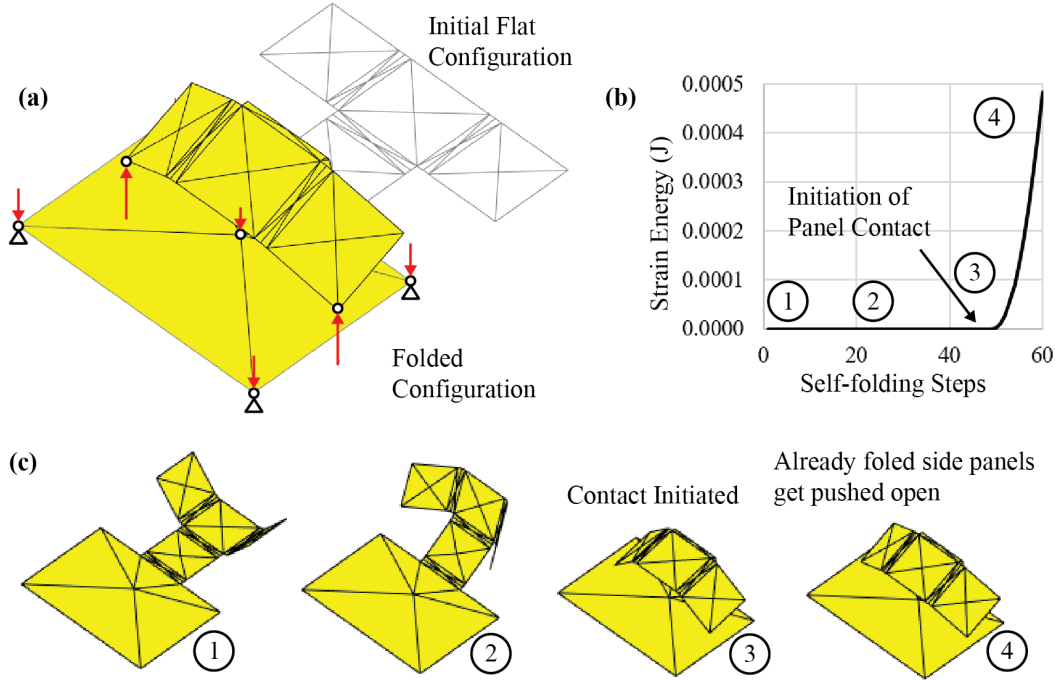


Figure 4.8: Self-folding of an origami box pattern with inter-panel contact.

### 4.5.1 Self-folding of a box

This example studies the self-folding of a box pattern (see Fig. 4.8 (a)). The four actively moving panels are  $2 \times 2 \text{ cm}^2$  and are connected with 3 mm wide creases. The potential scaling factor is set to be  $k_e = 0.002$  and the contact initiation distances are  $d_{0c} = d_{0e} = d_0 = 2 \text{ mm}$ . The self-folding is achieved by changing the stress free angle of the folds incrementally and tracing the equilibrium with a Newton-Raphson algorithm. In this example, folding is performed with two steps: (i) the two side panels are folded to  $0.3\pi$  (Fig. 4.8 (c) circle 1); (ii) the two center panels are next folded to  $0.8\pi$  such that the two side panels will contact with the anchored panel (Fig. 4.8 (c) circles 2 to 4). The corresponding strain energy is recorded and plotted in Fig. 4.8 (b). The strain energy is calculated based on the assumed linear elasticity in both the bar elements and the rotational spring elements, and the contact potential is excluded from the energy calculation such that the energy term only contains the elastic strain energy. With the assumed linear elasticity, the strain energy in bars is calculated as  $0.5 \frac{EA}{L_0} (\delta L)^2$  and the strain energy in rotational springs is calculated as  $0.5 K_{spr} (\delta \theta)^2$ , where  $\frac{EA}{L_0}$  gives the stiffness of the bar,  $\delta L$  gives the change in bar length from the stress free length,  $K_{spr}$  gives the spring stiffness, and  $\delta \theta$  gives the change in rotation angle from the stress free angle.

When no panel contact is initiated, the Newton-Raphson algorithm can always find an equilibrium configuration that is stress free, and thus, no strain energy is observed. However, when the

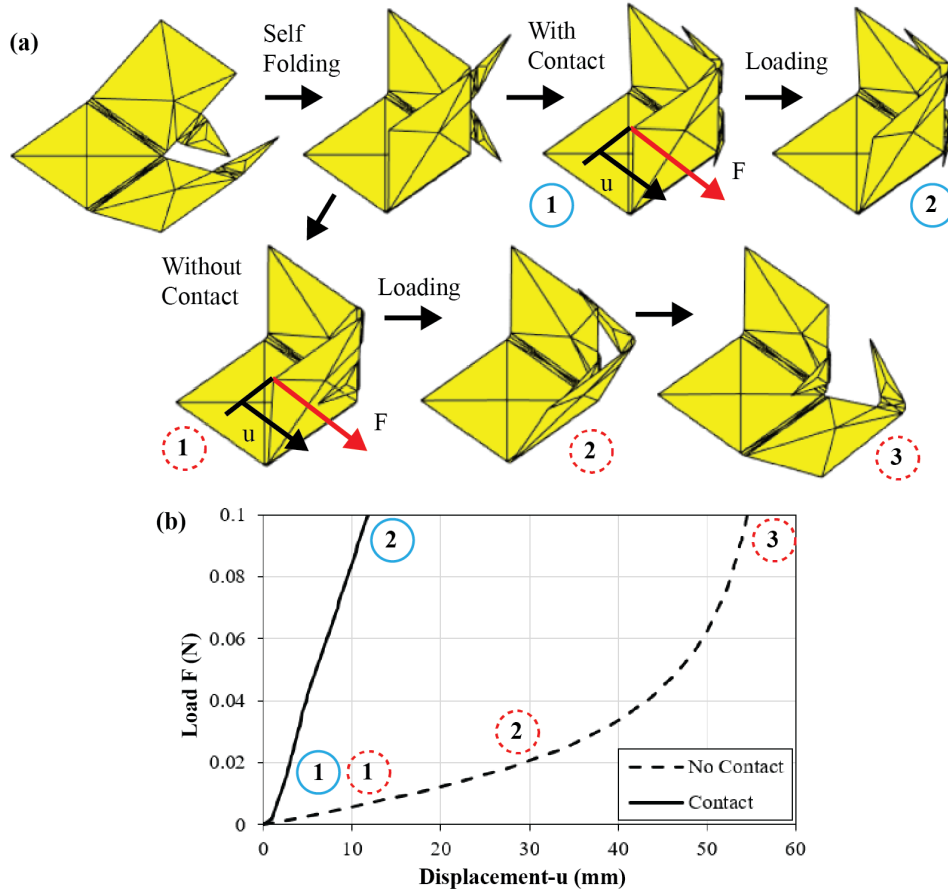


Figure 4.9: Self-folding and loading of the locking box corner.

panels come into contact with each other, the stress free configuration is no longer an equilibrium configuration. Strain energy is stored in the structure because panel contact interferes with the self-folding process. A wall-clock time of 20 sec was recorded on a desktop computer with an i7-7700 processor for this simulation, which demonstrates the efficiency of the proposed method.

#### 4.5.2 Loading of an inter-locking box corner

In this example, the folding and loading of an inter-locking box corner is studied. Both simulations with and without the panel contact are performed and the results are compared. Each panel of the box is a  $6 \times 6 \text{ cm}^2$  square. The width of the two creases that connect two large panels are 4 mm while the width of the two creases that connect the two teeth are 8 mm. The two teeth are about 2 cm wide at base and 3 cm tall. The potential scaling factor is selected as  $k_e = 0.02$  and the contact initiation thresholds are set as 4 mm for edge nodes and 2 mm for center nodes. The box is first folded to an interlocked configuration (see Fig. 4.9 (a)) by changing the stress free angle

of the creases incrementally and tracing the equilibrium with a Newton-Raphson algorithm. After reaching the interlocked configuration, a point load is added and the displacement is measured as indicated in Fig. 4.9 (a) bottom left. The recorded force displacement curves are shown on Fig. 4.9 (b) for the two cases and the deformed configurations are plotted on Fig. 4.9 (a).

The proposed method is capable of capturing the deformed configuration under the influence of panel contact. The force displacement curves plotted on Fig. 4.9 (b) show that the proposed model is capable of capturing the additional stiffness induced by the interlocking effects which in turn produces a higher force for the same displacement. Moreover, Fig. 4.9 (a) also demonstrate that the proposed model can capture panel deformation after contact in a global sense, although this simulation cannot capture localized panel deformation such as dimples near the contact point. Including the panel contact to stop panels penetrating each other is essential for capturing a realistic mechanical behavior of this box corner. The wall-clock time for running the entire analysis (including a sequential folding analysis and a loading analysis) was recorded to be 21 *sec* on the same computer with an i7-7700 processor.

### 4.5.3 Folding sequence of a box corner

The following example demonstrates how the proposed method can be used to study the folding sequence of a foldable origami pattern. The pattern studied here has four creases numbered with A, B, C, and D as shown in Fig. 4.10 (a). When the folding sequence is assigned correctly, the pattern can be folded to an interlocked configuration as shown Fig. 4.10 (b). Even with this simple pattern, there exists a large number of design parameters that can be varied and explored for an optimal design, including pattern geometry, folding speed, and folding sequence. We will only focus on the folding sequence and fix the pattern geometry and the folding speed for this example. The geometry of the pattern is shown in Fig. 4.10 (a), where all creases have the same width  $W = 4$  mm. Creases A, B, and C are all folded by 90 degrees while crease D is folded by 180 degrees in the folded configuration. To further simplify the simulation, the folding of all four creases is achieved with a fixed number of increments. Therefore, the folding speed of crease D is twice the folding speed of creases A, B, and C. We have also found several folding sequences where we cannot determine if the structure folds correctly or not as shown in Fig. 4.10 (d). In these folding sequences, there is a folding motion that involves pushing the triangle panel towards the vertical side panel. Because the two panels share the same plane, the triangle panel is pushed to either the correct position or the incorrect position depending on numerical errors, and different simulation setups such as total folding steps will yield different results. We mark these cases as “Maybe” to differentiate them.

The total number of combinations of folding sequence available for a  $n$ -crease pattern follows

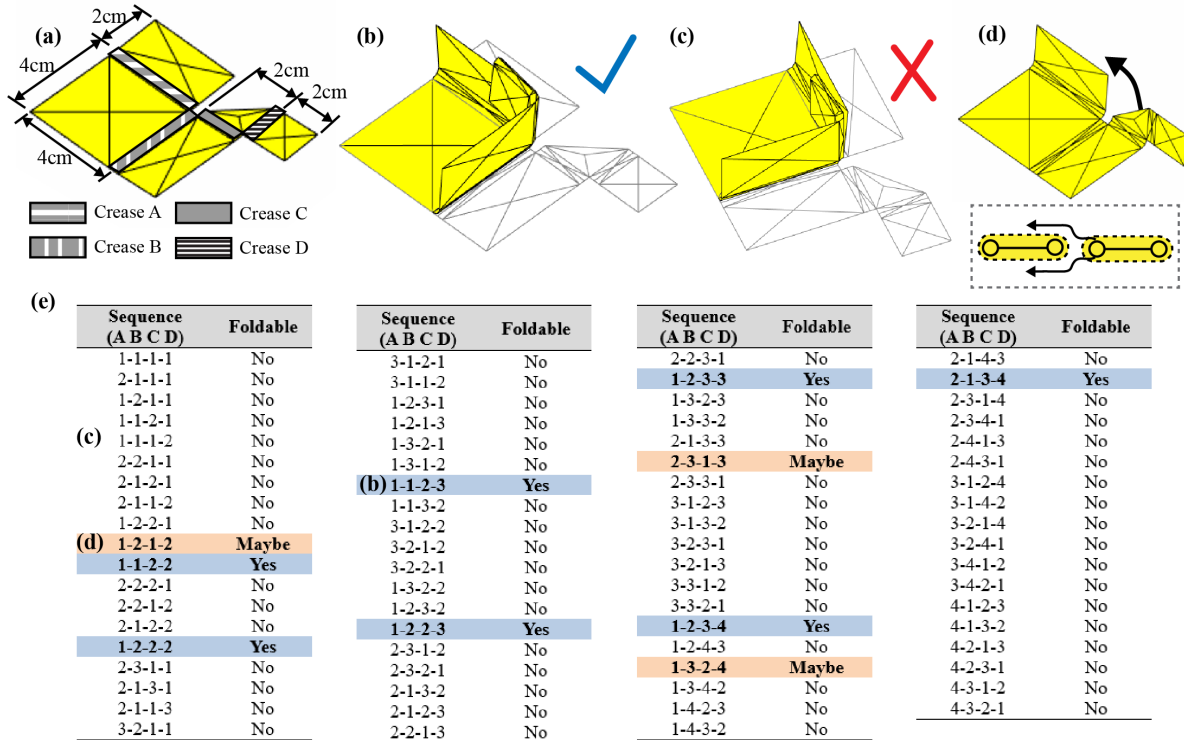


Figure 4.10: Studying the correct folding sequence to build an origami box corner using inter-panel contact.

the ordered bell number sequence or Fubini number sequence (A000670 sequence in online encyclopedia of integer sequences). This number sequence counts the number of weak orderings on a set of  $n$  elements ( $n$  folds in our case) [OEIS, 2019]. This integer number sequence scales faster than  $n!$  [OEIS, 2019] and thus for a general  $n$ -crease pattern, exhausting all possible folding sequence combinations requires a large amount of computational effort. At  $n = 4$ , the pattern gives a total number of 75 possible folding sequence combinations. The results for checking these 75 combinations are summarized in Fig. 4.10 (e). The required wall-clock time to run one single analysis is recorded to be 15sec on the same computer with an i7-7700 processor. To cycle through all 75 different combinations, it requires a total time of about 1200 sec, which by today's standards is small. Moreover, this analysis was performed on only one thread of the processor, yet each folding sequence test could be run in parallel, and the overall processing time would be divided by the number of tests run in parallel. However, if we use FE simulations to cycle through all combinations where each run of analysis can take tens of minutes or even hours, the required computation time can become unaffordable to fit into a desired design schedule. Also, the number of combinations can grow at an alarmingly fast rate if we start adding more design parameters such as folding speed and pattern geometry. If the analysis required us to further explore these

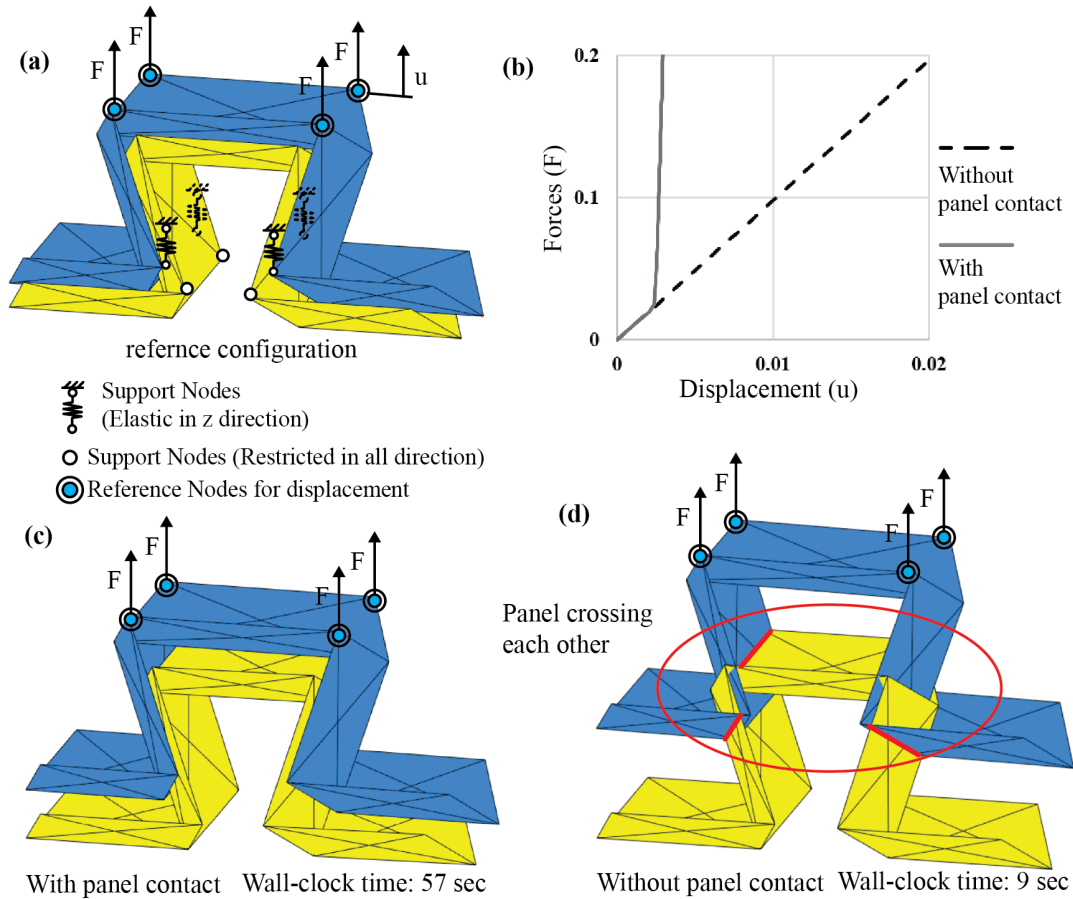


Figure 4.11: Studying the stiffness jumps in origami assemblages under the influence of global panel contact.

additional parameters, the efficiency in the proposed model can be of great benefit.

#### 4.5.4 Loading of an inter-locking origami

The following example analyzes one inter-locking origami of those studied in [Kamrava et al., 2017]. The basic pattern of the design is based on the Miura-pattern and thus is rigid foldable. When two such patterns are placed on top of each other and folded, they create an inter-locking system with which a considerable amount of force can be resisted without any gluing or adhesion. In the following example, we recreate the inter-locking origami with the proposed panel contact model. In order to demonstrate the versatility of the proposed model, the conventional bar and hinge model without compliant creases is used for the simulation. It is reasonable not to use the compliant hinge version of the bar and hinge model as the additional degrees of freedom in the crease region are not a significant factor in this particular example.

Figure 4.11 (a) shows the loading set up of the simulation. The origami on the bottom is fixed in space by the four supports (Fig. 4.11 (a) white support nodes), while the origami on the top has four fictitious elastic supports the in z-direction (Fig. 4.11 (a) spring support nodes) that are needed to avoid numerical instability associated with a free floating body. The loads are applied on the top four nodes on the top origami (Fig. 4.11 (a) blue nodes) and the displacement is measured using the z-direction height of one of the reference nodes.

Figure 4.11 (b) gives the force displacement curves and Fig. 4.11 (c) and (d) show the loaded configuration for both simulations with panel contact and without panel contact. When panel contact is not activated, the two origami patterns will cross each other and the only resisting force is the fictitious elastic support reaction. However, when the panel contact is activated, a jump in the stiffness is observed, which mimics the interlocking behavior of this particular origami design.

Although the contact is successfully captured by the model, we need to point out that the simulation code still assumes linear elasticity for the material model and thus captures no material failure. In real loading situations, material failure eventually happens and stops the loading forces from reaching infinity. Therefore, the predicted mechanical behavior may not be trusted if the contact force is too large to fail the structural material used in the system. However, we believe future enhancement of the material model embedded in the bar models and rotational spring models can solve the problem.

Although the interlocking behavior considered here is complicated, a wall-clock time of 57 seconds was recorded on a modern computer (2018) with i7-7700 processor. Not surprisingly, for this particular example, 80% of computation time is used to calculate the point to triangle distance and to check if the contact has happened. Because contact detection requires a double loop through all triangle elements, contact detection is quadratically more expensive computationally than nonlinear simulation (assembling stiffness matrix) of an origami pattern. This suggests that the previously mentioned two model approach can be a desirable method to simulate origami interlocking problems such as the one studied here. Knowing the contact pattern in advance would allow us to eliminate a large portion of unnecessary contact detection checking and thus bring down the computation cost of a detailed FE simulation.

## 4.6 Concluding Remarks

In this chapter, an efficient panel contact simulation technique is proposed to study the occurrence of contact, and contact induced behaviors in origami tessellations. The proposed model does not require a dense FE meshing so that it is computationally cheap and efficient to implement numerically. Because frictional forces are generally not significant when studying the foldability of origami systems, we assume that the contact force is conservative and thus has a potential. The



contact potential is constructed such that when a selected node (point) approaches a triangulated panel (triangle), a large contact force vector is triggered. To prevent panel penetration, the proposed contact potential gives an internal force vector and a stiffness matrix that approach infinity as the distance between the point and the triangle approaches zero. The model was tested numerically and the tests confirm that the proposed model complies with three requirements: (1) continuous internal forces; (2) infinite forces and stiffness as point to triangle distance approaches zero to prevent penetration; and (3) piecewise formulation for contact initiation and disengagement.

An implementation scheme for including the panel contact model within a bar and hinge model is also presented. Simple origami patterns are used to test the behavior of the contact simulation when combined with the bar and hinge model. These tests show that the model captures the contact geometry and forces correctly and efficiently. Moreover, by tuning the model parameters, the contact model can simulate thickness in origami panels. More complicated simulations are explored in the example section to demonstrate the validity and efficiency of the model. We showed that the proposed model can be combined with any bar and hinge type framework and thus has broad applicability in studying contact related problems in origami engineering. The model is suitable for detecting when contact occurs during the origami folding sequence, studying the foldability, and capturing the relevant mechanical behaviors in the origami structure after contact. This model can enable the discovery of origami patterns that can be folded either by avoiding contact, or despite self-contact, and can open up a new frontier for origami structures that harness contact to achieve new functionality.

## **Chapter 5. Multi-Physics Electro-Thermal Actuation Model**

In this chapter, a novel multi-physic actuation model for functional origami systems is established to resolve the Challenge 4 discussed in Chapter 1 Introduction. More specifically, this work focuses on the simulation of electro-thermal origami systems (those proposed in Chapter 2). This work provides the much needed simulation model for capturing the heat transfer within active origami systems that can be used to study the behaviors of thermal metamaterials. Although this work is tailored for thermally active systems, the model formulation could be extended to other active systems in the future.

This chapter is organized as the following. First, to echo with the Challenge 4, we give a more detailed discussion on why current origami simulations cannot capture the behaviors of functional active origami system with multi-physical actuation. Next, we introduce the proposed simulation framework in Section 5.2. We describe the three major steps of the framework and introduce the modeling techniques involved. Section 5.3 uses a series of calibration tests to fine tune the model parameters and to check the accuracy of the new heat transfer model against high-fidelity finite element simulations. Following the calibration, Section 5.4 verifies the performance of the proposed simulation framework by comparing it against physical experiments. Finally, three practical examples are presented to demonstrate the broad capability, efficiency, and usefulness of this rapid simulation framework.

### **5.1 Active Origami and Multi-Physical Simulation**

Over the past decades, a number of active origami systems have been built and tested. These origami are actuated with active materials or responsive systems, such as hydrogels [Na et al., 2015, Yoon et al., 2014, Kang et al., 2019], metallic morphs with residual stress [Leong et al., 2009, Leong et al., 2008, Bassik et al., 2009], shape memory polymers [Felton et al., 2014, An et al., 2018], magnetic active systems [Shaar et al., 2015, Iwase and Shimoyama, 2005], etc. Among these different systems, thermally active materials demonstrate great potential in building practical origami devices [Na et al., 2015, Leong et al., 2009, Leong et al., 2008], because thermally active material can achieve high energy efficiency and provide high work density [Yang et al., 2020]. Moreover, by designing proper electric circuits to control the heaters, one can control the folding motion of origami creases separately to achieve complex motions and functions [Zhu et al., 2020,

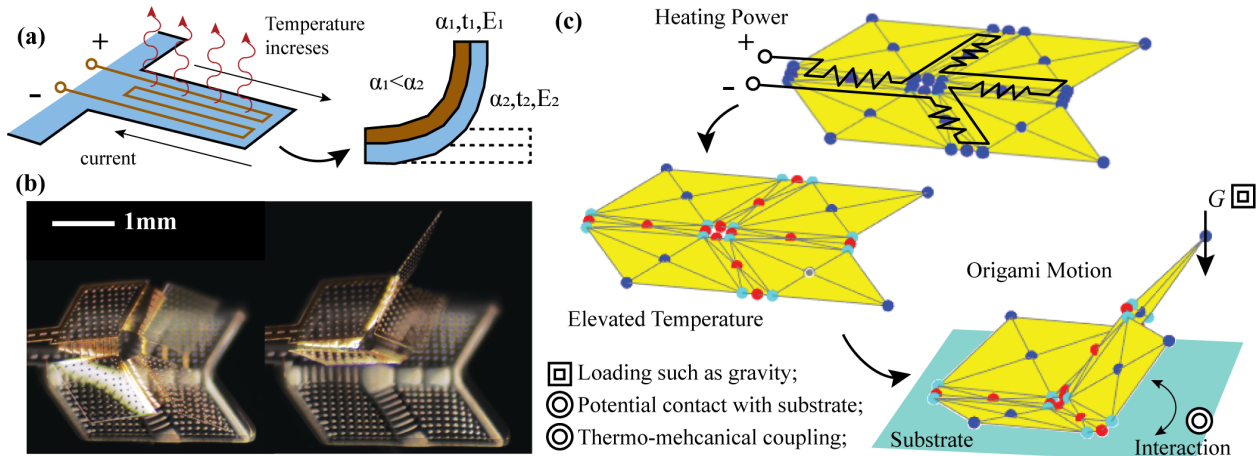


Figure 5.1: Simulating of electro-thermal actuation with a bar and hinge model.

Jager et al., 2000].

Figure 5.1 demonstrates how electro-thermal actuators can enable origami systems to achieve controllable folding at the micro-scale. This is the system proposed in the Chapter 2 of this dissertation. When passing current through the patterned metallic heaters, Joule heating will elevate the temperature of the crease regions. If the creases are made with a bi-material morph that has two different thermal expansion coefficients ( $\alpha$ ), the changing temperature will generate bending motion because one layer will expand more than the other.

However, simulation of electro-thermally actuated functional origami has remained substantially limited. Current simulation methods for origami are mostly kinematics-based [Tachi, 2009c, Tachi, 2010b] or mechanics-based [Liu and Paulino, 2017a, Liu and Paulino, 2016] and have incomplete abilities to capture the multi-physics based actuation. As demonstrated in Fig. 5.1 (c), properly capturing the folding motion is indeed difficult, as it requires simultaneously simulating the coupled electro-thermal heating, the interaction between heat dissipation and large deformation folding, the potential contact between substrate and origami panels, and other loading effects such as gravity. This difficulty in simulation has limited design methods for functional origami to mostly trial and error approaches [Na et al., 2015, Zhu et al., 2020]. Furthermore, without efficient simulation it is difficult to optimize designs or to construct control protocols for these functional origami systems.

Therefore, the primary goal of this Chapter is to build a multi-physics based simulation method to resolve the Challenge 4 proposed in the Introduction. Part of this problem is already addressed in Chapter 3 and Chapter 4 of this dissertation, where the compliant crease bar and hinge model and the inter-panel contact model is proposed. Thus, to fully resolve the problem, this Chapter will develop a heat transfer model within the bar and hinge formulation and design an integrated

simulation framework to merge these different capabilities.

## 5.2 A Simulation Framework for Functional Origami

In this section, we introduce the proposed rapid simulation framework for electro-thermal micro-origami systems, which is based on a simple but effective bar and hinge model. The simulation framework has three major steps: (1) simulate the temperature profile under applied heating power, (2) calculate the stress-free angle of creases based on the elevated temperature, and (3) solve the new equilibrium position of origami system (Fig. 5.2). The first step contains the new heat transfer model developed in this Chapter, whereas the following two steps use existing models developed in the Chapter 3 and Chapter 4 of this dissertation. In the following subsections, we will describe these steps in detail.

### 5.2.1 Step 1: Solving the heat transfer problem

First, we focus on how to capture the elevated temperature of the origami systems under applied heating power (see Fig. 5.3). This heat transfer problem has two major components: the heat transfer within the origami structure, and the heat transfer between the structure and the surrounding environment (Fig. 5.3 (a) to (c)). For the heat transfer problem within the origami structure, we use the existing nodes in the bar and hinge model to store the temperature information and use the planar triangular (T3) thermal elements to generate the conductivity matrix (see Fig. 5.3 (c)). This elements are a convenient choice because the bar and hinge model naturally provides triangulated meshing of the origami surface. Next, to consider the heat transfer between the origami and the surrounding environment, additional nodes are introduced to represent the temperature of the surrounding environment (e.g. air, water) near the surface of these active systems. The heat transfer between the structure and the surrounding environment is simplified as an 1-D thermal conduction problem and use multiple bars to represent the thermal conductivity between the structure and the surrounding environment. Generally speaking, simulating the heat transfer as a conduction problem is a valid assumption for small-scale systems, because convection is not significant. For most devices fabricated with MEMS processes, this is a valid assumption [Hussein et al., 2016, Ozsun et al., 2009]. In the remainder of this subsection, we will introduce how to calculate the model parameters based on the system geometry and the material properties to effectively capture the heat transfer between the origami and the surrounding environment.

A chain of nodes and bars is added to each node of the origami to represents the surrounding environment (Fig. 5.3 (a) to (c)). This chain of nodes and bars captures the heat transfer between the structure and the surrounding environment as an 1-D thermal conduction problem. It is assumed

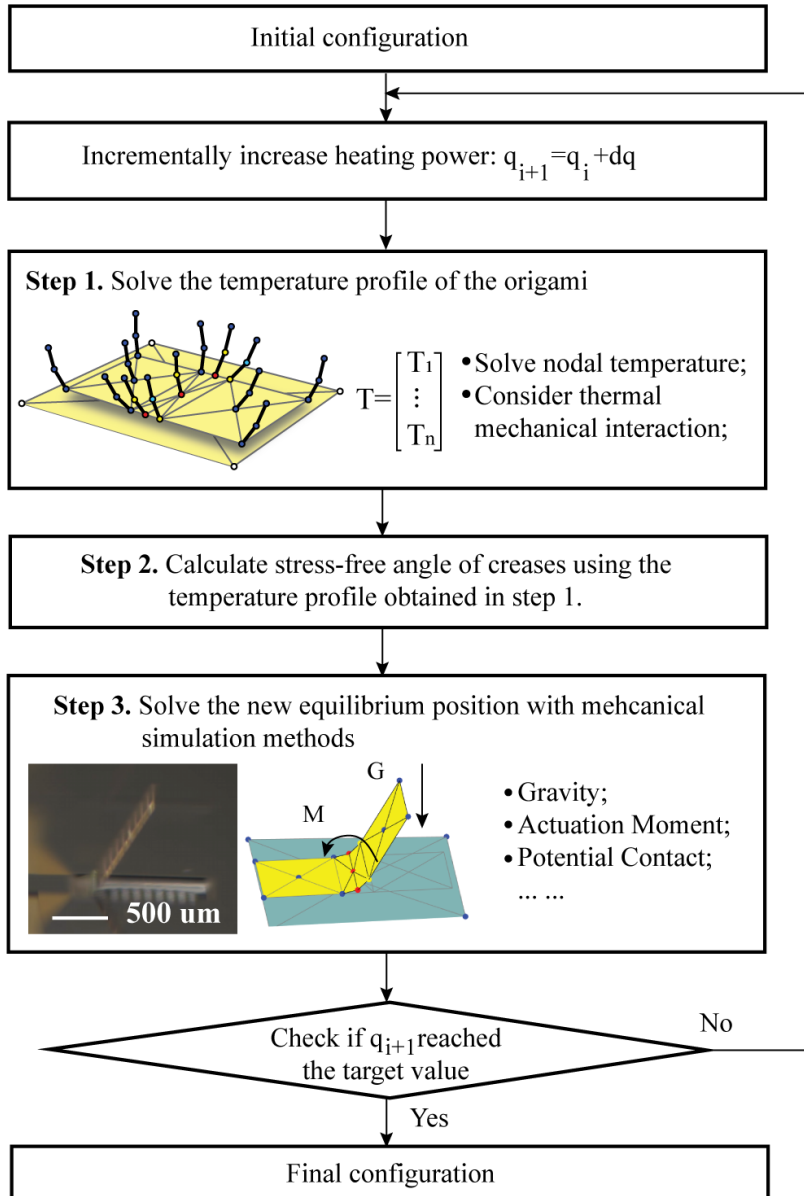


Figure 5.2: Flowchart for the rapid simulation framework for electro-thermally actuated origami systems.

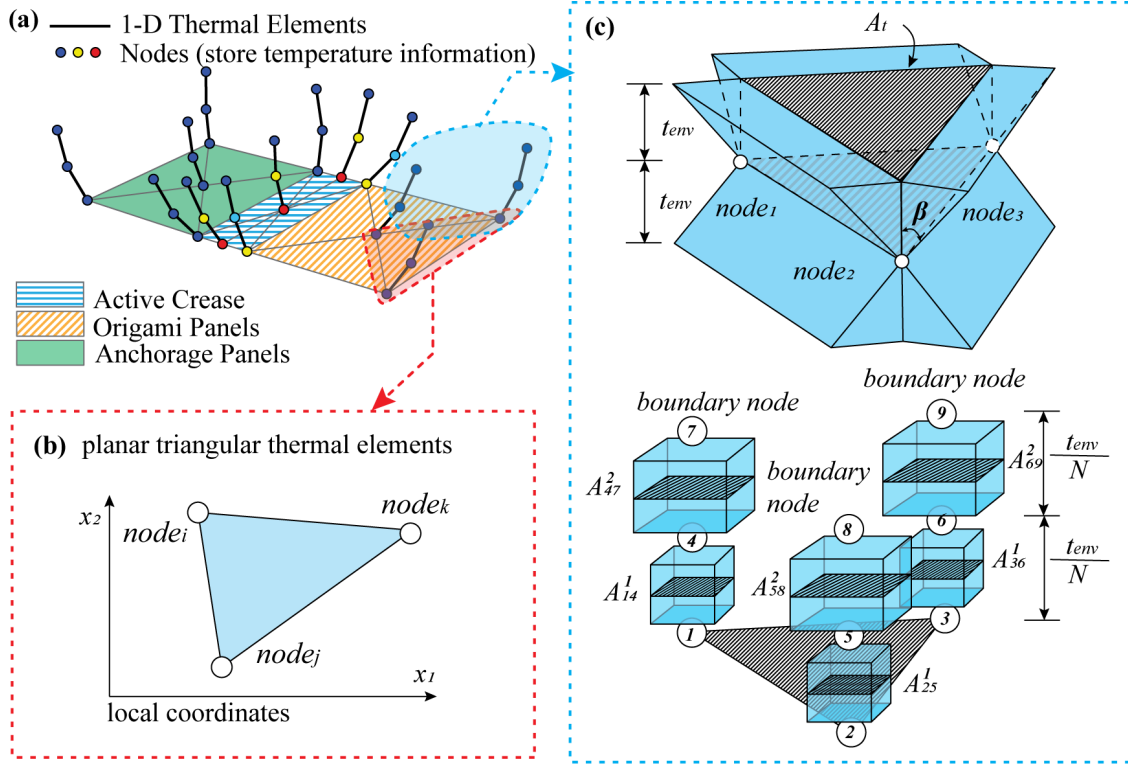


Figure 5.3: Simulating heat transfer using a bar and hinge model.

that the end nodes (farthest away from structure) are at room temperature (RT). The conductivity of bars in this chain representing the environmental substance column can be calculated as:

$$k_{ij} = \frac{k_{mat} A_{ij}}{L_{ij}}, \quad (5.1)$$

where  $k_{mat}$  is the thermal conductivity of the surrounding environment,  $L_{ij}$  is the bar length between node  $i$  and node  $j$ , and  $A_{ij}$  is the cross section area of the bar (see Fig. 5.3 (c)).

Figure 5.3 (b) and (c) introduce how to calculate the bar area  $A_{ij}$  connecting node  $i$  and node  $j$ . The equation for assigning the bar area  $A_{ij}$  is derived by preserving the total thermal conductivity of the bulk material of the surrounding environment. Consider a triangular heating panel as shown in Fig. 5.3 (b) and assume that at thickness  $t_{env}$  away from the panel, the surrounding environment is at room temperature. To model the effect that a larger volume of surrounding substance gets heated as the distance from the heating panel increases, we introduce the dissipation angle  $\beta$ . Then the total volume of surrounding substance at one side of the panel is the sum of four triangular prisms as pictured in Fig. 5.3 (c). We further introduce  $N$ , the total number of bars in the chain, to convert this gradually changing cross section into  $N$  bars with different constant cross sections  $A_{ij}^k$  (where the superscript  $k$  indicates that this area is for layer  $k$ ). To match the total thermal

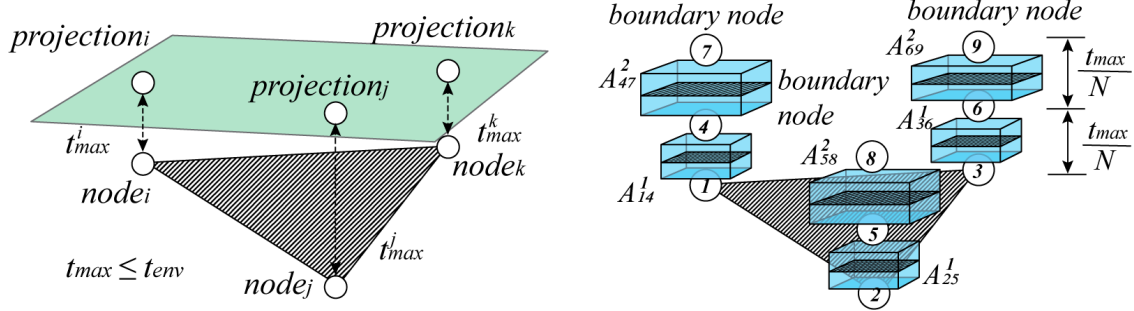


Figure 5.4: Capping  $t_{env}$  to simulate thermal boundaries.

conductivity for layer  $k$ , we need to preserve the total volume and thus we have:

$$\frac{3t_{env}A_{ij}^k}{N} = 2\frac{t_{env}}{N}(A_t + L_{sum}t_{env}\tan\beta(\frac{k-0.5}{N})), \quad (5.2)$$

where  $A_t$  is the area of the triangle heating panel and  $L_{sum}$  is the length of the perimeter of the heating panel. By rearranging the equation, we obtain the expression of the cross section of bars for each layer in the chain as:

$$A_{ij}^k = \frac{2}{3}(A_t + L_{sum}t_{env}\tan\beta(\frac{k-0.5}{N})). \quad (5.3)$$

Tuning the value of  $N$ ,  $\beta$ , and  $t_{env}$  allows us to capture the heat transfer between the origami and the surrounding environment properly. The effects of different combinations of these parameters are studied closely in the following section.

After solving the thermal conductivity of different bars, we can assemble the global thermal conductivity matrix and solve the nodal temperature as  $\mathbf{T} = \mathbf{K}^{-1}\mathbf{q}$ , where  $\mathbf{T}$  is the nodal temperature vector,  $\mathbf{K}$  is the global conductivity matrix, and  $\mathbf{q}$  is the input nodal heating power.

One major advantage of the proposed bar and hinge framework is that it can simulate the thermo-mechanical coupling by varying the  $t_{env}$  parameter based on the geometric configuration of origami. Figure 5.4 shows how the thickness of surrounding substance is capped to consider the changing thermal boundary. When a triangular heating panel gets close to a thermal boundary, the distances between the three nodes of the heating panel and the planar thermal boundary are calculated, and the average  $t_{max} = (t_{max}^i + t_{max}^j + t_{max}^k)/3$  is used to cap  $t_{env}$ . When  $t_{max} \leq t_{env}$ ,  $t_{max}$  is used to calculate the conductivity for structure-environment heat loss. When  $t_{env} \leq t_{max}$ , the boundary has limited effects on the heat transfer problem, and  $t_{env}$  is used to calculate the conductivity for structure-environment heat loss. In the verification section, we will show that this simple method allows the refined bar and hinge model to capture the thermo-mechanically coupled folding behavior of the functional origami effectively. While this thermal model is built specifically

for small-scale origami structures, we envision that it can be extended to model thermal behavior of other thin origami and kirigami inspired structures.

When following the flowchart on Fig. 5.2 for solving the heat transfer problem of functional origami system, it is important to select an appropriate step size for heating  $dq$ . If the heating step  $dq$  is too large, step 3 of the flowchart can have convergence problems. In general, it is suggested controlling the heating step  $dq$  to be relatively small so that step 3 can converge within 5 to 10 Newton iterations. A smaller  $dq$  value will require more increments to finish the simulation and thus makes the wall-clock time longer. However, this longer run time may be preferred because it stabilizes the simulation and ensures easier convergence of the problem.

### 5.2.2 Step 2: Solving the stress-free angle

Next, the stress-free angle of the folding crease is computed based on the nodal temperature profile obtained in step 1. This work assumes the crease region to be made of bi-material morph components that consist of two layered materials with different coefficients of thermal expansion. Because one of the material layers expands more when heated, the bi-material morph will develop curvature and folding in the crease region (Fig. 5.1 (a)). This is a common actuator design which has been used in many previous research efforts [Na et al., 2015, Zhu et al., 2020, Kang et al., 2019]. Furthermore, it is assumed that the panels of the origami will remain near to rigid, and that the elevated temperature will not introduce significant deformation in the panels that interferes with the crease folding. This is a reasonable assumption because most functional origami systems have panels that are rigid when compared to the creases, and also the panels remain passive to the applied stimulus [Zhu et al., 2020, Na et al., 2015, Kang et al., 2019, Felton et al., 2014]. Timoshenko's bi-material morph model [Timoshenko, 1925] is used to calculate the stress-free curvature of the creases based on the elevated crease temperature. This analytical model assumes that both the section level structural response and the material response are linear. Though simple, the model gives a good prediction of the curvature and rotation of the bi-material morphs, and its accuracy has been demonstrated in previous research [Zhu et al., 2020, Na et al., 2015, Pezzulla et al., 2015]. The curvature of the bending actuator under a given elevated temperature  $\delta T$  is calculated as:

$$\kappa = \frac{6(\alpha_1 - \alpha_2)(1 + m)^2 \delta T}{(t_1 + t_2)[3(1 + m)^2 + (1 + mn)(m^2 + \frac{1}{mn})]}, \quad (5.4)$$

where  $\alpha_1$  and  $\alpha_2$  are the thermal expansion coefficient of the two materials,  $E_1$  and  $E_2$  are the Young's moduli of the two materials,  $t_1$  and  $t_2$  are the thicknesses of the two materials,  $m = t_2/t_1$ , and  $n = E_2/E_1$ . The stress-free angle of the folding crease with length  $l$  can be next calculated as:  $\theta = \kappa l$ . The updated stress-free angle of folding creases will be used in the mechanics formulation in step 3 to determine the new equilibrium shape of the origami systems.



### 5.2.3 Step 3: Solving the equilibrium position

Finally, the compliant crease bar and hinge model (developed in Chapter 3) is used to simulate the new equilibrium position of the origami system. The total potential strain energy stored within the origami system can be expressed as the following:

$$U(x) = U_{bar}(x) + U_{spr}(x, \delta T) + U_{contact}(x), \quad (5.5)$$

where  $x$  is the nodal coordinates, and  $U_{bar}$ ,  $U_{spr}$ , and  $U_{contact}$  are the potential energies from stretching of bar elements, folding of rotational springs, and contact of system components. As can be seen in the equation, the elevated temperature can affect the potential of the rotational spring elements. Contact within the origami model can be detected based on the distance  $d$  between nodes and surfaces in the model (origami panels or substrate). To simulate the contact interactions, a contact penalty function (developed in Chapter 4) is included into the total potential of the system. The formulas for the contact potential term  $U_{contact}(x)$  can be found in Section 4.2. By the formulation of principle of stationary potential energy, searching for the configuration with the local minimum potential will yield a configuration that is in equilibrium.

Together, the simulation framework allows us to capture: the global temperature distribution induced by electro-thermal heating, crease curvature resulting from the elevated temperature, interaction between heating dissipation and the large deformation folding, mechanical deformation from gravity and other loading, and contact induced interactions within the origami systems.

## 5.3 Calibration and Parameter Selection

Since the heat transfer model (step 1 of the framework) is new, this section studies its behaviors and verifies its performance. The validity of the models for solving crease curvature (step 2) [Zhu et al., 2020, Na et al., 2015, Pezzulla et al., 2015] and for solving the large deformation origami motion (step 3) [Zhu and Filipov, 2020, Zhu and Filipov, 2019a] have been studied previously in Chapter 3, so we will not reiterate the material. Moreover, this section also demonstrates how to select the model parameters (thickness of surrounding environment at room temperature  $t_{env}$ , number of layers  $N$ , and dissipation angle  $\beta$ ) used to tune the behavior of the heat transfer between the structure and the surrounding environment. Additional studies further verify that the chosen set of parameters are applicable to a wide range of combinations of geometries and material properties.

### 5.3.1 Heat transfer within origami structures

We first study the validity of the proposed bar and hinge model for simulating the heat transfer problem within the origami structure. Because the proposed model uses a well established pla-

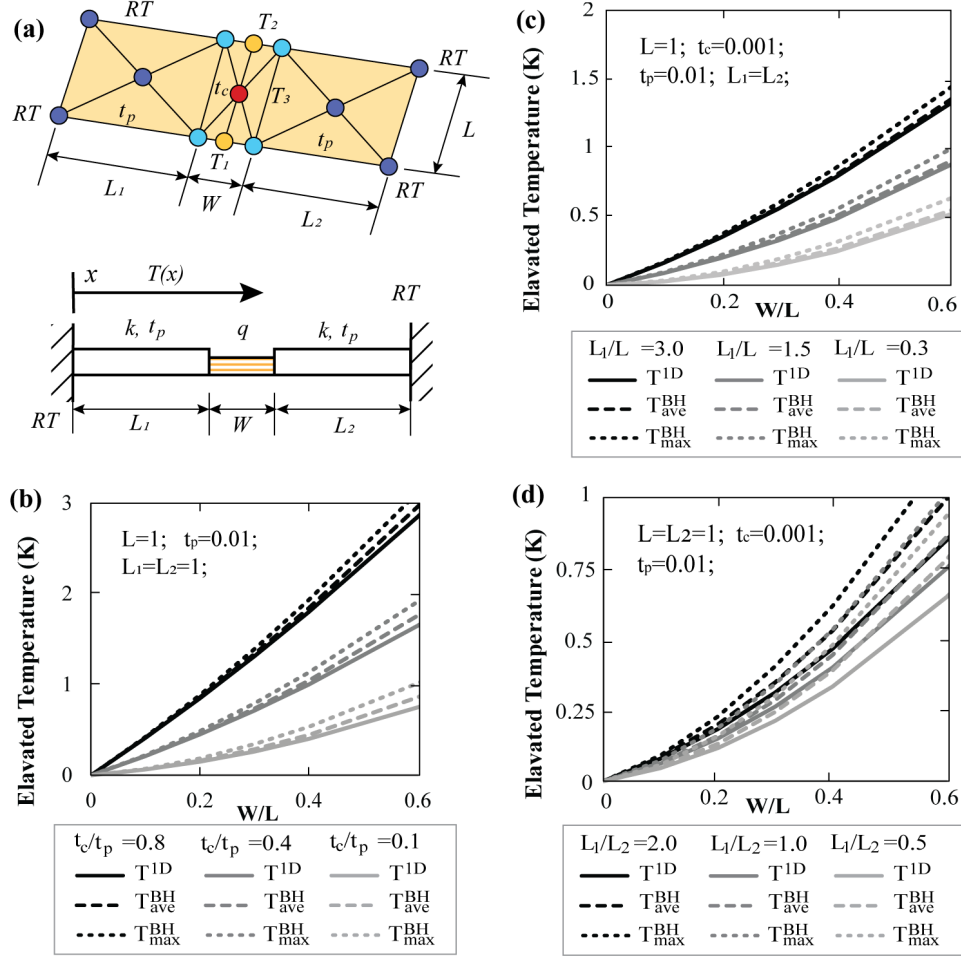


Figure 5.5: Verification of the proposed simulation for heat transfer within the origami structure.

nar triangular ( $T_3$ ) thermal element, the performance is guaranteed when fine meshing is used. However, because the proposed bar and hinge model only uses a coarse mesh, it is necessary to determine how much error is introduced in the temperature prediction. Figure 5.5 (a) shows the setup for a two-panel origami with one heating crease system, with which we explore the performance of the model. The far ends of the two panels are set to be at room temperature ( $RT = 0$ ), and apply a uniform body heat of magnitude  $q = 10$  in the center crease. The planar geometry of the panels is defined using  $L$ ,  $L_1$ , and  $L_2$ , while the crease is defined using  $L$  and  $W$ . The thickness of the panels is  $t_p$ , and the thickness of the crease is  $t_c$ . This system can be effectively modeled as an 1-D heat transfer problem with available analytical solutions.

A non-dimensionalized material thermal conductivity  $k = 1$  is assumed for all the verification studies in this subsection. A FE simulation of the two panel origami shows the 1-D characteristic of this heat transfer problem (Fig. 5.5 (c)). Four non-dimensional parameters are studied for this

comparison and they are: (1)  $W/L$  indicating the ratio between the width of the creases to the length of the creases; (2)  $t_c/t_p$  indicating the ratio between the thickness of the creases and the thickness of the panels; (3)  $L_1/L$  where  $L_1 = L_2$  indicating the aspect ratio of the panels; and (4)  $L_1/L_2$  indicating different lengths of the two panels.

The proposed bar and hinge model cannot capture the 1-D heat transfer feature perfectly because the three nodes on the center line of the crease give different temperature predictions. However, as will be shown, these predictions are close to the theoretical 1-D heat transfer solution. For the verification, we compare the difference between the maximum simulated temperature  $T_{max}^{BH} = T_3$ , the average simulated temperature  $T_{ave}^{BH} = (T_1 + T_2 + T_3)/3$ , and the analytical solution of the 1-D heat transfer problem  $T^{1D}$ .

First, we assume that the geometry of the two panels is identical by setting  $L_1 = L_2$  and study the performance of the model for different crease versus panel thicknesses ( $t_c/t_p$  - Fig. 5.5 (d)) and for different length versus width of the structure ( $L_1/L$  Fig. 5.5 (e)). The prediction from the proposed bar and hinge framework closely matches the analytical solution and captures the identical trends for different crease dimensions ( $W/L$ ). Both curves of  $T_{max}^{BH}$  and  $T_{ave}^{BH}$  match the analytical solution well and there is limited difference between the value of  $T_{max}^{BH}$  and  $T_{ave}^{BH}$ . Next, we break the assumed the symmetry of the system and study the performance of the model when the two panels have different geometries ( $L_1/L_2$  Fig. 5.5 (f)). Similarly, the bar and hinge model can capture the trends well. Although the maximum temperature of the crease is slightly overestimated, the average temperature of the crease is about the same as the analytical solution. These results indicate that the non-uniformity of the coarse bar and hinge mesh do not introduce a significant error regardless of the system geometries.

### 5.3.2 Heat transfer between origami structures and surrounding environments

To test the performance of the model for simulating heat transfer between the structure and the surrounding environment, we need to study how the three model parameters affect the model performance, namely: thickness of surrounding substance between the structure and the point at room temperature  $t_{env}$ , the number of discretizing layers  $N$ , and the dissipation angle  $\beta$ . We vary the combinations of these three parameters and compare the results from the bar and hinge model to a 2-D FE simulation and a 3-D FE simulation of the same two panel origami system (see Fig. 5.6 (a) for the set up). The 3-D FE simulation represents the realistic behavior of the system because it is able to consider heat loss in all directions. On the other hand, the 2-D FE simulation result is provided as an upper bound. We assume the surrounding environment to be air (with thermal conductivity of  $k_{air} = 0.026 W \cdot m^{-1} \cdot K^{-1}$  [Huang and Lee, 1999]) and assume the structure is made from an SU-8 polymer (with thermal conductivity of  $k_{SU8} = 0.3 W \cdot m^{-1} \cdot K^{-1}$  [MicroChem, 2019]),

(a) 3D FEM Result

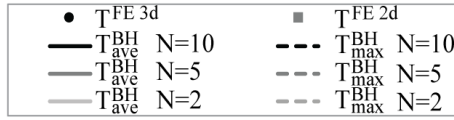
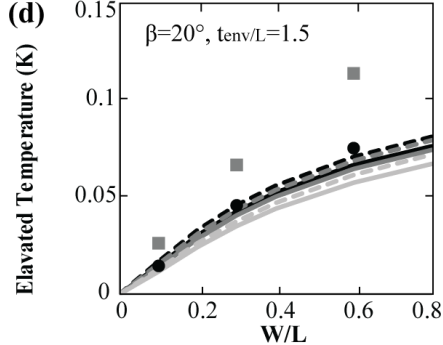
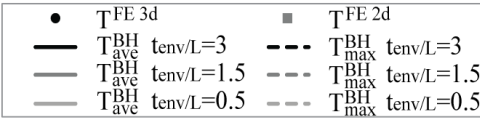
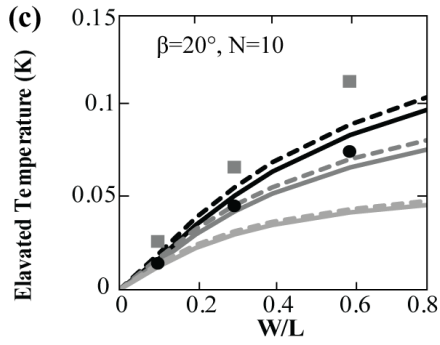
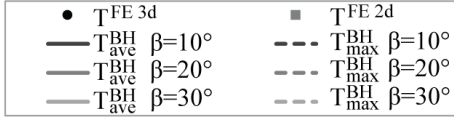
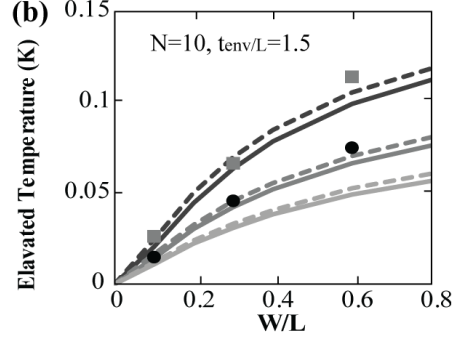
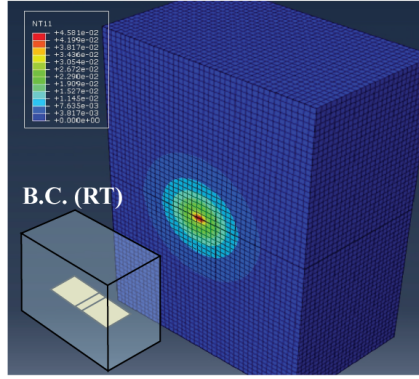


Figure 5.6: Calibration of the heat transfer between the origami and the surrounding environment.

which is a common polymer material for MEMS devices.

The comparisons of the results for different combinations of the three model parameters are summarized in Fig. 5.6 (b), (c), and (d). Figure 5.6 (b) suggests that our model is sensitive to the selection of the dissipation angle  $\beta$ . This  $\beta$  parameter allows us to consider the heat loss in different directions and is determined by the geometric characteristics of the system. The results presented suggest that  $\beta = 20^\circ$  matches the 3-D FE simulation well for a typical single crease origami system, and thus this value is selected for further simulations performed in the paper. Figure 5.6 (c) shows that a value of  $t_{env} = 1.5L$  is needed for the thickness of the surrounding substance such that the proposed model can properly capture the surrounding environment. Figure 5.6 (d) shows that the simulation is not sensitive to the number of discretizing layers  $N$ , once  $N$  is sufficiently large ( $5 \leq N$ ). The results presented in Fig. 5.6 show that when the proper combination of model parameters are selected ( $\beta = 20^\circ$ ;  $t_{env} = 1.5L$ ;  $N = 10$ ), the proposed bar and hinge model can capture heat

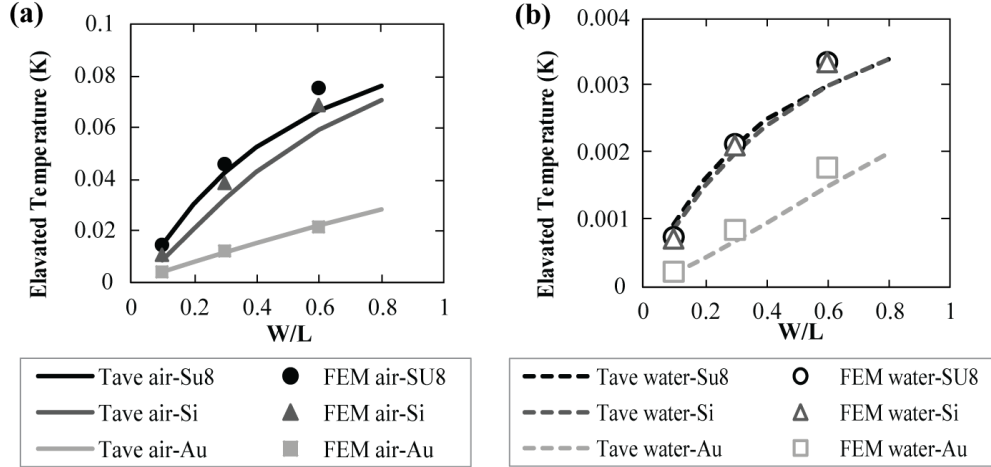


Figure 5.7: Checking the model accuracy for capturing the heat transfer between the origami and the surrounding environment with different material thermal conductivity.

transfer between the origami and the surrounding environment with reasonable accuracy. The model captures the trends with respect to the geometry of the system (W/L ratio) and provides a reasonable approximation of the actual temperature changes in the 3-D system.

Finally, we check the performance of the proposed model for different material combinations (Fig. 5.6 (e) and (f)). We select air and water as the surrounding environments and use Su-8, Si, and Au as the materials of origami structures (these environments/materials are common for functional origami systems). We use the same model parameters as those chosen through the parametric study in Fig. 5.6 ( $\beta = 20^\circ$ ;  $t_{env} = 1.5L$ ;  $N = 10$ ). The model shows a good match with the 3-D FE simulation regardless of the type of environmental substance and the type of material that is used for the origami structure. Thus the above model parameters are a reasonable choice for simulating different structure and environment combinations.

## 5.4 Experimental Verification

In this section, we will verify the performance of the proposed simulation framework by comparing the prediction of the folding motion from the model to physical micro-origami systems. The two cases to be studied are: a single-crease origami with a folding threshold and a double-crease origami with thermo-mechanical coupling.

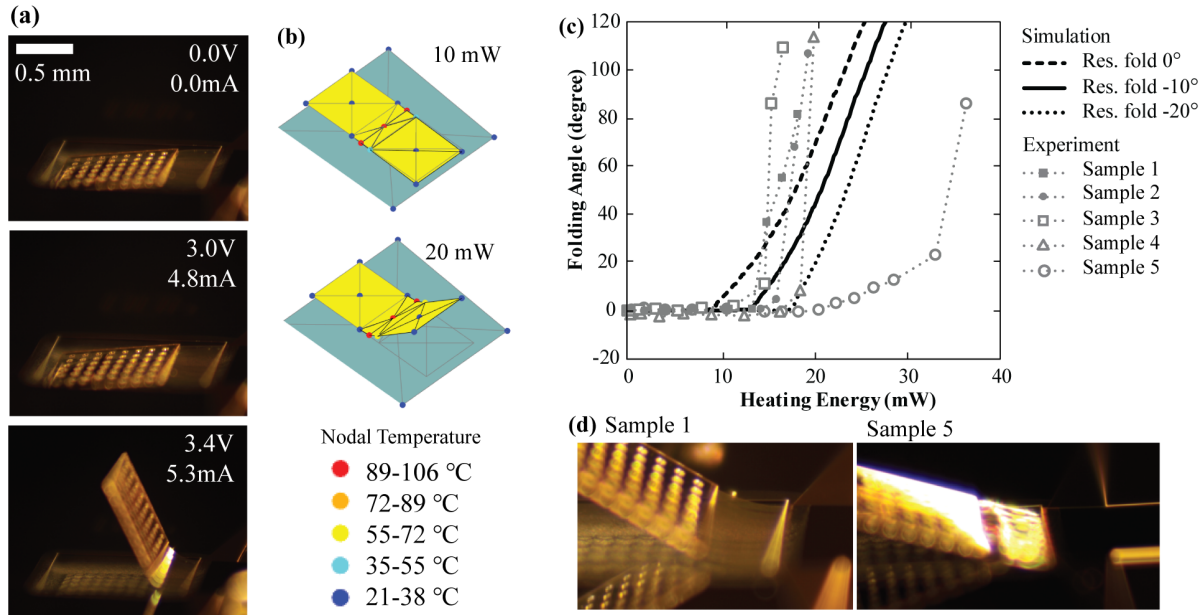


Figure 5.8: Comparison between the predicted folding behavior from simulation method and the measured folding behavior of electro-thermal one-panel micro origami.

### 5.4.1 Single-crease origami with a folding threshold

First, a single-crease micro-origami system, which experiences a gravity induced folding threshold, will be studied. The threshold effect occurs because gravity acting down on the origami causes it to come into contact with the substrate underneath. To fold the single crease origami, we need to apply power higher than a specific threshold to overcome the effects of gravity before observable folding is achieved (Fig. 5.8 (a)). This case study shows that the proposed model can accurately capture the multi-physics interaction between the heating induced self-folding, panel contact, and gravity.

Figure 5.8 (b) demonstrates the simulated folding behavior with our bar and hinge framework, and Fig. 5.8 (c) shows the comparison between the simulation and experimental measurements. The physical devices were fabricated and actuated with processes introduced in our previous work [Zhu et al., 2020]. The simulation curves are plotted with an assumed negative residual folding angle. This negative residual folding angle is a physical characteristic of the systems which occurs because of a residual stress generated during the fabrication of the polymer (SU-8) layer and the gold layer. This effect is difficult to quantify analytically, so we assume that the creases will develop about  $-10^\circ$  of residual folding, which matches the observation of testing beams with no panels [Zhu et al., 2020]. The simulation results for  $0^\circ$  and  $-20^\circ$  of residual folding are also plotted for comparison. The simulation is able to capture the threshold effects and the large folding

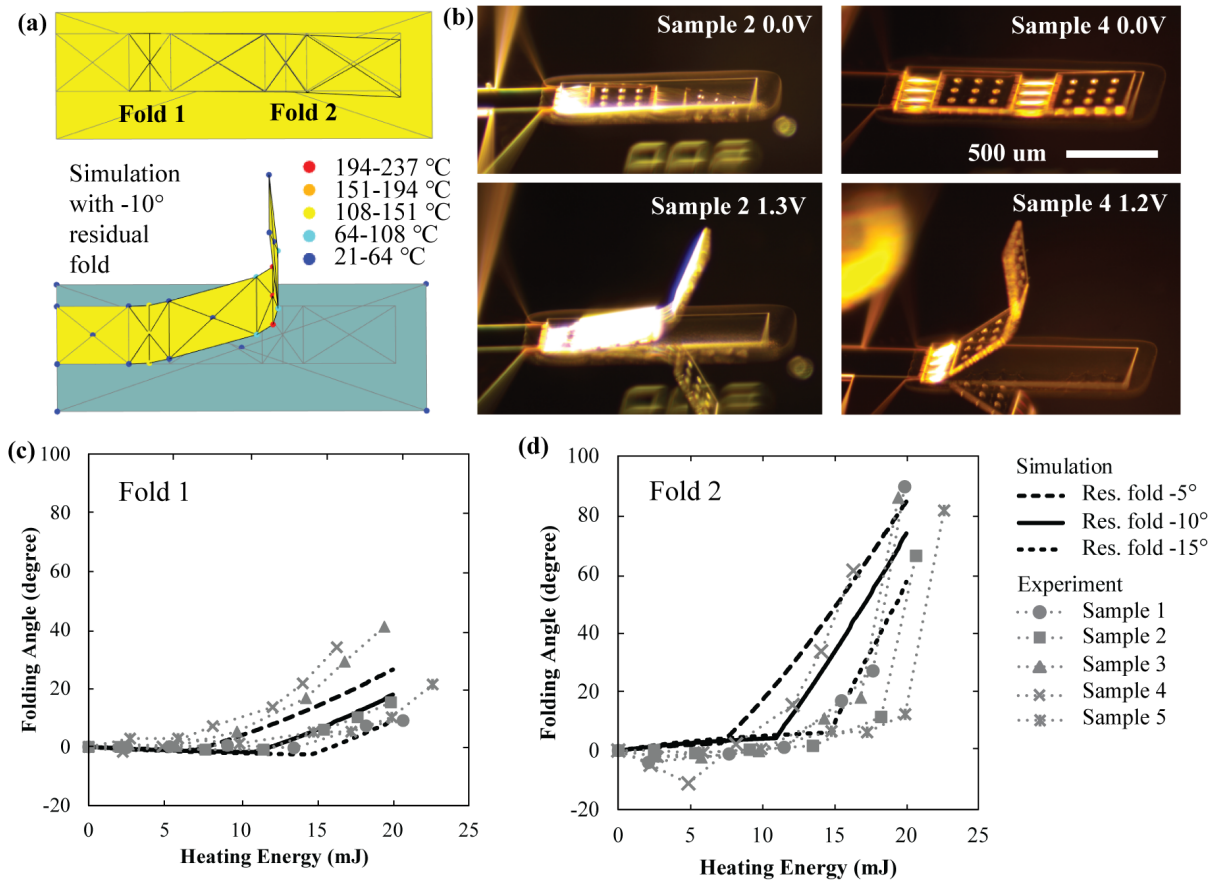


Figure 5.9: Comparison between the predicted folding behavior from simulation method and the measured folding behavior of electro-thermal two-panel micro origami.

of the origami accurately. The wall-clock time for running the entire simulation with 250 thermal increments is 13 seconds recorded on a modern laptop with i7-8750H processor. The model underpredicts the nonlinearity in the folding and a higher heating power is needed to reach the high folding angles. The more extreme nonlinearity observed in the real experiments is likely due to the nonlinear material responses and the complex thermal boundary generated by the etch holes surrounding the single-crease origami. Previous researches have shown that the mechanical and thermal properties of SU-8 is nonlinear [Robin et al., 2014, Xu et al., 2016], which can lead to the mismatch in Fig. 5.8 (c). Also, the thermal boundary with a complex 3-D shape is simplified as a 2-D plane in the proposed model so the heating dissipation is not captured exactly.

Figure 5.8 (c) also contains one outlier that we encountered during the physical testing (Sample 5). In this case, the specimen experienced a local defects during the fabrication which caused the wrinkling in the electro-thermal actuator crease and delayed the folding from happening (Fig. 5.8 (d)). Such localized behaviors cannot be captured with the proposed model as our model has

limited degrees of freedom and is dedicated to only simulating the global response of origami. Although this outlier illustrates the limitation of our model, we believe it does not compromise the usefulness of the proposed model. More robust fabrication methods will prevent such outliers from happening in the future.

#### **5.4.2 Double-crease origami with thermo-mechanical coupling**

Here, we study the thermo-mechanically coupled folding behavior within a double-crease origami pattern (Fig. 5.9). This system has two identical creases, however, the folding of the two creases is different because each crease has different thermal boundaries that results in different temperatures when heated. The second fold (fold 2 on Fig. 5.9 (a)) is folded further away from the substrate which leads to a slower heat dissipation, a higher temperature, and a higher curvature. This coupled thermo-mechanical effect can be captured accurately with the proposed model.

Figure 5.9 (a) shows the simulated folded geometry of the origami system, and Fig. 5.9 (b) shows the experimental pictures of the same systems. The physical devices are fabricated using the processes reported in [Zhu et al., 2020]. A single simulation of the double-crease origami pattern takes about 18 seconds to complete (recorded on a modern laptop with i7-8750H processor). Figure 5.9 (c) and (d) show a comparison between the simulation and the measured results for the folding angle of the two creases. Similar to the single-crease, the double-crease system also experiences the gravity induced threshold effect, which can be captured with the bar and hinge formulation accurately. More significantly, the results show that the proposed model can capture the thermo-mechanical interaction during the large folding deformation. The simulation successfully predicts that the fold 2 will develop a higher temperature and a larger folding angle as it moves away from the substrate.

The experimental results show that the fabricated physical samples have different residual folding as a result of the fabrication process (in Fig. 5.9 (b), the two samples rest at different configurations when no heating is applied). The difference in residual folding is mainly caused by the variation in residual stresses of the SU-8 layer and the gold layer. This residual folding can be measured and estimated using the testing beam samples from our previous work [Zhu et al., 2020]. These variations in residual stress are common for micro-scale fabrication but they are tremendously difficult to control [Kang et al., 2019]. We envision that the proposed simulation framework can be used to enumerate different combinations of design parameters efficiently to make the origami design robust against the influence of residual stress and other factors. Because the proposed framework is computationally efficient, it is possible to enumerate a large number of combinations of design parameters within a reasonable time schedule.



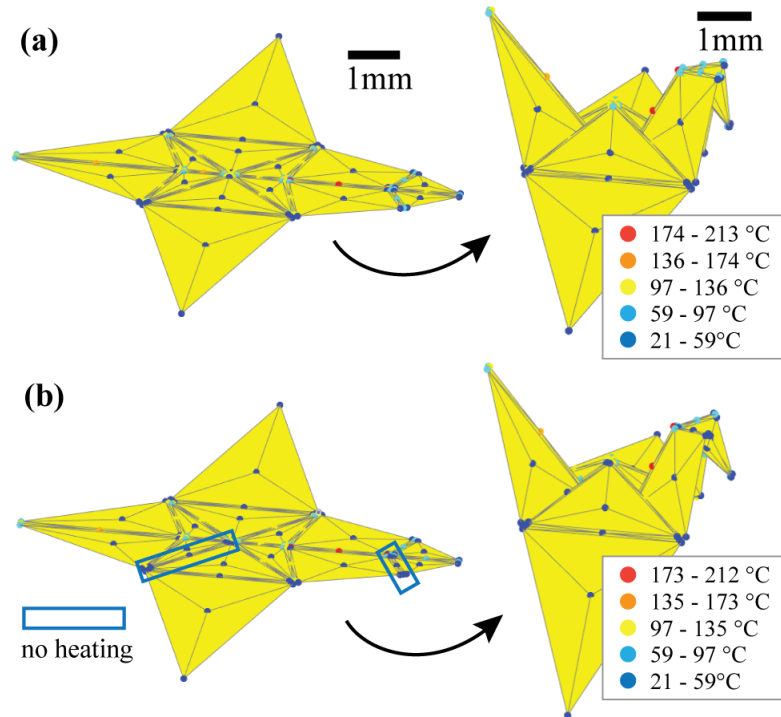


Figure 5.10: Simulation of the self-folding of an origami crane. (a) Folding the crane pattern with applied heating to all active creases. (b) Folding the crane pattern with two creases deactivated.

## 5.5 Application Examples

In this section, we will demonstrate the effectiveness and efficiency of the proposed method with three application examples: simulation of a crane pattern, folding of a Miura origami lifter, and an optimization study of an origami micro-gripper.

### 5.5.1 Simulation of a crane pattern

The first example studies the folding of an origami crane pattern as shown in Fig. 5.10. This crane pattern has 17 creases and is more complex than the single-crease and double-crease systems demonstrated previously. We use this example to demonstrate that the provided implementation code package can be easily adapted to simulate more complex origami systems. It is assumed that the crane pattern is made with the same fabrication method as discussed previously [Zhu et al., 2020] and thus the panels are made of thick SU-8 and the electro-thermal creases are made with Au and thin SU-8 films. The folding is accomplished by applying heating power to all creases of the crane pattern simultaneously. For simplicity, the effects of gravity and the thermal boundary of the

substrate are neglected in this example.

Figure 5.10 (a) demonstrates the folded geometry of this crane pattern, and the wall-clock time for running this simulation is about 30 seconds (recorded on a modern desktop with i9-10900K processor). When folding complex origami patterns, the folding speed of different creases tend to be different because of kinematic constraints by the pattern geometry [Zhu and Filipov, 2020]. However, common fabrication methods usually cannot ensure that different creases will fold with different speeds [Zhu et al., 2020, Na et al., 2015]. Thus, there will be interference between the different folding creases and strain energy will develop in the creases as their fold angles deviate from the computed stress-free state [Zhu and Filipov, 2020]. The proposed method can be used to study and simulate this interference effectively as demonstrated in Figure 5.10 (a). In general, by designing an origami pattern that has one-degree-of-freedom kinematic motion, one can also achieve the desired folding even if the actuation speed deviates from the kinematic folding speed. Moreover, it is also possible that real fabrication cannot actuate all creases simultaneously, and there may be a need to leave certain creases as passive rotational springs [Zhu et al., 2020]. Figure 5.10 (b) demonstrates one example of non-uniform actuation where two creases of the crane pattern are deactivated. The simulation shows that although we are not applying heating to these two creases, the folding can still proceed successfully. The successful folding is achieved because the pattern of this crane has one-degree-of-freedom folding kinematics. The two computation examples show that the proposed simulation framework is well suited for studying the complex folding motion of functional origami. Moreover, this example shows that the provided execution package can be easily adapted to efficiently simulate the electro-thermal folding of relatively complicated origami systems with non-uniform actuator placement. The relevant simulation code “Example06\_Crane.m” can be found on the GitHub page.

### 5.5.2 Folding of a Miura beam lifter

In this second example, a Miura beam based lifting device is studied. This example shows that the proposed simulation framework can capture complex thermo-mechanical interactions even when simulating a relatively complex origami pattern. Figure 5.11 shows the loading set up of the Miura beam, where the left end of the beam is anchored. All creases of the pattern are heated simultaneously so that the right end of the beam will be lifted as the pattern folds. We first consider folding the device when no substrate is presented under it. Figure 5.11 (a) shows the folded the geometry when no supporting substrate is presented and the dark line in Fig. 5.11 (c) gives the lifting displacement with respect to the normalized heating power.

This first loading set up is usually not realistic because a substrate is needed to support the device in a physical test. For small-scale devices, the large substrate supporting the devices will

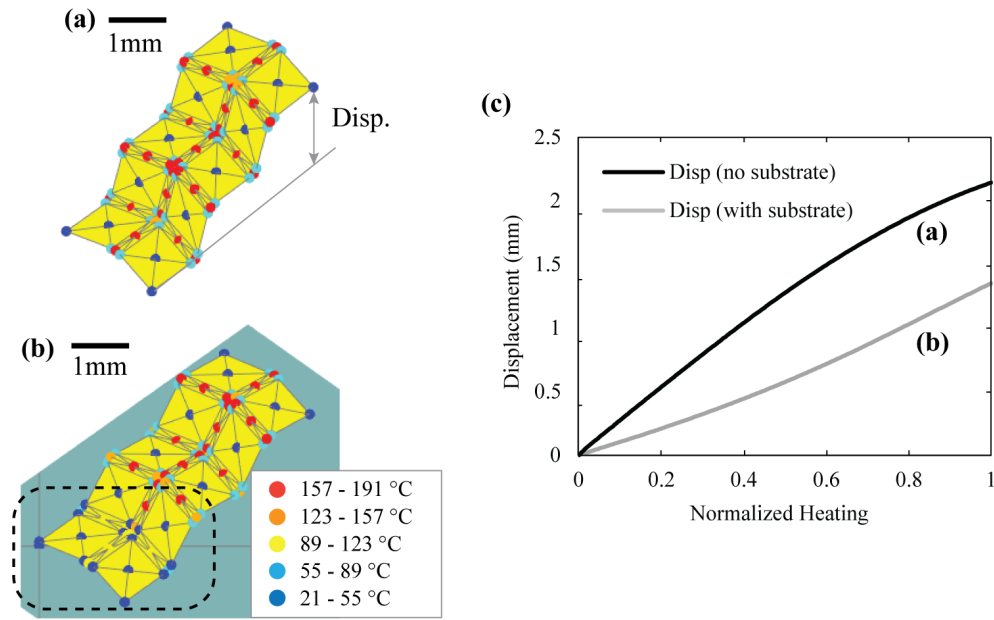


Figure 5.11: Simulation of a Miura-ori pattern lifting device.

naturally introduce a temperature boundary condition. Figure 5.11 (b) shows the deformed geometry of the same Miura beam under the same electrical heat loading when the substrate is presented underneath. We can see that those creases on the left end of the beam (in the dashed box) have a lower temperature than those creases on the right end. This temperature reduction is observed because the creases on the left end are closer to the substrate and thus dissipate the heating power quicker. Because part of the creases develop lower temperature, the lifting displacement of the device is also lower compared to the situation when no substrate is presented (see Fig. 5.11 (c) gray line). A wall clock time of about 50 seconds is recorded to run the analysis of this Miura beam example on a modern laptop with i7-8750H processor, which shows the efficiency and the capability of capturing changing thermal boundary of the proposed simulation framework. The simulation code “Example03\_Miura.m” can be found on our GitHub.

### 5.5.3 Optimization of origami gripper

The final example demonstrates how the simulation framework can be used as an efficient tool for optimizing the design of functional origami devices for realistic application. Over the past decades, there have been a number of research efforts to optimize origami designs [Dudte et al., 2016]. For example, particle swarm optimization can be used for finding new origami tessellations [Chen et al., 2021], a mixed-integer-program can be used for determining the mountain-valley assignment of origami creases in a pattern [Chen et al., 2020], and genetic algorithms could be

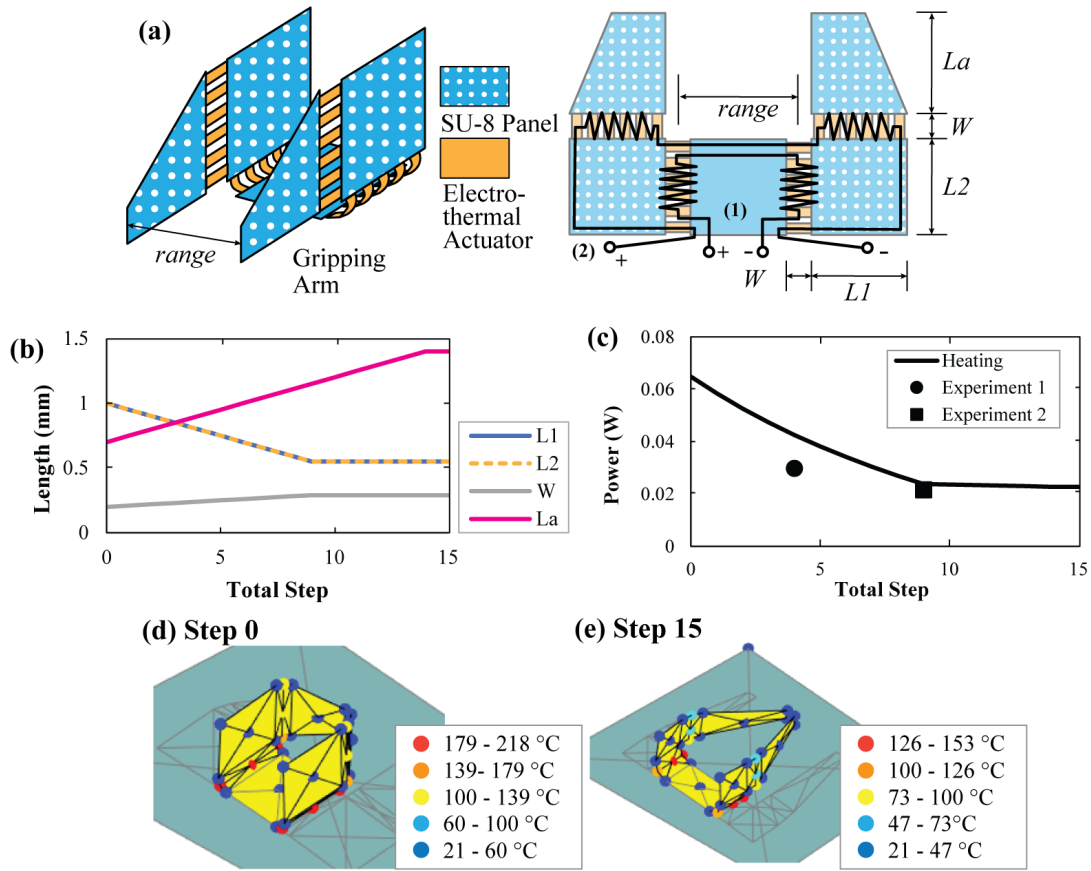


Figure 5.12: Optimizing the power consumption of a micro-origami 3-D gripper.

used for optimizing the geometry of origami patterns [Gillman et al., 2019]. However, most of the existing optimization studies are applied onto kinematic simulations of origami systems and thus have limited capability to optimize performance based metrics of origami like the power consumption. With the proposed model, we now have the capability to simulate function related metrics of functional origami efficiently and effectively, and thus can further achieve optimization of the performance of a functional origami.

Here, the proposed framework is used to optimize the design of an active origami gripper first demonstrated in Chapter 2. This micro-gripper has four foldable panels controlled by two separate circuits (see Fig. 5.12 (a) for system design and dimensions). The first circuit is used to fold the base panels to assemble the gripper into the 3-D geometry, and the second circuit is used to close the arms to achieve gripping functions. In Chapter 2, this gripper is designed using trial and error approaches so the gripping performance is not optimized. Here, we will search for a better geometrical design to minimize the input power needed to first assemble and then close the gripping arms. Practical constraints are considered and these include: (1) the size of the panels

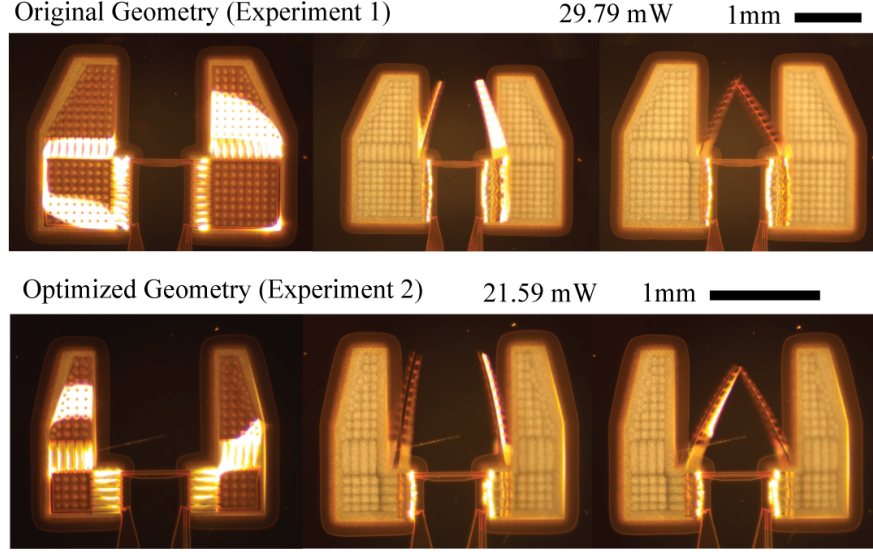


Figure 5.13: Verifying the results of optimization with experiments.

should not exceeds a prescribed range; (2) the gripping range is fixed as a constant; and (3) the temperature of the creases should not exceed the glass transition temperature of SU-8 so that the structure will not soften too much due to the excessive heating. The gripper optimization problem is formulated as follows:

$$\min (Power(W, L_1, L_2, L_a)) \quad (5.6)$$

$$s.t. L_{min} \leq L_1, L_2 \leq L_{max} \quad (5.7)$$

$$W_{min} \leq W \leq W_{max} \quad (5.8)$$

$$L_{a,min} \leq L_a \leq L_{a,max} \quad (5.9)$$

$$\max_i (T_i^{crease}) \leq 1.2 \times T_{g,SU8} \quad (5.10)$$

A coordinate descent with fixed step length is used to perform the optimization. The starting geometry is:  $L_1^0 = 1000\mu m$ ,  $L_2^0 = 1000\mu m$ ,  $L_a^0 = 700\mu m$ , and  $W^0 = 200\mu m$ , and the constraints are selected as:  $L_{min} = 500\mu m$ ,  $L_{max} = 1500\mu m$ ,  $W_{min} = 100\mu m$ ,  $W_{max} = 300\mu m$ ,  $L_{a,min} = 500\mu m$ , and  $L_{a,max} = 1500\mu m$ . Unlike the original design presented in [Zhu et al., 2020], the panels of these micro-origami grippers are made with  $5\mu m$  thick SPR photoresist rather than the  $20\mu m$  thick SU-8 photoresist. This reduction in thickness makes the folding motion of the gripper easier to control by reducing effects of gravity. Figures 5.12 (b) to (e) summarize the results of the optimization. We can see that as the optimization proceeds, the base panels become smaller and the actuator

creases become longer. These optimization results are obtained because the smaller base panels can reduce gravity loading and the longer actuator creases can achieve the same folding angle at a lower temperature with less input power. The optimized gripper not only demonstrates better energy performance, but also has lower functioning temperature, which makes it more robust and less likely to be overheated. Each simulation of the gripper can be done in 20 seconds and the entire optimization is accomplished in about 25 minutes without parallelization, demonstrating the high efficiency of the proposed simulation framework.

After running the simulation, the optimized gripper was fabricated and tested. The recorded folding motion and the power consumption are shown in Fig. 5.12 (f) and (g). The first gripper sample Fig. 5.12 (f) has a geometry that is close to the simulated gripper obtained in step 4 of the optimization, and the second gripper in Fig. 5.12 (g) has a geometry that is close to the simulated gripper obtained in step 9 of the optimization. The geometry of the fabricated samples does not match the simulated geometry exactly due to practical limitation of the fabrication. The first gripper design requires 29.8 mW to complete the full gripping function while the optimized sample requires 21.6 mW, demonstrating that the optimization successfully reduced the power consumption. However, the measured power consumption of the unoptimized gripper is lower than what is simulated. There are multiple factors that can lead to this overestimation. First of all, the residual curvature of the relatively thin SPR panel for the non-optimized gripper can interact with the folding process and contribute to the mismatch in the power calculation. Besides, a fixed heat dissipation angle  $\beta$  is used for the entire system without considering the thermal interaction between adjacent creases. When there are multiple creases and panels that are close to each other (such as in this gripper), the heat dissipation angles  $\beta$  should decrease to consider that the multiple creases/panels cannot dissipate as much heating power using a shared volume of air. Because the crease temperatures in the optimized design are substantially lower, there is less overall dissipation, and thus it matches simulated prediction better. Finally, variations in thickness, material properties, pattern sizes, and other factors during the fabrication could also contribute to the mismatch. Although the predicted power consumption does not match the the experiment perfectly, the revealed design principle is valid and useful and the power consumption of the gripper is reduced successfully, which demonstrate capability of using the simulation framework for design optimization.

## 5.6 Concluding Remarks

In this chapter, a novel simulation framework is proposed to capture the multi-physical behaviors of electro-thermally actuated origami systems. The framework is based on the compliant crease bar and hinge model developed in Chapter 3, which allows for a simplified and rapid simulation of the

active systems with thin-sheet geometry. This chapter establishes a new model for capturing the heat transfer and the thermo-mechanical coupling within the origami. Our approach recursively solves (1) the heat transfer problem for the nodal temperature of the origami under an applied heating power, (2) the curvature of each crease from the elevated crease temperature, and (3) the new equilibrium position of the origami using a mechanical solver that determines the global folding motion of the system.

In the proposed formulation, planar triangular thermal elements are used to capture heat transfer within the structure, while the structure to environment heat loss is simulated as a simplified 1-D heat conduction problem. This modeling technique is calibrated and verified against analytical solutions and FE simulations, and the result shows that the new model can accurately capture the two forms of heat transfer within functional origami systems.

Next, this chapter presents two verification examples where we compare the predicted folding motion from the proposed simulation framework to physical experiments of electro-thermally actuated micro-origami. The two verification examples show that the simulation can capture the gravity induced folding threshold, the contact between the origami and a substrate, and the thermo-mechanically coupled folding motions. These two examples highlight the capability and validity of the proposed simulation framework as a rapid method to capture the behaviors of origami-inspired systems.

Finally, three application examples are presented where the model is used to study (1) the folding motion of a relatively complex origami crane pattern, (2) the influence of having a substrate under a Miura origami lifting device, and (3) the design optimization of an origami gripper. With these three examples, we further demonstrate the efficiency and effectiveness of the proposed framework for simulating the interdependent electro-thermal actuation, large deformation folding, contact between different panels, and other loading effects.

This simulation framework provides a much needed method to simulate, design, and optimize electro-thermal or thermally actuated origami systems. Moreover, the proposed framework can be used at multiple length scales and is not limited to origami-type systems. By re-tuning the model parameters, we envision that the model can also be applied to simulate thermal and active multi-physical behaviors in other systems with planar features such as ribbon-based or kirigami-based structures. We believe that the proposed simulation framework will push the limits of origami systems, allowing engineers and researchers to explore new origami systems, to create new control protocols for functional origami structures, and to rapidly refine and optimize their designs.

## **Chapter 6. Origami Inverse Design with Interpretable Machine Learning**

In this chapter, we will introduce an interpretable machine learning based inverse design strategy for functional origami structures to address the Challenge 5 proposed in the Introduction. More specifically, this chapter will demonstrate that a decision tree-random forest method is particularly suitable for fitting origami performance databases, computed using simulation methods developed in Chapter 3 to Chapter 5, for the inverse design of functional origami. First, this interpretable machine learning method can reveal complex interactions between categorical features and continuous features for comparing and selecting different origami patterns. Next, this method can tackle multi-objective problems for designing functional origami with multiple multi-physical performance targets. Finally, this proposed method can extend existing origami shape fitting algorithms to further consider non-geometrical performance for a holistic origami inverse design. The proposed framework greatly expands the capability of existing origami inverse design methods from shape fitting to function design for applications in metamaterials, deployable structures, soft robots, biomedical devices, and many more.

This chapter is arranged as the following. First, we give an introduction of machine learning methods. We introduce how traditional machine learning method are used as surrogate models for physical simulations and how interpretable machine learning methods are different from those traditional ones. Next, we introduce how we can use the decision tree-random forest method (one interpretable method) to compute the design rules for origami structures. After establishing the methodology, we will use three demonstration examples to highlight the effectiveness and usefulness of the proposed method. More specifically, we will start with one simple design example and then show how categorical features and multi-objective problems can be integrated into the framework for a holistic inverse design. Finally, we will end this chapter with a brief discussion and a concluding remark.

### **6.1 Introduction of Machine Learning**

Machine learning is a powerful tool rooted in data science that can be used to solve problems in many disciplines like structural analysis [Mangalathu and Jeon, 2018], molecular simulation [Noe et al., 2020], financial analysis [Chi and Tang, 2006], and many others [Carleo et al., 2019]. In general, there are three major machine learning problem formulations and they are: supervised



learning, unsupervised learning, and reinforced learning. In supervised learning, a database is given with labels, and we apply the machine learning method to learn how to predict these labels based on data features. For example, we may have a database on the financial performance of companies, and the label information tells us whether the company goes bankrupted or not in some years [Chi and Tang, 2006]. Then, we can train machine learning methods to differentiate companies that may go bankrupt from those that are healthy. This trained machine learning model can then be used to guide investors to avoid bankrupting companies. In unsupervised learning, the goal is to train machine learning methods to spot patterns from data with no labels. These unsupervised learning algorithms can be used to address problems like clustering, dimension reduction, and anomaly detection. For example, we can use unsupervised learning to create image segmentation, where we represent an image with less than 4, 6, or 8 colors [Ng et al., 2018] for reducing the storage space. In reinforced learning, the goal is to train an agent to achieve better performances with superior strategies. For example, we can train machine learning method to learn the best strategies to win a video game (e.g. StarCraft II) [Vinyals et al., 2019]. In this chapter, we will focus on the supervised learning topic because many engineering problems can be cast as a supervised learning problem. More specifically, we will first take a look at how machine learning methods can be used as surrogate models to replace physical simulations.

### 6.1.1 Machine learning as surrogate models

Using machine learning algorithms as surrogate models to replace physical simulations is beneficial for optimization or designing for a large number of samples, where we need to run physical simulations repeatedly. Suppose we are interested in designing an electro-thermal origami gripper and our goal is to calculate the gripper performance (including stiffness  $stiff$ , fundamental frequency  $freq$ , applied heating needed to close the gripper  $Q$ , and the maximum nodal temperature of gripper  $T_{max}$ ) based on the design features (including origami geometrical features like:  $L_1$ ,  $L_2$ ,  $t_p$ ,  $rate$ , and actuator design features  $t_1$ ,  $t_2$ ,  $W$ ). A problem like this can be thought of as identifying a nonlinear function  $f$  to calculate the performance from the design features:

$$[Stiff, freq, Q, T_{max}] = f(L_1, L_2, rate, W, t_1, t_2, t_p). \quad (6.1)$$

In general, there exist no analytical solution of this function  $f$  so physical simulations are used to solve the performances based on the design features (top branch in Fig. 6.1). However, because of the non-linearity and the iterative solution methods, these physical simulations are slow. Therefore, people are interested in speeding up the simulation using machine learning. One way of understanding machine learning method for supervised learning problem is that machine learning is a powerful function generator that can approximate a nonlinear function with high

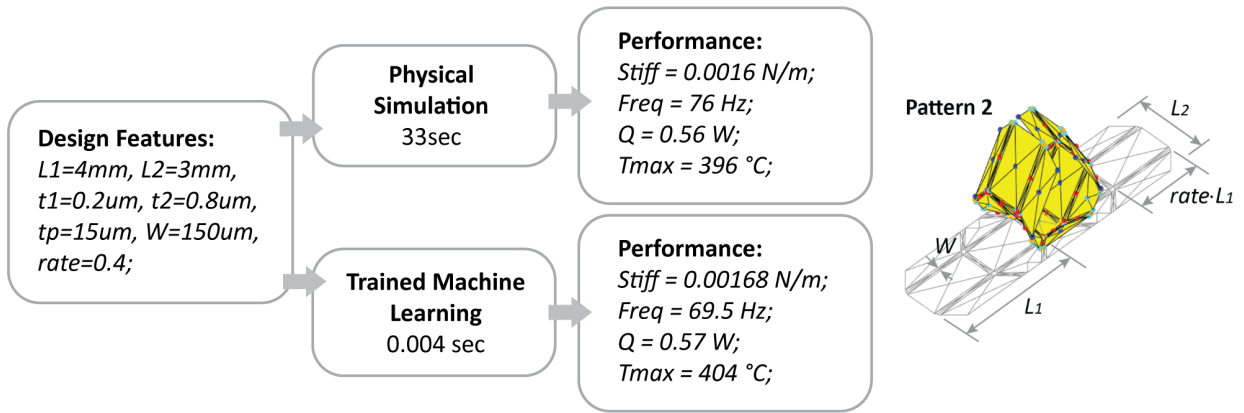


Figure 6.1: Using machine learning as surrogate models for physical simulations.

accuracy and efficiency. For example, we can train the machine learning method to fit the nonlinear function  $f$  using a performance database of the gripper, and after the training, the learned machine learning model can approximate the physical simulation with high precision. Moreover, using the trained machine learning model is much faster than using the physical simulation itself, because the internal structures of machine learning models require no iterations (bottom branch in Fig. 6.1). Figure 6.1 shows one computation example where running a physical simulation requires 33 sec but using the machine learning (a multi-layer-perceptron model with sklearn package) only needs 0.004 sec. More importantly, we can see that the difference between the machine learning method and the physical simulation is relatively small. Therefore, using machine learning methods as surrogate models can drastically speed up the simulation speed for applications like optimization or inverse design for engineering applications [Mangalathu and Jeon, 2018, Hanakata et al., 2018, Noe et al., 2020].

Next, we show how to train a machine learning method. The first step of training a machine learning is to generate a performance database using the simulation methods (or use existing database). Normally, a number of simulations are executed (e.g., 1000) with randomly generated design features to build the performance database (see table in Fig. 6.2). Building the database with random features can be thought of as a *sampling* process, where we sample the behaviors of an origami simulation using the randomly generated design features. After establishing the database, we can train the machine learning method to fit it so that the machine learning model can approximate the behaviors of the physical simulation. This training process is different when different machine learning method is used, and this training process can be thought of as a more advanced version of polynomial fitting or linear regression. Basically, the data points represent the underlying structure of the non-linear function  $f$ , and the machine learning is trained to fit that function. In this work, we will use the open-access sklearn package to implement the machine

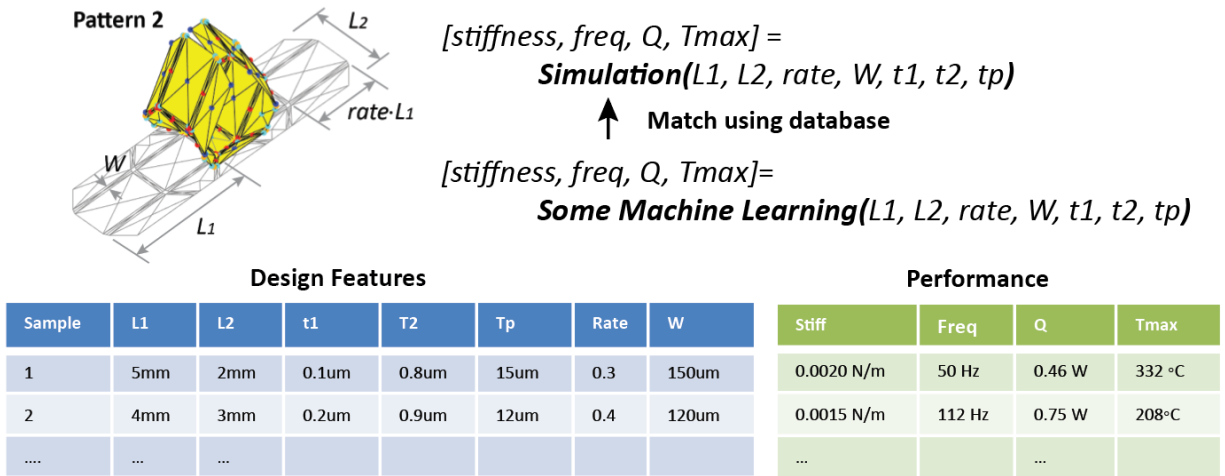


Figure 6.2: Training process of machine learning methods.

learning method [Buitinck et al., 2013].

### 6.1.2 Interpretable machine learning and decision trees

In this subsection, we want to focus on one specific type of machine learning method called interpretable machine learning. In general, interpretable machine is different from standard “black box” machine learning method because it can produce human understandable decision rules to explain why a decision is made [Rudin, 2019, Quinlan, 1986, Quinlan, 1993, Breiman et al., 1984]. This allows us to obtain an interpretable approximation of the nonlinear function (the Eqn. 6.1) that is more than accurate and efficient. This interpretability is crucial for the inverse design because it helps us to construct the inverse relationship to calculate design features from target performances as will be discussed in detail in the following sections. More specifically, we will use one interpretable machine learning method called decision tree and its ensemble version called random forest [Quinlan, 1986, Quinlan, 1993, Breiman et al., 1984].

Suppose we want to study a problem shown in Fig. 6.3 (a) with the decision tree-random forest method, where we want to classify the data points (with class label  $y = 0, 1$ ) based on its four-dimension features  $(x_0, x_1, x_2, x_3)$ . Figure 6.3 (b) gives a sample decision tree for classifying the data, which has a reversed tree shape. When using the decision tree method, the data point will flow into the tree from the root node on the top of the tree. Then, the algorithm will judge if the data point should go to the left branch or to the right branch based on if the data point meet the splitting rule given by the branch node or not. After a series of judgements, the data point will reach a leaf node where no more branching occurs. At the leaf node, the data point will be

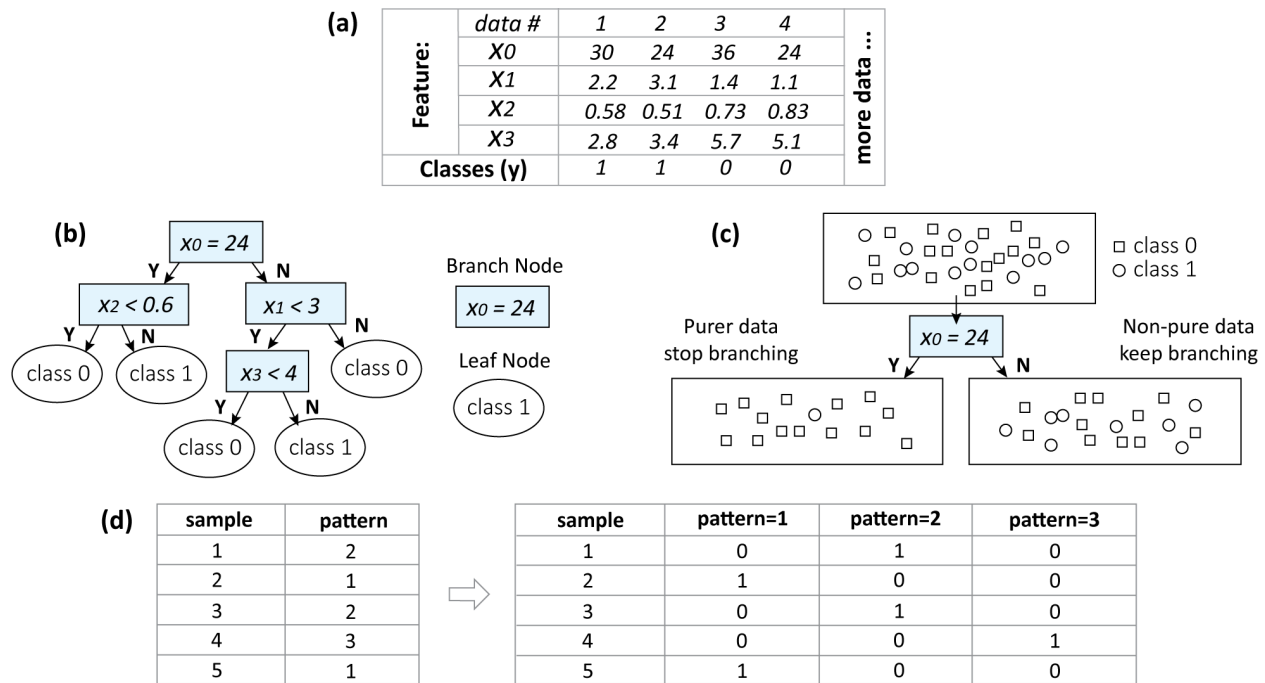


Figure 6.3: Decision tree method for solving supervised learning problems.

predicted as either class 0 or class 1. As shown, the internal structure of a decision tree method is highly interpretable.

The tree structure as well as the splitting rules are learned from the database automatically during the training process. Figure 6.3 (c) introduces a traditional greedy method to train a decision tree [Breiman et al., 1984]. The algorithm will generate the branch node one after another starting from the root node, and the algorithm will try to obtain purer sub-databases after creating the split. The purity of the data can be measured using the cross-entropy index and a purer database will have a smaller cross-entropy. With this index, the tree algorithm will enumerate different splitting rules to find the one that produces two sub-databases with smaller cross-entropy values after the split. The algorithm will keep generating new splits until the new sub-database is pure or when the tree reaches the maximum depth. At this point, a leaf node is generated and the class prediction is determined using the majority class of the data points within that node.

Although the formulation of the decision tree algorithm can naturally support the use of categorical data features, most implementation packages (e.g. the sklearn package [Buitinck et al., 2013]) do not support categorical features directly and treat all features as continuous. Consider having a categorical feature called “type of origami pattern”  $m = \{1, 2, 3\}$ , which is used to represent three different origami patterns. Clearly,  $m = 2$  and  $m = 3$  shall not happen at the same time. However, if the machine learning does not treat  $m$  as categorical, it can produce decision

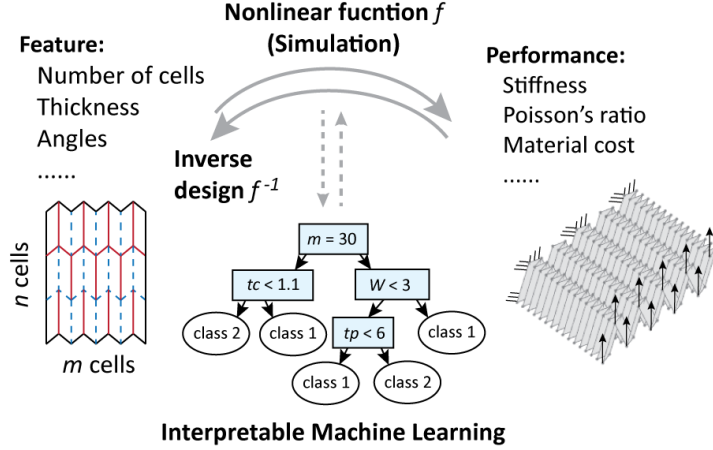


Figure 6.4: Using interpretable machine learning to compute design rules from origami design.

rules like “pattern  $m \geq 0.5$ ”, which has no physical meaning. To resolve this, a technique called one-hot encoder can be used. Figure 6.3 (d) explains how the encoder works. Basically, the categorical variable pattern  $m$  ( $m = \{1, 2, 3\}$ ) is converted to three different true-false binary variables as “ $m = 1$ ”, “ $m = 2$ ”, and “ $m = 3$ ”, each can take values of 1 for being true or 0 for being false. With this formulation, the machine learning will not produce unreasonable rules like “pattern  $m \geq 0.5$ ” and can treat  $m$  as categorical.

## 6.2 Computing Inverse Design Rules with the Tree Method

Before introducing the proposed inverse design method, we shall first revisit the main idea of origami design and inverse design conceptually. The design of origami can be thought of as creating a nonlinear function  $f$  (simulation) to calculate the performance indices (such as stiffness, Poisson’s ratio, material cost, etc.) based on the design features (such as number of origami cells, thickness of materials, sector angles of patterns, etc.). This is represented conceptually in Fig. 6.4 and in Eqn. 6.1. Therefore, understanding origami design means understanding how this nonlinear function  $f$  (simulation) behaves. Traditionally, this is done by deliberately picking a set of numbers for the features and calculating the associated performances using simulation methods [Ma et al., 2018b, Biswas et al., 2020, Xia and Wang, 2019, Fang et al., 2018, Li and Wang, 2015]. By plotting the relationships between the features and the performances based on these deliberately generated data points, one can understand the design rules embedded in this nonlinear function.

Unlike design, the inverse design tries to find an inverse function  $f^{-1}$  so that we can calculate the feature values for certain performance target. In general, this inverse function  $f^{-1}$  does not have a mathematically robust definition because a target performance can be achieved with

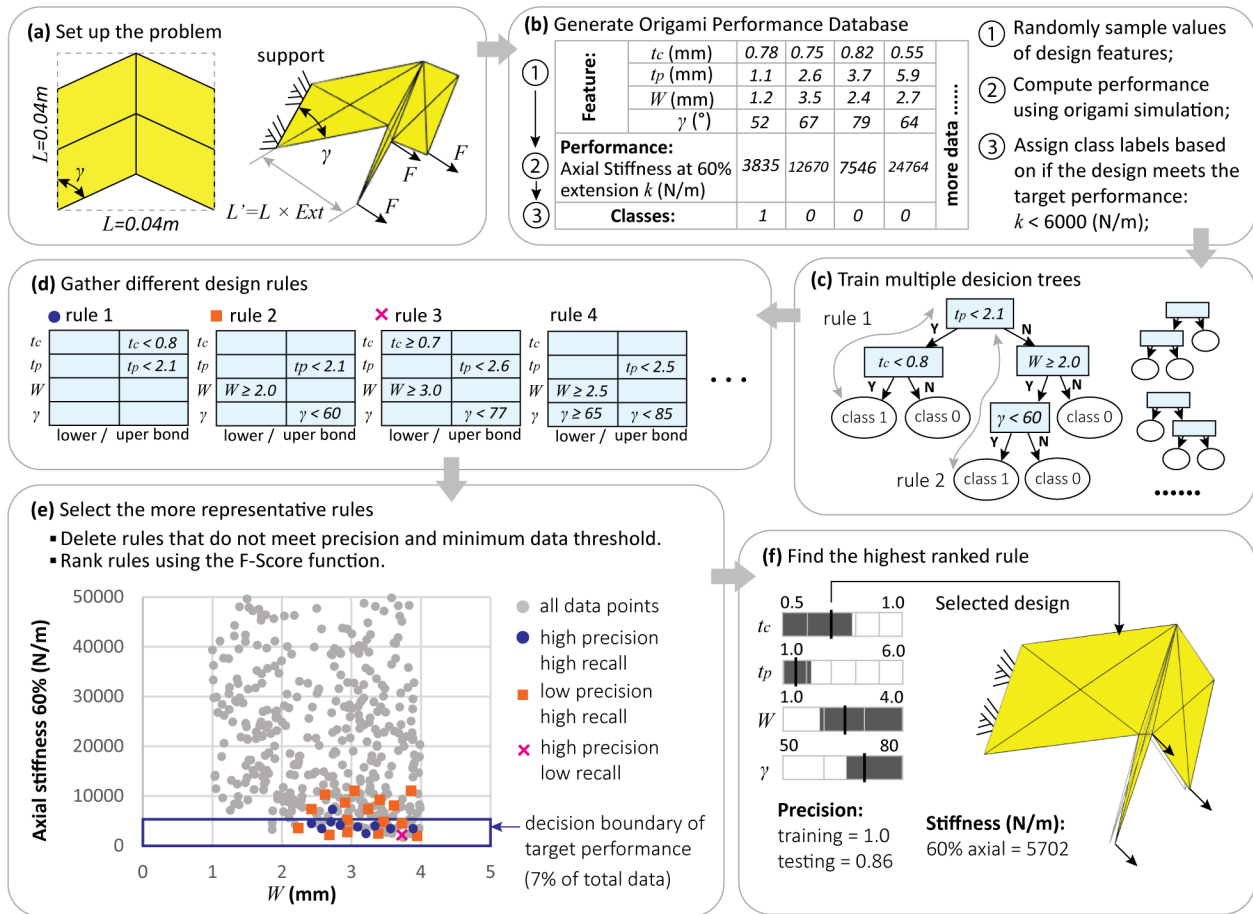


Figure 6.5: A detailed framework for pattern selection and feature design of origami.

multiple combinations of design features. However, understanding this inverse function as some relationship to calculate design features based on target performance is still a powerful idea. Traditional machine learning methods can only approximate the nonlinear function  $f$  without showing us how to reconstruct an approximation of the inverse function  $f^{-1}$  so they are not suitable for the inverse design problem. However, with interpretable machine learning, it is possible to reconstruct this inverse function to resolve the inverse design problem, because of the high interpretability.

Figure 6.5 shows a flowchart of the proposed methodology. In the following subsections, we use an example on the design of Miura origami cell to explain the proposed method. In this demonstration example we want to design the Miura origami cell to have a stiffness  $k$  that is smaller than 6000 N/m (see Fig. 6.5 (a)) and the design features include the sector angle ( $\gamma$ ), the thickness of panels and creases ( $t_c$  and  $t_p$ ), and the width of the creases ( $W$ ).

## 6.2.1 Generate origami performance database

To generate the origami performance database, we randomly sample values of the design features to first form the feature database (step number 1 in Fig. 6.5 (b)). We first determine the practical ranges of the design features based on fabrication considerations or other limits. In this example, we set  $0.5\text{mm} \leq t_c \leq 1.0\text{mm}$ ,  $1.0\text{mm} \leq t_p \leq 6.0\text{mm}$ ,  $1.0\text{mm} \leq W \leq 4.0\text{mm}$   $50^\circ \leq \gamma \leq 80^\circ$ . Next, we randomly generate different values for these design features to create the data points. For example, one column in the table on Fig. 6.5 (b) is associated with one data point.

After generating the feature data points, we can compute the performance of these different design realizations using origami simulation methods (step number 2 Fig. 6.5 (b)). We will use the simulation platform developed in the Chapter 3, Chapter 4, and Chapter 5 to execute the simulation. The simulation codes used to build this database and the other databases used in this work can be found in the following link: <https://github.com/zzhuyii/GenerateOrigamiDataSet>.

After the above two steps, we obtained an origami database with both features and performances. Finally, we can assign class labels to the data point based on if it meets the target performance or not, as demonstrated in the step number 3 on Fig. 6.5 (b). For example, suppose we are interested in having an origami unit cell with  $k < 6000\text{N/m}$ , we can assign a label 1 to those data points that meet the target and a label 0 to the rest.

## 6.2.2 Train decision trees to obtain design rules

After labeling the data points, we apply the decision tree-random forest method to learn the underlying structures of the database. The design features and the class labels are used to train the tree method to differentiate those designs that meet the target performance (with class label 1) from those that do not (with class label 0). Figure 6.5 (c) shows a sample decision tree for the design problem of Miura unit cells. Assume that we have an origami data point, we can determine its class by sending this data point into the tree from the top. Each time the data point flows into a branch node, a simple criterion is checked to further determine if the point should go the left or go to the right. For example, suppose a design data point with  $t_p = 1.1$  flows into the first node, it will be sent to the left branch according to the sample tree shown on Fig. 6.5 (c). After a series of judgements, the data point will be sent to a leaf node, where there is no more branching and a class label is predicted. For example, the data point listed in the column one of table in Fig. 6.5 (b) will follow the gray arrow marked as “rule 1” and be judged as a class 1 data. This means that the machine learning algorithm thinks the feature design in column one is most likely to produce a canopy that meets the performance target (stiffness  $k$  smaller than 6000 N/m) because the feature design value matches the rule:  $t_p < 2.1\text{mm}$  and  $t_c < 0.8\text{mm}$ . As demonstrated in this simple problem, the high interpretability of decision tree-random forest method gives us the capability of constructing the

inverse function  $f^{-1}$  easily. We can track the splitting criteria associated with class 1 data and the produced design rules (e.g. the rule 1:  $t_p < 2.1mm$  and  $t_c < 0.8mm$ ) will give us an approximation of this inverse function  $f^{-1}$ .

In practice, we will also train multiple decision trees to get more potential design rules. This can be done using randomly created sub-databases to train the decision trees, which creates an ensemble version of the decision tree method called random forest. After training multiple decision trees, we can gather more potential design rules as shown in Fig. 6.5 (d).

### 6.2.3 Select design rules with better precision

Now that we have a number of potential design rules, we need to select those with better performances. Figure 6.5 (e) illustrates two important aspects for selecting the better rules. First, a design rule should have high *precision*, which means that the data points that match the design rule should indeed meet the target performance. The *precision* index is a commonly used criterion for checking this aspect and it is defined as the ratio between the number of accurate predictions of class  $k$  over the number of all predictions of class  $k$  [Tharwat, 2020]. For example, the rule 1 marked with blue dots in Fig. 6.5 (e) has 9 correct predictions of class 1 and a total of 10 predictions of class 1 so it has a precision of 0.9. In addition to the precision, we also want the design rules to be statistically robust and span the target performance boundary as much as possible. There are two common ways of checking this: using the total number of data that meet the rules (which is the denominator of precision) and using the recall index. The recall is defined as the accurate predictions of class  $k$  over the number of all class  $k$  data [Tharwat, 2020]. Suppose we have a total number of 30 data points in the target zone, the rule 1 will have a recall of 0.3 (which is 9/30). In general, our target is to find rules that have higher precision and recall values. For instance, among the three sample rules shown on Fig. 6.5 (e), the rule 1 marked with the blue dot is better than the rule 2 and rule 3 marked with orange square and pink cross respectively.

In this work, we use the following routine to select the better design rules. First, two thresholds are used to remove design rules with bad performances: the precision of rules need to be greater than 0.9 and the design rule should contain a number of data points that is more than a minimum value of 10. After this elimination step, we rank the rules using the F-score function [Tharwat, 2020]:

$$F_{\beta} = (1 + \beta^2) \left( \frac{\text{precision} \cdot \text{recall}}{\beta^2 \cdot \text{precision} + \text{recall}} \right). \quad (6.2)$$

This F-score function creates an average score from both the precision and recall value, where the recall is seen as  $\beta$  times more significant as the precision value. In this work, we select a value of  $\beta = 0.2$ , so the precision is five times more significant than the recall. Focusing more on the



precision is reasonable for an inverse design problem, where the goal is to find “some designs” to meet the target performance not “all designs” to meet the target performance.

Finally, we can select the rules with the highest F-score after ranking them. Figure 6.5 (f) shows the top design rule that can be used to build an Miura origami cell with axial stiffness  $k < 6000(N/m)$ . In this example, the machine learning thinks that having  $t_c < 0.78mm$ ,  $t_p < 2.2mm$ ,  $W \geq 1.9mm$ , and  $\gamma \geq 67^\circ$  will give us a Miura unit cell that meets the performance target. In practice, we can compute more than one rules or reuse the database for other design targets. We will demonstrate these capabilities in the remainder of this chapter.

## 6.2.4 Hold out testing and hyperparameter selection

After picking the better design rules, we need to further test the rules to see how well they behave. This testing can be done by checking the *precision* of the rules using another testing database that is not used during the training. This is a common technique in machine learning called hold-out testing, where a portion of the data is hold out from the training process and only used in testing.

Figure 6.6 shows the setup of the hold out testing. In this work, the complete database is randomly split into two sets: one with 60% of the data for training the machine learning, and the other one with 40% of data for testing the performance. Moreover, we will use random sub sets of the entire training data to train different decision trees. The number of data points used in these random sub sets is determined using the “subset ratio”. With this approach, drastically different decision trees can be obtained because different random data sets are used to train them. In general, hold out testing is like creating two sets of questions: one for training the students, and the other for testing if how well the students learned from the training set of questions. Figure 6.5 (f) further shows the precision score of the computed design rules, and a high precision is obtained.

Hyperparameters refer to the variables in the machine learning algorithm that are explicitly specified by the users and are not learned from the training data. Usually, a grid search is performed to find the optimal hyperparameter values for the machine learning algorithm. In this work, we need to consider five variables and they are (1) the maximum depth of the trees, (2) the number of tree learners in the forest, (3) the cost-complexity pruning alpha value, (4) the criterion for splitting rules, and (5) the subset ratio for training. The testing precision of the final design rule is used to assess the selections of these hyperparameters. Five runs of hold out testing with different training-testing partition are implemented and the mean precision is recorded. Because the depths of trees and the number of tree trainers are the two major hyperparameters of a decision tree-random forest method, we mainly focus on the effects of these two values while briefly highlighting the others. In addition to the grid search results, we also trained two other machine learning algorithms for comparison, namely the kNN method, and Gradient Boosting method. The kNN method is usually

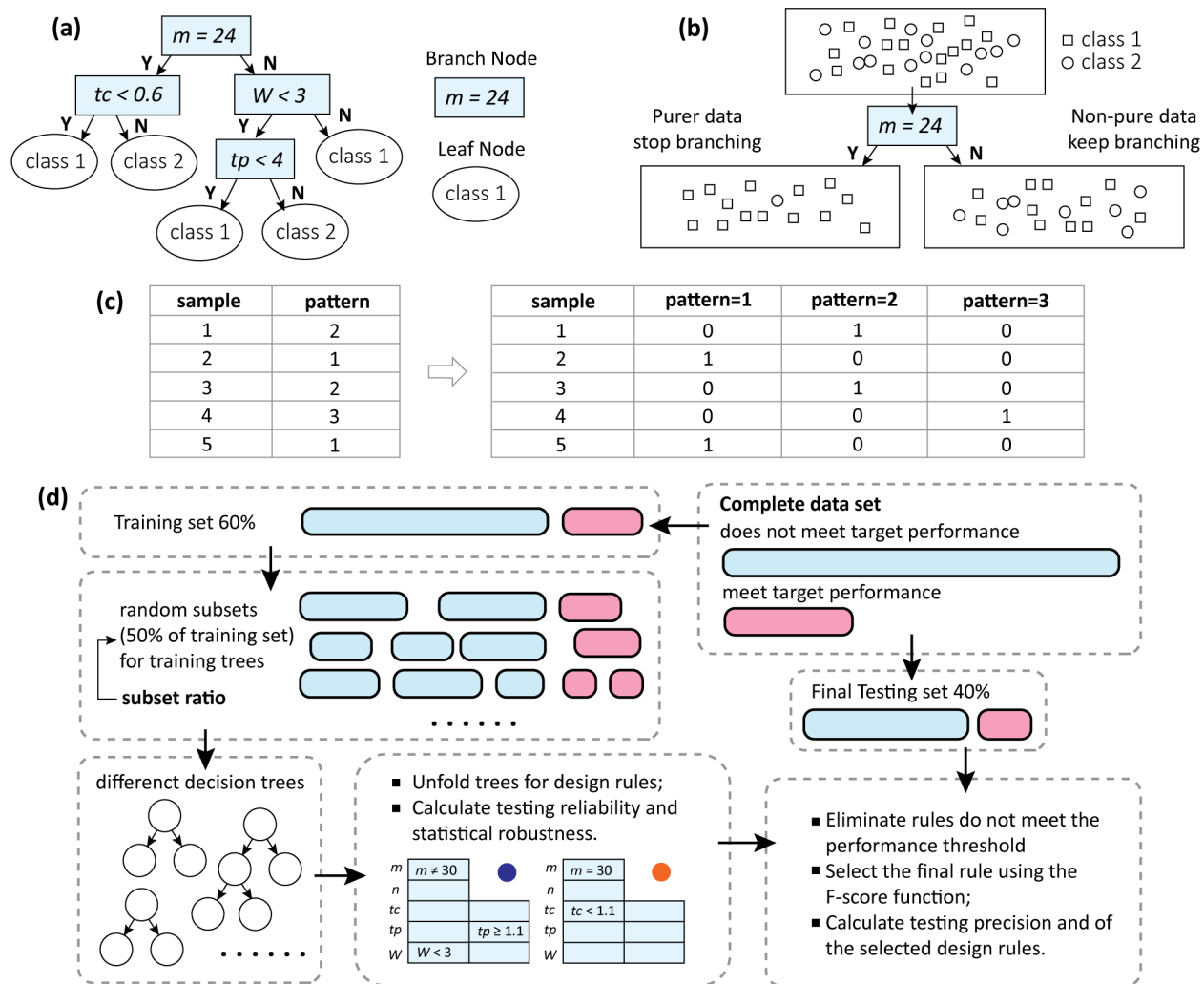


Figure 6.6: (a) Introduction of decision tree method. (b) Training a decision tree. (c) Using the one-hot encoder to convert categorical data. (d) Hold out testing setup.

used as a baseline method in machine learning because it has a simple formulation. In general, we expect the precision obtained from the target method to be superior to that obtained using the kNN method. The Gradient Boosting method is a “black box” machine learning method that tends to perform well on many databases. If the target method can achieve a testing precision that is close to that from the Gradient Boosting, the target method can be seen as competitive.

We perform grid searches using the three main databases built in this work. These three databases are the origami canopy database, the origami gripper database, and the origami arch database. We will introduce the details on these three databases later but focus on the hyperparameter selection for now. First, we give a brief discussion on the influence of the maximum depth of trees and the number of trees. We can see from Fig. 6.7 to 6.9 that there is a saturation effect

**Origami Canopy (60% bending stiffness < 15000 N/m; 90% axial stiffness < 150000 N/m; 700 N/m < 90% bending stiffness < 1600 N/m;)**

Precision of kNN: 0.639; Precision of Boosting: 0.748

**ccp\_alpha = 0.0001**

tree number	20	40	60	100	200
depth=8	0.837	0.769	0.769	0.913	0.910
depth=12	0.848	0.826	0.929	0.933	0.911
depth=16	0.848	0.826	0.927	0.933	0.913
depth=20	0.848	0.826	0.927	0.933	0.913
depth=24	0.848	0.826	0.927	0.933	0.913
depth=28	0.848	0.826	0.927	0.933	0.913
depth=32	0.848	0.826	0.927	0.933	0.913

**ccp\_alpha = 0.0005**

tree number	20	40	60	100	200
depth=8	0.837	0.769	0.769	0.913	0.910
depth=12	0.848	0.826	0.929	0.933	0.911
depth=16	0.848	0.826	0.927	0.933	0.913
depth=20	0.848	0.826	0.927	0.933	0.913
depth=24	0.848	0.826	0.927	0.933	0.913
depth=28	0.848	0.826	0.927	0.933	0.913
depth=32	0.848	0.826	0.927	0.933	0.913

**ccp\_alpha = 0.001**

tree number	20	40	60	100	200
depth=8	0.837	0.769	0.769	0.913	0.910
depth=12	0.848	0.826	0.929	0.933	0.911
depth=16	0.848	0.826	0.927	0.933	0.913
depth=20	0.848	0.826	0.927	0.933	0.913
depth=24	0.848	0.826	0.927	0.933	0.913
depth=28	0.848	0.826	0.927	0.933	0.913
depth=32	0.848	0.826	0.927	0.933	0.913

**ccp\_alpha = 0.002**

tree number	20	40	60	100	200
depth=8	0.774	0.610	0.622	0.798	0.923
depth=12	0.798	0.826	0.929	0.929	0.962
depth=16	0.798	0.826	0.929	0.929	0.937
depth=20	0.798	0.826	0.929	0.929	0.937
depth=24	0.798	0.826	0.929	0.929	0.937
depth=28	0.798	0.826	0.929	0.929	0.937
depth=32	0.798	0.826	0.929	0.929	0.937

Precision value is average of 5 run with different random training set

Figure 6.7: Grid search results for the canopy database.

in the maximum depth of trees. The precision first improves when increasing the maximum depth but stops once the maximum depth reaches certain values. This saturation is expected because if the tree-based learners are too deep, the leaf nodes will just have one or two data points, which is seen as “pure” by the algorithm. In this case, further increasing the depth of trees will not change the tree structure. Moreover, branches with just one or two data points are not representative and cannot be used to compute reliable design rules. Therefore, it is recommended to set the depth of trees such that the algorithm barely reaches the saturation point. In this work, we select a depth of 20. For the number of tree trainers in the forest, we found a similar trends. A relatively large number of tree trainer is helpful for improving the precision, but the precision can saturate once the number is too large. This saturation happens because we are “close to enumerate” all possible formulations of tree branches when using a large number of tree trainers. In this case, further adding in tree trainers may not produce new high performance branches. Thus, a value of 100 is picked for the number of trainers in this work.

With the canopy database shown in Fig. 6.7, we further study the effects of the cost-complexity-pruning alpha (ccp-alpha) value. The cost-complexity-pruning is another step in training the decision tree where the machine learning method will automatically remove some branch nodes from a tree to avoid over-fitting. In general, the larger the alpha value is, the more likely the algorithm will remove nodes. As demonstrated in Fig. 6.7, the pruning alpha value does not have a significant influence on the precision of our prediction, and increasing the alpha value does not improve the

**Origami Gripper (10Hz < frequency; heating power < 0.7W; maximum temperature < 500°C; 0.0015 N/m < stiffness)**

Precision of kNN: 0.413; Precision of Boosting: 0.753

gini (minData=5)						entropy					
tree number	20	40	60	100	200	tree number	20	40	60	100	200
depth=8	0.469	0.601	0.601	0.603	0.590	depth=8	0.796	0.816	0.843	0.829	0.846
depth=12	0.710	0.863	0.842	0.842	0.807	depth=12	0.816	0.815	0.828	0.850	0.860
depth=16	0.771	0.818	0.840	0.836	0.803	depth=16	0.816	0.815	0.828	0.844	0.874
depth=20	0.830	0.837	0.849	0.836	0.803	depth=20	0.816	0.815	0.828	0.844	0.874
depth=24	0.830	0.819	0.819	0.806	0.803	depth=24	0.816	0.815	0.828	0.844	0.874
depth=28	0.830	0.819	0.819	0.806	0.803	depth=28	0.816	0.815	0.828	0.844	0.874
depth=32	0.830	0.819	0.819	0.806	0.803	depth=32	0.816	0.815	0.828	0.844	0.874

Precision value is average of 5 run with different random training set

Figure 6.8: Gird search results for the gripper database.

precision for all cases. Therefore, this work uses a ccp-alpha value of 0.0001 in all the training performed.

Next, we study the splitting criterion used to separate data points. The sklearn package provides two different splitting criteria and they are the Gini index and the entropy index. The Gini index is similar to the entropy but is computed differently [Buitinck et al., 2013]. From Fig. 6.8 we see that entropy tends to provide better performance than the Gini index, so the entropy index is used in this work.

With the origami arch database, we further consider the effects of the subset ratio. To train an effective random forest algorithm, different decision trees need to be built [Breiman et al., 1984]. One way of achieving this goal is to use a randomly generated subset of training data to train the decision trees instead of using the entire training data set. The subset ratio is the ratio between the size of this sub dataset when compared to the entire training dataset. We can see from Fig. 6.9 that a smaller subset ratio can improve the performance of the machine learning algorithm. This is expected because a smaller subset ratio can encourage the algorithm to generate more different trees so that we have a larger likelihood to capture better tree branches. Thus, we select a subset ratio of 0.5 in this work. We did not explore the potential of having an even smaller subset ratio value because that will make the training set too small.

### 6.3 Handling Categorical Features for Comparing Different Patterns

The single unit Miura origami example shown on Fig. 6.5 demonstrates the basic formulation of the proposed methodology. In the following sections, we will show how this methodology can be extended to handle the categorical features and multi objective problems for a holistic origami inverse design. We will start with the categorical features.

**Origami Arch (Zstiff > 800 N/m; Xstiff > 600 N/m; error < 0.1;)**

Precision of kNN: 0.218; Precision of Boosting: 0.906

subset ratio: 50%						subset ratio: 60%					
tree number	20	40	60	100	200	tree number	20	40	60	100	200
depth=8	0.898	0.915	0.915	0.935	0.872	depth=8	0.842	0.875	0.881	0.881	0.849
depth=12	0.862	0.911	0.911	0.911	0.827	depth=12	0.888	0.843	0.814	0.814	0.815
depth=16	0.862	0.911	0.911	0.911	0.805	depth=16	0.888	0.843	0.814	0.814	0.815
depth=20	0.862	0.911	0.911	0.911	0.805	depth=20	0.888	0.843	0.814	0.814	0.815
depth=24	0.862	0.911	0.911	0.911	0.805	depth=24	0.888	0.843	0.814	0.814	0.815
depth=28	0.862	0.911	0.911	0.911	0.805	depth=28	0.888	0.843	0.814	0.814	0.815
depth=32	0.862	0.911	0.911	0.911	0.805	depth=32	0.888	0.843	0.814	0.814	0.815

subset ratio: 70%						subset ratio: 80%					
tree number	20	40	60	100	200	tree number	20	40	60	100	200
depth=8	0.895	0.832	0.832	0.843	0.826	depth=8	0.861	0.905	0.856	0.896	0.905
depth=12	0.828	0.814	0.814	0.811	0.808	depth=12	0.843	0.830	0.867	0.836	0.843
depth=16	0.828	0.814	0.814	0.822	0.808	depth=16	0.843	0.830	0.877	0.836	0.843
depth=20	0.828	0.814	0.814	0.822	0.808	depth=20	0.843	0.830	0.877	0.836	0.843
depth=24	0.828	0.814	0.814	0.822	0.808	depth=24	0.843	0.830	0.877	0.836	0.843
depth=28	0.828	0.814	0.814	0.822	0.808	depth=28	0.843	0.830	0.877	0.836	0.843
depth=32	0.828	0.814	0.814	0.822	0.808	depth=32	0.843	0.830	0.877	0.836	0.843

Precision value is average of 5 run with different random training set

Figure 6.9: Gird search results for the arch database.

Comparing different origami patterns is difficult because categorical variables are needed to represent different origami patterns. However, common optimization-based origami inverse design methods cannot handle these categorical features. Because of this limitation, existing origami inverse design methods are developed based on specific origami patterns [Dudte et al., 2016, Dang et al., 2022]. For example, the shape fitting algorithm developed in the work by Dudte et. al. is based on just one generalized Miura origami pattern [Dudte et al., 2016]. The proposed interpretable machine learning based methodology can be used to resolve this challenge because the decision tree-random forest method can handle categorical features naturally.

In this section, we will study a design problem on origami canopy as shown in Fig. 6.10. In this study, an origami canopy is cut out from a thin square plate with a footprint of  $0.2m \times 0.2m$ . Two different patterns are studied, and they are the standard Miura-origami pattern (Pattern 1) and the Tachi-Miura Polyhedron (TMP) [Yasuda and Yang, 2015] (Pattern 2). To represents the two patterns, an integer (binary) variable  $p = 1, 2$  is introduced. In addition, we further consider the situation where the two patterns can have different numbers of unit cells in them. The numbers of unit cells are represented as  $m$  and  $n$  in the two directions. In addition to these categorical features, three continuous design features are also added to the problem, and they are the thickness of panels  $1.0mm < t_p < 6.0mm$ , the thickness of creases  $0.5mm < t_c < 1.0mm$ , and the width of creases  $1.0mm < W < 4.0mm$ . An origami database is populated by randomly sampling values of these design features, and the database contains 2000 Miura origami samples and 2000 TMP

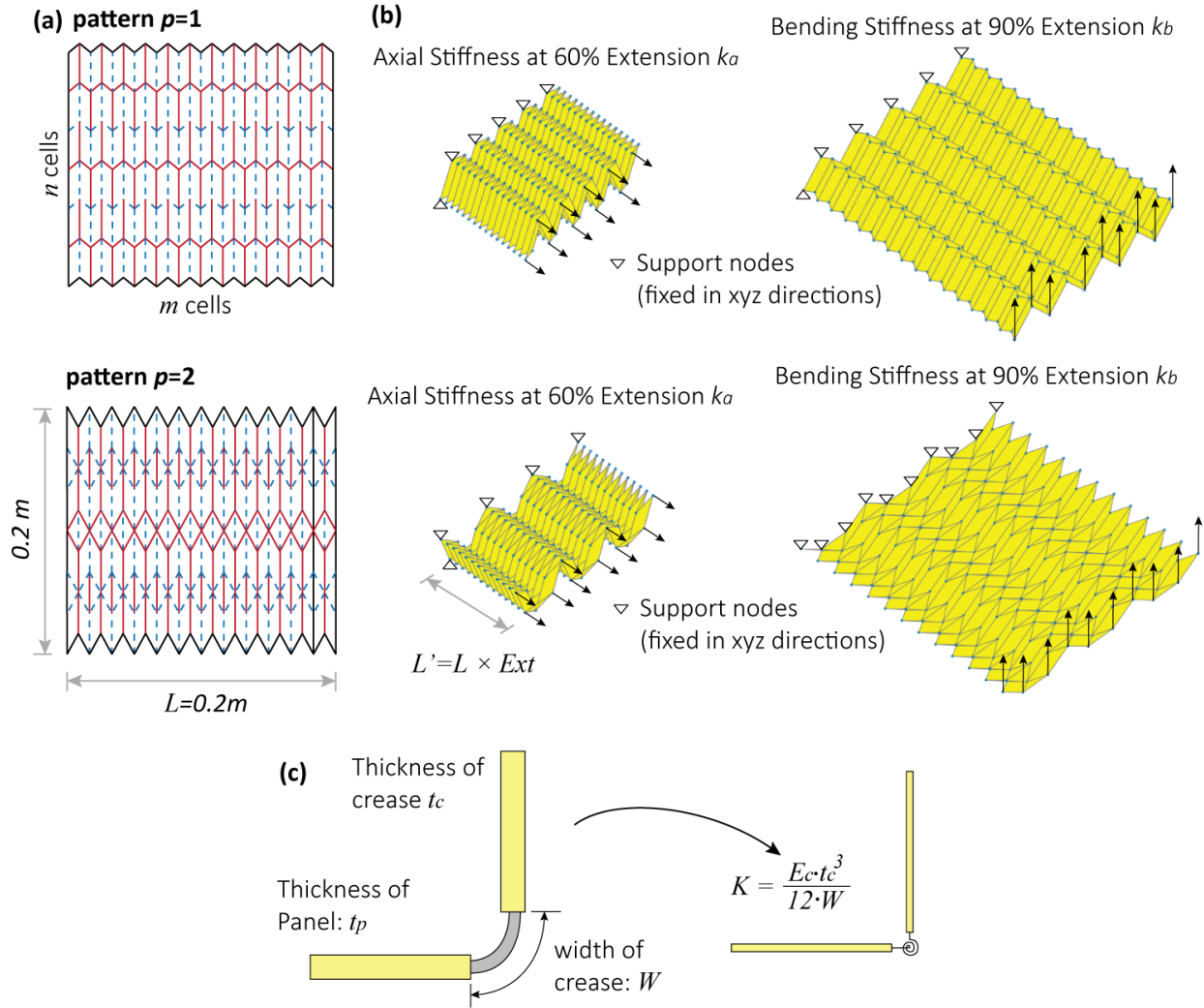


Figure 6.10: Building the origami canopy database.

origami samples. In this example, we will design for two targets, and they are the axial stiffness  $k_a$  at 60% extension and the bending stiffness  $k_b$  at 90% extension. The extension ratio ( $Ext$ ) is measured as the ratio between the folded length of the pattern and the flat length of the pattern.

We first study the design for axial stiffness  $k_a$  at 60% extension (see Fig. 6.11 (a)). Assume that we want to design an origami canopy to have  $15000\text{ N/m} < k_a < 30000\text{ N/m}$  (Zone a1), we can use the procedure in Fig. 6.5 to compute the design rules for this target. The computed design rule is shown in the left column of Fig. 6.11 (a). We can then repeat the process for the other three targets  $30000\text{ N/m} < k_a < 50000\text{ N/m}$ ,  $50000\text{ N/m} < k_a < 80000\text{ N/m}$ ,  $15000\text{ N/m} < k_a$ . This divides the data into four design target zones, and the computed rules for all four targets are shown in Fig. 6.11 (a). The training precision, testing precision, and sample realizations are also provided in Fig. 6.11. This series of results shows how we can design for an origami canopy to have increasingly stiffer

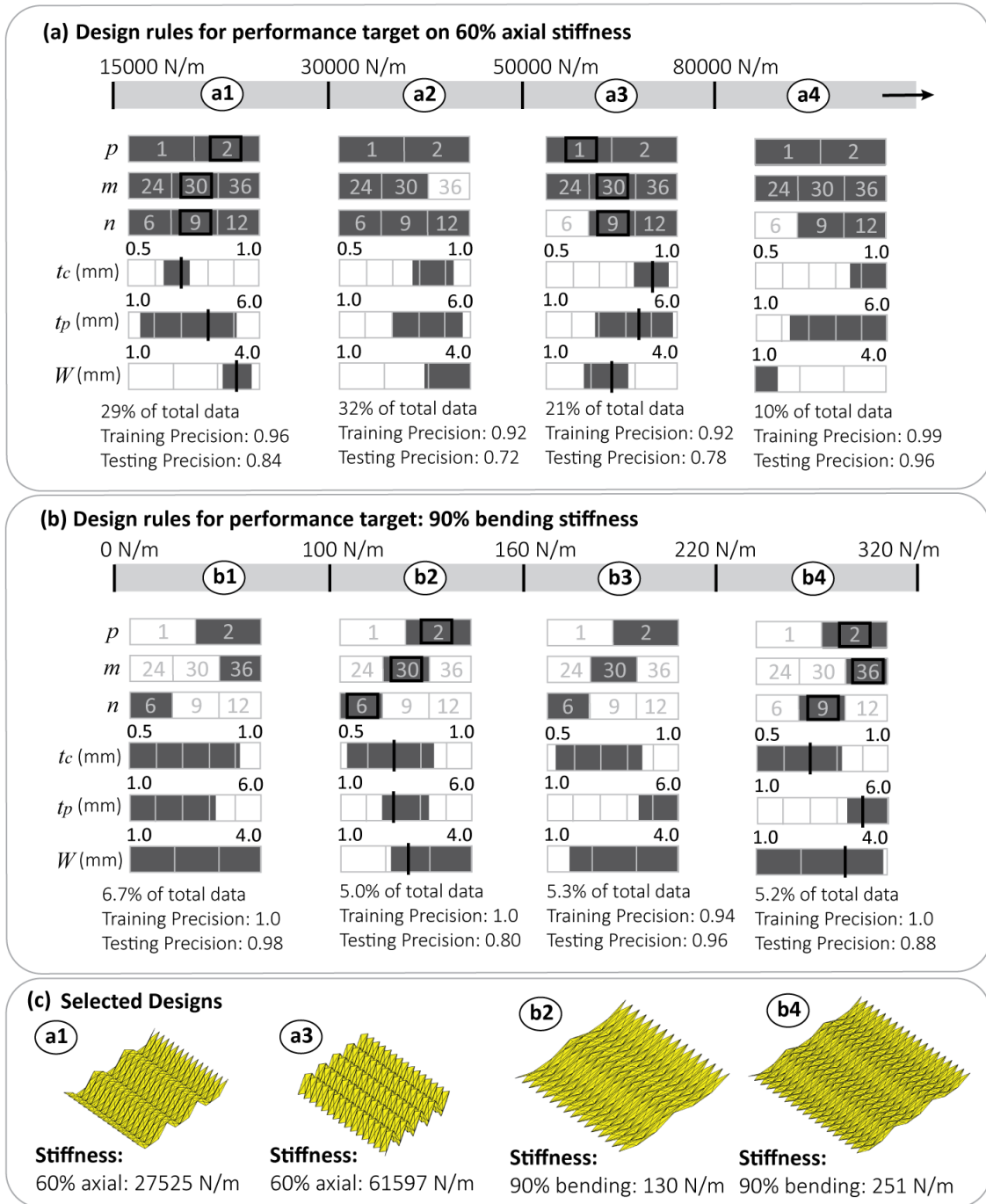


Figure 6.11: Design rules computed for the canopy database.

behaviors in axial compression. Interestingly, the machine learning method prefers changing the continuous variables to achieve the different stiffness targets in the axial compression. More specifically, the machine learning method thinks that controlling the thickness of creases and the width of the creases are more significant than other parameters because tighter thresholds are used for the two features.

However, the design rules can be very different when we study the 90% bending stiffness. We repeat the same process of labeling the data and computing the rules for 90% bending stiffness. Similarly, four design rules are computed for four different target zones as shown in Fig. 6.11 (b). When we investigate the result of this series of design rules, we can see that the machine learning method is paying more attention to the categorical features. As the target moves from one zone to another, the computed design rules change in a non-continuous manner because of the complex interactions between categorical variables and continuous variables. For example, when the target changes from Zone b2 to Zone b3 (stiffer target in 90% bending), the machine learning method indicates that increasing the thickness of panels is enough to achieve the target performance. However, when further increasing the requirement on bending stiffness (from Zone b3 to Zone b4), the machine learning method thinks it is better to change the categorical features and the continuous features simultaneously. A similar categorical jump is also observed when the target moves from Zone b1 to Zone b2. The proposed method can capture these complex interactions between the continuous features and categorical features, which are difficult to capture with optimization-based design methods. This capability allows us to compare different origami patterns while simultaneously designing for other continuous design features.

Moreover, this example highlights another advantage of using data science and machine learning method for solving origami design problems. Unlike optimization-based design methods, the database is reusable for different target performances. Thus, we can use the same database to design for different target performances (e.g. the different zones demonstrated in the example). This allows us to save computation time and design for functional origami efficiently.

## **6.4 Solving Multi-Objective Problems for Multi-Physical Performances**

Next, we want to show how the proposed methodology can tackle the multi-objective problems needed for handling multi-physical performance targets. In practice, the behaviors of functional origami structures are multi-physical so designing for these multi-physical performance targets will yield a multi-objective problem that is difficult to handle with common optimization based inverse design methods. Thus, in this section, we will use a sample design problem on functional origami gripper to demonstrate how the proposed method can handle multi-objective problems.

In this sample problem, functional origami grippers will be designed based on three candidate



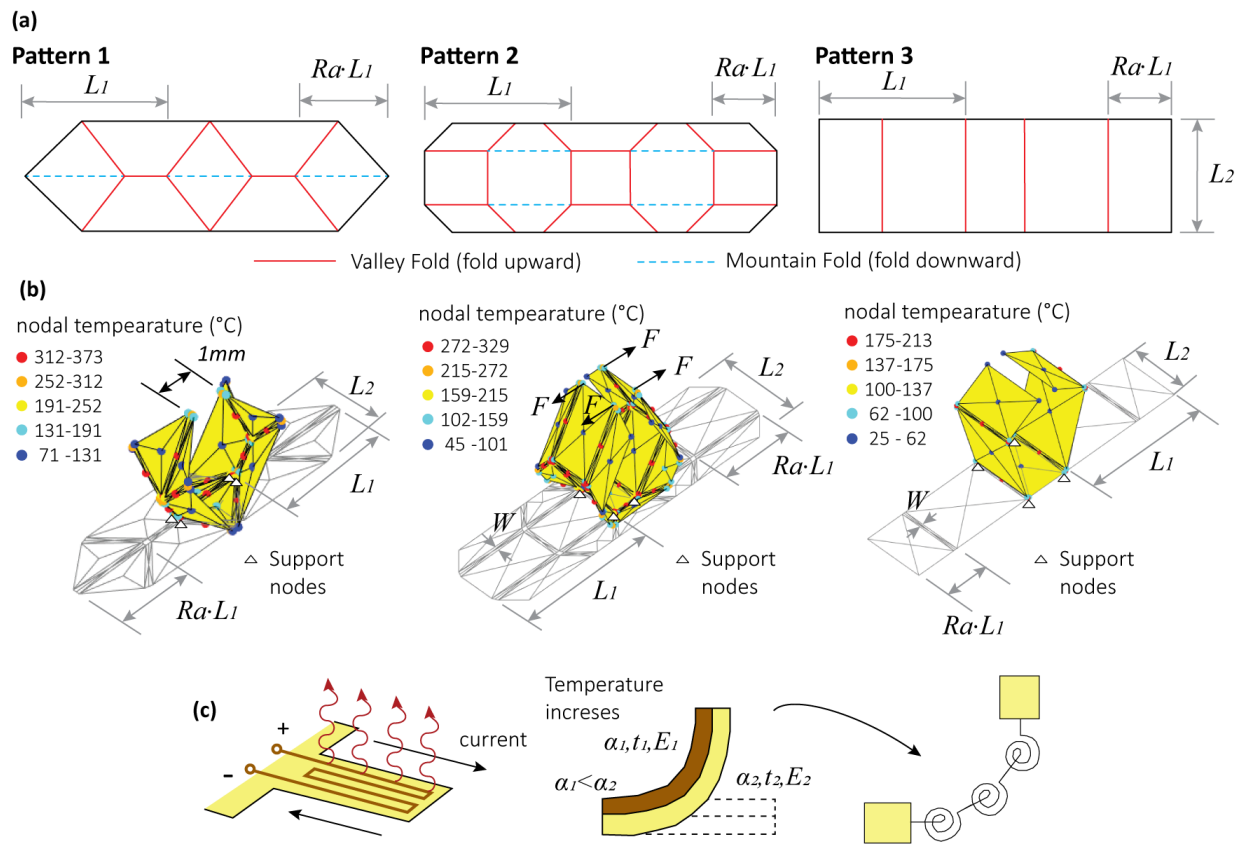


Figure 6.12: Building the origami gripper database.

origami patterns as shown on Fig. 6.12. To represent the three patterns, a categorical variable  $p = 1, 2, 3$  is used. Geometrical design features of the gripper include the length  $L_1$  and width  $L_2$  of the gripper arm and the location of the first hinge from base measured using  $Ra$ . Moreover, design features related to the actuator include thicknesses of the two material layers in the actuator  $t_1$  and  $t_2$  and the width of the actuator creases  $W$ . The actuator design used in this work is assumed to be similar to the electro-thermal actuator system proposed in Chapter 2. The bi-layer actuator contains one active layer and one passive heater layer. When current is applied to the passive heater layer, Joule heating will heat up the bi-layer system. Then, because the active layer expands more than the passive layer, folding motions are generated (see right sub-figure on Fig. 6.12 (c)). We can build the origami performance database using the model from Chapter 5 because it captures the multi-physical behaviors.

Four indices are used to measure the performance of the origami gripper and they are: (1) fundamental frequency of the gripper  $freq$ , (2) input heating power for the gripper to close its gripping arm  $Q$ , (3) maximum nodal temperature of the gripper during the gripping motion  $T$ , (4) stiffness to ply open the gripper  $k$ . These four indices contain information regarding the dynamic, thermal, and mechanical behaviors of the gripper. Simultaneously designing for these four performance targets will form a multi-objective problem that is difficult to solve using common optimization techniques. Here, show that the proposed inverse design method can handle problems like this.

Basically, the flexibility in labeling data when using machine learning methods allows us to handle the multi-objective problems easily. We can label those data that meet the target performance to have a label 1 regardless of the dimensions of the objective. For example, suppose we want to simultaneously design an origami gripper to have the following performance target:  $10Hz < freq < 40Hz$ , heating power  $Q < 0.2W$ , and maximum temperature  $T < 200^\circ C$  (Target 1). We can just label those data points that satisfy the performance target to be Class 1 and label the rest of the data as Class 0. Then, by computing the more representative decision rules for Class 1, we can obtain an active origami that satisfy all three performance targets simultaneously.

Figure 6.13 (a) shows the computed design rules for this Target 1. In addition to the rule with the highest F-score, the second-highest rule is also computed and plotted in Fig. 6.13 (a). Interestingly, we can see that both rules have high precision and are similar to each other (except for a small difference in the selection of  $t_1$  and  $t_p$ ). Similarly, we can extend the results to simultaneously design for all four performance indices (Target 2: frequency  $10Hz < freq$ , heating power  $Q < 0.7W$ , and maximum temperature  $T < 500^\circ C$ , and stiffness  $0.002N/m < k$ ), and the result is presented in Fig. 6.13 (b). If we compare the computed rules for Target 2 with those for Target 1, we can see that the machine learning method has picked another pattern after adding in the stiffness requirement. This is because Pattern 3 selected for achieving Target 1 only has horizontal creases, which cannot provide additional stiffness compared to Pattern 2 selected for achieving

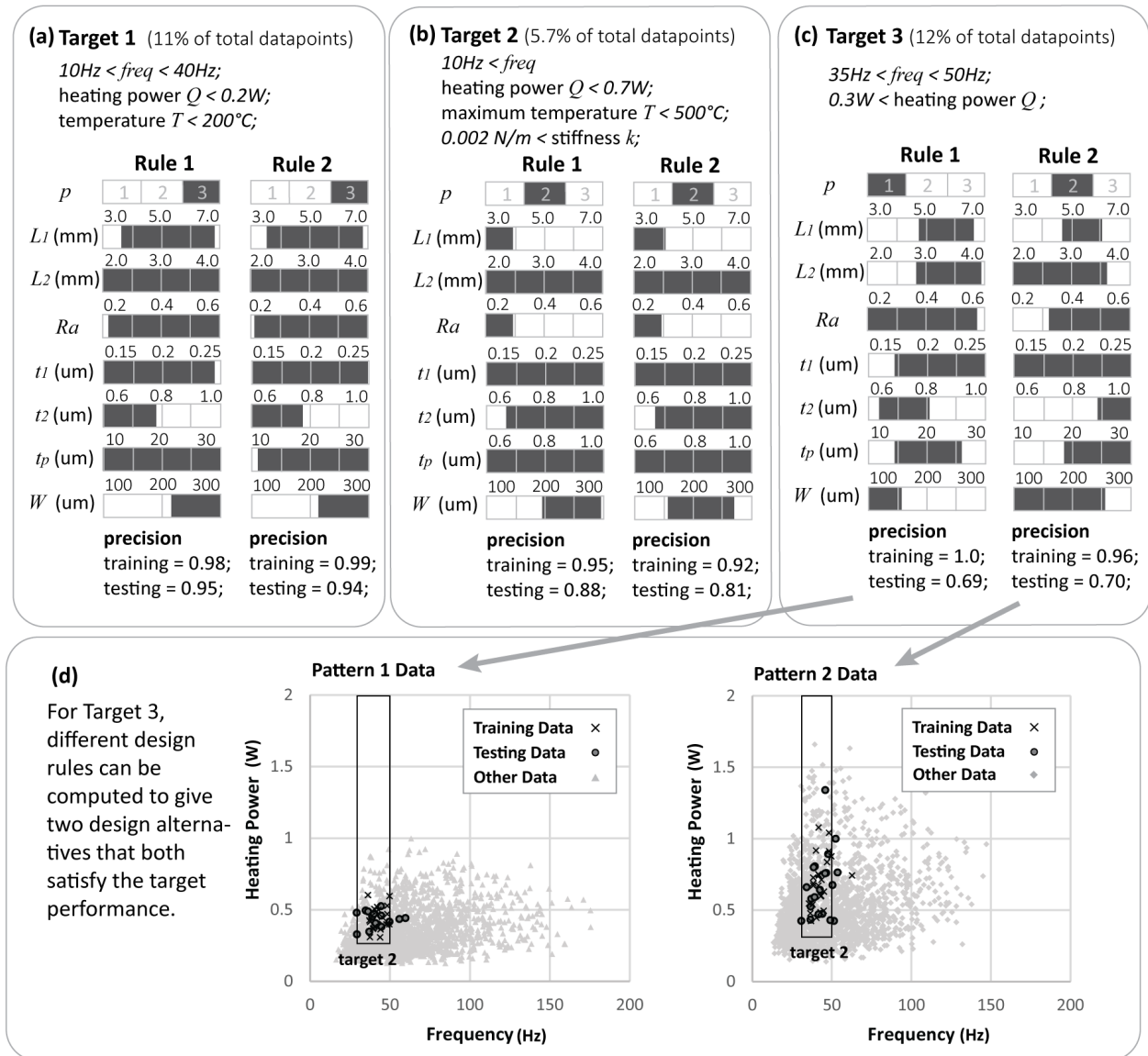


Figure 6.13: Design rules computed for the origami gripper database.

Target 2. This high interpretability of the tree methods helps users to better understand and reason about the behaviors of functional origami systems. Moreover, the machine learning method also demonstrates that the significant features can be different for different design targets. For example, controlling the values of the gripping arm length  $L_1$  and the location of the first creases (defined by  $Ra$ ) is only significant for Target 2.

In general, the two design rules with the highest F-score value tend not to be very different from each other. This is commonly seen especially when the machine learning method prefers selecting the same origami patterns for achieving a target performance. However, Fig. 6.13 (c) shows one interesting result where the two computed rules have relatively large differences between them because they are based on different patterns. For Target 2, the Rule 1 is computed based on Pattern 1 while the Rule 2 is computed based on Pattern 2. This is significant because it highlights that by computing multiple rules with high F-score rather than picking the one with the top rank, it is possible to find more flexible design rules to be chosen from. In addition, comparing the Rule 1 and Rule 2 for the Target 2 also reveals the complex interaction between the categorical features and continuous features in origami designs. Because the Target 2 is 2-dimensional, we further extract the data point that fits the rules in both the training dataset and the testing dataset and plot them in Fig. 6.13 (d). The result shows that the data points that fit the computed rules trace the design boundary nicely and fills the design boundary with reasonable coverage.

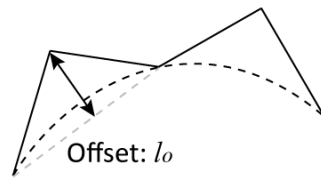
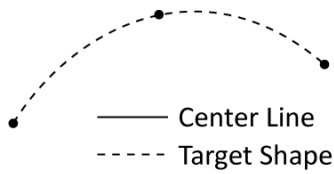
## 6.5 Enabling Holistic Origami Inverse Design

Finally, this section will show how the proposed method can enable existing origami shape fitting algorithms to achieve holistic origami inverse design. So far, there has been a number of studies on designing an origami system to fit a target geometry [Tachi, 2010a, Tachi, 2010d, Dudte et al., 2016, Lang and Howell, 2018, Chen et al., 2020]. Usually, the shape fitting problem can be constructed as an optimization and the error between the target geometry and the origami is minimized given certain constraints [Dudte et al., 2016, Dang et al., 2022]. However, these existing methods cannot consider other non-geometrical properties of origami structures that tend to be the final design targets. Moreover, these optimization schemes often leave tremendous flexibility for a designer to vary the origami pattern (e.g. number of panels used or maximum size of panels), without showing which combination can produce more superior performances. We will resolve these challenges in this section using the proposed method.

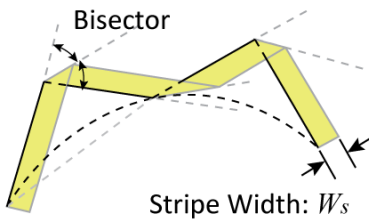
As a demonstration, we implement our method on top of an existing shape fitting approach introduced in [Dudte et al., 2016], where an analytical solution was derived to build Miura-origami strips to fit arbitrary planar curves. Figure 6.14 shows how this shape fitting method can generate different origami strips to fit a target planar curve. In this method, the target curves are first

**(a) Generate miura strip to fit arbitrary curve**

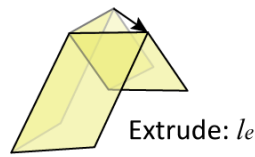
1. Create segments of a curve
2. Use offset to determine the center line of Miura Origami



3. Use width and bisector to determine the shape

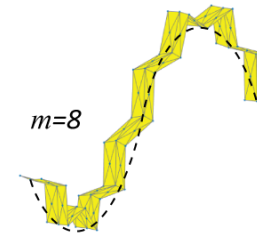


4. Extrude to form 3D geometry

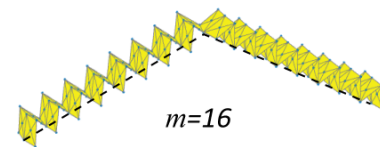


**(b) Generate differeng shapes**

sine function



roof top



**(c) Half circle arch shape**

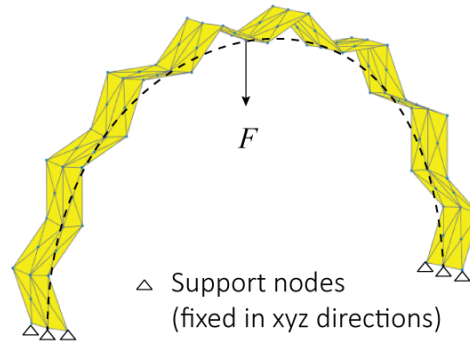
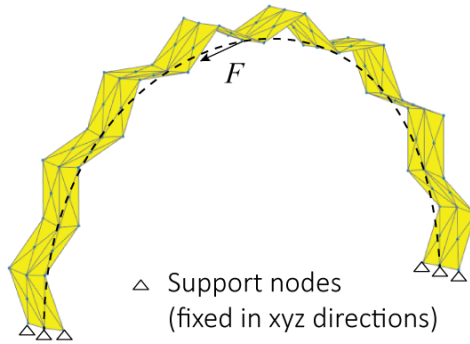


Figure 6.14: Populating the origami arch database using an origami shape fitting algorithm.

separated into different sections and the number of segments is measured by  $m$ . Then a planar origami strip geometry is generated by setting the offset length  $l_o$  of the center node and the width of the strip  $W_s$ . Finally, the 3D origami is created by extruding the planar geometry to form the Miura geometry with an extrusion  $l_e$ . Figure 6.14 also shows the shape fitting results for three different curves. As can be seen, there is great flexibility in selecting these parameters for shape fitting and the selection should depend on which combination can give the more desirable origami performances (which tend to be non-kinematical). Suppose our target is to build an origami structure that can achieve a given stiffness performance while fitting a half-circle arch shape, how should we select these shape fitting parameters? The proposed machine learning based method will be able to answer questions like this.

Without loss of generality, we will focus on designing a Miura-origami half-circle arch with a 2m radius. The origami arch database is generated by randomly picking shape fitting design features to build different arch geometries. These variables include the number of segments  $m$ , the offset length  $l_o$ , the strip width  $W_s$ , and the extrude dimension  $l_e$ . Other design features such as the thicknesses of panels  $t_p$  and creases  $t_c$  and the width of creases  $W$  are also included because they affect the stiffness of the arch. Based on the random set of design features, we compute and record the responses of the origami using the SWOMPS simulation package, and the database consists of 3000 data samples. The performance indices include the stiffness in X-direction  $k_x$  and Z-direction  $k_z$ , the error of shape fitting  $e$ , and whether the structure will snap under a 5 N load applied vertically  $S_z$  (see Fig. 6.15 (a)).

With the database established, we can apply the interpretable machine learning method to analyze the database for different targets and the results are shown on Fig. 6.15 (b). Moreover, we can demonstrate the trade-off between requirements on shape fitting errors and the mechanical performances of origami systems using the proposed method. The performance Target 1 on Fig. 6.15 (b) shows the computed design rules for a target with stricter stiffness requirement but less strict shape fitting target while the performance Target 2 has more relaxed stiffness requirement but stricter error target. The testing precision indicates that both rules are highly reliable and accurate. The result demonstrates that the machine learning method can produce different design rules to accommodate the trade-offs between the shape fitting error and mechanical performances. More significantly, we want to point out that the proposed machine learning based method is not tied to specific origami patterns or shape fitting methods, and thus the method can be combined with other origami shape fitting method (such as those in [Tachi, 2010a, Tachi, 2010d, Dudte et al., 2016, Lang and Howell, 2018, Chen et al., 2020]) to further consider other non-geometrical origami behaviors.

Finally, we want to show that the proposed method can be used to design origami systems with complex mechanical behaviors such as bistability and multi-stability [Faber et al., 2018, Zhu and Filipov, 2019b]. Target 3 in the Fig. 6.15 (b) shows the results of the computed design rules

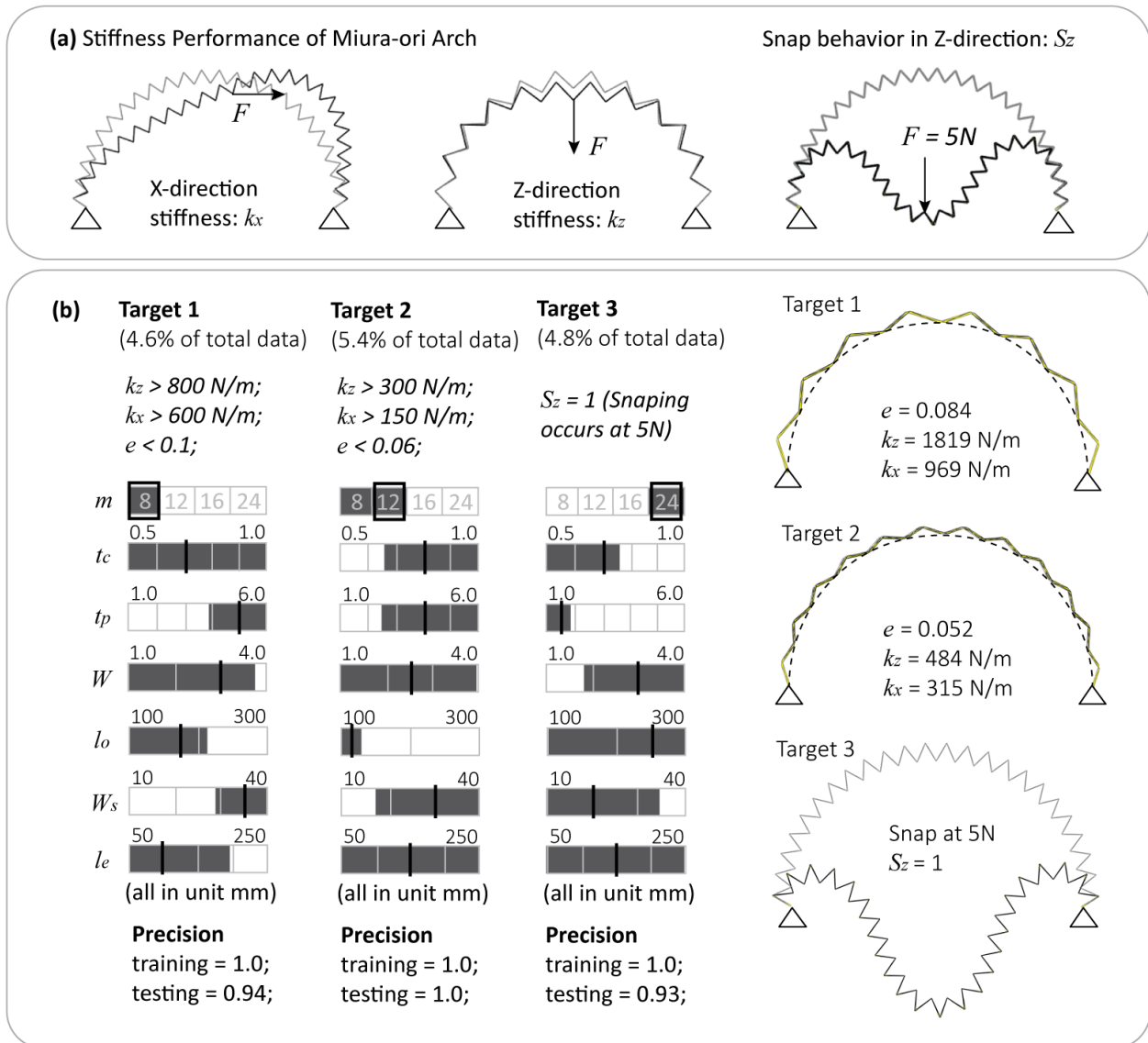


Figure 6.15: Design rules computed for the origami arch database.

for the designed origami arch to exhibit the snap through behavior under the applied 5N forces. Unlike designing for a stiff arch with relatively small errors, the machine learning method shows that introducing more segmentation (larger  $m$ ) into the origami stripe can give rise to the snapping behavior. Moreover, it is necessary to keep the thickness of panels and crease thin. The testing precision of this design rule is high, indicating that the design rule is reliable and accurate.

## 6.6 Concluding Remarks

This work introduces a novel interpretable machine learning based method for designing origami systems. We showed that by populating an origami performance database and training an interpretable machine learning method called decision tree to fit the database we can obtain useful design rules of origami systems. More specifically, we pick the more informative branches (design rules) in multiple decision trees using the F-score. The results presented in the work showed that the proposed method can compute accurate design rules of origami systems and these design rules can achieve a high precision in the testing database.

From a machine learning point of view, the proposed method basically uses the F-score to select the better tree branches from the others. It is similar to selecting the better learned classifiers from a number of trained classifiers using the F-score. The advantage of focusing on a single branch in the decision tree (or the ensembled version random forest) is that the produced design rules that are sparser and thus easier to be understood by human. Moreover the computed feature threshold from a single branch of the tree is useful for guiding the design of complex origami systems. This method particularly fits the design of origami systems because it can consider complex interactions between categorical design features and continuous design features.

There are a number of benefits of using a data science and interpretable machine learning based approach when compared to the optimization-based design and other inverse design strategies for origami in the existing literature. First, the generated database can be reused for multiple times when computing rules for new targets. Suppose we want to build an origami canopy with another target stiffness, we will not need to recreate the database. All we need to do is to retrain the machine learning method with the new labels and compute the new set of rules. Second, the method can simultaneously analyze the significances of each design features for certain design targets, which is not provided in optimization-based design method for origami systems. If a design feature is significant for achieving certain target performances, a relatively tight threshold of that feature will be computed. Third, as demonstrated in the example with origami canopy, the proposed method can demonstrate the complex interaction between continuous variables and categorical variables, because the decision tree based machine learning method can naturally support categorical data. This is significant for origami design because many origami features are represented with cate-



gorical data types, and these categorical data is difficult to capture using the optimization-based design method. In addition, we also showed that the proposed method can handle multi-physical and multi-objective design target for origami system, and more importantly, we demonstrated that the proposed method can be integrated into existing origami shape fitting inverse design schemes so that origami researchers and engineers can start considering the trade-off between shape fitting error and other non-geometrical origami performances. This is important because origami engineering is more about achieving superior performances by folding to form 3D configuration rather than folding complex geometries to match the target configuration itself.

In summary, this chapter demonstrates that it is possible to compute useful design rules of origami systems using database and interpretable machine learning based methods. We showed that the interpretable machine learning can reveal the complex interaction between categorical and continuous variables in origami design, can create design rules for origami systems with multi-physical and multi-dimensional targets, and can enhance existing origami shape fitting methods to allow them to further consider the trade-off between shape fitting error and non-geometrical performances. We envision that the proposed methodology can be used to resolve complex origami design problems in practice and be used for creating functional origami systems with superior performances for various applications in biomedical devices, soft robotics, metamaterials, deployable structures, and many more.

## Chapter 7. Conclusion and Future Challenges

### 7.1 Major Contributions

This PhD dissertation establishes a novel framework for the fabrication, simulation, and design of functional origami structures. In practice, this proposed framework can be used for analyzing and building functional origami structures for applications in robotics, biomedical devices, deployable structures, reconfigurable metamaterials, and many more.

For fabrication, this work introduces a novel micro-origami that can fold both elastically and plastically to achieve complex motions and functions. A novel electro-thermal actuator design is proposed and its folding capacity is tested. A versatile fabrication method is established to integrate this actuator system into micro-origami structures. Different functional devices are built and tested to highlight the superior controllability and precise motion of the proposed micro-origami systems. These micro-origami structures can achieve complex motions and functions, like folding an origami crane that can then flap its wings and folding an inter-locked gripper to grip small objects.

For simulation, this work introduces three separate models, including a compliant crease bar and hinge model, an inter-panel contact model, and an electro-thermal actuation model, for capturing the behaviors of functional origami structures. First, this work adjusts the traditional bar and hinge model to capture the compliant creases, which are folding creases with distributed width, within functional origami systems explicitly. With both computational and physical experiments, this work shows that the proposed compliant crease model is critical for simulating bistable behaviors in functional origami. In addition, this compliant crease origami model enables better representations of origami configurations for thickness accommodation and contact simulation. Next, this work introduces a method to capture the global inter-panel contact within the bar and hinge model. This inter-panel contact model provides a much needed method to capture stiffness jumps and inter-locking behaviors triggered by panel contact within origami assemblages. Moreover, this inter-panel contact model provides a method to check if an origami pattern can be folded accurately without having panel intersections. Finally, this dissertation introduces a multi-physics based simulation method to capture active folding in the electro-thermally actuated origami structures. A reduced-order heat transfer model is integrated within the bar and hinge model to capture the electro-thermo-mechanically coupled behaviors in these functional origami

structures. Although this electro-thermal simulation model is only calibrated for the micro-scale origami systems fabricated in this work, the principle can be scaled up for simulating thermally active origami systems at larger scales.

In addition, this work establishes an open-access simulation package to implement the three proposed models and provides a thorough review on the recent advancements in origami simulation. A Matlab based simulation code package called Sequentially Working Origami Multi-Physics Simulator (SWOMPS) is developed and made open-access on GitHub. This package enables rapid simulation of multi-physical behaviors in active origami and the GitHub webpage is gaining increasing traffic from researchers who are interested in using functional origami systems. The Appendix of this work gives a thorough review of recent advancements in origami simulation. Three major groups of origami simulation methods, namely the kinematic simulation, the mechanical simulation, and the multi-physical simulation, are thoroughly categorized and introduced. The review introduces the formulation of different origami simulation techniques for researchers to select and develop appropriate simulation techniques for their specific applications.

For design, this work demonstrates an interpretable machine learning based method to compute human-understandable design rules for functional origami. This inverse design method can capture the interaction between categorical and continuous features for representing different origami patterns, and can handle the multi-objective problem formulations needed for considering the multi-physical performance targets. This inverse design method provides a holistic solution to design active origami structures for different engineering applications.

Together, the integrated framework presented in this thesis can capture and design the complex behaviors of functional origami structures. This work directly connects knowledge from structural engineering, computational mechanics, microelectromechanical systems, and machine learning with origami engineering to build novel and functional origami structures. The proposed work can be directly used to analyze and build programmable metamaterials, active micro-robots, biomedical surgery tools, deployable structures, and many other engineering systems. Moreover, the presented material highlights the advantage and superiority of solving engineering problems with origami assemblages.

## **7.2 Future Challenges**

In this section, we discuss future challenges in the field of origami engineering and functional origami structures. More specifically, this work identifies three challenges and they are: (1) Integration of controllers and sensors into micro-origami systems, (2) Reduced-order multi-physical simulation for functional origami, and (3) Design of large-scale functional origami structures.

**Integration of controllers and sensors into micro-origami systems** This work demonstrates that active micro-origami structures have superior shape morphing capability and can achieve complex functions. However, it is not yet clear how to integrate more elaborate control circuits and sensors into micro-origami systems. In general, integration of different sensors requires using different active materials and designs. However these sensors and circuits are difficult to build with existing photo-lithography based processes, which have strict compatibility requirements. Alternative approaches like using additive manufacturing and digital fabrication techniques, which provide high flexibility in handling multiple active materials, can help integrate sensors and controllers into the micro-origami structures. Integration of controllers and sensors is crucial because it allows micro-origami structures to increase their functionality and act autonomously in complex environments.

**Reduced-order multi-physical simulation for functional origami** The next challenge we want to discuss is on developing reduced-order multi-physical simulation for functional origami structures. This work provides one reduced-order model to integrate electro-thermal actuation into an origami simulation platform, but the method is tailored to just a specific form of active folding. Functional origami structures can be folded using other mechanisms such as magnetic actuations, active hydro-gels, shape memory alloys, shape memory polymers, and many other active designs. Future origami simulation methods need to capture these other actuation mechanisms. In addition to the active folding, functional origami can also display multi-physical properties that are of interest. New reduced-order simulation methods for capturing these multi-physical properties are also needed for different projects. These new reduced-order simulation techniques for multi-physical and functional origami systems can enable origami researchers to design better origami-inspired engineering devices.

**Design of large-scale functional origami structures** Scaling up functional origami structures for civil applications remains a difficult challenge in the field of origami engineering. Existing design and simulation methods for origami systems are not appropriate for capturing the behaviors of larger origami-inspired systems because they tend to assume origami panels to have zero thickness. To design for large-scale origami structures, new fundamental theorems are needed to analyze and design the behaviors of thick and non-developable origami systems. Moreover, common actuation mechanisms for small-scale functional origami structures, like active hydrogels and shape memory polymers, are not directly scalable to large-scale civil systems. Therefore, it is necessary to build thick origami structures with hinge connections and design other practical actuators for folding origami inspired structures at large scales. These large-scale functional origami structures can be used to design smart facade and deployable buildings for future cities.

## Appendix A. A Review on Origami Simulation

### A.1 Introduction, History, and Organization

This appendix is dedicated to give a thorough summary of origami simulation techniques. Simulating the physical behavior of origami forms the basis for understanding, analyzing, designing, and optimizing origami-inspired systems. In light of this, we believe that it is beneficial to categorize different simulation techniques, to summarize the underlying mathematical models and solution methods involved, and to present the strengths and weaknesses of different simulation techniques. Although origami simulation borrows widely from analyses and techniques in other disciplines in science and engineering, there are unique challenges; for example, the pattern geometry and localised crease behavior can significantly impact the global response, and efficient simulations require careful consideration of the degrees of freedom of the origami system. The presented material aims to help future origami scientists and engineers to select and develop appropriate methods for specific projects. Moreover, because different simulation techniques were developed to answer different questions regarding origami systems, learning about the underlying principles for simulation techniques can also help origami researchers to ask the right questions.

Figure A.1 depicts the history of origami simulations in broad brush strokes. Of course, no histories are complete and technical developments are not necessarily sequential; moreover, related simulations can be found in advance of the specific development related to origami. The simulation of origami starts with the analysis of their kinematics, dating back to the early 1970s. The pioneering works by Huffman [Huffman, 1976] and by Resch [Resch and Christiansen, 1970] demonstrate such early efforts to simulate origami folding in a virtual environment. In the 1990s and 2000s, a number of studies proposed approaches and concepts to simulate the kinematic folding motions of origami [Kawasaki and Yoshida, 1988, Kawasaki, 1989, Belcastro and Hull, 2002, Tachi, 2009c, Mitani, 2008]. These studies pinned down many fundamental ideas for the kinematic simulation techniques of origami. During this period, there were also early works studying the mechanical behavior of origami [Guest and Pellegrino, 1994, Guest and Pellegrino, 1996]. Starting around 2010, researchers began exploring origami for creating mechanical metamaterials, crash boxes, and other engineering structures [Yang and Silverberg, 2017b, Schenk and Guest, 2013, Fang et al., 2016]. To capture the mechanical properties of origami systems for these application scenarios, various mechanics-based simulation techniques were created [Schenk and Guest, 2010, Wei et al.,

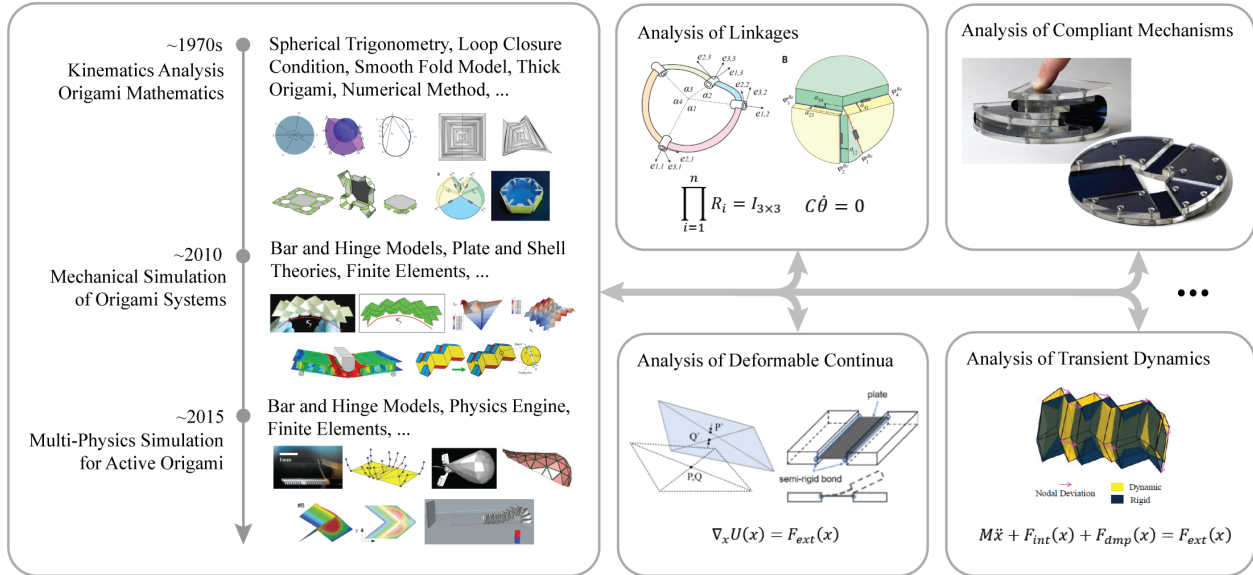


Figure A.1: The history of simulation of origami systems in a broad brush stroke (left) and related simulations and analyses from other engineering disciplines (right).

2013, Liu and Paulino, 2017a]. More recently, researchers have started exploring active origami systems that can fold autonomously in response to environmental stimuli and can generate unique non-mechanical behaviors [Na et al., 2015, Zhu et al., 2020, Yoon et al., 2014]. In response to the need for capturing the folding behaviors and the non-mechanical properties of active origami systems, researchers have started building multi-physics based simulation platforms to capture advanced behaviors of origami systems [Zhu and Filipov, 2021a, Hathcock et al., 2021, Nauroze et al., 2018].

The history of origami simulation also gives us a rationale for separating the simulation techniques into three major groups: kinematics-based simulations, mechanics-based simulations, and multi-physics simulations. These three groups form the three major sections of this review; within each section, we will categorize the simulations based on their formulation rather than their chronological order. First, we will briefly discuss the scope of this work and terminology, before expanding on each of the three identified categories. Following these three sections, we will summarize existing simulation packages, discuss how to select appropriate simulation techniques, and discuss future challenges in the field.

## A.2 Scope and Terminology

This section outlines the scope of the appendix and introduces important terminologies related to origami simulations. The focus of this work is the simulation of origami systems, which answers

the question of how to simulate the folding motions and the corresponding property changes in origami systems. This review will therefore not focus on the design of origami systems, which includes problems such as how to generate new origami patterns, solve mountain-valley assignments, adjust existing patterns for certain applications, *etc.* Nonetheless, we expect that this review will provide useful information for origami designers to select and build suitable simulation techniques for their specific problems.

Moreover, we will focus on the simulation of origami with straight creases. Modeling and simulating the behavior of curved creases often requires drastically different formulations [Dias et al., 2012]. For example, defining a straight crease only requires specifying two nodes at the end of the crease and the folding can be represented with a single scalar variable. In contrast, defining a curve crease requires using mathematical tools such as spline or polynomial functions, and the fold angle can vary along the length of the crease. The simulation techniques covered in this review will also be applicable to the analysis of a wide range of kirigami systems, where cuts are introduced, provided that the folding creases remain straight.

**Model, solution method, simulation** Before introducing specific origami terminologies, we first discuss three fundamental terms used in the simulation of physical systems: *model*, *solution method*, and *simulation*. In many situations, these three terms are used interchangeably; however, we believe it is best to define and use these terms more carefully.

*model*: In this work, we define a model as a mathematical representation of physical objects. This primarily includes variables to describe the state of the system and governing relationships between these variables. The number of independent variables within the system is referred to as the *degrees-of-freedom* or DOF. For example, the configuration of a single-degree-of-freedom (SDOF) system can be determined using just one scalar variable; a multi-degrees-of-freedom (MDOF) system needs to be defined using multiple scalar variables. In addition, a model gives mathematical equations to describe the governing relationships between these variables. For example, we can use constitutive relationships to correlate fold angles and crease moments or use kinematic constraining equations to coordinate folding angles between different creases. We are usually interested in how these variables evolve over “time” (or loading step) without violating the governing equations. However, a model alone cannot tell us how these variables evolve as it only formulates a mathematical problem to be solved. To further solve the evolution problem, solution methods are needed.

*solution method*: We define solution methods as ways of solving mathematical problems. For sufficiently simple origami models, analytical solutions can be found for the folding motion. More complicated origami models, however, require the solution of partial differential equations (PDEs) or ordinary differential equations (ODEs) with no analytical solution. In such cases, numerical

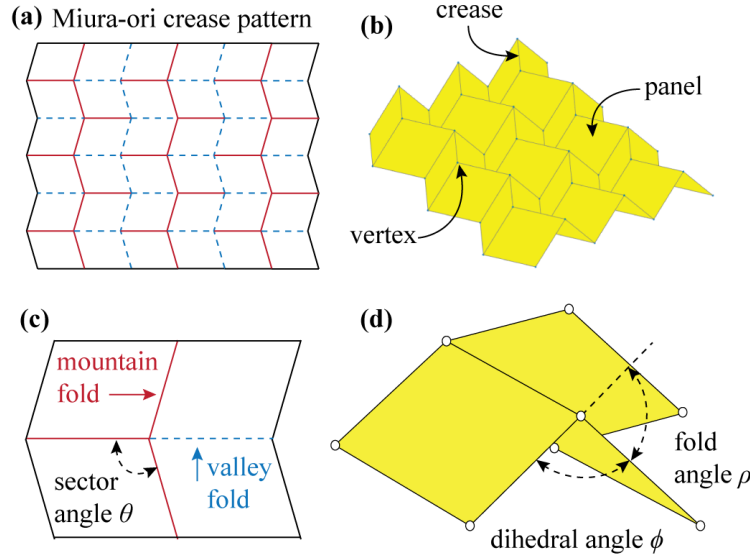


Figure A.2: Definitions of common origami terminologies.

solution methods are used to analyze the problem.

*simulation:* In general, simulation refers to imitating the behaviors of physical systems over time in virtual environments. More specifically, a simulation includes a model to represent a physical system and a solution method to solve how the system evolves over “time” (or loading step). A suitable origami model is developed based on the characteristics of the physical origami system and a solution method is chosen based on the characteristics of the mathematical problem embedded in the origami model.

**Origami terminology** Next, we introduce common origami terminologies, which will be used throughout the remainder of this review.

*crease:* The creases (or folds) of an origami pattern are the lines about which the folding occurs; see Fig. A.2 (a,b). Common origami models idealize creases as 1D fold lines with zero width and the adjacent panels rotate about these creases. The terms ‘creases’ and ‘folds’ are often used interchangeably.

*compliant crease:* Unlike creases that provide rotation about a 1D axis (like a door hinge), the folding motion of compliant creases relies on a distributed bending deformation over the width of a crease. The non-negligible width of these compliant creases requires additional considerations when building models for origami systems. Compliant membranes often serve as origami creases for actuation [Zhu et al., 2020, Na et al., 2015] or for panel thickness accommodation [Butler et al., 2020].

*vertex:* The vertex is a “point” where multiple “creases” meet; see Fig. A.2 (b). In most



origami models, the vertex is indeed a point in 3D space. However, when modeling origami with thick panels or with compliant creases, the intersection of creases is no longer a defined point — nonetheless, a vertex can still be identified intuitively.

*panel:* The panel is the facet of an origami pattern; see Fig. A.2 (b). For straight-crease origami, it is the polygon enclosed by origami creases and boundary lines.

*origami crease pattern:* The crease pattern is the geometry formed by the vertices and creases of an origami in the flat configuration; see Fig. A.2 (a). In combination with the mountain/valley assignment of each of the folds, the crease pattern determines the folding motion of an origami pattern and has significant influence on the properties of an origami.

*mountain fold and valley fold:* The mountain/valley fold convention denotes the direction of folding in origami. For example, the Miura-ori pattern shown in Fig. A.2 (c) and (d) has three mountain folds, indicated with red solid lines, and one valley fold, indicated with blue dashed lines.

*sector angles:* The sector angles are the in-plane angles around vertices used to describe origami patterns; see Fig. A.2 (c). In this work, we use  $\theta$  to represent sector angles.

*dihedral angles:* The dihedral angle is the crease angle between two adjacent origami panels; see Fig. A.2 (d). It can be calculated using the normal vectors of the two adjacent panels. In this work, we use  $\phi$  to denote dihedral angles.

*fold angles:* The fold angle is similar to the dihedral angle, but it measures how much a crease folds from its initial configuration. In general, the sum of the fold angle and the corresponding dihedral angle is  $180^\circ$  as indicated in Fig. A.2 (d). In this work, we use  $\rho$  to denote the fold angles.

*thick origami:* In applications where the thickness of panels cannot be neglected, as is often done for origami models, thick origami models integrate thickness into the model formulations.

*rigid foldable origami:* An origami system is rigid foldable if the folding process can happen without panel deformation. That is, all deformations occur in the form of crease folding.

*developable origami:* An origami pattern is developable if it forms a flat surface after all creases are unfolded (to flat). Equivalently, a developable origami pattern has all sector angles at each vertex adding to  $2\pi$ .

*flat foldable origami:* An origami is flat foldable if it forms a flat surface after all creases are folded (to  $180^\circ$ ). We will revisit developable origami and flat foldable origami in Section A.3.

### A.3 Kinematics-Based Simulations

This section introduces kinematics-based simulations of origami systems. First, we briefly review how to perform kinematic simulations for a generic mechanism. Consider the analysis of the simple linkage shown in Fig. A.3. The first step is to select the variables to describe its current

Table A.1: A summary of kinematics-based simulations for thin and rigid origami.

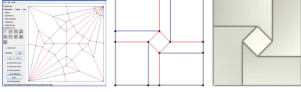
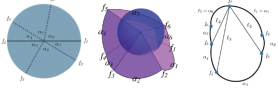
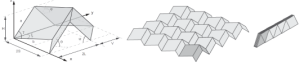
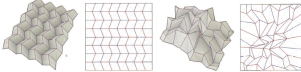
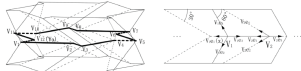
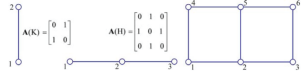
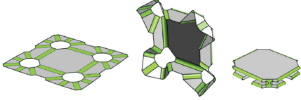
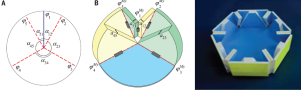
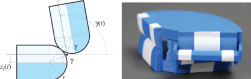
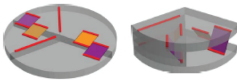
Simulation technique	Formulation	Note
<b>Reflection based simulation</b> 	Reflection operation is used to capture the flat folding process of origami systems.	The simulation technique predicts no intermediate folding steps.
<b>Reference</b> [Mitani, 2008, Mitani, 2012] figure from [Mitani, 2008]		
<b>Spherical trigonometry</b> 	Solve the folding angle of origami directly (see Eqn. (A.4) to Eqn. (A.7)).	This simulation is mostly used for analyzing SDOF systems and the origami kinematic is solved analytically.
<b>Reference</b> [Huffman, 1976], [Lang et al., 2016], [Lang and Howell, 2018], [Evans et al., 2015c], [Evans et al., 2015b], [Evans et al., 2015a], [Tachi, 2009a], [Hull, 2013], [Zimmermann et al., 2019], [Waitukaitis et al., 2015], [Chen et al., 2016], [Hanna et al., 2014], [Silverberg et al., 2014], [Wang et al., 2018], [Zhao et al., 2018], [Lv et al., 2014] figure from [Evans et al., 2015c]		
<b>Basic trigonometry</b> 	Solve the nodal coordinates and folding angles of origami using basic trigonometry.	This simulation is usually applicable to specific patterns with periodically repeating unit cells.
<b>Reference</b> [Schenk and Guest, 2013], [Yasuda et al., 2013], [Yasuda and Yang, 2015], [Kamrava et al., 2017], [Kamrava et al., 2018], [Wu and You, 2011], [Balkcom et al., 2009] figure from [Schenk and Guest, 2013]		
<b>Loop closure condition</b> 	The simulation technique solves the folding motion that complies with the loop closure condition (Eqn. (A.16)).	Equivalent to using spherical trigonometry. Numerical solution methods can be used for MDOF systems.
<b>Reference</b> [Kawasaki and Yoshida, 1988], [Belcastro and Hull, 2002], [Tachi, 2009c], [Tachi, 2010b], [Hu and Liang, 2020], [Xi and Lien, 2015], [Feng et al., 2020a], [Peng et al., 2017], [Bowen et al., 2014], [Wei and Dai, 2014], [Tachi, 2010a], [Demaine and Tachi, 2017], [Tachi, 2010d], [Tachi, 2013], [Feng et al., 2020b], [Silverberg et al., 2015] figure from [Tachi, 2010a]		
<b>Quaternion</b> 	Expressing the loop closure condition using quaternions instead of the rotation matrix.	Quaternions can be more efficient and can capture the panel contact [Wu and You, 2010].
<b>Reference</b> [Wu and You, 2010], [Broyles et al., 2020], [Cai et al., 2016b], [Cai et al., 2017a] figure from [Cai et al., 2016b]		
<b>Geometric-graph-theory</b> 	The graph product is used to represent the origami geometry with periodic unit, such as the Miura-ori tessellation.	The simulation technique can capture the periodic folding motion in origami.
<b>Reference</b> [Chen et al., 2019b] figure from [Chen et al., 2019b]		

Table A.2: A summary of kinematics-based simulations for compliant crease origami systems and thick origami systems.

Simulation technique	Formulation	Note
<p><b>Smooth fold model</b></p> 	<p>The simulation technique is an extension of the loop closure condition. In addition to the rotational constraint, a translational constraint is added to ensure the compatibility at a vertex.</p>	<p>The formulation is similar to simulating openings using loop closure condition. Extensions of the model enables it for considering mechanical loading [Hernandez et al., 2017c].</p>
<p><b>Reference</b> [Hernandez et al., 2017c], [Hernandez et al., 2016b], [Hernandez et al., 2017b], [Hernandez et al., 2017a], [Hur et al., 2017] figure from [Hernandez et al., 2017c]</p>		
<p><b>Spatial linkages</b></p> 	<p>The simulation technique captures the motion of degree-4, degree-5, and degree-6 thick origami vertices as spatial 4R, 5R and 6R linkages.</p>	<p>The technique can be used to model thick origami made with shift-hinge technique.</p>
<p><b>Reference</b> [Chen et al., 2015], [Chen and You, 2012] figure from [Chen et al., 2015]</p>		
<p><b>Rolling hinges</b></p> 	<p>Kinematic constraining equations can be derived based on the geometry of the rolling surface and the motion can be solved analytically.</p>	<p>This technique is designed specifically for the thick origami with rolling hinge connection.</p>
<p><b>Reference</b> [Lang et al., 2017], [Cai, 2016] figure from [Lang et al., 2017]</p>		
<p><b>4-bar linkages</b></p> 	<p>Kinematic constraining equations can be derived based on the geometry of the 4-bar linkage and the motion can be solved analytically.</p>	<p>This technique is designed specifically for the offset linkage based thick origami systems.</p>
<p><b>Reference</b> [Lang et al., 2020] figure from [Lang et al., 2020]</p>		

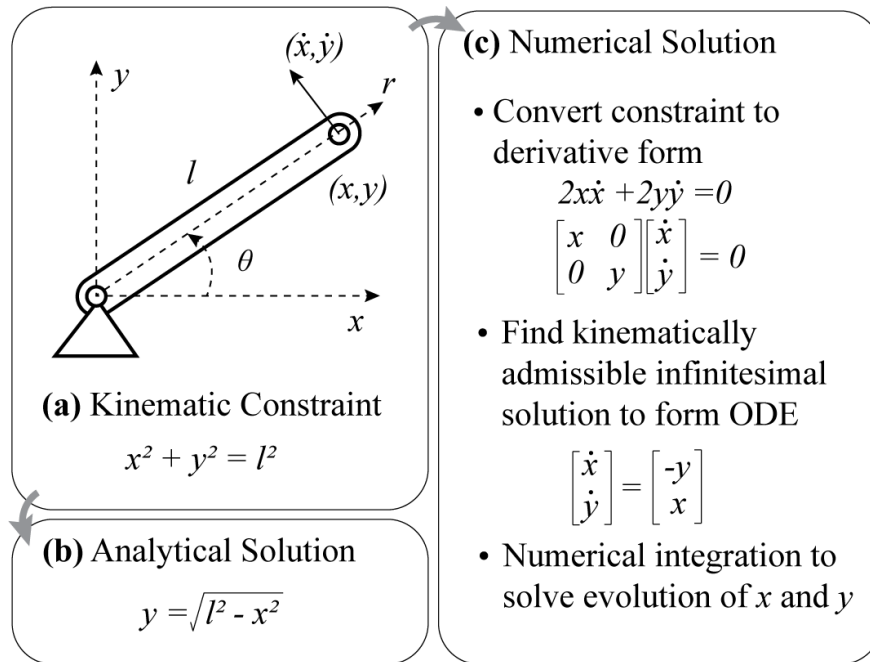


Figure A.3: An introduction to kinematics-based simulations.

configuration; here, we use the Cartesian coordinates  $(x, y)$  of the free moving end. Next, a kinematic constraining equation is established for the variables; here, the constraint is the fixed length  $l$  of the rigid member. After deriving this constraint, the kinematically admissible motion can be solved analytically or numerically. For an analytical solution, coordinate  $y$  can be directly calculated from coordinate  $x$  through rearranging the kinematic constraint. For a numerical solution, the constraining equations are first linearized with respect to time. Then, we find the kinematically admissible infinitesimal solution (the velocity solution of  $\dot{x}$  and  $\dot{y}$ ) which does not violate the linearized constraints. In this simple example, the velocity vector needs to be perpendicular to the rigid bar. Finally, an ODE solver can be used to solve how  $y$  and  $x$  vary over time. This simple example also illustrates how the selection of the variables can affect the solution process of the problem significantly; using polar coordinates here would have been more straightforward.

The remainder of this section addresses how to pick variables to represent an origami, how to form the constraining equations, and how to solve folding trajectories based on the constraining equations.

A key assumption in the kinematics-based simulations of origami is that the origami panels are assumed to be rigid throughout the folding process, meaning that the origami panels (or facets) do not change shape and remain planar. Usually, a kinematics-based origami model represents an origami structure using crease folding angles as variables. Based on the folding angles, kinematic

constraining equations can be derived. Additional constraints can be added for enforcing developability and flat foldability of the origami pattern if necessary. These kinematic constraints will be relaxed when using mechanics-based simulations of origami systems where the panel deformations are allowed. For sufficiently simple systems, the embedded mathematical problem can be solved directly and the evolution of the folding angles is found analytically. However, for more complicated systems, we often rely on numerical methods to solve for the folding trajectory.

In this section, we introduce different origami model formulations and solution methods used to analyze the kinematic folding motions of origami systems. The subsections are categorized based on the characteristics of the origami systems: (1) developable and flat-foldable origami; (2) thin and rigid origami; (3) compliant crease origami; and (4) thick origami. Subsection A.3.1 introduces the constraining equations for developability and flat-foldability, and a simulation technique for solving this type of origami system. Subsections A.3.2 to A.3.5 introduce kinematic simulations for thin and rigid origami models (with rigid panels that have assumed zero thickness). More specifically, subsection A.3.2 and subsection A.3.3 introduce simulations that are based on analytical solution methods while subsection A.3.4 and subsection A.3.5 focus on simulations that use numerical solution methods. After introducing the thin and rigid origami model, we will discuss how to extend this model to capture the motions of compliant crease origami (subsection A.3.6) and thick origami systems (subsection A.3.7). Table A.1 and Table A.2 gives a summary of kinematics-based simulations covered in this section.

### A.3.1 Developable and flat-foldable origami and reflection based simulations

The first simulation technique we will introduce is the reflection-based simulation for computing the folded configurations of developable and flat-foldable origami systems. Before introducing the formulation of this simulation technique, we further discuss developability and flat-foldability of origami patterns. These two concepts can be used to generate kinematic constraining equations for many origami models.

If an origami vertex is developable, it should form a flat surface when there is no folding at all creases. Equivalently, a developable origami vertex should have:

$$\sum_{i=1}^N \theta_i = 2\pi, \quad (\text{A.1})$$

where  $\theta_i$  are the sector angles within the vertex. Figure A.4 (a) provides an intuitive explanation of this equation. If the sum of all sector angles is smaller than  $2\pi$ , a cone is obtained. If the sum of all sector angles is larger than  $2\pi$ , the additional angles will prevent the paper from reaching a flat configuration and a saddle-like configuration is obtained. A more mathematically rigorous

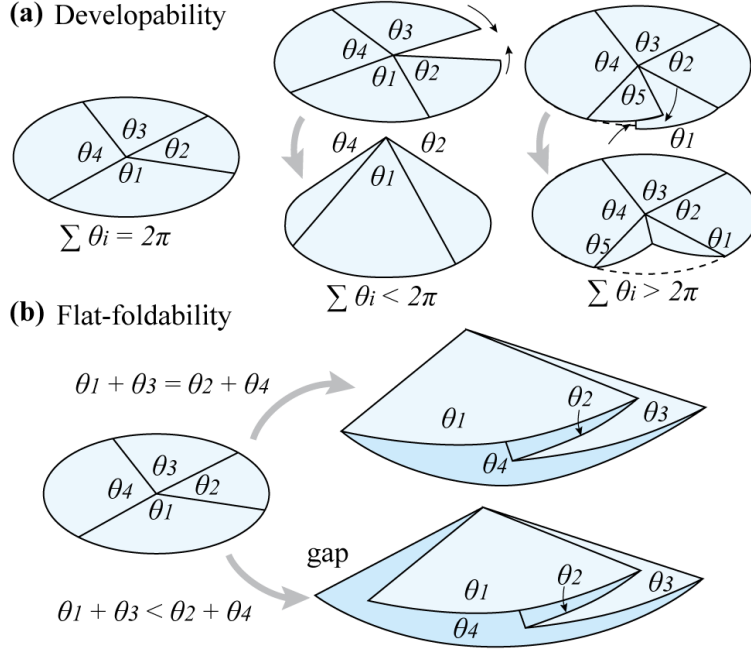


Figure A.4: Developability and flat-foldability of an origami with a single vertex.

definition for developability can be found in the textbook by Demaine and O’Rourke [Demaine and O’Rourke, 2007]. Developability is particularly valuable for the fabrication of origami structures: planar fabrication techniques like lithography [Zhu et al., 2020, Bassik et al., 2009, Kang et al., 2019] or laser cutting [An et al., 2018, Felton et al., 2014] can be used to build the origami structure before folding it into a 3D shape.

Flat-foldability is another important characteristic of an origami vertex. An origami vertex is flat-foldable if it forms a flat surface after all creases are folded by  $\pm 180^\circ$ . The flat foldability is useful for densely packing engineering systems [Filipov et al., 2015, Filipov et al., 2019, Seymour et al., 2018]. The Kawasaki-Justin theorem [Justin, 1989, Kawasaki, 1989] provides one necessary condition for a degree- $n$  vertex to be flat-foldable:

$$\theta_1 + \theta_3 + \dots \theta_{n-1} = \theta_2 + \theta_4 + \dots \theta_n = 180^\circ, \quad (\text{A.2})$$

where  $n$  needs to be even. In addition to this angular relationships, the necessary mountain-valley assignment is given by the Maekawa theorem [Kasahara and Takahama, 1987] which states that the number of mountain folds and valley folds should differ by  $\pm 2$ . Figure A.4 (b) gives a graphical explanation of these two theorems. The origami in Fig. A.4 (b) is a degree-4 vertex and has four sector angles,  $\theta_1$  to  $\theta_4$ . If the vertex is cut from a unit circle, then the arc lengths associated with these four sector angles are also  $\theta_1$  to  $\theta_4$ . For the vertex to be folded flat, the sum of arc lengths from

odd sector angles should equal the sum of arc lengths from even sector angles, that is:  $\theta_1 - \theta_2 + \theta_3 - \theta_4 = 0$ . If this condition is not satisfied, the origami will be torn apart and develop a “gap” if forced to fold flat, as illustrated in Fig. A.4 (b). More rigorous mathematical proofs and derivations for flat-foldability can be found in [Demaine and O’Rourke, 2007]. Both developability and flat-foldability were discussed extensively in the early works on kinematic simulations of origami, such as in the work by Bern and Hayes [Bern and Hayes, 1996], Hull [Hull, 1994], Kawasaki [Kawasaki, 1989], and Justin [Justin, 1989].

Finding the flat folded configuration of a developable and flat-foldable origami can be done directly, as demonstrated in the work by Mitani [Mitani, 2008]. In his work, a reflection based simulation is used to generate the flat folded configuration of origami by using seven reflection based operations summarized in [Mitani, 2008]. After generating the flat folded configuration, one can determine the overlapping conditions of panels using a brute-force searching approach. This simulation technique is implemented in a Java software package called ORIPA and can be found at [Mitani, 2012]. The reflection based simulation was later used to study the folding of curved crease origami by Mitani and his coworkers [Mitani and Igarashi, 2011]. Although the simulation was one of the early achievements in the field of computational origami, it cannot reproduce the intermediate folding process.

### A.3.2 Spherical Trigonometry and analytical methods

Not all origami systems are developable or flat-foldable, and these constraints can therefore be relaxed. For thin and rigid origami models, the only assumption is that the panels of the origami are rigid with zero thickness. In this section, we introduce the use of spherical trigonometry to model this origami systems.

Spherical trigonometry provides one direct way of simulating the folding motions of a thin and rigid origami system [Huffman, 1976, Lang and Howell, 2018, Evans et al., 2015c, Lang et al., 2016, Hull, 2013]. We represent the relationship between crease dihedral angles at a vertex using spherical trigonometry and solve how these dihedral angles evolve analytically. Figure A.5 (a) shows a spherical triangle, which is the intersection of a three-face box corner and a unit sphere. Angles  $a$ ,  $b$ , and  $c$  are the angles of the three-face box corner measured at the center of the sphere, while the angles  $A$ ,  $B$ , and  $C$  are the angles measured on the curved surface of the sphere (using the tangent line of the great circle arc). For a unit sphere the arc lengths corresponding to the center angles  $a$ ,  $b$ , and  $c$  are also  $a$ ,  $b$ , and  $c$ . These angles (or arc lengths) can be related using the cosine

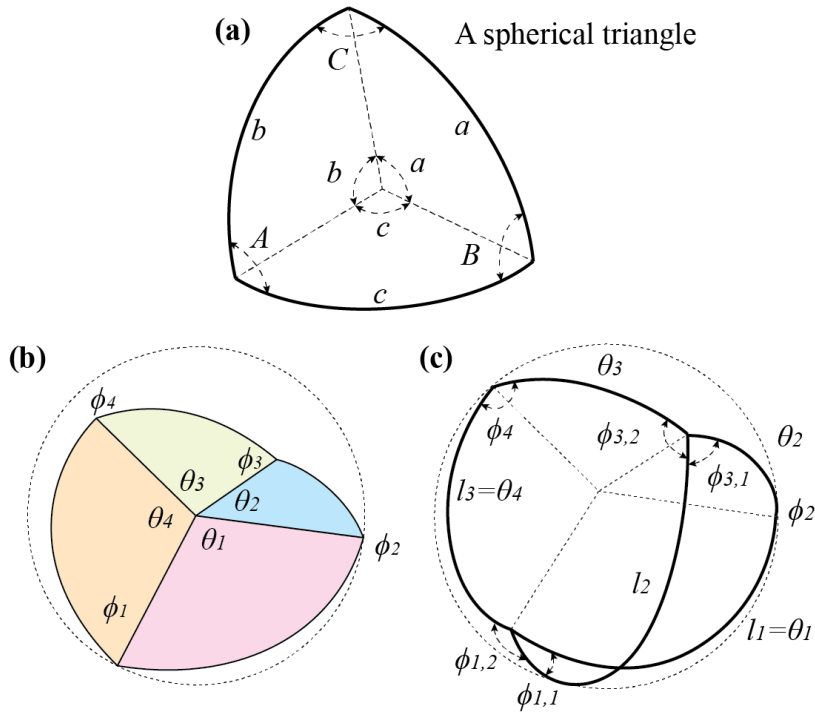


Figure A.5: Simulating origami folding using spherical trigonometry.

rule:

$$\begin{aligned}
 \cos(a) &= \cos(b)\cos(c) + \sin(b)\sin(c)\cos(A), \\
 \cos(b) &= \cos(a)\cos(c) + \sin(a)\sin(c)\cos(B), \\
 \cos(c) &= \cos(a)\cos(b) + \sin(a)\sin(b)\cos(C).
 \end{aligned}
 \tag{A.3}$$

Using these relationships, we can directly solve for the dihedral angles of creases. For the degree-4 vertex shown in Fig. A.5 (b), applying the spherical trigonometry equations with added



arc  $l_2$  (see Fig. A.5 (c)) allows us to relate the dihedral angles of these four creases as:

$$\begin{aligned}\phi_1 &= \phi_{1,1} + \phi_{1,2} \\ &= \cos^{-1}\left(\cos(\theta_2) - \frac{\cos(l_2)\cos(l_3)}{\sin(l_2)\sin(l_3)}\right) \\ &\quad + \cos^{-1}\left(\cos(\theta_3) - \frac{\cos(l_1)\cos(l_2)}{\sin(l_1)\sin(l_2)}\right),\end{aligned}\tag{A.4}$$

$$\phi_2 = \cos^{-1}\left(\frac{\cos(l_2) - \cos(\theta_1)\cos(\theta_2)}{\sin(\theta_1)\sin(\theta_2)}\right)\tag{A.5}$$

$$\begin{aligned}\phi_3 &= 2\pi - \phi_{3,1} - \phi_{3,2} \\ &= 2\pi - \cos^{-1}\left(\frac{\cos(l_1) - \cos(l_2)\cos(\theta_2)}{\sin(l_2)\sin(\theta_2)}\right) \\ &\quad - \cos^{-1}\left(\frac{\cos(l_3) - \cos(l_2)\cos(\theta_3)}{\sin(l_2)\sin(\theta_3)}\right),\end{aligned}\tag{A.6}$$

$$\phi_4 = \cos^{-1}\left(\frac{\cos(l_2) - \cos(\theta_3)\cos(\theta_4)}{\sin(\theta_3)\sin(\theta_4)}\right).\tag{A.7}$$

These equations are obtained by applying the cosine rules to the two spherical triangles marked with arc  $\{\theta_1, \theta_2, l_2\}$  and  $\{\theta_3, \theta_4, l_2\}$  of the degree-4 vertex. Generic equations for an arbitrary degree- $n$  vertex can be found in [Evans et al., 2015c, Zimmermann et al., 2019]. For simplicity, we will focus on the degree-4 vertex. Assuming that all sector angles are given, it can be seen from the above four equations that the degree-4 vertex has a single degree of freedom. Although this simulation is derived for more generic thin and rigid origami systems, it can still be applied to developable and flat-foldable origami systems. Substituting the developability and flat-foldability constraints for a degree-4 vertex,  $\theta_1 + \theta_3 = \pi$  and  $\theta_2 + \theta_4 = \pi$ , into Equations (A.4-A.7) will yield:

$$\phi_1 = -\phi_3$$

$$\phi_2 = \phi_4,$$

which shows that that the dihedral angles at the opposite sides of such a degree-4 vertex are equal [Huffman, 1976, Lang et al., 2016, Lang and Howell, 2018, Evans et al., 2015c]. By convention, folds 1 and 3 are referred to as minor folds and folds 2 and 4 as major folds. The minor folds have opposite mountain-valley assignments while the major folds have the same assignments.

For this developable and flat-foldable degree-4 vertex, we can further express the relation between dihedral angles  $\phi_1$  and  $\phi_2$  using the *fold angle multiplier*  $\mu_{1,2}$  as:

$$\mu_{1,2} = \frac{\tan\left(\frac{1}{2}\phi_1\right)}{\tan\left(\frac{1}{2}\phi_2\right)} = \frac{\sin\left(\frac{1}{2}(\theta_1 + \theta_2)\right)}{\sin\left(\frac{1}{2}(\theta_1 - \theta_2)\right)}.\tag{A.8}$$

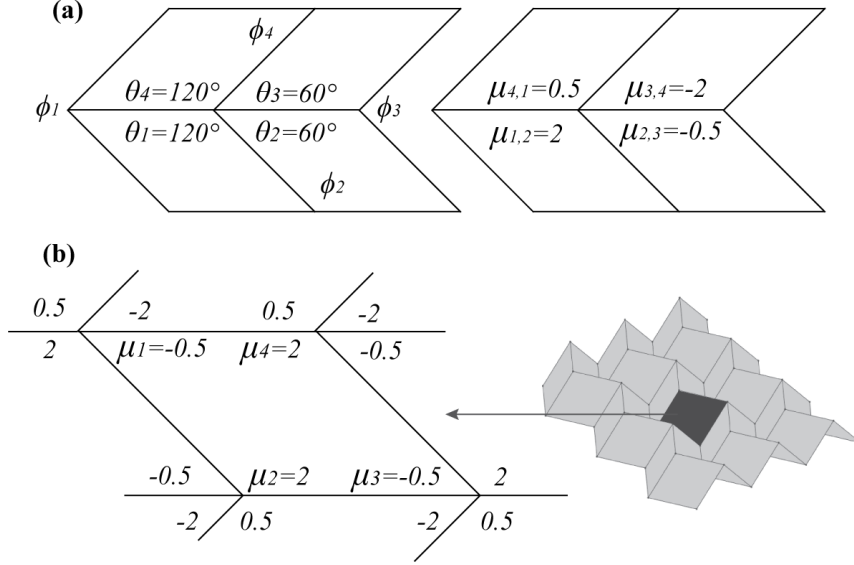


Figure A.6: Applying the fold angle multiplier to analyze the folding motion of an Miura origami pattern.

The general form of dihedral angle multiplier  $\mu_{i,j}$  and the calculation of the remaining three folding angle multipliers for the degree-4 vertex are:

$$\mu_{i,j} = \frac{\tan\left(\frac{1}{2}\phi_j\right)}{\tan\left(\frac{1}{2}\phi_i\right)}. \quad (\text{A.9})$$

$$\mu_{3,4} = -\mu_{1,2}; \quad \mu_{2,3} = -\frac{1}{\mu_{1,2}}; \quad \mu_{4,1} = \frac{1}{\mu_{1,2}}. \quad (\text{A.10})$$

This fold angle multiplier is thoroughly discussed in [Evans et al., 2015a], while detailed derivations can be found in textbook by Hull [Hull, 2013] (Activity 29 and 30) and in the appendix by Lang et. al. [Lang et al., 2016]. The fold angle multiplier provides a useful technique to extend the study of a single vertex to the study of an entire origami pattern [Evans et al., 2015a]. To further ensure that the vertices around a polygonal panel are rigid foldable, we need to ensure that:

$$\prod_{i=1}^n \mu_i = 1, \quad (\text{A.11})$$

where  $\mu_i$  are the fold angle multiplier of the angles within a polygonal panel. Figure A.6 shows an example based on the Miura-ori tessellation. Using Eqn. (A.8) and Eqn. (A.10), the fold angle multipliers of the Miura-ori unit cell are calculated. Next, we place these values at the corresponding locations on the pattern. To ensure that the four vertices around a quad panel can fold, we need

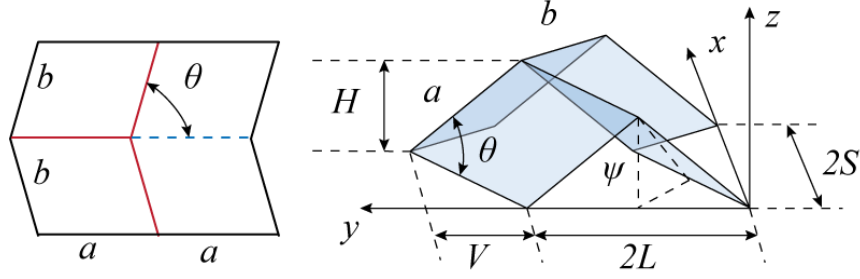


Figure A.7: Geometry of Miura-ori using standard trigonometry.

to have  $\mu_1\mu_2\mu_3\mu_4 = 1$ . In this example, the Miura-ori pattern indeed satisfies the requirement and thus it is rigid foldable.

This fold angle multiplier is particularly useful for designing and studying the kinematics of quad-based developable and flat-foldable origami, which are origami patterns with degree-4 vertices and quadrilateral panels [Lang et al., 2016, Lang and Howell, 2018, Evans et al., 2015b, Feng et al., 2020a, Kamrava et al., 2017, Kamrava et al., 2018]. Based on this fold angle multiplier, Evans et al. summarize various rigid-foldable quad-based origami patterns (such as the Miura pattern, Huffman grid pattern, chicken wire pattern, *etc.*) and introduce multiple ways to adjust these existing patterns for developing new patterns in [Evans et al., 2015b]. Similar but equivalent techniques for quad-based origami systems were also developed by Tachi [Tachi, 2009a], Lang et al. [Lang and Howell, 2018], and Feng et al. [Feng et al., 2020a].

### A.3.3 Trigonometry and analytical methods

The simulation techniques introduced in subsection A.3.2 only use dihedral angles to describe the folded geometry of an origami structure. It is common to further include the nodal coordinates as model variables for representing the configurations of origami structures when working on simple patterns with repeating unit cells [Schenk and Guest, 2013, Lv et al., 2014, Silverberg et al., 2014]. For example, the folding motions of Miura-ori patterns can be calculated using standard trigonometry and the nodal coordinates of the Miura unit are found using the following equations [Schenk

and Guest, 2013]:

$$H = a \cdot \sin(\psi) \sin(\theta), \quad (\text{A.12})$$

$$S = b \cdot \frac{\cos(\psi) \tan(\theta)}{\sqrt{1 + \cos^2(\psi) \tan^2(\theta)}}, \quad (\text{A.13})$$

$$L = a \cdot \sqrt{1 - \sin^2(\psi) \sin^2(\theta)}, \quad (\text{A.14})$$

$$V = b \cdot \frac{1}{\sqrt{1 + \cos^2(\psi) \tan^2(\theta)}}, \quad (\text{A.15})$$

where the variables are depicted in Fig. A.7. Solving the nodal coordinates of an origami structure directly is useful in some situations. For example, the above equations relate the length  $2L$  and width  $2S$  of the unit cell, so the Poisson's ratio of Miura-ori metamaterials can be found directly [Wei et al., 2013, Schenk and Guest, 2013, Evans et al., 2015c]. However, direct calculation of the nodal coordinates is usually only applicable to simple patterns with repeating unit cells such as the Miura-ori and its variations [Kamrava et al., 2017, Kamrava et al., 2018, Yasuda et al., 2013, Yasuda and Yang, 2015]. In special situations, this approach can also be applied to study the folding motions of specific patterns such as the shopping bag packing problem in [Balkcom et al., 2009, Wu and You, 2011].

The simulation techniques introduced in subsection A.3.2 and subsection A.3.3 are primarily suitable for analyzing the folding motion of SDOF origami patterns. Certain origami patterns with higher-degree vertices (and therefore MDOF kinematics) can also be solved analytically by introducing additional symmetry constraints. Symmetry constraints enforce the same folding angles in specific sets of creases, which reduces the kinematics to SDOF. For instance, the waterbomb pattern (which contains degree-6 or degree-8 vertices) has been studied by adding symmetry conditions [Chen et al., 2016], which has revealed multi-stability [Hanna et al., 2014] and the ability to program 3D surfaces [Zhao et al., 2018]. Wang et al. have given a summary of various patterns with degree-6 vertices [Wang et al., 2018].

### A.3.4 Loop closure condition and numerical methods

In order to create a simulation technique for generic origami systems with MDOF kinematics, a more scalable and compact formulation of the kinematic constraints is required.

Over the years, origami researchers have realized that the study of origami systems shares great similarities with the study of linkages [Demaine and O'Rourke, 2007, Bowen et al., 2014, Peng et al., 2017, Wei and Dai, 2014]. More specifically, a thin and rigid origami vertex can be represented by an equivalent spherical linkage model (Fig. A.8). This similarity provides an approach to construct the loop closure constraint, which can be solved using numerical methods.

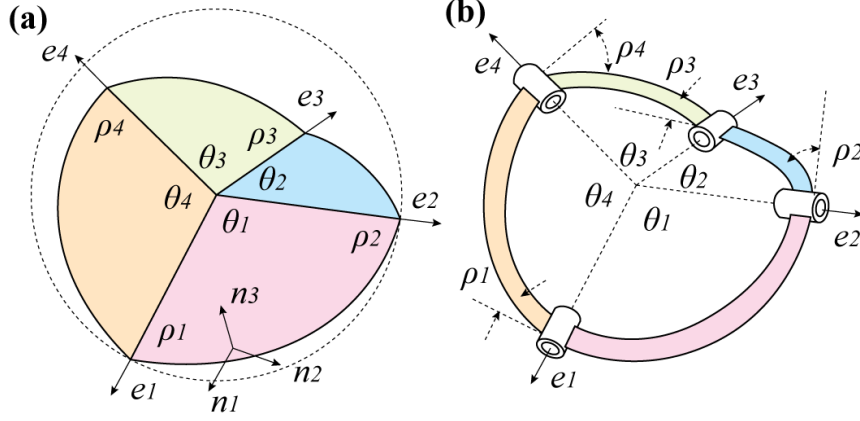


Figure A.8: Simulating “thin and rigid” origami vertex as spherical linkage. (a) An origami system. The  $n_1, n_2, n_3$  denotes a local coordinates for the first panel (corresponds to  $\theta_1$ ), where we have  $n_1 \parallel e_1$  and  $n_3$  perpendicular to the panel. (b) The corresponding spherical linkage model.

The mathematical equation of loop closure constraint is first developed by Kawasaki [Kawasaki and Yoshida, 1988] and Belcastro and Hull [Belcastro and Hull, 2002] without highlighting the connection with spherical linkages.

Figure A.8 demonstrates how the loop closure constraint for an origami matches that of a spherical linkage. In this formulation, the loop closure constraint can be represented using rotation matrices as:

$$F(\rho_1, \dots, \rho_n) = R_{3,n} R_{1,n} \dots R_{3,1} R_{1,1} = I_{3 \times 3}, \quad (\text{A.16})$$

where  $R_{1,i}$  and  $R_{3,i}$  are defined as:

$$R_{1,i} = \begin{bmatrix} 1 & 0 & 0 \\ 0 & \cos \rho_i & -\sin \rho_i \\ 0 & \sin \rho_i & \cos \rho_i \end{bmatrix}, \quad (\text{A.17})$$

$$R_{3,i} = \begin{bmatrix} \cos \theta_i & -\sin \theta_i & 0 \\ \sin \theta_i & \cos \theta_i & 0 \\ 0 & 0 & 1 \end{bmatrix}. \quad (\text{A.18})$$

The two matrices describe the rotation around local coordinate axis 1 and axis 3 of a folding crease as shown in Fig. A.8. These matrices are expressed in the local coordinates and are counter

clockwise. To understand this equation, imagine that we walk around the vertex. Every time we cross the panel with sector angle  $\theta_i$  we rotate about axis 3 using  $R_{3,i}$ , and every time we cross a crease  $\phi_i$ , we rotate by fold angle  $\rho_i$  about axis 1 using  $R_{1,i}$ . Thus, the relationship between the adjacent crease direction vectors  $\mathbf{e}_i$  and  $\mathbf{e}_{i+1}$  can be expressed as  $\mathbf{e}_{i+1} = R_{3,i}R_{1,i}\mathbf{e}_i$ .

In this fashion, if we combine all the rotations around a given vertex, we should have  $R_{3,n}R_{1,n} \dots R_{3,1}R_{1,1}\mathbf{e}_1 = \mathbf{e}_1$ , which is equivalent to saying that  $R_{3,n}R_{1,n} \dots R_{3,1}R_{1,1}$  equals the identity matrix. Or in terms of walking, we return to the starting position. In addition to using Eqn. (A.17) and Eqn. (A.18), there are various equivalent and similar formulations, such as those demonstrated in Feng et al. [Feng et al., 2020a] or in Belcastro and Hull [Belcastro and Hull, 2002].

There are a few properties worth mentioning regarding this loop closure constraint. First, this constraining equation is applicable to an arbitrary degree- $n$  vertex (including non-developable vertices). Second, the loop closure constraint is mathematically equivalent to using spherical trigonometry, as pointed out in [Tachi, 2009c, Lang and Howell, 2018]. Third, Equation (A.16) gives three constraining equations for a single vertex so a generic degree- $n$  vertex will have  $n - 3$  degrees-of-freedom. Finally, to extend this loop closure constraint from a vertex to an entire pattern, we need to ensure that all internal vertices of the pattern satisfy the constraint.

Now that we have the loop closure constraint, we can follow the process identified in Fig. A.3 (c) to solve for the folding motion numerically. First, taking the derivative of the the loop closure constraint with respect to time (Eqn. (A.16)) will give a linearized constraining equation. This equation shows how the loop closure constraint acts on the folding velocity of each fold. Next, we identify the non-trivial solution of the folding velocity that satisfies the linearized constraint. Finally, we numerically integrate this folding velocity solution to solve for the folding motion.

With this general process in mind, the first task is to calculate the derivative of this loop closure constraint to obtain the following governing equation:

$$C\dot{\boldsymbol{\rho}} = \begin{bmatrix} [C_1] \\ \vdots \\ [C_M] \end{bmatrix} \begin{bmatrix} \dot{\rho}_1 \\ \vdots \\ \dot{\rho}_N \end{bmatrix} = 0, \quad (\text{A.19})$$

where the matrix  $C$  is the Jacobian of the loop closure constraint,  $M$  is the number of vertices,  $N$  is the number of creases, the matrix  $[C_k]$  is the derivative matrix for the  $k^{\text{th}}$  vertex, and  $\dot{\rho}_i$  is the folding velocity of the  $i^{\text{th}}$  crease. Details of the calculation can be found in [Tachi, 2009c].

The next task is to find the velocity vector  $\dot{\boldsymbol{\rho}}$  that satisfies this linearized constraining equation. Equation (A.19) shows that the solution must lie in the null-space of the Jacobian  $C$  to satisfy the loop closure constraint. Following the work by Tachi, this non-trivial solution of  $\dot{\boldsymbol{\rho}}$  is calculated

using a trial velocity vector  $\dot{\rho}_0$  and the pseudo-inverse of matrix  $C$  as:

$$\dot{\rho} = [I_N - C^+C]\dot{\rho}_0, \quad (\text{A.20})$$

where  $\dot{\rho}$  is the projection of the trial vector  $\dot{\rho}_0$  onto the null space of the constraint matrix  $C$ . By selecting different trial vectors  $\dot{\rho}_0$  one can also track different folding trajectories and study the bifurcation of different folding paths.

Finally, to find the evolution of the folding angles over time, we numerically integrate the folding velocity  $\dot{\rho}$ . There are numerous solution methods available to handle this ODE. Tachi [Tachi, 2009c] used Euler’s method to simulate the motion of rigid origami, and many coding packages provide built-in ODE solvers such as the `ode45` function in MATLAB. In addition to these methods, Hu et al. introduce a Lagrange multiplier based method to calculate the folding trajectory [Hu and Liang, 2020]. Xi and Lien give a solution method that uses the pattern symmetry to speed up the algorithm when searching for the folding trajectory [Xi and Lien, 2015].

This loop closure based simulation has enabled numerous works on the design of origami systems. In subsequent work by Tachi and Demaine [Tachi, 2010a, Tachi, 2010d, Demaine and Tachi, 2017], they developed an approach to tuck fold an origami pattern to fit arbitrary surfaces based on this simulation. Feng et al. studied helical Miura origami [Feng et al., 2020b] using an equivalent loop closure formulation [Feng et al., 2020a]. Their modified formulation was also used in [Velvaluri et al., 2021] to study the folding motion of an origami-inspired shape memory alloy medical stent. Silverberg et al. studied the mechanical behaviors of origami by adding rotational springs to the kinematic relationships derived based on the loop closure constraints [Silverberg et al., 2015].

It should be noted that the numerical integration of the loop closure conditions described here cannot be applied directly to quad-based origami patterns with SDOF kinematics. The simulation relies on the existence of a null-space in the Jacobian matrix  $C$ , to follow the folding motion. Due to the numerical errors accumulated in the simulation, the constraining equation may no longer be singular. To avoid this, Tachi suggests triangulating the quad panels by introducing additional crease lines [Tachi, 2009c, Tachi, 2010b]. In this way, the SDOF quad-based origami is modeled as a MDOF system.

Finally, we wish to point out one fundamental limitation of the trigonometry-based simulations and the loop closure based simulations. Both techniques cannot guarantee that the origami pattern is folded to a valid configuration. This is because the mathematical theories behind both simulations do not consider the intersection of panels at a vertex and thus only provide necessary but non-sufficient conditions for having a valid folding process [Belcastro and Hull, 2002, Demaine and O’Rourke, 2007] (see Fig. A.9). More difficulties emerge when considering intersections be-

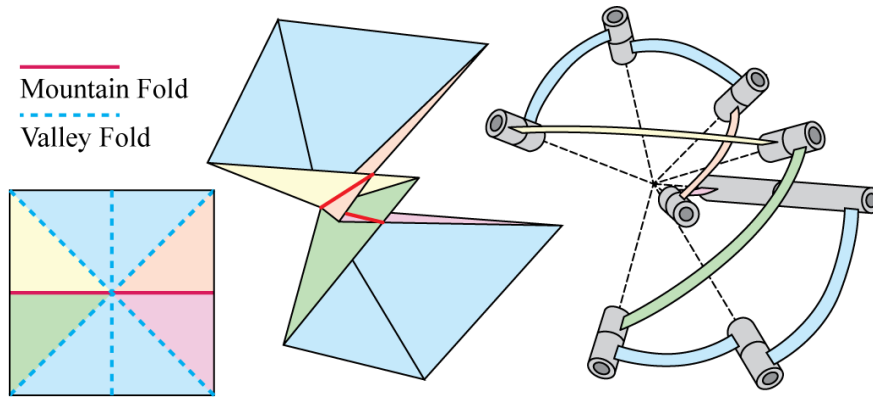


Figure A.9: Loop closure based simulation techniques cannot capture situations where panels intersect.

tween different parts of the origami that do not share a single vertex. The search of a sufficient and necessary condition for folding a thin and rigid origami remains an open question [Demaine and O’Rourke, 2007].

### A.3.5 Other simulations of thin and rigid origami

In addition to the use of spherical trigonometry and loop closure constraints, other simulations have also been developed to study the kinematics of rigid and thin origami structures. Although these simulations utilize different mathematical representations for the thin and rigid origami model, their formulations remain mathematically equivalent.

Wu and You [Wu and You, 2010] first used quaternions to describe the kinematics of thin and rigid origami, replacing the rotation matrices when expressing the loop closure constraint. Using quaternions offers a number of advantages when compared to rotation matrices. For example, quaternions give more compact representations of rigid body rotations, are numerically more stable and allow users to potentially determine panel intersection to rule out invalid origami configurations [Wu and You, 2010]. The quaternion-based simulation was used to study Miura-ori inspired structures and to demonstrate the non-rigid-foldability of Kresling patterns in the works by Cai et al. [Cai et al., 2016b, Cai et al., 2017a]. Despite their benefits, quaternions have not been popular among the origami community, likely because engineers and scientists are less familiar with this mathematical tool.

More recently, a paper by Chen et al. [Chen et al., 2019b] demonstrated a new approach for representing the geometry of origami using an integrated geometric-graph-theoretic approach. In this approach, the graph product is used to generate the origami pattern with periodic geometries. The paper applies this approach to study the folding motion of the Miura-ori and Kresling patterns.



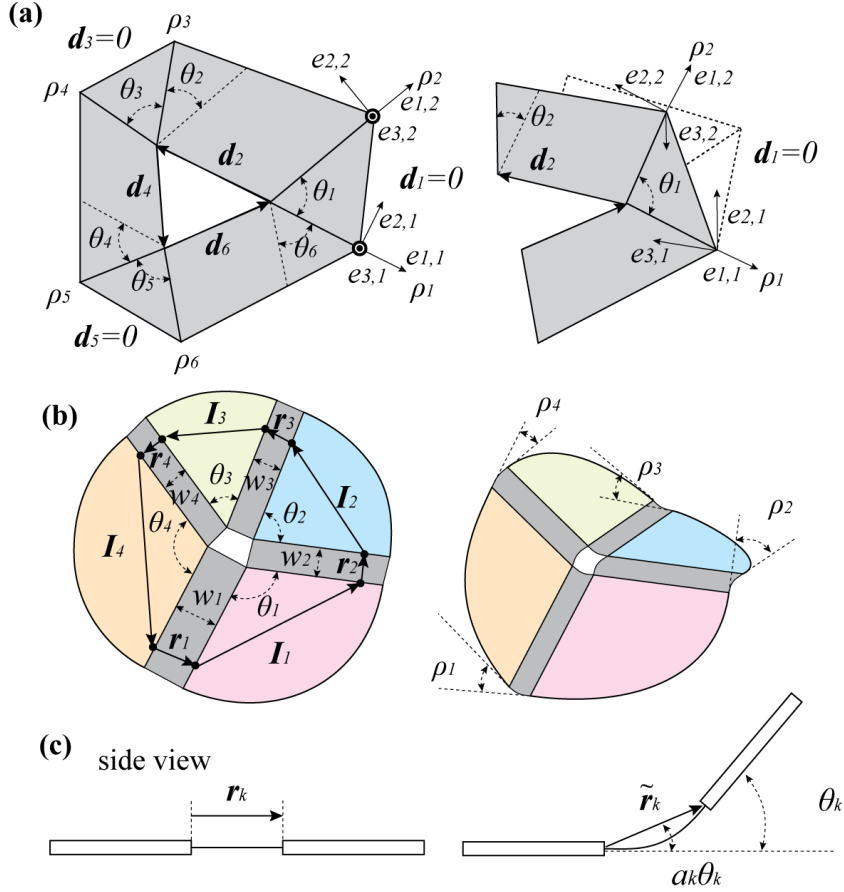


Figure A.10: Origami with openings (a), and those with compliant creases (b,c) can be modeled similar to spherical linkages, but with additional constraints.

However, the current formulations have difficulties representing origami with non-periodic characteristics (*i.e.* free-form origami patterns [Tachi, 2010a]). The use of this graph product based approach provides an efficient technique for studying the uniform folding behavior (as well as the corresponding loading behavior under uniform load), but future studies are needed to extend the formulation to capture non-periodic patterns.

### A.3.6 Openings and compliant creases

If the origami has internal openings or contains compliant creases, new constraints, in addition to the loop closure constraint (Eqn. (A.16)) are needed to ensure valid folded configurations. In previous simulations of origami with internal openings and compliant creases, the two topics are discussed separately. However, a closer look at the formulations of these two techniques will reveal that they share great similarities.

Figure A.10 (a) shows an origami loop with an opening. A loop pattern like this can be modeled as a spatial linkage [Peng et al., 2017]. As pointed out by Tachi [Tachi, 2010b], an additional constraint is required in addition to the loop closure condition in Eqn. (A.16). This extra constraint takes the form of:

$$\sum_{k=1}^n \left( \Pi_{i=1}^k (R_{1,i}(\rho_i) R_{3,i}(\theta_i)) \mathbf{d}_k \right) = \mathbf{0}_{3 \times 1}, \quad (\text{A.21})$$

where  $\mathbf{d}_k$  is the edge vector following the internal loop boundary. The edge vector  $\mathbf{d}_k$  is expressed in the local facet coordinate system and can be zero, as illustrated in Fig. A.10 (a). The rotation  $\Pi_{i=1}^k (R_{1,i}(\rho_i) R_{3,i}(\theta_i))$  is applied to  $\mathbf{d}_k$  to express it in the global coordinate system. In effect, this additional Eqn. (A.21) ensures that we return to the location where we started after looping around the opening and the original loop closure Eqn. (A.16) ensures that we recover a direction that is parallel to the starting orientation. A single vertex discussed in the previous subsection is a special case of the loop pattern with an opening where all edge vectors  $\mathbf{d}_k$  are zero and Eqn. (A.21) is therefore automatically satisfied. This modeling technique for origami patterns with openings enables the design of “geometrically misaligned” patterns, which are origami patterns with missing panels, proposed by Saito et al. [Saito et al., 2016].

Figure A.10 (b) gives an illustration of a single vertex with compliant creases. Similarly, in addition to the rotational constraint expressed in Eqn. (A.16) another translational constraint is needed. This additional constraint was developed by Hernandez et al. [Hernandez et al., 2017c] and is referred to as the “smooth fold model”. This constraint has the form:

$$\sum_{k=1}^n \left( \Pi_{i=1}^{k-1} (R_{1,i}(\rho_i) R_{3,i}(\theta_i)) R_{1,k}(a_k \rho_k) \tilde{\mathbf{r}}_k + \Pi_{i=1}^{k-1} (R_{1,i}(\rho_i) R_{3,i}(\theta_i)) R_{1,k}(\rho_k) \mathbf{I}_k \right) = \mathbf{0}_{3 \times 1} \quad (\text{A.22})$$

where  $\tilde{\mathbf{r}}_k$  is a reference vector in the creases and  $\mathbf{I}_k$  is a reference vector in the panels (both expressed in local coordinates). The rotation matrices in front of the two vectors convert them back to the same global coordinates. Setting the sum of all vectors to a zero vector ensures that the loop around the compliant crease vertex is not broken.

Detailed calculations of the reference vectors  $\tilde{\mathbf{r}}_k$  can be found in the original work [Hernandez et al., 2017c]. In a nutshell, a polynomial deformation shape function is used to describe the compliant crease geometry, and this shape function is used to calculate  $\tilde{\mathbf{r}}_k$  and  $a_k$  based on the crease rotation and the width of crease. Hernandez et al. has enabled this model to further capture the strain energy stored within compliant creases for simulating mechanical loading [Hernandez et al., 2016b]. This simulation technique was used for designing 3D surfaces for different engineering applications [Hernandez et al., 2017a, Hernandez et al., 2017b, Hur et al., 2017].

The above discussion shows that simulating the openings within origami patterns and the compliant creases requires adding an additional vector-based constraining equation. The additional

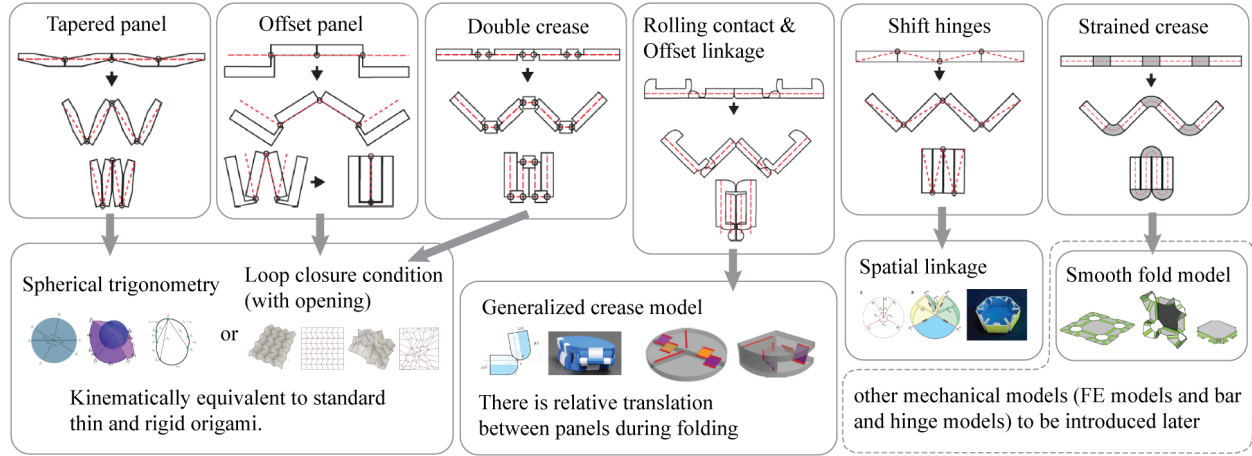


Figure A.11: Design and modeling techniques for thick origami systems.

constraint is needed because the “vertex” has higher degrees-of-freedom for both cases. Therefore, even if the rotational constraint is satisfied, the linkage can still be broken due to translational motions. If we can close the vertex by removing the opening [Tachi, 2010b] or by removing the width of the creases [Hernandez et al., 2017c], both models can be reduced to the loop closure constraint shown in Eqn. (A.16) and the constraints given in Eqn. (A.21) and Eqn. (A.22) will be satisfied automatically.

### A.3.7 Thick origami

In this subsection, we discuss techniques for simulating thick origami structures. In general, different thickness accommodation techniques need to be simulated using different approaches. Therefore, this subsection is organised based on the classification of different techniques for accommodating panel thickness (see Fig. A.11) as provided in the review article by Lang [Lang et al., 2018].

We begin with two simple thickness accommodation techniques: the tapered panel technique [Tachi, 2011] and the offset panel technique [Edmondson et al., 2014, Edmondson et al., 2016]. The thick origami systems generated using these two techniques have the same kinematic folding motions as their corresponding thin origami systems. Thus, any simulation technique for thin and rigid origami systems (those introduced in subsection A.3.2 to A.3.5) can be used to solve the folding motion of these two types of thick origami. One limitation to consider is that, the range of the folding angle can no longer reach  $180^\circ$  when using the tapered panel technique [Tachi, 2011].

Next, the double crease technique is also used for creating thick origami structures [Ku and Demaine, 2016, Hoberman, 1991]. Here, the single crease is separated into two creases to accom-

modate the thick panels. Although the technique itself does not preserve the kinematics (because one crease is separated into two), the generated new crease pattern with double creases can still be analyzed with simulations based on the loop closure constraint as demonstrated in the paper by Ku and Demaine [Ku and Demaine, 2016]. In this case, the incorporation of double creases will generate openings within the origami pattern and thus the additional constraints for the openings (introduced in subsection A.3.6) are required to simulate the behavior accurately.

The rolling contact technique and the offset linkage technique are two approaches to build thick origami that have unique kinematics. Because of the special designs of these two thickness accommodation techniques, both rotational and translational motion occurs between adjacent panels during the folding process. Thus, simulating the folding kinematics requires using a generalized crease model that can further consider the additional translational motion between adjacent panels. When using the rolling contact technique, the two adjacent panels each have a curved edge and can roll against each other [Lang et al., 2017]. The paper by Cai [Cai, 2016] and the work by Lang et al. [Lang et al., 2017] provide kinematic models and the analytical solutions for origami systems built with rolling contact. When using the offset linkage technique, the two adjacent panels are connected using a four bar linkage [Lang et al., 2020]. The work by Lang et al. [Lang et al., 2020] provides an approach to simulate the kinematics of an offset linkage.

When using hinge-shift techniques, the hinges of the origami structures are placed on the opposite side of the panels to accommodate the thickness [Hoberman, 1988, Chen et al., 2015]. When the origami pattern is sufficiently simple (such as the Miura-ori pattern with symmetric bird foot vertices), the technique can be applied directly to accommodate the thickness as demonstrated in [Hoberman, 1988]. In this case, using the thin and rigid origami model to analyze the folding kinematics is sufficient. However, when more complex vertices are encountered, one needs to rely on more sophisticated models to simulate the folding kinematics. In the pioneering paper by Chen et al., they showed that the folding motions of thick origami vertices built with hinge-shift techniques can be simulated using well established spatial linkage models [Chen et al., 2015]. In their work, the degree-4, degree-5, and degree-6 thick origami vertices are modeled as spatial 4R, 5R, and 6R linkages. With this simulation technique, the folding kinematics of these thick origami vertices can be solved using analytical methods. A summary of existing mechanical linkages can be found in reference [Chen and You, 2012].

Finally, we introduce the strained crease technique. Instead of using a hinge to connect adjacent panels, this technique connects two thick panels with a bendable soft plate to serve as a crease [Butler et al., 2020, Delimont et al., 2015]. A design like this is commonly seen in active origami structures and has been widely used in previous studies [Na et al., 2015, Zhu et al., 2020, Leong et al., 2009, Yoon et al., 2014]. These strained (compliant) creases can be made with active materials such as shape memory polymers [Liu et al., 2011, Mao et al., 2015], hydrogels [Yoon et al.,

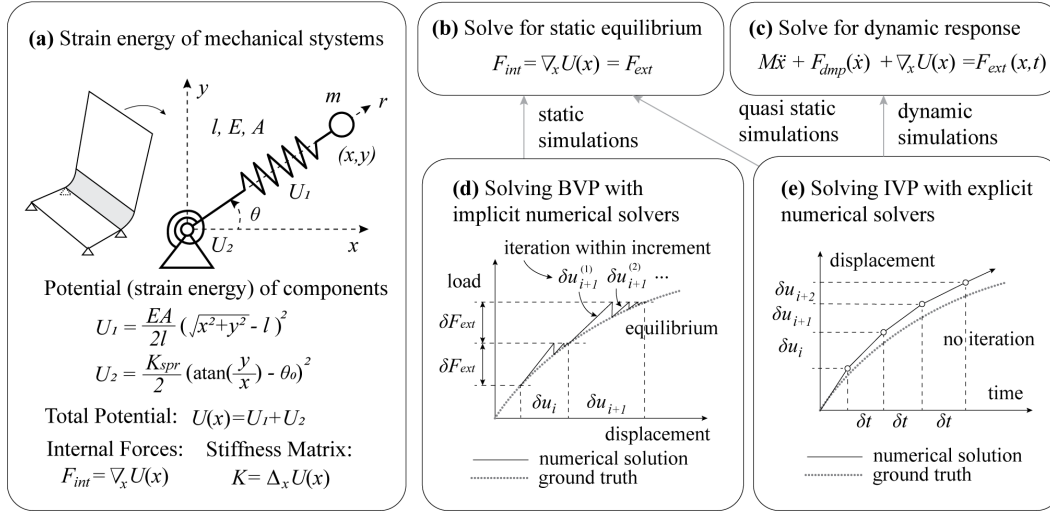


Figure A.12: An introduction to mechanics-based simulations of physical systems.

2014, Na et al., 2015], shape memory alloys [Hawkes et al., 2010], light activated polymers, and others [Bassik et al., 2009, Leong et al., 2009]. The smooth fold model can be used to study the folding behavior of this type of thick origami [Hernandez et al., 2016b, Hernandez et al., 2017c] because it can capture the widths of creases explicitly. Because the mechanical characteristics of the compliant creases (*e.g.* their bending stiffness) can affect the behavior of compliant crease origami systems significantly, it is more common to simulate these systems with mechanics-based simulation techniques. For example, both the compliant crease bar and hinge model [Zhu and Filipov, 2019b, Zhu and Filipov, 2020] and finite element model [Fang et al., 2018] were used to simulate origami of this type. We will discuss these models when introducing mechanics-based simulations in Section A.4 and multi-physics simulations in Section A.5.

## A.4 Mechanics-Based Simulations

In this section, we introduce mechanics-based simulations for origami systems. The first step in creating a mechanics based simulation is to formulate a model that represent the origami structure and its internal properties. Figure A.12 (a) provides an illustrative example, where the single fold origami is represented using a point mass connected to an extensional spring (for panel stretching) and a linear-elastic rotational spring (for crease bending).

These mechanics-based models can then be used to simulate the physical behaviors of the origami due to applied loading, self-folding, or other external effects. The physical behaviors can be broadly separated into *static* or *dynamic* responses. In a static process, the kinetic energy of the system is assumed to be negligible. The goal is to solve for the deformed configuration  $x$

Table A.3: A summary of rigid panel-based models and bar and hinge models for origami.


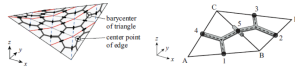
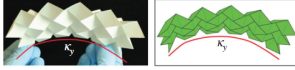
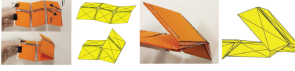
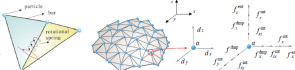
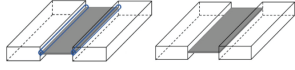
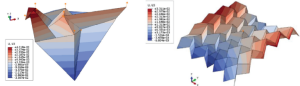
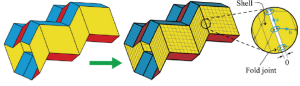
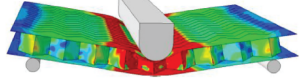
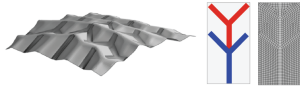

Simulation technique	Formulation	Note
<b>Rigid bar based simulation</b> 	<p>This technique uses rigid bars to represent triangulated origami panels for deriving kinematic constraining equations.</p>	<p>The technique could be seen as a transition from kinematic simulations to mechanic simulations and the precursor of bar and hinge models.</p>
<b>Reference</b> [Zhang et al., 2018], [Schenk and Guest, 2010], [Zhang and Kawaguchi, 2021] figure from [Zhang et al., 2018]		
<b>Rigid frame based simulation</b> 	<p>This model represents rigid origami panels using rigid frame elements and simulates creases as rotational hinges.</p>	<p>Rigid frame are used to preserve the folding kinematics. It is difficult to correlate frame deformation to panel deformation so the model is primarily suited for kinematic analyses.</p>
<b>Reference</b> [Hayakawa and Ohsaki, 2021], [Hayakawa and Ohsaki, 2019] figure from [Hayakawa and Ohsaki, 2021]		
<b>Standard bar and hinge model</b> 	<p>The model uses bar elements to capture panel stretching and shearing and uses rotational spring elements to capture crease folding and panel bending.</p>	<p>Bar and hinge model based simulations are computationally efficient and can capture the global mechanical behavior of origami.</p>
<b>Reference</b> [Filipov et al., 2015], [Filipov et al., 2017], [Filipov and Redoutey, 2018], [Liu et al., 2020], [Liu et al., 2019], [Gillman et al., 2018], [Gillman et al., 2019], [Kaufmann et al., 2021], [Li and Wang, 2015], [Mukhopadhyay et al., 2020], [Pagano et al., 2017], [Wei et al., 2013], [Cai et al., 2016a], [Greco et al., 2006], [Kidambi and Wang, 2020], [Fuchi et al., 2015] figure from [Liu and Paulino, 2017a]		
<b>Compliant crease bar and hinge model</b> 	<p>This model represents the geometry of compliant creases by adding additional bar elements and rotational spring elements in the crease region.</p>	<p>This model captures the bistability and multistability induced by having compliant creases.</p>
<b>Reference</b> [Zhu and Filipov, 2019b], [Zhu and Filipov, 2019a], [Zhu and Filipov, 2020], [Zhu and Filipov, 2021a] figure from [Zhu and Filipov, 2020]		
<b>Particle bar and hinge model</b> 	<p>This model lumps the mass of the origami onto the nodes for simulating the dynamic behaviors of origami.</p>	<p>Particle bar and hinge model based simulations can be used to analyze the transient dynamics of origami rapidly.</p>
<b>Reference</b> [Xia et al., 2021a], [Xia et al., 2021b], [Yu et al., 2019], [Xia and Wang, 2019], [Dong et al., 2021], [Dong and Yu, 2021], [Bhovad and Li, 2021] figure from [Yu et al., 2019]		

Table A.4: A summary of plate theory based simulations and FE simulations for origami.

Simulation technique	Formulation	Note
<b>Plates models for creases</b> 	<p>This technique represents the origami compliant crease as a plate and solves its deformation under applied forces.</p>	<p>The technique can be used to calculate spring stiffness for bar and hinge models as shown in [Zhang, 2021]</p>
<p><b>Reference</b> [Zhang et al., 2021], [Zhang, 2021] figure from [Zhang et al., 2021]</p>		
<b>Plates models for panels</b> 	<p>This technique simulates the small-strain bending behavior of origami panels using plate theory.</p>	<p>This formulation can be seen as a coarse meshed finite element simulation with limited capability for nonlinearity but better efficiency.</p>
<p><b>Reference</b> [Hu et al., 2021], [Soleimani et al., 2021], [Filipov et al., 2017] figure from [Hu et al., 2021]</p>		
<b>Shell element panels &amp; hinges</b> 	<p>This formulation models origami panels using shell elements and origami creases as rotational springs or rotational hinges.</p>	<p>This formulation is suitable for studying origami systems with softer creases. The fold line can deform and buckle during the loading process.</p>
<p><b>Reference</b> [Filipov et al., 2015], [Filipov et al., 2016], [Filipov et al., 2017], [Grey et al., 2019] figure from [Filipov et al., 2017]</p>		
<b>Shell element panels &amp; rigid creases</b> 	<p>This formulation models origami systems as shell elements connected with rigid creases (that do not fold).</p>	<p>This formulation is widely used for simulating origami unit cells and sheets, metamaterials, sandwich cores, and crash boxes when the creases are rigidly connected.</p>
<p><b>Reference</b> [Yuan et al., 2020], [Karagiozova et al., 2019], [Ma et al., 2018b], [Zhang et al., 2019], [Cai et al., 2017b], [Liu et al., 2015], [Ma et al., 2018a], [Thai et al., 2018], [Schenk et al., 2014], [Heimbs et al., 2007], [Heimbs et al., 2010], [Xiang et al., 2020], [Ma and You, 2014], [Wang and Zhou, 2017], [Song et al., 2012], [Yang et al., 2016], [Zaghloul and Bone, 2020], [Xiang et al., 2018] figure from [Xiang et al., 2018]</p>		
<b>Shell elements for both panels and creases</b> 	<p>This formulation simulates both creases and panels using shell elements so that the compliant creases can be captured.</p>	<p>This formulation is useful for simulating active origami because active origami systems usually have actuating compliant creases.</p>
<p><b>Reference</b> [Zhu and Filipov, 2019b], [Zhu and Filipov, 2020], [Hernandez et al., 2016b], [Hernandez et al., 2016a] figure from [Hernandez et al., 2016a]</p>		
<b>Solid elements</b> 	<p>This formulation can capture the non-negligible thickness in origami.</p>	<p>Suitable for simulating thick origami or origami-inspired systems with blocked volume.</p>
<p><b>Reference</b> [Fang et al., 2018], [Kwok, 2020] figure from [Kwok, 2020]</p>		

under applied loading (or self-folding) to where the system is in equilibrium. This case usually forms a boundary value problem (BVP) where the internal forces (the Jacobian of the internal strain energy  $U$ ) are equal to the external applied loads:  $\nabla_x U(\mathbf{x}) = F_{ext}$ . These BVPs can be solved using various nonlinear BVP solvers (implicit solvers). Figure A.12 (d) demonstrates how typical nonlinear BVP solvers break the target load into small increments of load ( $\delta F_{ext}$ ). Within each increment, the deformed state is iteratively updated to minimize error so that the solver can find the real solution (following the zig-zag curves in Fig. A.12 (d) to find the ground truth curve).

For dynamic behaviour, the deformations occur rapidly, the kinetic energy of the system is no longer negligible, and we solve for the origami motions over time. Solving for the dynamic behaviors usually forms an initial value problem (IVP) (see Fig. A.12 (c)). The numerical integration methods previously introduced for kinematic simulations can also be used to solve these IVPs. These are explicit solution methods because they do not have iterative loops within their formulations (see Fig. A.12 (e)), which makes them faster than implicit methods per incremental step. However, because no iterative loops are used to minimize error, the numerical errors can accumulate over time. The accumulation of error limits the step length ( $\delta t$ ) of explicit methods, so these methods need to take large number of small steps for convergence and for achieving reasonable fidelity. Overall, this large number of steps typically makes solving dynamic simulations with explicit solvers more time consuming when compared to solving static problems with implicit solvers.

A quasi-static simulation is a dynamic simulation that assumes a slow loading rate so kinetic energy is insignificant and instead the structural response is governed only by the static behaviors. The quasi-static simulation is useful when simulating origami with contact related behaviors such as the graded stiffness studied in [Ma et al., 2018b].

In the following subsections, we introduce mechanics-based origami simulations and focus on the models to represent origami structures (i.e. part (a) of Fig. A.12). After constructing the origami model, applying implicit or explicit solvers to run the simulation follows common procedures of mechanical analysis. A summary of different implicit solvers can be found in the work by Leon et al. [Leon et al., 2014] and common explicit solvers for dynamics simulations can be found in structural dynamics text books [Chopra, 2014, Clough and Penzien, 1975]. This section is arranged as follows. First, we introduce rigid panel models for kinematic analysis which can be seen as the transition from kinematics-based simulations to mechanics-based simulations. Next, we present bar and hinge models and plate theory based models, which are two popular reduced-order models for origami structures. We then introduce finite element simulations for origami structures that can offer high fidelity results. Following the discussion of these models, we proposed building hybrid reduced-order models for origami systems, and discuss how contact behaviors can be simulated for origami systems. Table A.3 and Table A.4 summarizes the models we cover in this section.



### Study simple mechanical behaviors using kinematic simulations

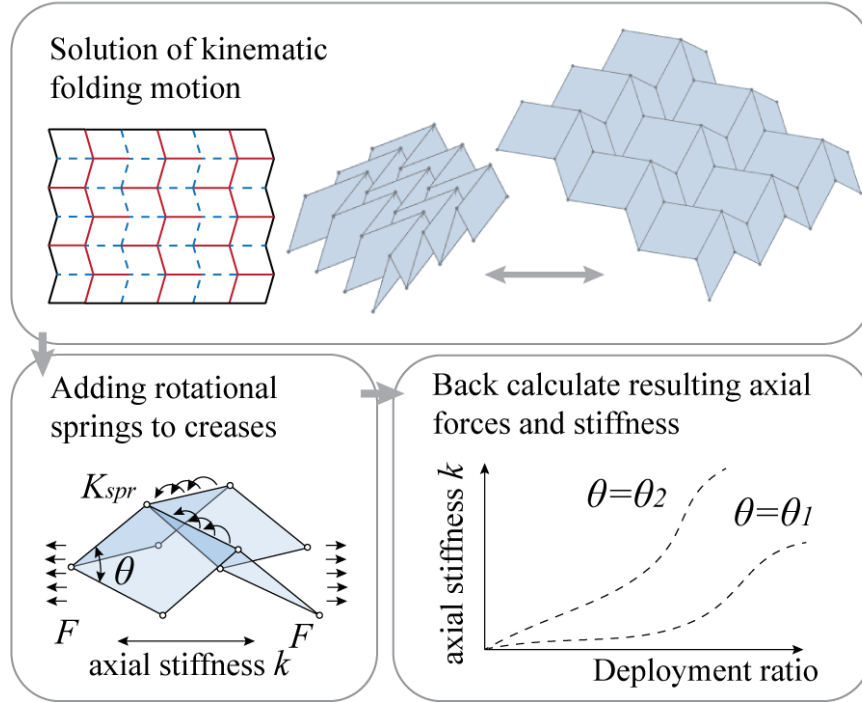


Figure A.13: Using kinematic simulations to capture simple mechanical responses.

#### A.4.1 Rigid panel models

The close connection between kinematic and mechanical simulations of origami can be illustrated by considering the folding stiffness of a Miura-ori structure; see Fig. A.13. After assigning rotational springs to the folding creases of this origami pattern, the internal hinge moments and total elastic potential energy at any rigid-foldable configuration can be calculated using the kinematics given in Eqn. (A.12-A.15). From the elastic potential energy, the force-displacement response (and thus stiffness) of the fold pattern can be found using Castigliano’s theorem. This approach allows for rapid parametric studies, but is only suitable for obtaining simple mechanical behavior of rigid-foldable origami with known kinematics [Wei et al., 2013, Kamrava et al., 2018, Hanna et al., 2014, Yasuda and Yang, 2015, Yasuda et al., 2020, Yang and Silverberg, 2017a].

Next, we introduce rigid panel models for origami structures. These models can be seen as transitional models that lie between kinematic simulations and mechanical simulations. They usually use rigid truss elements or frame elements to represent the panels of origami structures and can capture the folding kinematics of origami.

Figure A.14 (a) demonstrates a technique to represent rigid origami panels using rigid bar elements and pin-joints. To analyze the kinematic folding motions of the origami system, one can

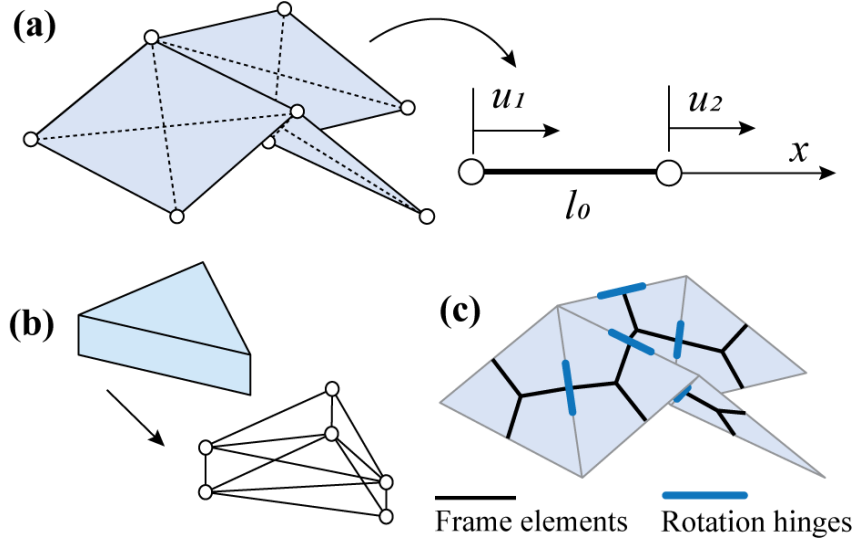


Figure A.14: Rigid panel models for kinematic studies. (a) Rigid bar models; (b) Rigid truss model for thick origami; (c) Rigid frame models.

study the compatibility matrix  $C_{bar}$  of the rigid bar system [Schenk and Guest, 2010, Zhang and Kawaguchi, 2021, Zhang et al., 2018]. This compatibility matrix relates the nodal deformation of the structure  $\mathbf{u}$  to the internal member strains  $\mathbf{e}$  as:

$$C_{bar}(\mathbf{u}) \mathbf{u} = \mathbf{e}, \quad (\text{A.23})$$

We use the 1D bar shown on Fig. A.14 (a) to demonstrate how this compatibility matrix can be calculated. The engineering strain of this bar is expressed as  $e = (u_2 - u_1)/l$ . Reorganizing the equation gives  $e = [-1/l, 1/l][u_1, u_2]^T$  so the compatibility matrix is  $[-1/l, 1/l]$ . More systematic ways of deriving the compatibility matrix for complex structures can be found in structural analysis textbooks [McGuire et al., 2000] or in the following papers [Schenk and Guest, 2010, Zhang and Kawaguchi, 2021, Zhang et al., 2018]. This compatibility matrix also relates the velocity of bar strains with respect to the velocity of nodal displacements:

$$C_{bar}(\mathbf{u}) \dot{\mathbf{u}} = \dot{\mathbf{e}}, \quad (\text{A.24})$$

Assuming the panel is rigid, there would be no bar strains throughout the kinematic motion which is equivalent to:

$$C_{bar} \dot{\mathbf{u}} = 0. \quad (\text{A.25})$$

This Eqn. (A.25) is similar to Eqn. (A.19) introduced in subsection A.3.4. Both of these equations

form an ODE and can be solved using the numerical integration methods and explicit solvers. The  $C_{bar}$  matrix demonstrated in Eqn. (A.25) plays the same role as the  $C$  matrix in Eqn. (A.19). However, the derivation of  $C_{bar}$  is directly obtained by solving the compatibility matrix rather than taking a kinematic approach. On top of the rigid bar constraint, rotational springs can be added to enable the simulation of mechanical loading and other stiffness properties [Schenk and Guest, 2010, Fuchi et al., 2015].

In addition to modeling thin origami panels, rigid truss models can also be used to capture the kinematic motion of thick origami panels [Zhang and Kawaguchi, 2021]. In this formulation, a set of truss-based pyramids are used to represent the thick and rigid origami panels (see Fig. A.14 (b)). Although the current model has not been used to study deformable thick panels, this model can be extended for such studies in the future.

Hayakawa et al. introduced a related frame element based alternative for origami kinematic simulation [Hayakawa and Ohsaki, 2021, Hayakawa and Ohsaki, 2019] (Figure A.14 (c)). Here, triangulated panels of the origami are represented using three frame elements that are rigidly connected at the panel center, and the folding creases are represented by rotational hinges at the crease line where two panels connect. If the frame elements remain rigid during the deformation, the system will preserve the kinematics of the rigid and thin origami. After deriving the compatibility matrix, numerical integration allows to track kinematically admissible motions. The work by Hayakawa et al. also demonstrated that this model can be used for inverse design of origami patterns that fit arbitrary surfaces [Hayakawa and Ohsaki, 2021, Hayakawa and Ohsaki, 2019].

## A.4.2 Bar and hinge models

The bar and hinge model has become a widely used reduced-order mechanical model for simulating origami systems [Filipov et al., 2015, Mukhopadhyay et al., 2020, Kaufmann et al., 2021, Wei et al., 2013]. The model is sometimes referred to as the truss-based mechanism model [Greco et al., 2006, Gillman et al., 2018, Gillman et al., 2019] or the pin-jointed bar framework [Schenk and Guest, 2010], but here, will use the name *bar and hinge model* because it is an expressive name (directly pointing to the two elements involved).

The model represents an origami using bar elements and rotational spring elements (hinges with rotational stiffness) as shown in Fig. A.15 (a). The bar elements are extensional springs in 3D space that can capture the stretching and shearing of origami panels (and creases). On the other hand, the rotational spring elements are rotating hinges with stiffness that can capture the crease folding or panel bending. The strain energy stored within the entire origami system can be

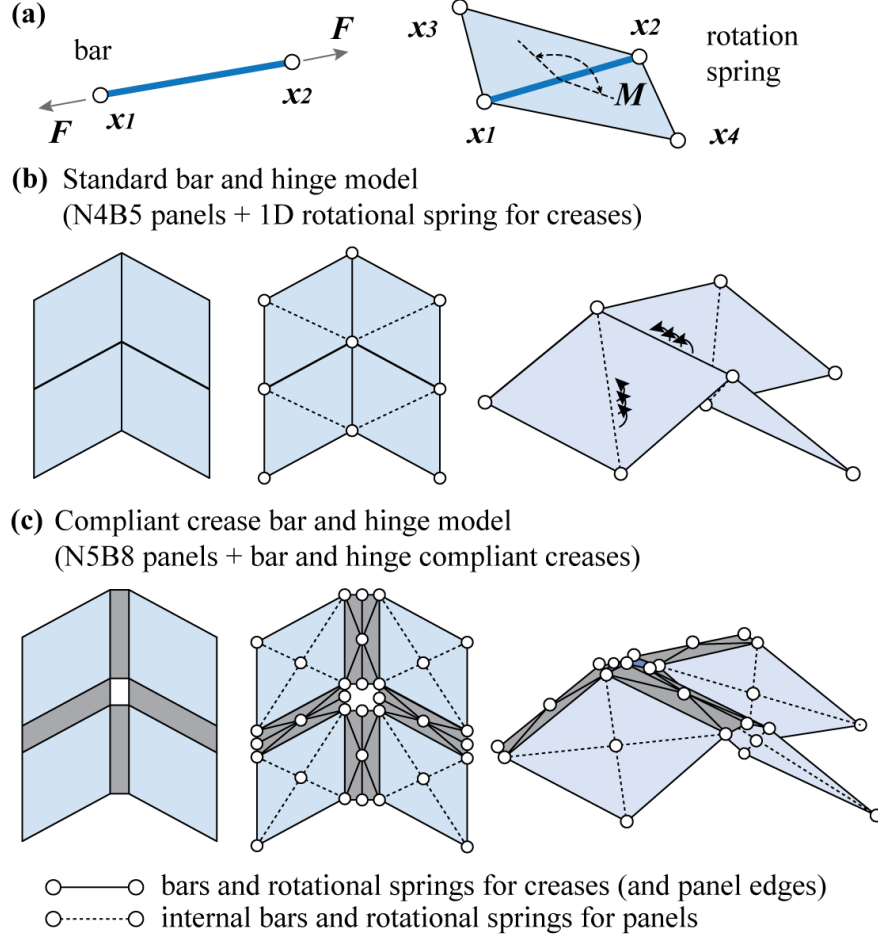


Figure A.15: (a) The bar element and the rotational spring element; (b) standard bar and hinge model for simulating origami; (c) compliant crease bar and hinge model for simulating origami.

expressed as:

$$U = \sum_{i=1}^{N_{bar}} U_{bar,i} + \sum_{j=1}^{N_{spr}} U_{spr,j}, \quad (\text{A.26})$$

where  $U_{bar,i}$  represents the strain energy in bar  $i$  and the  $U_{spr,j}$  gives the strain energy of rotational spring  $j$ . The simplest bar element is a linear spring and can be expressed as:

$$U_{bar,i} = \frac{1}{2} \frac{E_i A_i}{l_{0,i}} ((\mathbf{x}_1 - \mathbf{x}_2) - l_{0,i})^2, \quad (\text{A.27})$$

where  $E_i$  is the Young's modulus,  $A_i$  is the bar area,  $\mathbf{x}_1$  and  $\mathbf{x}_2$  are the nodal coordinates, and  $l_{0,i}$  is the original length of the bar. Many studies use this linear elastic bar formulation because it is simple and easy to derive [Gillman et al., 2018, Gillman et al., 2019, Kaufmann et al., 2021, Kidambi

and Wang, 2020, Li and Wang, 2015, Zhu and Filipov, 2020, Mukhopadhyay et al., 2020, Pagano et al., 2017]. More advanced hyper-elastic formulations are also available for deriving the total potential of the bar element [Liu and Paulino, 2016, Liu and Paulino, 2017a, Liu and Paulino, 2018a]. Similarly, the linear elastic rotational spring model is the simplest hinge element and it can be expressed as:

$$U_{spr,i}(\mathbf{x}_1, \mathbf{x}_2, \mathbf{x}_3, \mathbf{x}_4) = \frac{1}{2} K_{spr,i} (\phi(\mathbf{x}_1, \mathbf{x}_2, \mathbf{x}_3, \mathbf{x}_4) - \phi_0)^2, \quad (\text{A.28})$$

where  $K_{spr,i}$  is the spring stiffness,  $\mathbf{x}_1$  to  $\mathbf{x}_4$  are the nodal coordinates, and  $\phi_0$  is the stress free dihedral angle of the fold. The current dihedral angle can be calculated using the current nodal coordinates of the four nodes adjacent to the fold (see Fig. A.15 (a)), and detailed calculations of this function  $\phi$  can be found in [Liu and Paulino, 2017a, Gillman et al., 2018, Hu et al., 2021]. Most existing studies use this linear elastic rotational spring formulation [Pagano et al., 2017, Mukhopadhyay et al., 2020, Gillman et al., 2018, Gillman et al., 2019, Kaufmann et al., 2021, Kidambi and Wang, 2020, Li and Wang, 2015, Zhu and Filipov, 2020].

There are different ways of meshing an origami structure using the bar elements and the rotational spring elements. The N4B5 model [Schenk and Guest, 2010, Liu and Paulino, 2017a] and the N5B8 model [Filipov et al., 2017, Liu and Paulino, 2018a] are two common models for a quad origami panel. The N4B5 model represents a quad panel with 4 nodes and 5 bar elements (see Fig. A.15 (b)). This N4B5 model can capture the bending behavior across one diagonal axis of the quad panel but produces a skewed deformation under in-plane axial loading. In order to avoid this skewed deformation, the N5B8 model (see Fig. A.15 (c)) was proposed by Filipov et al. in [Filipov et al., 2017]. This panel model contains 5 nodes and 8 bars. With the additional bars, it produces a more accurate deformation under the applied axial loading and can capture bending across both diagonals of the panel. In addition to these models for quad based origami, the generalized N4B5 and generalized N5B8 models are also proposed for panels with arbitrary number of edges by Liu and Paulino in [Liu and Paulino, 2018a]. Finally, explicit derivations for trapezoidal and hexagonal panels are provided by Redoutey et al. in [Redoutey et al., 2021].

In a standard bar and hinge model, the folding creases of the origami structure are represented with individual rotational springs [Filipov et al., 2015, Filipov et al., 2017, Filipov and Redoutey, 2018, Liu et al., 2020, Liu et al., 2019, Gillman et al., 2018, Gillman et al., 2019, Kaufmann et al., 2021, Li and Wang, 2015, Mukhopadhyay et al., 2020, Pagano et al., 2017, Wei et al., 2013]. In this formulation, the folding creases are simplified as lines with no width (see Fig. A.15 (b)). This type of model can capture the crease folding, panel bending, panel stretching, and panel shearing deformations. However, the model cannot capture possible extensional and torsional crease motions in compliant creases.

More recently, the bar and hinge model has been extended to capture compliant creases within active origami [Zhu and Filipov, 2019b, Zhu and Filipov, 2020]. In this formulation, the compliant creases are represented using 7 nodes, 12 bars, and 8 rotational springs (see Fig. A.15 (c)). Using compliant crease bar and hinge model can further capture the extensional strain energy in folding creases, which is necessary for simulating some bistable behaviors in origami structures [Zhu and Filipov, 2019b, Zhu and Filipov, 2020].

There are three main approaches to assigning stiffness parameters (bar areas and rotational spring stiffness) when using bar and hinge models. First, it is possible to assign fictitious values to the bar area and the rotational spring stiffness [Ghassaei et al., 2018]. This technique can be used when studying the algorithmic properties of origami simulations (such as studying parallel computation or convergence properties), where we are less interested in predicting the exact physical origami behaviors. Second, we can derive the stiffness parameters by matching the stiffness of a bar and hinge model to that of a theoretical plate model [Filipov et al., 2017, Zhu and Filipov, 2020, Liu and Paulino, 2018a]. Because these derivations tend to be based on a small-deformation assumption, the generated stiffness parameters can produce mechanical behaviors that are stiffer than physical experiments where large deformations such as panel buckling occur. Finally, it is possible to assign the bar area and the rotational spring stiffness by doing curve fitting using experiments [Masana and Daqaq, 2019]. This approach tends to produce a more accurate prediction of the origami stiffness because curve fitting can artificially account for large panel deformations. In other words, using curve fitting is similar to using the secant stiffness of the behavior, while matching with theoretical plates is similar to using the initial tangent stiffness.

Simulating origami mechanical behaviors using bar and hinge models and static nonlinear solvers has become popular because these models have a simple formulation and are computationally efficient. This simulation technique can capture the global response of origami structures and allows richer deformation to be simulated when compared to kinematics-based simulations. So far, bar and hinge model simulation techniques have been successfully used for studying the bistability and multistability in origami hypars [Liu et al., 2019, Filipov and Redoutey, 2018] and Kresling patterns [Cai et al., 2016a, Liu and Paulino, 2017a, Pagano et al., 2017, Kidambi and Wang, 2020], simulating the folding motions of tubular origami [Filipov et al., 2015, Mukhopadhyay et al., 2020], studying the behaviors of compliant crease origami [Zhu and Filipov, 2019b, Zhu and Filipov, 2020], designing origami metamaterials [Wei et al., 2013, Pratapa et al., 2021], optimizing the performance of origami patterns [Gillman et al., 2019, Fuchi et al., 2015], studying the influence of origami defects [Liu et al., 2020], and more. However, the bar and hinge model cannot capture localized behaviors such as crease buckling, panel buckling, stress concentration, and local material plasticity in the origami structures.

The bar and hinge model can also be used to study the dynamics of origami systems. To do

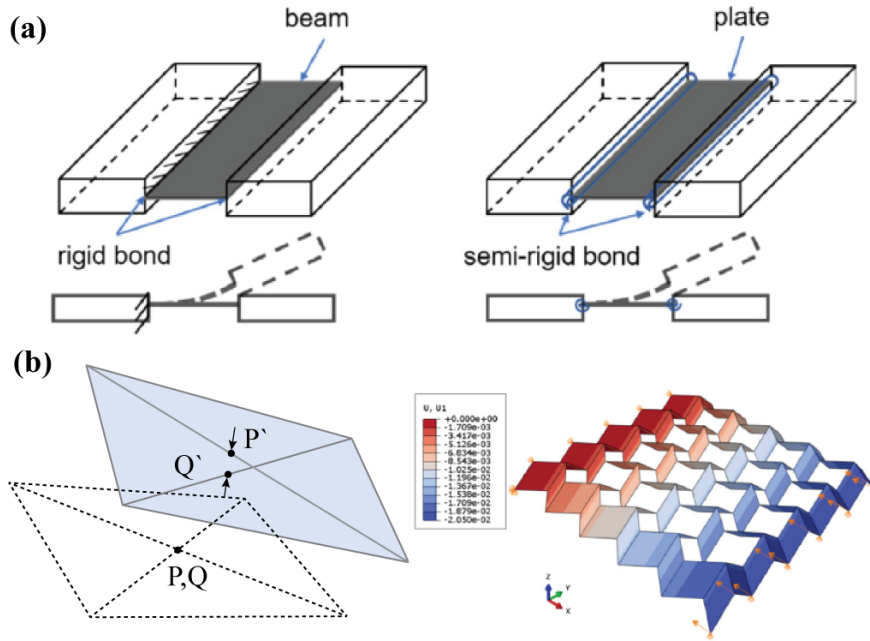


Figure A.16: Using plate theory based models to simulate origami systems. (a) from [Zhang et al., 2021], (b) right from [Hu et al., 2021].

that, one needs to use a particle bar and hinge formulation. This formulation captures the mass of origami by assigning “particle” mass to the nodes of the origami models [Xia and Wang, 2019, Xia et al., 2021a, Yu et al., 2019, Dong et al., 2021]. The velocity and acceleration of the origami are also stored at these mass nodes. [Xia and Wang, 2019, Xia et al., 2021a, Yu et al., 2019, Dong et al., 2021]. The dynamic motions of the origami structure can be solved using explicit solvers such as those introduced in [Yu et al., 2011, Chopra, 2014, Clough and Penzien, 1975]. This model is used to study the folding dynamics of various origami structures including Miura tubes [Xia et al., 2021a], Miura sheets [Bhovad and Li, 2021], waterbomb tubes [Dong et al., 2021], and Ron-Resch patterns [Yu et al., 2019]. This model can also be used to study “chaotic” type dynamic folding behaviors in origami [Fonseca et al., 2019, Yasuda et al., 2020, Han et al., 2020].

### A.4.3 Plate theory based simulations

Because origami tends to have planar characteristics, plate theories can be used for simulating both compliant creases and deformable origami panels. In the work by Zhang et. al., an analytical plate model for simulating the mechanics of compliant creases is proposed [Zhang et al., 2021]. In their work, additional rotational springs were added at the connection between the origami panels and the compliant creases so that richer deformations could be enabled (Fig. A.16 (a)). In recent work

by Zhang [Zhang, 2021], this advanced plate theory based model is incorporated into a bar and hinge model to simulate the behaviors of an entire origami pattern.

Plate theory based models can also be used for capturing the behavior of origami panels. Hu et. al. [Hu et al., 2021] created a user defined quad element in ABAQUS to capture the small-deformation behaviors of origami plates. In their approach, the quad element is designed such that it can capture the panel bending using the separation distance between the center points of the two straight lines that connect opposite corners of the quad panel (Fig. A.16 (b)). The potential of this quad element is calculated as:

$$U = \frac{D^e}{2}(\Delta w)^2 = \frac{D^e}{2}(u_P - u_Q)^2. \quad (\text{A.29})$$

This formulation is derived with assumed small curvature deformation [Hu et al., 2021]. In the equation, the term  $D^e$  is a modified bending rigidity of the plate and the subtraction  $u_P - u_Q$  obtains the distance between point P' and Q' (see Fig. A.16 (b)). Their work demonstrates that if the panel deformation is governed by small-strain bending, the model can capture the origami behaviors rapidly. In addition to this formulation, the study by Soleimani et. al. [Soleimani et al., 2021] derived a plate theory based panel model using the first order shear deformation theory.

Using plate theory based panel models and crease models can be thought of as using finite element simulations with coarse meshes. These plate theory based simulations can provide a lower fidelity but more computationally efficient approaches to capture the behaviors of origami compared to the use of finite element simulation. However, plate theory based origami models cannot capture extreme local buckling and kinking because these models are derived with strict assumptions on the deformation shapes.

#### A.4.4 Finite element simulations

Finite element (FE) simulation is another popular technique for analyzing origami-inspired engineering structures. FE simulations provide approaches to capture the complicated local behaviors (such as local buckling and stress concentration [Heimbs et al., 2007, Heimbs et al., 2010, Ma et al., 2018a]) and material nonlinearity (such as plasticity [Karagiozova et al., 2019, Zhang et al., 2019]) in origami structures. Most commercial FE packages also have automated internal static and dynamic solvers so that users do not need to code their own numerical solvers. In this subsection, we focus on how FE simulations are used for studying the mechanical behaviors of origami systems such as stiffness under static loading and energy absorption under dynamic loading. In addition to these purely mechanical studies, FE simulations are also widely used for simulating multi-physical behaviors of origami systems, and this topic will be discuss in section A.5.

One way to model origami using FE is to represent the panels using shell elements and connect



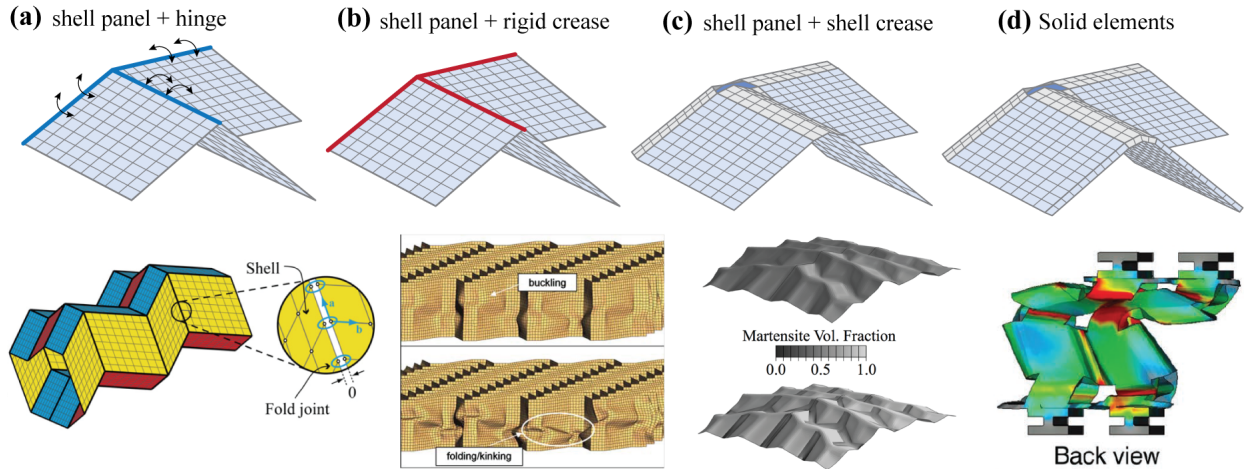


Figure A.17: Different types of FE models used for simulation of origami structures. The lower figures of (a) to (d) are from [Filipov et al., 2016], [Heimbs et al., 2007], [Hernandez et al., 2016a], and [Fang et al., 2016] respectively.

the panels using rotational springs or hinges [Filipov et al., 2015, Filipov et al., 2016, Filipov et al., 2017, Grey et al., 2019] (see Fig .A.17 (a)). This approach is commonly used for studying the mechanical properties of origami sheet and tubular structures because it can capture the relatively soft creases in such systems. Filipov et. al. have used this approach to study a reconfigurable tubular origami structure [Filipov et al., 2016] and a stiff zig-zag origami tube [Filipov et al., 2015]. Both the load bearing capacity and the eigen properties of origami tubes are investigated [Filipov et al., 2015, Filipov et al., 2016]. A similar approach was used in work by Grey et. al. [Grey et al., 2019] to study the deployment process of Miura-ori tubes with crease actuation.

Another way of modeling origami structures using FE simulation is to connect the shell element panels with fixed and rigid fold lines (see Fig .A.17 (b)). This formulation is suitable for studying the behaviors of origami-inspired devices such as metamaterials, crash boxes, and sandwich cores. These origami-inspired devices are not fabricated to be “deployed”. Instead, these devices are over-constrained and used as a single block of material with fixed creases. This FE simulation setup was used for exploring the static response [Yuan et al., 2020, Zhang et al., 2019] and the dynamic response [Karagiozova et al., 2019] of origami metamaterials. In addition, this formulation has been used for analyzing origami crash boxes for energy absorption applications [Ma and You, 2014, Wang and Zhou, 2017, Song et al., 2012, Yang et al., 2016]. In this prior research, physical experiments were also conducted and good agreements between the FE simulations and experiments were obtained. Wang and Zhou [Wang and Zhou, 2017] use this approach to study the influence of imperfection sensitivity of origami crash boxes. Xiang et. al. [Xiang et al., 2020] provided a detailed review on using origami-inspired structures for energy absorption. Moreover,

Heimbs et. al. [Heimbs et al., 2007, Heimbs et al., 2010] used this approach to study the behavior of an origami sandwich core. In their work, complex material failures such as delamination was also captured using a special technique of overlaying shell elements in LS-DYNA. Schenk et. al. [Schenk et al., 2014] used this approach to study the behavior of stacked Miura-ori sandwich beams for blast-resistance. In all of the above studies, the deployment of the origami structure is restricted and the systems are kinematically over constrained. Typical deformation of these systems include panel buckling and stretching, and the local crease deformations are not considered to be important for the global behaviors.

Compliant origami creases can also be modeled using shell elements as shown in Fig. A.17 (c) [Zhu and Filipov, 2019b, Zhu and Filipov, 2020, Hernandez et al., 2016b, Hernandez et al., 2016a]. In this modeling approach, the geometry and stiffness of the compliant creases can be accurately captured using shell elements with fine meshes. Simulating the compliant creases explicitly can be important for many reasons. For example, it allows users to simulate the active folding from plate-based bending actuators [Hernandez et al., 2016a].

Finally, solid elements can also be used for simulating origami-inspired system [Fang et al., 2018, Kwok, 2020]. In these cases, the thickness of the origami-inspired systems is of importance so solid elements are needed to properly capture the full system geometry. Using this approach is computationally expensive because fine meshes across the thickness of origami panels are needed to capture the accurate panel bending behavior. Thus, solid elements are usually not used for origami simulation unless explicitly capturing the thickness is of essential importance.

One major reason behind the popularity of using FE simulation for origami structures is the existence of commercially available software programs such as ABAQUS [Ma and You, 2014, Ma et al., 2018b, Yuan et al., 2020], ANSYS [Heimbs et al., 2007, Zaghoul and Bone, 2020], and LS-DYNA [Heimbs et al., 2007, Heimbs et al., 2010, Zaghoul and Bone, 2020]. These commercially available programs provide a wide variety of material models and element types, and allow researchers to perform static loading, quasi-static loading, or dynamic loading using standardized procedures through convenient user interfaces. The FE simulations also capture local structural responses such as stress concentration and local buckling [Ma et al., 2018a, Heimbs et al., 2007, Heimbs et al., 2010, Liu et al., 2015], which is otherwise difficult to simulate with reduced-order simulation techniques. However, building FE models and running the analyses is time consuming, especially if the origami is made with non-repetitive base patterns. Because of those difficulties, most of the studies covered in this subsection were based on simple patterns such as the Miura-ori pattern. Transforming “freeform” origami designs into executable FE simulation programs in a stream-lined manner is still a difficult task to be resolved. Another limitation of using FE simulation is that an FE simulation acts like a black box. Many scientific explorations and theoretical developments still favor the use of reduced-order simulations because they can reveal

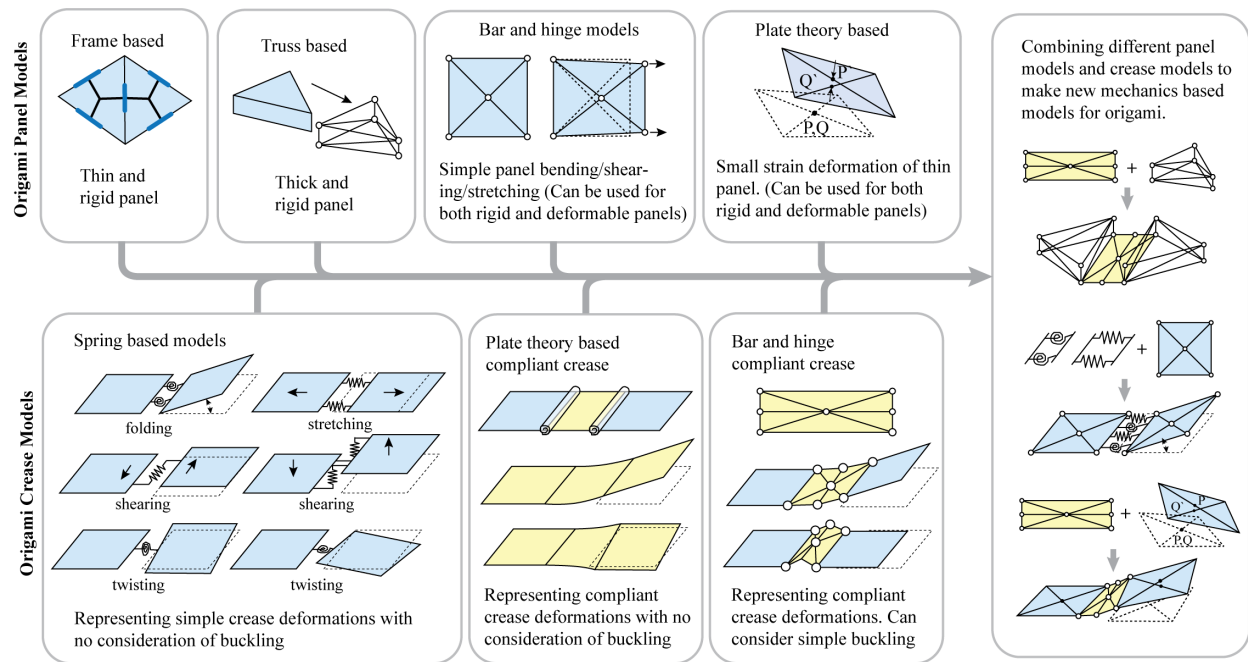


Figure A.18: Different types of mechanical models for origami panels and creases.

the underlying theoretical behaviors (as discussed further in Section A.7).

#### A.4.5 Rethinking reduced order mechanical models: Hybrid formulations

In this subsection, we take a step back and provide a holistic discussion on the formulation of reduced-order mechanical models for origami systems. Unlike kinematics-based simulations for origami systems, mechanics-based simulations allow users to combine different panel models and crease models to assemble new “element-based” formulations. We can think of the formulation of a mechanical model as “gluing” different “elements” at the nodes of the origami structure. These different elements will generate the relationships between internal forces and nodal deformations needed to simulate the folding and loading behaviors of origami systems. When FE models are used for simulating origami systems, we are already modeling the origami by grouping different panel models and different crease models. The same perspective can be applied to the reduced-order origami models for creating new hybrid formulations. Figure A.18 demonstrates how combining different simplified origami panel models and crease models can potentially create new reduced-order simulation techniques. The key of achieving this combination is to ensure that the panel models have identical boundary setups (number of nodes and number of DOF per node) as the crease models.

All models demonstrated in Fig. A.18 were discussed previously except the spring based mod-

els for creases, which we will now briefly discuss. The simplest way of modeling the mechanical behavior of origami creases is to use a single spring element. In addition to the common rotational springs for modeling crease folding motions [Liu and Paulino, 2017a, Gillman et al., 2018, Gillman et al., 2019, Zhu and Filipov, 2019b, Filipov et al., 2015], other deformations between the two panels can also be captured using spring elements with different forms. In general, there are six different forms of relative deformations between the two panels as shown in the bottom left box of Figure A.18. In many situations, we do not need all six forms of deformations to simulate the accurate global mechanical behaviors of origami systems. For example, studying the Poisson's effects or the stretching stiffness of Miura sheet only requires using rotational springs for the folding motion [Schenk and Guest, 2010, Wei et al., 2013] and the simulation of a bistable origami cone can be accomplished with rotational springs and extensional springs [Faber et al., 2018]. There are also models including all six forms of springs such as the one proposed by Soleimani et al. [Soleimani et al., 2021]. These six forms of springs provide a useful tool to model the behaviors of lamina emergent mechanism (LEM) type joints for origami. Using these LEM type joints provides a novel technique for building thick origami systems (introduced in section A.3.7). The work by Delimont et al. provides a summary of different LEM joints and equations for calculating the corresponding spring stiffness [Delimont et al., 2015]. Spring based models are appropriate for simulating linear origami crease behaviors or behaviors with small deformations. However, the models are not suitable for capturing the distributed width of compliant creases or for simulating localized behaviors such as buckling of creases.

Considering the variety of different panel and crease models, one can create new origami models tailored for specific origami systems by combining appropriate models (Fig. A.18). In this way, one can create a hybrid origami model that inherits both the capabilities from the selected crease model and the selected panel model. For example, the truss-based thick panel model [Zhang and Kawaguchi, 2021] can be grouped with the bar and hinge compliant crease model [Zhu and Filipov, 2020, Zhu and Filipov, 2019b] to capture the behaviors of origami systems with strained creases and thick panels. Alternatively, the plate theory based panels [Soleimani et al., 2021, Hu et al., 2021] could be grouped with spring based creases to simulate deformable origami with small-strain plate bending and linear crease deformations.

Some of the currently implemented packages for origami simulation already allow users to choose between different combinations. For example, the bar and hinge MERLIN2 package allows users to switch between the N4B5 and N5B8 panel models [Liu and Paulino, 2018a, Liu and Paulino, 2018b] and the bar and hinge SWOMPS package allows users to switch between the spring based creases and compliant creases [Zhu and Filipov, 2021a, Zhu and Filipov, 2021b]. However, the variability provided with current packages is still limited. Future studies on reduced-order mechanical models for origami systems can explore the potential of generating a more uni-

fied formulation to incorporate different panel models and crease models. In addition, future implementations can expand built-in panel models and crease models so that users can create more on-demand combinations for the specific origami that they are working with.

#### **A.4.6 Capturing panel contact**

One fundamental limitations in the kinematics-based simulations of origami is that panel contact within origami systems cannot be easily simulated (see Fig. A.9). With the help of mechanics-based simulation techniques, the issue of contact can be resolved. Capturing the occurrence and behavior of panel contact can be important for studying origami-inspired metamaterials or crash boxes as shown in [Yuan et al., 2020, Zhang et al., 2019, Ma and You, 2014]. In this subsection, we briefly discuss how mechanics-based simulation techniques can capture the panel contact within origami systems. We discuss panel contact models for static simulations and dynamic simulations separately because they tend to have different formulations and characteristics.

To prevent the origami panels from penetrating each other in a static simulation, the internal strain energy (potential) of the origami structure needs to be adjusted. This can be achieved by changing the strain energy formulation of the rotational springs. In the work by Liu and Paulino [Liu and Paulino, 2017a, Liu and Paulino, 2016] a piecewise penalty function is added to the strain energy of the rotational springs. This additional penalty function gives a large stiffness when the crease folds towards  $180^\circ$  so that the crease is prevented from over-folding (see Fig. A.19 (a)). Similarly, a slightly different but continuous strain energy formulation of rotational springs is provided by Gillman et. al. [Gillman et al., 2018, Gillman et al., 2019] (see Fig. A.19 (b)). This continuous form can also avoid local penetration.

However, these formulations only prevent panels from penetrating each other locally (the two panels need to share a common hinge). A more thorough penetration prevention technique was developed in [Zhu and Filipov, 2019a]. In their work, the penalty function for panel contact is developed based on the distance between a contacting triangle panel and a contacting node. This technique can prevent panel penetration globally and the contacting panels do not need to share a common crease. Figure A.19 (c) demonstrates a sample application of this model, where contact results in a stiffness jump between two separate but interlocked origami strips. This model also provides the capability to capture thickness in origami within a mechanical simulation [Zhu and Filipov, 2019a] (see Fig. A.19 (d)).

Both the local and the global panel contact models introduced above have a potential based formulation. That is to say, the panel contact forces can be determined based on the current configuration of the origami (without the history of prior configurations). Because these are potential based formulations, the contact forces within these models are conservative (there is no energy

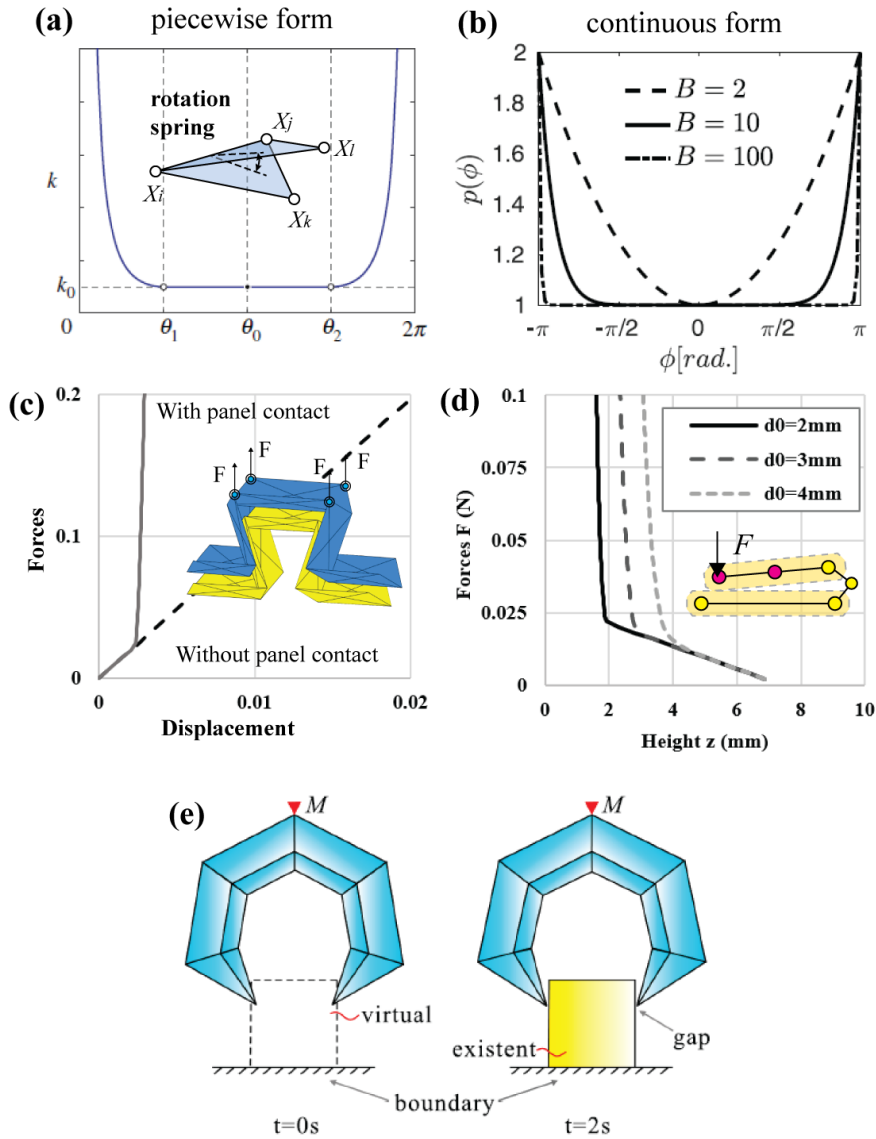


Figure A.19: Panel contact and prevention of panel penetration in origami simulation. Figure (a) from [Liu and Paulino, 2017a], figure (b) from [Gillman et al., 2018], figures (c) and (d) from [Zhu and Filipov, 2019a], and figure (e) from [Dong and Yu, 2021].

dissipation). One advantage of these contact models is that they are fast to solve because they form a BVP that can be solved statically using implicit solution methods. However, these potential based contact models cannot capture frictional forces. To resolve this limitation, one needs to construct IVPs and use dynamic based (or quasi static based) simulation techniques such as those proposed in the work by Dong and Yu [Dong and Yu, 2021] (see Fig. A.19 (e)). In their model, the panel contact forces are not only calculated using the current origami configuration, but are also calculated using the velocity of origami motion (see Eqn. (14) in reference [Dong and Yu, 2021]). This panel contact model forms an IVP because calculating the velocity of origami motion needs to use the origami configurations from previous steps. Solving these dynamic contact models are more time consuming because they need to use the explicit dynamic solution methods.

In addition to using the above mentioned reduced-order models for simulating contact, commercial FE simulation software can also be used to study contact related origami behaviors. For example, Ma et. al. studied the quasi-static loading of an origami-inspired structure with graded stiffness [Ma et al., 2018b] and an origami crash box for energy absorption [Ma et al., 2016]. Similarly, Heimbs et. al. studied dynamic impact loading [Heimbs et al., 2010] and quasi-static loading [Heimbs et al., 2007] of origami sandwich fold cores using FE simulations. Usually, even when exploring static contact behaviors in origami, a dynamic simulation (in a quasi-static manner) is performed [Song et al., 2012, Ma et al., 2018b, Wang and Zhou, 2017, Ma and You, 2014, Xiang et al., 2018]. The reasoning is that explicit solvers in FE simulation packages often provide better contact models and contact searching algorithms [MIT, 2017a, MIT, 2017b, MIT, 2017c].

## **A.5 Multi-Physics Based Simulations**

Recently, there has been an increased need to analyze the multi-physics based active folding and other non-mechanical properties of origami-inspired systems such as thermally active folding, magnetic active folding, electromagnetic properties of origami-inspired systems, drag force of origami surfaces in submerged environments, heat conduction properties of origami, etc. Figure A.20 (a) gives a general flow-chart for analyzing origami using multi-physics based simulations. Generally speaking, there are two parts of the analysis process that involve the use of multi-physics simulations and they are: simulation of the actuation for active folding and the simulation of non-mechanical properties. In this section, we discuss these two aspects of origami multi-physics.

Traditionally, origami artists fold an origami using their hands and their craftsmanship. But nowadays, origami engineers take other approaches and fold origami-inspired engineering systems using active materials or responsive systems. For example, origami-inspired systems can be folded using active hydrogels [Na et al., 2015, Yoon et al., 2014, Kang et al., 2019], metallic morphs

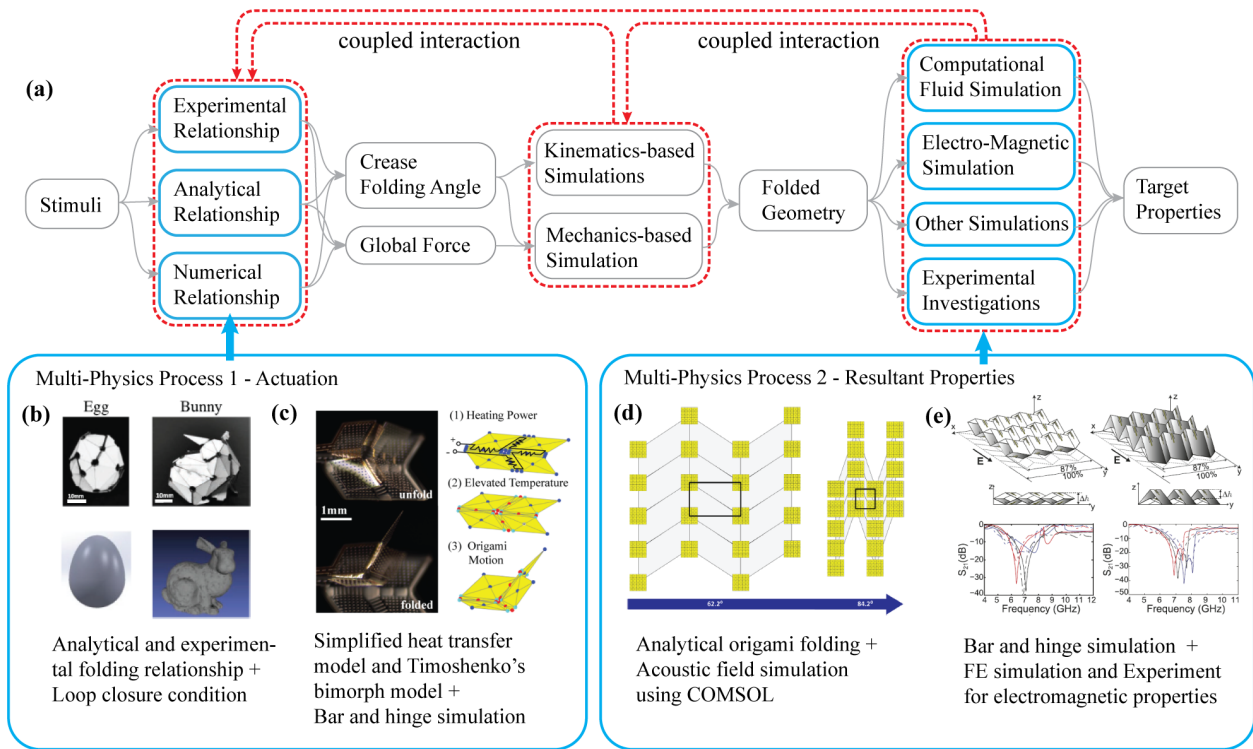


Figure A.20: Multi-physics simulation of active origami. Figure (b) from [An et al., 2018], figure (c) from [Zhu and Filipov, 2021a], figure (d) from [Hathcock et al., 2021], figure (e) from [Nauroze et al., 2018].

with residual stresses [Leong et al., 2009, Leong et al., 2008, Bassik et al., 2009, Arora et al., 2006], shape memory polymers [Felton et al., 2014, An et al., 2018, Mao et al., 2015], shape memory alloys [Hawkes et al., 2010, Paik and Wood, 2012, Hernandez et al., 2016a], electro-thermal actuators [Zhu et al., 2020, Zhu and Filipov, 2021a], active magnetic systems [Shaar et al., 2015, Iwase and Shimoyama, 2005, Xu et al., 2019, Swaminathan et al., 2021], etc. The folding motions generated using these actuation mechanisms have a multi-physical nature, and thus, multi-physics based simulations are needed.

The multi-physics based actuation can act on the origami through two major types of action: by triggering crease folding or by triggering globally applied forces. In the first type, the applied stimuli first trigger the material in the crease region to develop strains and stresses. The strains and stresses then force the crease to bend and transform the origami into a folded geometry. Most active origami systems achieve shape morphing using this form of actuation. When determining the relationship between the applied stimuli and the crease folding, both experiment-based and simulation-based approaches can be used. For example, in the work by Leong et al. [Leong et al., 2009, Leong et al., 2008], experiments were used to determine the folding angle given the heat-



ing or other applied stimuli. In the work by Zhu and Filipov [Zhu and Filipov, 2021a], a bar and hinge model with heat transfer and a Timoshenko's bi-material morph model are used to solve the crease temperature and the folding motion from the applied heating power [Timoshenko, 1925]. In general, active-material crease folding tends to rely on using compliant creases with distributed crease regions and bi-material layers. Therefore, the behavior of these active origami can be better captured using models such as the smooth fold model, the compliant crease bar and hinge model, or with finite element simulations. The analysis of the bi-material morph by Timoshenko [Timoshenko, 1925] also provides a direct analytical solution to correlate material strains and the crease folding of active compliant creases.

Stimuli can also generate globally applied forces onto the origami to achieve the folding motion. Magnetically activated origami are one major genre of active origami using this form of actuation [Shaar et al., 2015, Iwase and Shimoyama, 2005, Xu et al., 2019, Swaminathan et al., 2021]. Magnetic forces acting on the origami structure can be calculated based on the orientation of the embedded magnets and the applied magnetic field. After calculating the magnetic forces, the folded configuration can be tracked using mechanics-based origami simulations. The work by Swaminathan et al. [Swaminathan et al., 2021] provides a simulation technique that can capture these magnetic forces using the Kangaroo solver in Rhino [Piker, 2017, Piker, 2013]. Apart from magnetic systems, the forces could also be applied directly by connecting the passive origami system to an active supporting mechanism [Chen et al., 2019a]. With such a system, the connected origami is deployed by forces from the supporting mechanism.

In addition to using multi-physics simulations to capture the actuation of active origami, multi-physics simulations are also needed to capture the non-mechanical properties of origami-inspired structures for design and for optimization. For example, origami-inspired structures have been used to create frequency selective surface (FSS) for filtering electro-magnetic waves [Nauroze et al., 2018, Nauroze and Tentzeris, 2019, Fuchi et al., 2012, Fuchi et al., 2016, Cui et al., 2019, Biswas et al., 2020]. To analyze and design the performance of these FSS devices, electro-magnetic simulation through commercial FE software such as ANSYS HFSS can be used [Nauroze et al., 2018]. Moreover, similar multi-physics based simulations have been used to analyze origami-inspired engineering systems for acoustic wave manipulation [Babaei et al., 2016, Hathcock et al., 2021, Pratapa et al., 2018, Thota and Wang, 2018, Zhu et al., 2019], as thermal metamaterials [Boatti et al., 2017], and for their drag forces in submerged environments [Hur et al., 2017].

Capturing variable multi-physics properties of origami usually requires one simulation environment to capture the origami folding and a separate environment to capture the non-mechanical properties. In light of this complexity, it is important for future work on origami simulation to generate easy to use output formats that can easily interface with multi-physics based simulation environments. A unified format such as the FOLD structure [Demaine et al., 2021] could be useful for

achieving trouble-free data transfer between different environments. However, additional information regarding the active folding systems, the compliant crease geometry, the material properties, the localized circuit designs, and other origami properties of interest would need to be included. Another challenge of multi-physics simulation of origami is the coupling between the origami folding, the multi-physics actuation, and the non-mechanical performance (red dashed lines in Fig. A.20). Simulating these coupled behavior and interactions requires passing information between different environments which is still difficult to accomplish effectively. An alternative way to solve the coupling problem is to build reduced-order simulations within the same environment such as the simulation of electro-thermal crease folding in [Zhu and Filipov, 2021a] or the simulation of magnetically actuated origami in [Swaminathan et al., 2021]. However, the capabilities of current reduced-order simulations is still limited so further work is needed.

## A.6 Available Simulation Packages

In this section, we introduce existing implementation packages for simulating origami systems and discuss their capabilities and potential application scenarios. Table A.5 to Table A.7 summarizes these packages.

First, Mitani’s ORIPA [Mitani, 2008, Mitani, 2012] implements a reflection-based simulation for flat-foldable origami systems. The package directly solves the folded configuration using reflection based theories and calculates the panel sequence using brute force enumeration. This package is one of the earliest computational tools developed for origami engineers. ORIPA cannot simulate the intermediate folding states, the folding process, or physical behaviors, which are all important for the analysis and design of engineering origami systems.

Next, the Rigid Folding Simulator, the Origamizer, and the Freeform Origami developed by Tachi share some similarities [Tachi, 2020, Tachi, 2009b, Tachi, 2010c]. The Rigid Folding Simulator can capture the folding motion of origami systems based on the loop closure constraint (Eqn. A.16). Kinematically feasible folding motion is solved using numerical integration such as Euler’s method (see subsection A.3.4). The simulation package provides a rapid and effective implementation to study the kinematic folding of thin and rigid origami, providing one of the most popular computational tools for simulating origami folding. Based on the rigid folding simulator, Origamizer [Tachi, 2010c] and Freeform Origami [Tachi, 2020] were developed. Origamizer can be used to design an origami to fit arbitrary 3D surfaces using a tuck folding technique, and Freeform origami allows users to design new origami patterns by directly editing existing tessellations. However, these three packages cannot capture compliant creases, panel deformations, mechanical properties, and other multi-physics based properties of origami.

The smooth fold model developed by Hernandez and coworkers [Hernandez et al., 2016b, Her-

Table A.5: A summary of available kinematic simulation packages for origami structures.

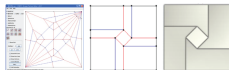

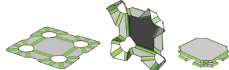
Package	Formulation	Reference and Links
<b>Flat-foldable origami</b>		
ORIPA 	If the input pattern is rigidly flat foldable, the program will use reflection based simulation to directly generates the folded geometry of the origami. The program then calculate the panel sequence using brute-force approach.	Ref. [Mitani, 2008, Mitani and Igarashi, 2011, Mitani, 2012] Package found at: <a href="https://mitani.cs.tsukuba.ac.jp/oripa/">https://mitani.cs.tsukuba.ac.jp/oripa/</a>
<b>Loop closure condition</b>		
Rigid folding simulator & Origamizer & Freeform Origami 	The rigid folding simulator uses Euler's integration to track the folding trajectory complying with the loop closure condition. The Origamizer can fit any triangulated 3D surface using origami with tuck-folding technique. The Freeform origami is based on the rigid folding simulator and allows users to drag vertices of origami for creating new origami designs.	Ref. [Tachi, 2009c, Tachi, 2009b, Tachi, 2010d, Tachi, 2010c, Tachi, 2010a, Tachi, 2020] Package found at: <a href="https://tsg.ne.jp/TT/software/index.html">https://tsg.ne.jp/TT/software/index.html</a>
<b>Kinematic compliant crease model</b>		
Smooth fold model 	This is a MATLAB based implementation of the smooth fold model. This kinematics-based simulation can capture the compliant crease geometry in origami structures.	Ref. [Hernandez et al., 2016b, Hernandez et al., 2017c] Package found in the supplementary information of articles [Hernandez et al., 2017c]

Table A.6: A summary of available mechanical simulation packages for origami structures.

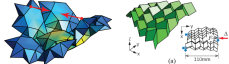
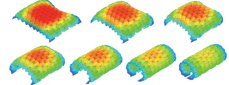
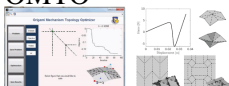

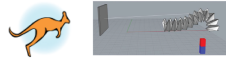
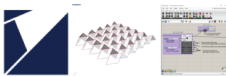
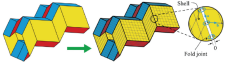
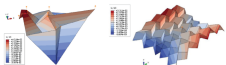
Package	Formulation	Reference and Links
<b>Bar and hinge models</b>		
<p>MERLIN &amp; MERLIN 2</p> 	<p>MERLIN is a MATLAB based implementation of the standard bar and hinge model. MERLIN implements the N4B5 panel formulation and solve the mechanical behavior using a modified generalized displacement controlled method. The MERLIN 2 provides updated N5B8, generalized N4B5, and generalized N5B8 panel models.</p>	<p>Ref. [Liu and Paulino, 2016, Liu and Paulino, 2017a, Liu and Paulino, 2018a, Liu and Paulino, 2018b]            Package found at: <a href="http://paulino.ce.gatech.edu/software.html">http://paulino.ce.gatech.edu/software.html</a></p>
<p>Origami Simulator</p> 	<p>This is a GPU accelerated version of the standard bar and hinge model. The simulation is based on the formulation demonstrated in [Schenk and Guest, 2010] and the pattern editing is based on [Tachi, 2010a]. With the GPU acceleration, the simulation is 1000X faster than MERLIN per step.</p>	<p>Ref. [Ghassaei et al., 2018, Ghassaei, 2017]            Package found at: <a href="https://origamisimulator.org/">https://origamisimulator.org/</a></p>
<p>OMTO</p> 	<p>This package implements the standard bar and hinge model proposed in [Gillman et al., 2018, Gillman et al., 2019], and can perform topological optimization to generate origami patterns for optimal actuation.</p>	<p>Ref. [Gillman et al., 2018, Gillman et al., 2019, Gillman, 2018]            Package found at: <a href="https://www.mathworks.com/matlabcentral/fileexchange/51811-origami-mechanism-topology-optimizer-omtoll">https://www.mathworks.com/matlabcentral/fileexchange/51811-origami-mechanism-topology-optimizer-omtoll</a></p>
<p>SWOMPS</p> 	<p>This package implements the compliant crease bar and hinge model, a global inter-panel contact model, and an electro-thermal actuation model for active origami. The program support loading the origami with arbitrary number and sequence of the provided five loading solvers.</p>	<p>Ref. [Zhu and Filipov, 2020, Zhu and Filipov, 2019b, Zhu and Filipov, 2019a, Zhu and Filipov, 2021a, Zhu and Filipov, 2021b]            Package found at: <a href="https://github.com/zzhuyii/OrigamiSimulator">https://github.com/zzhuyii/OrigamiSimulator</a></p>

Table A.7: A summary of adds-on packages and commercial packages for origami structures.

Package	Formulation	Reference and Links
<b>Kangaroo</b> 	<p>This a physics engine developed for Rhino and Grasshopper. The package can be used to model origami system and was used for simulating magnetic active origami in [Swaminathan et al., 2021].</p>	<p>Ref. [Swaminathan et al., 2021, Piker, 2017, Piker, 2013]            Package found at:  <a href="https://www.food4rhino.com/en/app/kangaroo-physics">https://www.food4rhino.com/en/app/kangaroo-physics</a></p>
<b>Crane</b> 	<p>This is a Grasshopper plugin for Rhino. The folding simulation and form finding is based on the Freeform Origami. The package also can simulate thickness in origami systems.</p>	<p>Ref. [Tachi, 2010a, Suto and Tanimichi, 2021]            Package found at: <a href="https://www.food4rhino.com/en/app/crane">https://www.food4rhino.com/en/app/crane</a></p>
<b>Commercial FE programs</b> 	<p>Commonly used commercial FE software programs include ANSYS, ABAQUS, LS-DYNA, COMSOL, and many others.</p>	<p>See section A.4.4 for details</p>
<b>Small strain plate</b> 	<p>User defined elements for origami panels implemented in ABAQUS. The plate model can capture the small-strain bending of panels.</p>	<p>Ref. [Hu et al., 2021]            Code found in the appendix of [Hu et al., 2021].</p>

nandez et al., 2017c] is one of the first kinematic models to explicitly consider compliant creases within origami systems (see subsection A.3.6). A MATLAB implementation was published as electronic supplementary material in [Hernandez et al., 2017c]. This package can capture the geometry and mechanics of compliant creases within active origami. However, because the simulation was developed based on rigid panel assumptions, this package cannot simulate behaviors related to panel deformations.

Here, we give a short description of existing implementations of the bar and hinge model. MERLIN [Liu and Paulino, 2016, Liu and Paulino, 2017a, Liu and Paulino, 2017b] is a public implementation of the bar and hinge model that can track origami folding and mechanical deformations using a modified generalized displacement control method. The package is implemented in MATLAB and is based on the standard bar and hinge model formulation with the N4B5 panel model and the linear rotational spring based crease model. MERLIN 2 [Liu and Paulino, 2018b, Liu and Paulino, 2018a] is an updated implementation which further supports the use of N5B8, generalized N4B5, and generalized N5B8 panel models, and provides useful functions to read OBJ format. These two packages are rapid and powerful tools for simulating origami folding and exploring mechanical properties such as stiffness, bistability, and multi-stability. The Origami Simulator [Ghassaei, 2017, Ghassaei et al., 2018] is a parallelized GPU accelerated version of the bar and hinge model. It is based on a standard bar and hinge model with N4B5 panels and linear elastic rotational springs. This package uses an explicit solver so that it can parallelize its computation. With parallelization, the package can compute one loading step orders of magnitude faster than the MERLIN package (measured using wall clock time). However, the package does require manually softening the material stiffness (from its actual value) and using a much shorter loading step to obtain converging results. OMTO [Gillman et al., 2018, Gillman et al., 2019, Gillman, 2018] is another bar and hinge type software implementation specially designed for topological optimization applications. The underlying folding simulation of this package is similar to MERLIN but is designed to perform topological optimization of origami systems. MERLIN, MERLIN 2, and OMTO can capture localized panel contact and prevent creases from folding more than  $180^\circ$  (see Fig A.19 (a) and (b)). SWOMPS [Zhu and Filipov, 2021a] is a MATLAB based object oriented implementation of the bar and hinge model. The package uses a generalized N5B8 panel model and allows users to choose between a simple rotational spring crease model and a compliant crease model. SWOMPS can simulate global panel contact (see Fig A.19 (c)), it can approximate panel thickness, and can capture electro-thermal-mechanically coupled actuation within active origami. The SWOMPS implementation gives users multiple options in how the origami can be modeled and allows for sequential and arbitrary loading of the origami.

In general, these bar and hinge model implementations are suitable for studying the kinematics, capturing the mechanical and non-mechanical properties, simulating the active folding, and

performing pattern optimization of origami systems. The models have the capability of real-time simulation [Ghassaei et al., 2018], and can be updated for rapid simulations with origami multi-physics [Zhu and Filipov, 2021a]. However, because the bar and hinge model uses a coarse mesh for the origami these packages are only suitable for capturing global behaviors. Localized nonlinear behaviors such as panel buckling, kinking, and stress concentrations are beyond the capabilities of these packages.

Finally, a number of commercial software and the associated extension packages can also be used to simulate origami systems. Rhino and Grasshopper based physics-engine Kangaroo [Piker, 2017] can be used to model origami systems. The Crane package [Suto and Tanimichi, 2021] is an extension that implements the Freeform origami algorithm within the Rhino and Grasshopper environment. The Rhino and Grasshopper environment is more suitable for parametric design of origami systems but tends to provide limited fidelity in its physical simulation. When high accuracy simulations are needed, commercial FE software programs tend to be used. A variety of different FE software programs have been used for simulating the behaviors of origami systems such as ABAQUS [Cai et al., 2017b, Karagiozova et al., 2019, Liu et al., 2015, Ma et al., 2018b, Ma et al., 2018a, Ma and You, 2014, Schenk et al., 2014, Song et al., 2012, Wang and Zhou, 2017, Xiang et al., 2020, Yang et al., 2016, Yuan et al., 2020, Zhang et al., 2019], ANSYS [Heimbs et al., 2007, Zaghoul and Bone, 2020, Nauroze et al., 2018], LS-DYNA [Heimbs et al., 2007, Heimbs et al., 2010, Thai et al., 2018], and COMSOL [Zhu et al., 2019, Hathcock et al., 2021]. These packages also support origami researchers to create user-defined elements. For example, the work by Hu et al. [Hu et al., 2021] created a small-strain plate model for simulating origami panels with small curvature deformation that are more computationally efficient than using the fine meshed FE models. Using commercial FE software programs can achieve high fidelity solutions and capture localized nonlinear behaviors in origami systems. However, using FE simulations requires longer computation time and an extended model building schedule. In addition, FE simulations can act like “black boxes” in some situations, which make them not suitable for developing fundamental theories of origami structures.

## **A.7 Selecting and Developing Appropriate Origami Simulations**

In this section, we discuss how to select or develop a simulation technique for capturing the behavior of origami systems. After evaluating the challenges in selecting and developing appropriate techniques, we present a flowchart to help guide the process, along with a number of accompanying case studies.

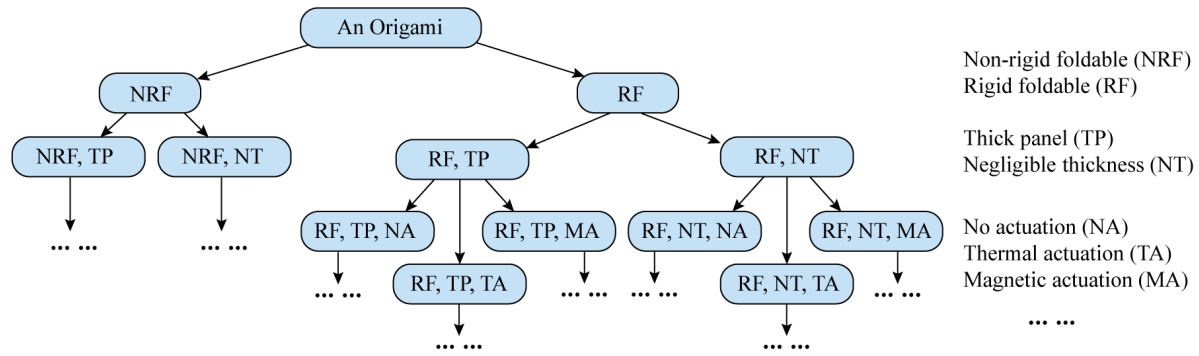


Figure A.21: A universal origami simulation approach is not achievable; instead, there is an exponential growth in tailored models that can capture distinct properties and characteristics for individual origami problems.

**Appropriate models** What constitutes an appropriate model for a particular origami system demands a significant element of judgement from the engineer or scientist investigating the problem. A common guiding scientific principle (“Occam’s Razor”) is to use the simplest model that still captures the observed behavior of interest. This model might be called a “minimal model”. In many cases, lower-fidelity models with a greater number of assumptions provide greater insight into the behavior of origami systems. Consider, for instance, the analysis of rigid-foldable origami systems; these systems can be modeled using high-fidelity finite element simulations, but this approach will not provide an understanding of the mathematical conditions for rigid-foldability that could be obtained from kinematics-based modeling [Belcastro and Hull, 2002]. Moreover, reduced-order bar and hinge models can provide insight into the mechanics of an origami system, not offered by detailed FE simulations with continuum elements. For example, in the study of bistable origami hypars [Filipov and Redoutey, 2018], comparing different bar and hinge meshes (*i.e.* with different panel bending direction) provides insight into which deformations are most significant to the bistability of origami hypars. Similarly, in the analysis of origami tubes [Grey et al., 2019], the bar and hinge models provide a method to independently change the in-plane, bending, and folding stiffness to gain insight into the dominant contributors. These types of comparative studies are difficult to execute in FE simulations. Finally, such “minimal models” can reveal theoretical connections between origami and other disciplines, which helps origami engineers develop new simulation techniques. For example, the development of simulation techniques for thick and rigid origami has revealed the close connection between origami and linkage mechanisms.

From an engineering perspective, an appropriate simulation should also consider the balance between the speed and the fidelity of the model. Here, speed could refer to the number of floating point operations (not affected by the programming language that is used), the wall-clock run time



(affected by the programming language), or even the duration of developing the simulation and implementing a model. An illustrative example where analysis speed and model simplicity are traded off against fidelity is the analysis of tubular origami structures such as the Kresling pattern; their non-rigid foldable properties require the use of a mechanics-based simulation. In various works, the behavior of the Kresling pattern is simulated using a bar and hinge model [Liu and Paulino, 2017a, Novelino et al., 2020, Kidambi and Wang, 2020] because it captures the panel deformation, is computationally efficient, and rapid to set up for different geometries. However, bar and hinge models cannot capture the buckling of crease lines, which are observed in some physical experiments [Masana and Daqaq, 2019]. Masana and Daqaq therefore modified their formulation of the bar and hinge model by introducing additional nodes and springs along the fold lines [Masana and Daqaq, 2019]. These additional nodes and springs allow the creases to buckle so that the model can better simulate the global physical behavior. An alternative to capture this local crease buckling in the Kresling pattern is to use FE simulations as shown in the work by Hwang [Hwang, 2021]. Another consideration is the time required to formulate the model and set up the simulation for a specific problem. In this case, human factors can play a large role. A researcher familiar with reduced-order simulations may choose the bar and hinge approach as in [Masana and Daqaq, 2019] and a researcher familiar with commercial FE simulation packages may choose the FE simulations as in [Hwang, 2021]. These cases illustrate that finding a ‘balanced’ model is subjective, and in addition to the features of the different simulation options one should also consider their prior knowledge and experience.

Lastly, as the community continues to design increasingly sophisticated origami structures for engineering applications, selecting and developing origami simulations becomes more complex due to the exponentially growing number of origami characteristics that need to be captured; see Fig. A.21. This exponential growth makes it challenging to find a “minimal model” that satisfies the desire for simplicity or a “balanced model” that trades optimum speed and fidelity.

**Flowchart** To help navigate the complexity of selecting and developing origami simulation techniques, we offer a non-exhaustive flowchart, shown in Fig. A.22, to aid the selection and development process. The three aspects to consider when selecting and building simulation techniques are: the origami characteristics, objectives of the simulation, and other factors. To select an appropriate simulation for origami, the left flowchart identifies potential simulations that can capture the target characteristics of the origami systems, and the right flowchart helps find a simulation that fits the given objectives. Once a potential simulation techniques is identified, other factors such as available facilities and capabilities can be taken into consideration. In developing a new or modified simulation method, the flowchart can help users select a base simulation technique. The following text discusses the flowchart and presents a number of examples.

### Selecting and Developing Appropriate Origami Simulation

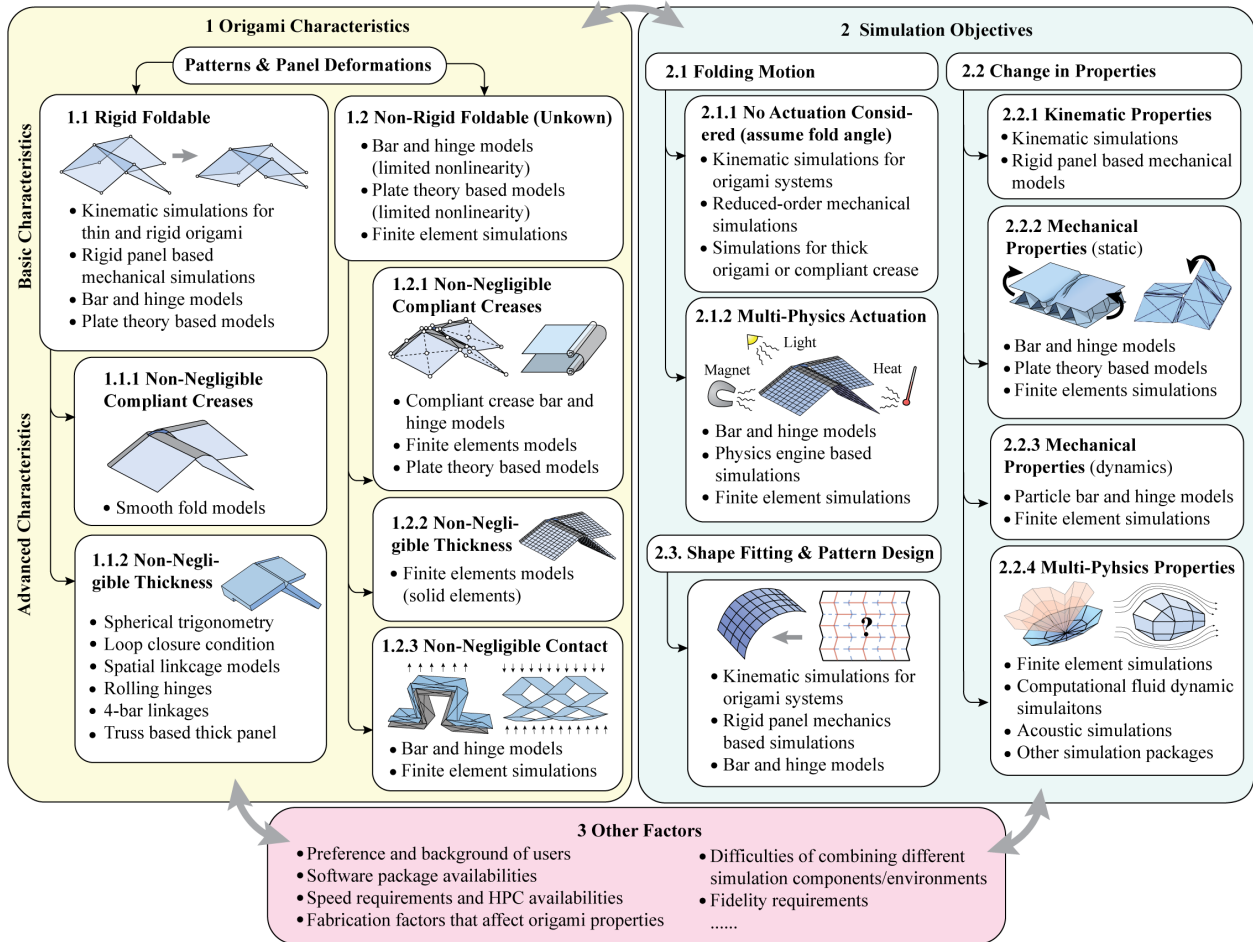


Figure A.22: Considerations for selecting and developing simulation techniques for origami systems.

Starting with the flowchart for origami characteristics in section 1 of Fig. A.22, one of the most fundamental features of an origami system is whether it is rigid-foldable or not. If the origami is rigid-foldable, their folding motions can be captured using kinematic simulations or rigid panel based mechanical simulations (item 1.1). However, if the origami is non-rigid-foldable, simplified mechanical simulations like the bar and hinge model [Liu and Paulino, 2017a, Filipov et al., 2017] and the plate theory based models [Soleimani et al., 2021, Hu et al., 2021] or more advanced options like FE simulations are needed (item 1.2). Next, more detailed features of the origami system can be considered. For example, studying rigid-foldable origami with non-negligible compliant creases can be accomplished using the smooth fold model [Hernandez et al., 2017a, Hernandez et al., 2016b, Hernandez et al., 2017c] (item 1.1.1), while studying the non-rigid-foldable origami with non-negligible compliant creases can use compliant crease bar and hinge models [Zhu and Filipov, 2020], plate theory based models [Zhang et al., 2021], or FE simulations [Hernandez et al., 2016a] (item 1.2.1).

In addition to the properties of the origami, the objectives of the simulation should also be considered, as shown in section 2 of Fig. A.22. Broadly, there are three types of objectives that may be of interest: to study the origami folding motion, to study the change in origami properties, and to achieve pattern design and shape fitting. For the simulation of origami folding motions, the primary factor to consider is its means of actuation; if no actuation mechanisms are considered, conventional kinematic and mechanical origami simulation techniques can be used (item 2.1.1). On the other hand, if multi-physics actuation is intended (item 2.1.2), building new origami simulations may be necessary. For example, Swaminathan et al. [Swaminathan et al., 2021] introduce a magnetic actuation module into a physics-based origami simulation program. Capturing the property changes in origami is a common objective in origami simulation. For changes in the kinematic and mechanical properties, using existing origami simulations tends to be sufficient (item 2.2.1 to 2.2.3), but analysing multi-physical properties may require combining different simulation environments, as discussed in Section A.5. In this case, finding an origami simulation method that integrates with other multi-physics simulation environments can become crucial (item 2.2.4). Lastly, selecting simulations for pattern design and origami shape fitting focuses more on the balance between the computational speed and the model fidelity (item 2.3). In general, kinematics simulations and reduced-order mechanical simulations are preferred for such objectives.

**Case studies** Finally, we present a number of case studies on selecting and developing origami simulations. The first example is to design an origami that fits a desired target surface (item 2.3 in Fig. A.22). Research efforts have mainly focused on using rigid-foldable patterns for shape fitting [Zhao et al., 2018, Peraza-Hernandez et al., 2018, Feng et al., 2020a], with potential applications as deployable structures. As indicated in item 1.1 and item 2.3, kinematic simulations are

popular for this objective because they are computationally efficient [Zhao et al., 2018, Dudte et al., 2016, An et al., 2018, Peraza-Hernandez et al., 2018, Feng et al., 2020a]. Moreover, some of these kinematic simulations can be extended such that origami structures with thick panels [Tachi, 2011] or those with compliant creases [Peraza-Hernandez et al., 2018] can also be designed in a similar fashion (item 1.1.2). Alternatively, reduced-ordered mechanical models for origami could be used because they can capture non-rigid foldable origami [Gillman et al., 2018, Gillman et al., 2019] while also remaining computationally efficient (item 1.1).

The second example is the analysis of origami frequency selective surfaces (FSS). A number of publications have studied the performance of origami FSS, often using the Miura-ori pattern [Biswas et al., 2020, Nauroze and Tentzeris, 2019, Nauroze et al., 2018, Cui et al., 2019, Fuchi et al., 2012, Fuchi et al., 2016]. Because the Miura-ori tessellation is rigid-foldable, a simulation method from item 1.1 on Fig. A.22 can be employed to capture the geometry. However, capturing the electro-magnetic properties of the origami FSS requires more sophisticated models and is thus performed using separate simulation packages (item 2.2.4). In this case, it is important to build an origami simulation that can output and transfer the origami geometry to the separate simulation package smoothly.

Lastly, consider origami for use as an energy absorption system or as a metamaterial with graded stiffness. The objective of such simulations is to find the mechanical properties of the origami (item 2.2.2 or item 2.2.3 in Fig. A.22). Usually, the origami structure will experience large panel deformations with potential panel contact, as listed in item 1.2.3. Here, FE simulations can be the preferred choice because they are capable of capturing nonlinear and plastic deformations [Ma et al., 2018b, Yang et al., 2016]. However, if the origami is rigid-foldable and does not experience large panel deformations, a reduced-order mechanical model may also be suitable [Miyazawa et al., 2021, Zhu and Filipov, 2019a, Fang et al., 2018].

## A.8 Future Challenges and Concluding Remarks

Despite the significant advances in the field of origami simulations, there remains a range of open challenges. Here, we offer our view on key themes within the future challenges: model validation, enhancement of simulation capabilities, and integration with design.

**Model validation** A large number of different simulation techniques have been proposed for capturing the behavior of origami-inspired structures. What are the limits of these simulations? How accurate are these simulations when applied to different origami patterns, across different scales and manufactured from different materials? These are open questions that have not been systematically addressed in existing research. To resolve the problem, we propose the develop-

ment of a high-quality open-access library of experimental benchmarks of origami. This approach is inspired by experimental benchmark libraries created for other engineering problems (*e.g.* radar cross-sections [Woo et al., 1993]). What patterns should be chosen for these high quality experiments? At the very least, the selection should include both rigid foldable patterns (such as the Miura-ori) and non-rigid foldable patterns (such as the Kresling pattern). However, as demonstrated by Pinson et al. [Pinson et al., 2017], the strain energy from origami folding can span orders of magnitude depending on how well the pattern complies with the rigid-foldability conditions; this makes it challenging to select representative patterns that sufficiently capture this energy landscape. In addition, the physical length scale of origami needs to be considered. For example, origami systems at meter and millimeter scale show different responses, because gravity has a greater impact at larger scales. Moreover, what materials should the library contain? The use of paper would seem to be a straightforward answer because of its ubiquitous use in origami prototyping. However, as pointed out by Grey et al. [Grey et al., 2020], paper is not suitable for validation because of its nonlinear and pseudo-plastic behavior. Thus future benchmarks should consider multiple materials with different elasto-plastic behaviors. Finally, these benchmark experiments should also reflect information on the variability in material properties and dimensions because origami structures can be significantly affected by even small imperfections [Liu et al., 2020].

**Enhancement of simulation capabilities** Future research needs to enhance the capabilities of current simulation techniques and packages. These enhancements include but are not limited to supporting more elaborate material models, developing advanced multi-scale simulations, building multi-physics interaction models, capturing interaction between origami modules, *etc.* For instance, current reduced-order origami simulation capabilities have been mostly limited to linear-elastic material models, whereas materials used for origami prototyping and applications are generally nonlinear elasto-plastic [Grey et al., 2020] and can be further affected by the ambient environment such as temperature and humidity (especially for active folding). Simulating the global response of origami systems requires accurately capturing local details such as the properties at creases and small manufacturing imperfections [Liu et al., 2020]. In order to develop origami-inspired systems with increased numbers of unit cells, as might be needed for shape-adaptive surfaces, multi-scale simulation methods should be developed. High-fidelity models of local features and unit cell geometry would feed into larger-scale, reduced-order simulations of the behavior of origami systems. Further, in order to better capture the coupling between actuation, response to external stimuli, origami folding, and the non-mechanical properties of origami devices, more comprehensive multi-physics models must be developed. Another less visited topic in the simulation of origami is the interaction between origami modules. Many origami-inspired metamaterials are constructed by integrating repeating origami unit cells [Overvelde et al., 2016]. These unit

cells are often fabricated individually and then assembled to form an origami metamaterial. The interaction between individual origami modules can affect the bulk behavior of the metamaterial, and developing reliable simulations to capture such interactions is also an important task for the future.

**Integration of simulation and design** Lastly, the effective integration of origami simulation with different origami design methodologies remains an open challenge. Currently, many origami simulation techniques and tools are developed without considering how these tools can be systematically integrated into origami design methodologies. A unified workflow, data format, and parameterization of the origami design space would be important for connecting simulation to design. A standardized data format can help origami researchers to develop computational tools more efficiently and the FOLD format [Demaine et al., 2021] demonstrates a first attempt to accomplish this goal. However, further developments are needed to include additional origami properties related to active folding, mechanical behavior, and non-mechanical performance. In addition, improving the accessibility of the simulation package is also important. Many new users of origami simulation software programs may not have prior background in computational mechanics or even general programming. Therefore, future origami simulation packages will need to enhance their accessibility to researchers from non-computational disciplines and the general public. For example, the Crane package [Suto and Tanimichi, 2021] for Rhino/Grasshopper demonstrates one successful attempt to bring origami design and simulation techniques [Tachi, 2010a] to the architecture and design community.

In conclusion, in this work we reviewed the state-of-the-art in origami simulations, and broadly categorised origami simulation techniques into kinematics-based, mechanics-based, and multi-physics simulations. We analyzed the underlying origami models and solution methods, discussed the theoretical background of these techniques, evaluated the advantages and disadvantages of different simulations, and demonstrated the connection between origami simulations and other engineering disciplines. Based on the overview of available simulations techniques, we discussed why developing origami simulations is challenging and how to select and develop appropriate origami simulation techniques for specific applications. Lastly, we identified promising directions of future research, focusing on model validation, enhanced modeling capabilities, and improved integration of simulation and design. Origami simulation is a rapidly evolving field of research and we believe that future developments will yield faster, more robust, and easier-to-use simulation techniques and packages for researchers and designers from different disciplines.

## Bibliography

- [Adams and Nosonovsky, 2000] Adams, G. and Nosonovsky, M. (2000). Contact modeling – forces. *Tribology International*, 33(5-6):431–442.
- [An et al., 2018] An, B., Miyashita, S., Ong, A., Tolley, M. T., Demaine, M. L., Demaine, E. D., Wood, R. J., and Rus, D. (2018). An end-to-end approach to self-folding origami structures. *IEEE Transactions on Robotics*, 34(6):1409–1424.
- [Arora et al., 2006] Arora, W. J., Nichol, A. J., Smith, H. I., and Barbastathis, G. (2006). Membrane folding to achieve three-dimensional nanostructures: nanopatterned silicon nitride folded with stressed chromium hinges. *Applied Physics Letters*, 88(053108).
- [Ataka et al., 1993] Ataka, M., Omodaka, A., Takeshima, N., and Fujita, H. (1993). Fabrication and operation of polyimide bimorph actuators for a ciliary motion system. *Journal of Microelectromechanical Systems*, 2(4):146–150.
- [Babae et al., 2016] Babae, S., Overvelde, J. T. B., Chen, E. R., Tournat, V., and Bertoldi, K. (2016). Reconfigurable origami-inspired acoustic wave guides. *Science Advances*, 2(e1601019).
- [Babilio et al., 2019] Babilio, E., Miranda, R., and Fraternali, F. (2019). On the kinematics and actuation of dynamic sunscreens with tensegrity architecture. *Frontiers in Materials*, 6(7).
- [Balkcom et al., 2009] Balkcom, D. J., Demaine, E. D., Demaine, M. L., Ochsendorf, J. A., and You, Z. (2009). Folding paper shopping bags. In *Origami 4*, pages 315–334. A.K.Peters.
- [Bassik et al., 2009] Bassik, N., Stern, G. M., and Gracias, D. H. (2009). Microassembly based on hands free origami with bidirectional curvature. *Applied Physics Letters*, 95(091901).
- [Belcastro and Hull, 2002] Belcastro, S.-M. and Hull, T. C. (2002). Modelling the folding of paper into three dimensions using affine transformations. *Linear Algebra and its Applications*, 348:273–282.
- [Belke and Paik, 2017] Belke, C. H. and Paik, J. (2017). Mori: A modular origami robot. *IEEE/ASME Transactions on Mechatronics*, 22(5):2153–2164.
- [Bern and Hayes, 1996] Bern, M. and Hayes, B. (1996). The complexity of flat origami. In *Annual ACM-SIAM Symposium on Discrete Algorithms (SODA)*.

- [Bertsimas and Tsitsiklis, 1997] Bertsimas, D. and Tsitsiklis, J. N. (1997). *Introduction to Linear Optimization*. Athena Scientific.
- [Bhovad and Li, 2021] Bhovad, P. and Li, S. (2021). Physical reservoir computing with origami and its application to robotic crawling. *Scientific Reports*, 11(13002).
- [Biswas et al., 2020] Biswas, A., Zekios, C. L., and Georgakopoulos, S. V. (2020). Transforming single-band static FSS to dual-band dynamic FSS using origami. *Scientific Reports*, 10(13884).
- [Boatti et al., 2017] Boatti, E., Vasios, N., and Bertoldi, K. (2017). Origami metamaterials for tunable thermal expansion. *Advanced Materials*, 29(1700360).
- [Bowen et al., 2014] Bowen, L. A., Baxter, W. L., Magleby, S. P., and Howell, L. L. (2014). A position analysis of coupled spherical mechanisms found in action origami. *Mechanism and Machine Theory*, 77:13–24.
- [Breger et al., 2015] Breger, J. C., Yoon, C., Xiao, R., Kwag, H. R., Wang, M. O., Fisher, J. P., Nguyen, T. D., and Gracias, D. H. (2015). Self-folding thermo-magnetically responsive soft microgrippers. *ACS Applied Materials and Interfaces*, 7(5):3398–3405.
- [Breiman et al., 1984] Breiman, L., Friedman, J., Olshen, R., and Stone, C. (1984). Classification and regression trees. *Monterey: CA: Wadsworth and Brooks*.
- [Broyles et al., 2020] Broyles, Z., Talbot, S., Johnson, J., Halverson, D. M., and Howell, L. L. (2020). Unpacking the mathematics of modeling origami folding transformations with quaternions. In *USCToMM Symposium on Mechanical Systems and Robotics*, pages 225–241.
- [Buitinck et al., 2013] Buitinck, L., Louppe, G., Blondel, M., Pedregosa, F., Mueller, A., Grisel, O., Niculae, V., Prettenhofer, P., Gramfort, A., Grobler, J., Layton, R., VanderPlas, J., Joly, A., Holt, B., and Varoquaux, G. (2013). Api design for machine learning software: experiences from the scikit-learn project. In *ECML PKDD Workshop: Languages for Data Mining and Machine Learning*, pages 108–122.
- [Butler et al., 2020] Butler, J., Pehrson, N., and Magleby, S. (2020). Folding of thick origami through regionally sandwiched compliant sheets. *Journal of Mechanisms and Robotics*, 12(011019).
- [Cai, 2016] Cai, J. (2016). Kinematic analysis of foldably plate structures with rolling joints. *Journal of Mechanisms and Robotics*, 8(034502).
- [Cai et al., 2016a] Cai, J., Deng, X., Zhang, Y., Feng, J., and Zhou, Y. (2016a). Folding behavior of a foldable prismatic mast with kresling origami pattern. *Journal of Mechanisms and Robotics*, 8(031004).
- [Cai et al., 2017a] Cai, J., Liu, Y., Ma, R., Feng, J., and Zhou, Y. (2017a). Nonrigidly foldability analysis of Kresling cylindrical origami. *Journal of Mechanisms and Robotics*, 9(041018).
- [Cai et al., 2017b] Cai, J., Ren, Z., Ding, Y., Deng, X., Xu, Y., and Feng, J. (2017b). Deployment simulation of foldable origami membrane structures. *Aerospace Science and Technology*, 67:343–353.



- [Cai et al., 2019] Cai, J., Zhang, Q., and Feng, J. (2019). Modeling and kinematic path selection of retractable kirigami roof structures. *Computer-Aided Civil and Infrastructure Engineering*, 34(4):352–363.
- [Cai et al., 2016b] Cai, J., Zhang, Y., Xu, Y., Zhou, Y., and Feng, J. (2016b). The foldability of cylindrical foldable structures based on rigid origami. *Journal of Mechanical Design*, 138(031401).
- [Carleo et al., 2019] Carleo, G., Cirac, I., Cranmer, K., Daudet, L., Schuld, M., Tishby, N., Vogt-Maranto, L., and Zdeborova, L. (2019). Machine learning and the physical sciences. *Reviews of Modern Physics*, 91(045002).
- [Chen et al., 2019a] Chen, T., Bilal, O. R., Lang, R., Daraio, C., and Shea, K. (2019a). Autonomous deployment of a solar panel using elastic origami and distributed shape-memory-polymer actuators. *Physical Review Applied*, 11(064069).
- [Chen et al., 2020] Chen, Y., Fan, L., Bai, Y., Feng, J., and Sareh, P. (2020). Assigning mountain-valley fold lines of flat-foldable origami patterns based on graph theory and mixed-integer linear programming. *Computers and Structures*, 239(106328).
- [Chen et al., 2016] Chen, Y., Feng, H., Ma, J., Peng, R., and You, Z. (2016). Symmetric waterbomb origami. *Proceedings of the Royal Society A*, 472(20150846).
- [Chen et al., 2015] Chen, Y., Peng, R., and You, Z. (2015). Origami of thick panels. *Science*, 349(6246):396–400.
- [Chen et al., 2019b] Chen, Y., Sareh, P., Yan, J., Fallah, A. S., and Feng, J. (2019b). An integrated geometric-graph-theoretica approach to representing origami structures and their corresponding truss framework. *Journal of Mechanical Design*, 141(091402).
- [Chen et al., 2021] Chen, Y., Yan, J., Feng, J., and Sareh, P. (2021). Particle swarm optimization based metaheuristic design generation of non-trivial flat-foldable origami tessellations with degree-4 vertices. *Journal of Mechanical Design*, 143(011703-1).
- [Chen and You, 2012] Chen, Y. and You, Z. (2012). Spatial overconstrained linkages – the lost jade. In *Explorations in the History of Machines and Mechanisms*, volume 15, pages 535–550. Springer.
- [Chi and Tang, 2006] Chi, L.-C. and Tang, T.-C. (2006). Bankruptcy prediction: Application of logit analysis in export credit risks. *Australian Journal of Management*, 31(1):17–27.
- [Choi et al., 2017] Choi, J., Shin, M., Rudy, R. Q., Kao, C., Pulskamp, J. S., Polcawich, R. G., and Oldham, K. R. (2017). Thin-film piezoelectric and high-aspect ratio polymer leg mechanisms for millimeter-scale robotics. *International Journal of Intelligent Robotics and Applications*, 1(2):180–194.
- [Chopra, 2014] Chopra, A. K. (2014). *Dynamics of Structures 4th edition*. Pearson.

- [Chronis and Lee, 2005] Chronis, N. and Lee, L. P. (2005). Electrothermally activated su-8 microgripper for single cell manipulation in solution. *Journal of Microelectromechanical Systems*, 14(4):857–863.
- [Clough and Penzien, 1975] Clough, R. W. and Penzien, J. (1975). *Dynamics of Structures 2nd edition*. McGraw-Hill College.
- [Cui et al., 2019] Cui, Y., Nauroze, S. A., and Tentzeris, M. M. (2019). Origami tunable frequency selective surfaces. *IEEE/MTT-S International Microwave Symposium*, 11:1367–1370.
- [Dahlstrom and Lindkvist, 2007] Dahlstrom, S. and Lindkvist, L. (2007). Variation simulation of sheet metal assemblies using the method of influence coefficients with contact modeling. *Journal of Manufacturing Science and Engineering*, 129(3):615–622.
- [Dang et al., 2022] Dang, X., Feng, F., Plucinsky, P., James, R. D., Duan, H., and Wang, J. (2022). Inverse design of deployable origami structures that approximate a general surface. *International Journal of Solids and Structures*, 234-235(111224).
- [Delimont et al., 2015] Delimont, I. L., Magleby, S. P., and Howell, L. L. (2015). Evaluating compliant hinge geometries for origami-inspired mechanisms. *Journal of Mechanisms and Robotics*, 7(011009-1).
- [Demaine et al., 2021] Demaine, E., Ku, J., and Lang, R. (2021). FOLD. <https://github.com/edemaine/fold>.
- [Demaine and O’Rourke, 2007] Demaine, E. D. and O’Rourke, J. (2007). *Geometric Folding Algorithm*. Cambridge University Press.
- [Demaine and Tachi, 2017] Demaine, E. D. and Tachi, T. (2017). Origamizer: A practical algorithm for folding any polyhedron. In Aronov, B. and Katz, M. J., editors, *33rd International Symposium on Computational Geometry (SoCG 2017)*, volume 77 of *Leibniz International Proceedings in Informatics (LIPIcs)*, pages 34:1–34:16, Dagstuhl, Germany. Schloss Dagstuhl–Leibniz-Zentrum fuer Informatik.
- [Dias et al., 2012] Dias, M. A., Dudte, L. H., Mahadevan, L., and Santangelo, C. D. (2012). Geometric mechanics of curved crease origami. *Physical Review Letters*, 109(114301).
- [Dobson, 2003] Dobson, C. M. (2003). Protein folding and misfolding. *Nature*, 426:884–890.
- [Dong and Yu, 2021] Dong, S. and Yu, Y. (2021). Numerical and experimental studies on capturing behaviors of the inflatable manipulator inspired by fluidic origami structures. *Engineering Structures*, 245(112840).
- [Dong et al., 2021] Dong, S., Zhao, X., and Yu, Y. (2021). Dynamic unfolding process of origami tessellations. *International Journal of Solids and Structures*, 226-227(111075).
- [Dudte et al., 2016] Dudte, L. H., Vouga, E., Tachi, T., and Mahadevan, L. (2016). Programming curvature using origami tessellations. *Nature Materials*, 15:583–588.

- [Edmondson et al., 2014] Edmondson, B. J., Lang, R. J., Magleby, S. P., and Howell, L. L. (2014). An offset panel technique for thick rigidly foldable origami. In *International Design Engineering Technical Conferences and Computers and Information in Engineering Conference*, number DETC2014-35606.
- [Edmondson et al., 2016] Edmondson, B. J., Lang, R. J., Morgan, M. R., Magleby, S. P., and Howell, L. L. (2016). Thick rigidly foldable structures realized by an offset panel technique. In *Origami 6*, pages 149–161. American Mathematical Society.
- [Evans et al., 2015a] Evans, T. A., Lang, R. J., and Magleby, S. P. (2015a). Rigidly foldable origami twists. In *Origami 6*, pages 119–130. American Mathematical Society.
- [Evans et al., 2015b] Evans, T. A., Lang, R. J., Magleby, S. P., and Howell, L. L. (2015b). Rigidly foldable origami gadgets and tessellations. *Royal Society Open Science*, 2(150067).
- [Evans et al., 2015c] Evans, T. A., Lang, R. J., Magleby, S. P., and Howell, L. L. (2015c). Rigidly foldable origami twists. In *Origami 6*, pages 119–130. American Mathematical Society.
- [Faber et al., 2018] Faber, J., Arrieta, A. F., and Studart, A. R. (2018). Bioinspired spring origami. *Science*, 359(6382):1386–1391.
- [Fang et al., 2018] Fang, H., Chu, S.-C. A., Xia, Y., and Wang, K.-W. (2018). Programmable self-locking origami mechanical metamaterials. *Advanced Materials*, 30(1706311).
- [Fang et al., 2016] Fang, H., Li, S., and Wang, K. (2016). Self-locking degree-4 vertex origami structures. *Proceedings of the Royal Society A*, 472(20160682).
- [Felton et al., 2014] Felton, S., Tolley, M., Demaine, E., Rus, D., and Wood, R. (2014). A method for building self-folding machines. *Science*, 345(6197):644–646.
- [Feng et al., 2020a] Feng, F., Dang, X., James, R. D., and Plucinsky, P. (2020a). The designs and deformations of rigidly and flat-foldable quadrilateral mesh origami. *Journal of the Mechanics and Physics of Solids*, 142(104018).
- [Feng et al., 2020b] Feng, F., Plucinsky, P., and James, R. D. (2020b). Helical Miura origami. *Physical Review E*, 101(033002).
- [Filipov et al., 2017] Filipov, E., Liu, K., Schenk, M., and Paulino, G. (2017). Bar and hinge models for scalable analysis of origami. *International Journal of Solids and Structures*, 124(1):26–45.
- [Filipov et al., 2016] Filipov, E. T., Paulino, G. H., and Tachi, T. (2016). Origami tubes with reconfigurable polygonal cross-sections. *Proceedings of the Royal Society A*, 472(20150607).
- [Filipov et al., 2019] Filipov, E. T., Paulino, G. H., and Tachi, T. (2019). Deployable sandwich surfaces with high out-of-plane stiffness. *Journal of Structural Engineering*, 145(04018244).
- [Filipov and Redoutey, 2018] Filipov, E. T. and Redoutey, M. (2018). Mechanical characteristics of the bistable origami hyper. *Extreme Mechanics Letters*, 25:16–26.

- [Filipov et al., 2015] Filipov, E. T., Tachi, T., and Paulino, G. H. (2015). Origami tubes assembled into stiff yet reconfigurable structures and metamaterials. *PNAS*, 40(112):12321–12326.
- [Fonseca et al., 2019] Fonseca, L. M., Rodrigues, G. V., Savi, M. A., and Paiva, A. (2019). Non-linear dynamics of an origami wheel with shape memory alloy actuators. *Chaos, Solitons and Fractals*, 122:245–261.
- [Fu et al., 2018] Fu, H., Nan, K., Bai, W., Huang, W., Bai, K., Lu, L., Zhou, C., Liu, Y., Liu, F., Wang, J., Han, M., Yan, Z., Luan, H., Zhang, Y., Zhang, Y., Zhao, J., Cheng, X., Li, M., Lee, J. W., Liu, Y., Fang, D., Li, X., Huang, Y., Zhang, Y., and Rogers, J. A. (2018). Morphable 3d mesostructures and microelectronic devices by multistable buckling mechanics. *Nature Materials*, 17:268–276.
- [Fuchi et al., 2016] Fuchi, K., Buskohl, P. R., Bazzan, G., Durstock, M. F., Joo, J. J., Reich, G. W., and Vaia, R. A. (2016). Spatial tuning of a rf frequency selective surface through origami. In Sadjadi, F. A. and Mahalanobis, A., editors, *Automatic Target Recognition XXVI*, volume 9844, pages 234–243. International Society for Optics and Photonics, SPIE.
- [Fuchi et al., 2015] Fuchi, K., Buskohl, P. R., Bazzan, G., Durstock, M. F., Reich, G. W., Vaia, R. A., and Joo, J. J. (2015). Origami actuator design and networking through crease topology optimization. *Journal of Mechanical Design*, 137(091401).
- [Fuchi et al., 2012] Fuchi, K., Tang, J., Crowgey, B., Diaz, A. R., Rothwell, E. J., and Ouedraogo, R. O. (2012). Origami tunable frequency selective surfaces. In *IEEE Antennas and Wireless Propagation Letters*, volume 11, pages 473–475.
- [Ghassaei, 2017] Ghassaei, A. (2017). Origami simulator. <https://origamisimulator.org/>.
- [Ghassaei et al., 2018] Ghassaei, A., Demaine, E. D., and Gershenfeld, N. (2018). Fast, interactive origami simulation using GPU computation. In *Origami 7*, volume 4, pages 1151–1166. Tarquin.
- [Gillman, 2018] Gillman, A. (2018). Origami topology optimization w/ nonlinear truss model. <https://www.mathworks.com/matlabcentral/fileexchange/69612-origami-topology-optimization-w-nonlinear-truss-model>.
- [Gillman et al., 2018] Gillman, A., Fuchi, K., and Buskohl, P. R. (2018). Truss-based nonlinear mechanical analysis for origami structures exhibiting bifurcation and limit point instabilities. *International Journal of Solids and Structures*, 147:80–93.
- [Gillman et al., 2019] Gillman, A. S., Fuchi, K., and Buskohl, P. R. (2019). Discovering sequenced origami folding through nonlinear mechanics and topology optimization. *Journal of Mechanical Design*, 141(041401).
- [Greco et al., 2006] Greco, M., Gesualdo, F. A. R., Venturini, W. S., and Coda, H. B. (2006). Non-linear positional formulation for space truss analysis. *Finite Elements in Analysis and Design*, 42:1079–1086.

- [Grey et al., 2019] Grey, S. W., Scarpa, F., and Schenk, M. (2019). Strain reversal in actuated origami structures. *Physical Review Letters*, 123(025501).
- [Grey et al., 2020] Grey, S. W., Scarpa, F., and Schenk, M. (2020). Mechanics of paper-folded origami: A cautionary tale. *Mechanics Research Communications*, 107(103540).
- [Guest and Pellegrino, 1994] Guest, S. D. and Pellegrino, S. (1994). The folding of triangulated cylinders, part ii: The folding process. *Journal of Applied Mechanics*, 61:778–783.
- [Guest and Pellegrino, 1996] Guest, S. D. and Pellegrino, S. (1996). The folding of triangulated cylinders, part iii: Experiments. *Journal of Applied Mechanics*, 63:77–83.
- [Han et al., 2020] Han, H., Tang, L., Cao, D., and Liu, L. (2020). Modeling and analysis of dynamic characteristics of multi-stable waterbomb origami base. *Nonlinear Dynamics*, 102:2339–2362.
- [Hanakata et al., 2018] Hanakata, P. Z., Cubuk, E. D., Campbell, D. K., and Park, H. S. (2018). Accelerated search and design of stretchable graphene kirigami using machine learning. *Physics Review Letters*, 121(255304).
- [Hanna et al., 2014] Hanna, B. H., Lund, J. M., Lang, R. J., Magleby, S. P., and Howell, L. L. (2014). Waterbomb base: a symmetric single-vertex bistable origami mechanism. *Smart Materials and Structures*, 23(094009).
- [Hathcock et al., 2021] Hathcock, M., Ioan Popa, B., and Wang, K. W. (2021). Origami inspired phononic structure with metamaterial inclusions for tunable angular wave steering. *Journal of Applied Physics*, 129(145103).
- [Hawkes et al., 2010] Hawkes, E., An, B., Benbernou, N. M., Tanaka, H., Kim, S., Demaine, E. D., Rus, D., and Wood, R. J. (2010). Programmable matter by folding. *PNAS*, 107(28):12441–12445.
- [Hayakawa and Ohsaki, 2019] Hayakawa, K. and Ohsaki, M. (2019). Optimization approach to form generation of rigid-foldable origami for deployable roof structure. In *The World Congress of Structural and Multidisciplinary Optimization, May 20-24, Beijing, China*.
- [Hayakawa and Ohsaki, 2021] Hayakawa, K. and Ohsaki, M. (2021). Form generation of rigid origami for approximation of a curved surface based on mechanical property of partially rigid frames. *International Journal of Solids and Structures*, 216:182–199.
- [Heimbs et al., 2010] Heimbs, S., Cichosz, J., Klaus, M., Kilchert, S., and Johnson, A. F. (2010). Sandwich structures with textile-reinforced composite foldcores under impact loads. *Composite Structures*, 92:1485–1497.
- [Heimbs et al., 2007] Heimbs, S., Middendorf, P., Kilchert, S., Johnson, A. F., and Maier, M. (2007). Experimental and numerical analysis of composite folded sandwich core structures under compression. *Applied Composite Materials*, 14:363–377.

- [Hernandez et al., 2016a] Hernandez, E. A. P., Hartl, D. J., Jr., R. J. M., Akleman, E., Gonen, O., and Kung, H. W. (2016a). Design tools for patterned self-folding reconfigurable structures based on programmable active laminates. *Journal of Mechanisms and Robotics*, 8(031015).
- [Hernandez et al., 2017a] Hernandez, E. A. P., Hartl, D. J., and Lagoudas, D. C. (2017a). Design and simulation of origami structures with smooth folds. *Proceedings of the Royal Society A*, 473(20160716).
- [Hernandez et al., 2016b] Hernandez, E. P., Hartl, D. J., Akleman, E., and Lagoudas, D. C. (2016b). Modeling and analysis of origami structures with smooth folds. *Computer-Aided Design*, 78:93–106.
- [Hernandez et al., 2017b] Hernandez, E. P., Hartl, D. J., and Lagoudas, D. C. (2017b). Analysis and design of an active self-folding antenna. In *Proceedings of the ASME 2017 International Design Engineering Technical Conference and Computers and Information in Engineering Conference*, number DETC2017-67855. August 6-9, 2017, Cleveland, Ohio, USA. ASME.
- [Hernandez et al., 2017c] Hernandez, E. P., Hartl, D. J., and Lagoudas, D. C. (2017c). Kinematics of origami structures with smooth folds. *Journal of Mechanisms and Robotics*, 8(061019).
- [Hirota, 2002] Hirota, G. (2002). *An improved finite element contact model for anatomical simulations*. PhD thesis, University of North Carolina at Chapel Hill.
- [Hoberman, 1988] Hoberman, C. (1988). Reversibly expandable three dimensional structure. *US patent No. 4,780,344*.
- [Hoberman, 1991] Hoberman, C. (1991). Reversibly expandable structure. *US patent No. 4,981,732*.
- [Howell, 2001] Howell, L. (2001). *Compliant Mechanisms*. John Wiley and Sons, Inc.
- [Hu and Liang, 2020] Hu, Y. and Liang, H. (2020). Folding simulation of rigid origami with lagrange multiplier method. *International Journal of Solids and Structures*, 202:552–561.
- [Hu et al., 2021] Hu, Y. C., Zhou, Y. X., Kwok, K. W., and Sze, K. Y. (2021). Simulating flexible origami structures by finite element method. *International Journal of Mechanics and Materials in Design*.
- [Huang and Lee, 1999] Huang, Q.-A. and Lee, N. K. S. (1999). Analysis and design of polysilicon thermal flexure actuator. *Journal of Micromechanics and Microengineering*, 9:64–70.
- [Huffman, 1976] Huffman, D. A. (1976). Curvature and creases: a primer on paper. *IEEE Transaction on Computers*, 25(10):1010–1019.
- [Hull, 1994] Hull, T. (1994). On the mathematics of flat origamis. *Congressus Numerantium*, 100:215–224.
- [Hull, 2013] Hull, T. (2013). *Project Origami*. CRC Press.

- [Hur et al., 2017] Hur, D. Y., Hernandez, E. P., Galvan, E., Hartl, D., and Malak, R. (2017). Design optimization of folding solar powered autonomous underwater vehicles using origami architecture. In *Proceedings of the ASME 2017 International Design Engineering Technical Conferences and Computers and Information in Engineering Conference*, number DETC2017-67848. August 6-9 2017, Cleveland, Ohio, USA. ASME.
- [Hussein et al., 2016] Hussein, H., Tahhan, A., Moal, P. L., Bourbon, G., Haddab, Y., and Lutz, P. (2016). Dynamic electro-thermal-mechanical modelling of a u-shaped electro-thermal actuator. *Journal of Micromechanics and Microengineering*, 26(025010).
- [Hwang, 2021] Hwang, H.-Y. (2021). Effects of perforated crease line design on mechanical behaviors of origami structures. *International Journal of Solids and Structures*, 230-231:111158.
- [Iwase and Shimoyama, 2005] Iwase, E. and Shimoyama, I. (2005). Multistep sequential batch assembly of three-dimensional ferromagnetic microstructures with elastic hinges. *Journal of Microelectromechanical Systems*, 14(6):1265–1271.
- [Jager et al., 2000] Jager, E. W. H., Inghanas, O., and Lundstrom, I. (2000). Microrobots for micrometer-size objects in aqueous media: Potential tools for single-cell manipulation. *Science*, 288:2335–2338.
- [Justin, 1989] Justin, J. (1989). Aspects mathématiques du pliage de papier (mathematical aspects of paper folding). In *Proc. 1st Int. Meeting Origami Sci. Tech.*, pages 263–277.
- [Kamrava et al., 2017] Kamrava, S., Mousanezhad, D., Ebrahimi, H., Ghosh, R., and Vaziri, A. (2017). Origami-based cellular metamaterial with auxetic, bistable and self-locking properties. *Scientific Reports*, 7(46046).
- [Kamrava et al., 2018] Kamrava, S., Mousanezhad, D., Felton, S. M., and Vaziri, A. (2018). Programmable origami strings. *Advanced Materials Technologies*, 3(1700276).
- [Kang et al., 2019] Kang, J.-H., Kim, H., Santangelo, C. D., and Hayward, R. C. (2019). Enabling robust self-folding origami by pre-biasing buckling direction. *Advanced Materials*, 31(0193006).
- [Karagiozova et al., 2019] Karagiozova, D., Zhang, J., Lu, G., and You, Z. (2019). Dynamic inplane compression of Miura-ori patterned metamaterials. *International Journal of Impact Engineering*, 129:80–100.
- [Kasahara and Takahama, 1987] Kasahara, K. and Takahama, T. (1987). Origami for the connoisseur. In *Japan Publications*.
- [Kaufmann et al., 2021] Kaufmann, J., Bhovad, P., and Li, S. (2021). Harnessing the multistability of Kresling origami for reconfigurable articulation in soft robotic arms. *Soft Robotics*, 00(00).
- [Kawasaki, 1989] Kawasaki, T. (1989). On the relation between mountain-creases and valley-creases of a flat origami. In *Proc. 1st Int. Meeting Origami Sci. Tech.*, pages 153–157.

- [Kawasaki and Yoshida, 1988] Kawasaki, T. and Yoshida, M. (1988). Crystallographic flat origamis. *Memoirs of the Faculty of Science, Kyushu University*, 42(2):153–157.
- [Kidambi and Wang, 2020] Kidambi, N. and Wang, K. W. (2020). Dynamics of Kresling origami deployment. *Physical Review E*, 101(063003).
- [Kim et al., 2011] Kim, J., Chung, S. E., Choi, S.-E., Lee, H., Kim, J., and Kwon, S. (2011). Programming magnetic anisotropy in polymeric microactuators. *Nature Materials*, 10:747–752.
- [Ku and Demaine, 2016] Ku, J. S. and Demaine, E. D. (2016). Folding flat crease patterns with thick materials. *Journal of Mechanisms and Robotics*, 8(031003).
- [Kwok, 2020] Kwok, T.-H. (2020). Geometry-based thick origami simulation. *Journal of Mechanical Design*, 143(061701).
- [Lang, 1997] Lang, R. J. (1997). The tree method of origami design. In Miura, K., editor, *Origami Science and Art: Proceedings of the Second International Meeting of Origami Science and Scientific Origami*, pages 73–82, Ohtsu, Japan.
- [Lang, 2009] Lang, R. J. (2009). Mathematical methods in origami design. In *Bridges 2009: Mathematics, Music, Art, Architecture, Culture*, pages 11–20.
- [Lang et al., 2020] Lang, R. J., Brown, N., Ignaut, B., Magleby, S., and Howell, L. (2020). Rigidly foldable thick origami using designed-offset linkages. *Journal of Mechanisms and Robotics*, 12(021106).
- [Lang and Howell, 2018] Lang, R. J. and Howell, L. L. (2018). Rigidly foldable quadrilateral meshes from angle arrays. *Journal of Mechanisms and Robotics*, 10(021004).
- [Lang et al., 2016] Lang, R. J., Magleby, S., and Howell, L. (2016). Single degree-of-freedom rigidly foldable cut origami flashers. *Journal of Mechanisms and Robotics*, 8(031005).
- [Lang et al., 2017] Lang, R. J., Nelson, T., Magleby, S., and Howell, L. (2017). Thick rigidly foldable origami mechanisms based on synchronized offset rolling contact elements. *Journal of Mechanisms and Robotics*, 9(021013).
- [Lang et al., 2018] Lang, R. J., Tolman, K. A., Crampton, E. B., Magleby, S. P., and Howell, L. L. (2018). A review of thickness accommodation techniques in origami-inspired engineering. *Applied Mechanics Reviews*, 70(010805).
- [Leon et al., 2014] Leon, S. E., Lages, E. N., DeAraujo, C. N., and Paulino, G. H. (2014). On the effect of constraint parameters on the generalized displacement control method. *Mechanics Research Communications*, 56:123–129.
- [Leon et al., 2011] Leon, S. E., Paulino, G. H., Pereira, A., Menezes, I. F. M., and Lages, E. N. (2011). A unified library of nonlinear solution schemes. *Applied Mechanics Reviews*, 64(040803-1).



- [Leong et al., 2008] Leong, T. G., Christina, Randall, L., Benson, B. R., Zarafshar, A. M., and Gracias, D. H. (2008). Self-loading lithographically structured microcontainers: 3d patterned, mobile microwells. *Lab on a Chip*, 8:1621–1624.
- [Leong et al., 2009] Leong, T. G., Randall, C. L., Benson, B. R., Bassik, N., Stern, G. M., and Gracias, D. H. (2009). Tetherless thermo-biochemically actuated microgrippers. *PNAS*, 106:703–708.
- [Leong et al., 2010] Leong, T. G., Zarafshar, A. M., and Gracias, D. H. (2010). Three-dimensional fabrication at small size scales. *Small*, 6:792–806.
- [Li et al., 2017] Li, S., Vogt, D. M., Rus, D., and Wood, R. J. (2017). Fluid-driven origami-inspired artificial muscles. *PNAS*, 114(50):13132–13137.
- [Li and Wang, 2015] Li, S. and Wang, K. W. (2015). Fluidic origami: a plant-inspired adaptive structure with shape morphing and stiffness tuning. *Smart Materials and Structures*, 24(105031).
- [Liu et al., 2020] Liu, K., Novelino, L. S., Gardoni, P., and Paulino, G. H. (2020). Big influence of small random imperfections in origami-based metamaterials. *Proceedings of the Royal Society A*, 476(20200236).
- [Liu and Paulino, 2016] Liu, K. and Paulino, G. (2016). Merlin: A matlab implementation to capture highly nonlinear behavior of non-rigid origami. In *Proceedings of IASS Annual Symposium*, pages 1–10. September 26-30, 2016, Tokyo, Japan. International association for shell and spatial structures.
- [Liu and Paulino, 2017a] Liu, K. and Paulino, G. (2017a). Nonlinear mechanics of non-rigid origami: an efficient computational approach. *Proceedings of the Royal Society A*, 473(20170348).
- [Liu and Paulino, 2018a] Liu, K. and Paulino, G. (2018a). Highly efficient structural analysis of origami assemblages using the merlin2 software. In *Origami 7. the 7th International Meeting on Origami in Science, Mathematics and Education (7OSME)*, September 5-7, 2018, Oxford University, United Kingdom. Tarquin.
- [Liu and Paulino, 2017b] Liu, K. and Paulino, G. H. (2017b). MERLIN. <http://paulino.ce.gatech.edu/software.html>.
- [Liu and Paulino, 2018b] Liu, K. and Paulino, G. H. (2018b). MERLIN 2. <http://paulino.ce.gatech.edu/software.html>.
- [Liu et al., 2019] Liu, K., Tachi, T., and Paulino, G. H. (2019). Invariant and smooth limit of discrete geometry folded from bistable origami leading to multistable metasurfaces. *Nature Communications*, 10(4238).
- [Liu et al., 2021] Liu, Q., Wang, W., Reynolds, M. F., Cao, M. C., Miskin, M. Z., Arias, T. A., Muller, D. A., McEuen, P. L., and Cohen, I. (2021). Micrometer-sized electrically programmable shape-memory actuators for low-power microrobotics. *Science Robotics*, 6(eabe6663).

- [Liu et al., 2015] Liu, S., Lu, G., Chen, Y., and Leong, Y. W. (2015). Deformation of the Miura-ori patterned sheet. *International Journal of Mechanical Sciences*, 99:130–142.
- [Liu et al., 2011] Liu, Y., Boyles, J. K., Genzer, J., and Dickey, M. D. (2011). Self-folding of polymer sheets using local light absorption. *Soft Material*, 8(6).
- [Luo et al., 2006] Luo, J., Huang, R., He, J., Fu, Y., Flewitt, A., Spearing, S., Fleck, N., and Milne, W. (2006). Modelling and fabrication of low operation temperature microcages with a polymer/metal/dlc trilayer structure. *Sensors and Actuators A*, 132:346–353.
- [Luo et al., 2005] Luo, J. K., He, J. H., Fu, Y. Q., Flewitt, A. J., Spearing, S. M., Fleck, N. A., and Milne, W. (2005). Fabrication and characterization of diamond-like carbon/ni bimorph normally closed microcages. *Journal of Micromechanics and Microengineering*, 15:1406–1413.
- [Lv et al., 2014] Lv, C., Krishnaraju, D., Konjevod, G., Yu, H., and Jiang, H. (2014). Origami based mechanical metamaterials. *Scientific Report*, 4(5979).
- [Ma et al., 2016] Ma, J., Hou, D., Chen, Y., and You, Z. (2016). Quasi-static axial crushin of the thin-walled tubes with a kite-shape rigid origami pattern: Numerical simulation. *Thin-Walled Structures*, 100:38–47.
- [Ma et al., 2018a] Ma, J., Hou, D., Chen, Y., and You, Z. (2018a). Peak stress relief of cross folding origami. *Thin-Walled Structures*, 123:155–161.
- [Ma et al., 2018b] Ma, J., Song, J., and Chen, Y. (2018b). An origami-inspired structure with graded stiffness. *International Journal of Mechanical Sciences*, 136:134–142.
- [Ma and You, 2014] Ma, J. and You, Z. (2014). Energy absorption of thin-walled square tubes with a prefolded origami pattern–part 1: Geometry and numerical simulation. *Journal of Applied Mechanics*, 81(011003-1).
- [Mangalathu and Jeon, 2018] Mangalathu, S. and Jeon, J.-S. (2018). Classification of failure mode and prediction of shear strength for reinforced concrete beam-column joints using machine learning techniques. *Engineering Structures*, 160:85–94.
- [Mao et al., 2015] Mao, Y., Yu, K., Isakov, M. S., Wu, J., Dunn, M. L., and Qi, H. J. (2015). Sequential self-folding structures by 3d printed shape memory polymers. *Scientific Reports*, 5(13616).
- [Martinez et al., 2012] Martinez, R. V., Fish, C. R., Chen, X., and Whitesides, M. (2012). Elastomeric origami: Programmable paper-elastomer composites as pneumatic actuators. *Advanced Functional Materials*, 22(7):1376–1384.
- [Masana and Daqaq, 2019] Masana, R. and Daqaq, M. F. (2019). Equilibria and bifurcations of a foldable paper-based spring inspired by kresling-pattern origami. *Physical Review E*, 100(063001).
- [McGuire et al., 2000] McGuire, W., Gallagher, R. H., and Ziemian, R. D. (2000). *Matrix Structural Analysis, 2nd Edition*. Faculty Books.

- [MicroChem, 2019] MicroChem (2019). Su-8 permanent photoresists. Technical report, MicroChem.
- [MIT, 2017a] MIT (2017a). About contact interactions. <https://abaqus-docs.mit.edu/2017/English/SIMACAEITNRefMap/simaitn-c-contactoverview.htm>.
- [MIT, 2017b] MIT (2017b). Common difficulties associated with contact modeling in abaqus/standard. <http://194.167.201.93/English/SIMACAEITNRefMap/simaitn-c-contacttrouble.htm>.
- [MIT, 2017c] MIT (2017c). Common difficulties associated with contact modeling using contact pairs in abaqus/explicit. <https://abaqus-docs.mit.edu/2017/English/SIMACAEITNRefMap/simaitn-c-expcontacttrouble.htm>.
- [Mitani, 2008] Mitani, J. (2008). The folded shape restoration and the rendering method of origami from the crease pattern. In *13th International Conference on Geometry and Graphics*.
- [Mitani, 2012] Mitani, J. (2012). ORIPA. <https://mitani.cs.tsukuba.ac.jp/oripa/>.
- [Mitani and Igarashi, 2011] Mitani, J. and Igarashi, T. (2011). Interactive design of planar curved folding by reflection. In Chen, B.-Y., Kautz, J., Lee, T.-Y., and Lin, M. C., editors, *Pacific Graphics Short Papers*. The Eurographics Association.
- [Miyazawa et al., 2021] Miyazawa, Y., Yasuda, H., Kim, H., Lynch, J. H., Tsujikawa, K., Kunimine, T., Raney, J. R., and Yang, J. (2021). Heterogeneous origami-architected materials with variable stiffness. *Communications Materials*, 2(110).
- [Mukhopadhyay et al., 2020] Mukhopadhyay, T., Ma, J., Feng, H., Hou, D., Gattas, J. M., Chen, Y., and You, Z. (2020). Programmable stiffness and shape modulation in origami materials: Emergence of a distant actuation feature. *Applied Materials Today*, 19(100537).
- [Munjiza and Andrews, 1998] Munjiza, A. and Andrews, K. R. F. (1998). Nbs contact detection algorithm for bodies of similar size. *International Journal for Numerical Methods in Engineering*, 43:131–149.
- [Na et al., 2015] Na, J.-H., Evans, A. A., Bae, J., Chiappelli, M. C., Santangelo, C. D., Lang, R. J., Hull, T. C., and Hayward, R. C. (2015). Programming reversibly self-folding origami with micropatterned photo-crosslinkable polymer trilayers. *Advanced Materials*, 27:79–85.
- [Nauroze et al., 2018] Nauroze, S. A., Novelino, L. S., Tentzeris, M. M., and Paulino, G. H. (2018). Continuous-range tunable multilayer frequency-selective surfaces using origami and inkjet printing. *PNAS*, 115(52):13210–13215.
- [Nauroze and Tentzeris, 2019] Nauroze, S. A. and Tentzeris, M. M. (2019). A thermally actuated fully inkjet-printed origami inspired multilayer frequency selective surface with continuous-range tunability using polyester-based substrates. *IEEE Transactions on Microwave Theory and Techniques*, 67(12):4944–4954.

- [Ng et al., 2018] Ng, H., Ong, S., Foong, K., Goh, P., and Nowinski, W. (2018). Medical image segmentation using k-means clustering and improved watershed algorithm. In *2006 IEEE Southwest Symposium on Image Analysis and Interpretation, 26-28 March 2006*, page 5 pages. IEEE.
- [Ning et al., 2018] Ning, X., Yu, X., Wang, H., Sun, R., Corman, R. E., Li, H., Lee, C. M., Xue, Y., Chempakasseril, A., Yao, Y., Zhang, Z., Luan, H., Wang, Z., Xia, W., Feng, X., Ewoldt, R. H., Huang, Y., Zhang, Y., and Rogers, J. A. (2018). Mechanically active materials in three-dimensional mesostructures. *Science Advances*, 4(eaat8313).
- [Noe et al., 2020] Noe, F., Tkatchenko, A., Muller, K. R., and Clementi, C. (2020). Machine learning for molecular simulation. *Annual Review of Physical Chemistry*, 71:361–390.
- [Novelino et al., 2020] Novelino, L. S., Ze, Q., Wu, S., Paulino, G. H., and Zhao, R. (2020). Untethered control of functional origami microrobots with distributed actuation. *PNAS*, 117(39):24096–24101.
- [OEIS, 2019] OEIS (2019). (a000670).
- [Oldenburg and Nilsson, 1994] Oldenburg, M. and Nilsson, L. (1994). The position code algorithm for contact searching. *International Journal of Numerical Methods in Engineering*, 37:359–386.
- [Oldham et al., 2007] Oldham, K., Pulskamp, J., Polcawich, R., Ranade, P., and Debey, M. (2007). Thin-film piezoelectric actuators for bio-inspired micro-robotic applications. *Integrated Ferroelectrics*, 95:54–65.
- [Overvelde et al., 2016] Overvelde, J. T., DeJong, T. A., Shevchenko, Y., Becerra, S. A., Whitesides, G. M., Weaver, J. C., Hoberman, C., and Bertoldi, K. (2016). A three-dimensional actuated origami-inspired transformable metamaterial with multiple degrees of freedom. *Nature Communications*, 7(10929).
- [Ozsun et al., 2009] Ozsun, O., Alaca, B. E., Yalcinkaya, A. D., Yilmaz, M., Zervas, M., and Leblebici, Y. (2009). On heat transfer at microscale with implications for micro actuator design. *Journal of Micromechanics and Microengineering*, 19(045020).
- [Pagano et al., 2017] Pagano, A., Yan, T., Chien, B., Wissa, A., and Tawfick, S. (2017). A crawling robot driven by multi-stable origami. *Smart Materials and Structures*, 26(094007).
- [Paik and Wood, 2012] Paik, J. K. and Wood, R. J. (2012). A bidirectional shape memory alloy folding actuator. *Smart Materials and Structures*, 21(065013).
- [Peng et al., 2017] Peng, R., Ma, J., and Chen, Y. (2017). Rigid foldability of triangle twist origami pattern and its derived 6r linkage. In *International Design Engineering Technical Conference and Computers and Information in Engineering Conference, Aug 6-9, Cleveland, Ohio, USA*.

- [Peraza-Hernandez et al., 2018] Peraza-Hernandez, E. A., Hartl, D. J., and Lagoudas, D. C. (2018). Design and simulation of origami with smooth folds. *Proceedings of the Royal Society A*, 473(20160716).
- [Perkins and Williams, 2001] Perkins, E. and Williams, J. R. (2001). A fast contact detection algorithm insensitive to object sizes. *Engineering computations*, 18(1-2):48–61.
- [Pezzulla et al., 2015] Pezulla, M., Shilig, S. A., Nardinocchi, P., and Holmes, D. P. (2015). Morphing of geometric composites via residual swelling. *Soft Matter*, 11:5812–5820.
- [Piker, 2013] Piker, D. (2013). Kangaroo: Form finding with computational physics. *Architectural Design*, 83:136–137.
- [Piker, 2017] Piker, D. (2017). Kangaroo. <https://www.food4rhino.com/en/app/kangaroo-physics>.
- [Pinson et al., 2017] Pinson, M. B., Stern, M., Ferrero, A. C., Witten, T. A., Chen, E., and Murugan, A. (2017). Self-folding origami at any energy scale. *Nature Communications*, 8(15477).
- [Potekhina and Wang, 2019] Potekhina, A. and Wang, C. (2019). Review of electrothermal actuators and applications. *Actuators*, 8(69).
- [Pratapa et al., 2021] Pratapa, P. P., Liu, K., Vasudevan, S. P., and Paulino, G. H. (2021). Reprogrammable kinematic branches in tessellated origami structures. *Journal of Mechanisms and Robotics*, 13(031102).
- [Pratapa et al., 2018] Pratapa, P. P., Suryanarayana, P., and Paulino, G. H. (2018). Bloch wave framework for structures with nonlocal interactions: Application to the design of origami acoustic metamaterials. *Journal of the Mechanics and Physics of Solids*, 118:115–132.
- [Quinlan, 1993] Quinlan, J. (1993). C4.5: Programs for machine learning. *San Francisco: CA: Morgan Kaufmann*.
- [Quinlan, 1986] Quinlan, J. R. (1986). Induction of decision trees. *Machine Learning*, 1:81–106.
- [Randhawa et al., 2010] Randhawa, J. S., Keung, M. D., Tyagi, P., and Gracias, D. H. (2010). Reversible actuation of microstructures by surface-chemical modification of thin-film bilayers. *Advanced Materials*, 22:407–410.
- [Redoutey et al., 2021] Redoutey, M., Roy, A., and Filipov, E. T. (2021). Pop-up kirigami for stiff, dome-like structures. *International Journal of Solids and Structures*, 229(111140).
- [Resch and Christiansen, 1970] Resch, R. and Christiansen, H. N. (1970). Kinematic folded plate system. In *Proceedings of IASS Symposium on Folded Plates and Prismatic Structures*.
- [Robin et al., 2014] Robin, C. J., Vishnoi, A., and Joonalagadda, K. N. (2014). Mechanical behavior and anisotropy of spin-coated su-8 thin films for mems. *Journal of Microelectromechanical Systems*, 24(1).

- [Rogers et al., 2016] Rogers, J., Huang, Y., Schmidt, O. G., and Gracias, D. H. (2016). Origami mems and nems. *MRS Bulletin*, 41:123–129.
- [Rudin, 2019] Rudin, C. (2019). Stop explaining back box machine learning models for high stakes decisions and use interpretable models instead. *Nature Machine Learning*, 1:206–215.
- [Saito et al., 2016] Saito, K., Tsukahara, A., and Okabe, Y. (2016). Designing of self-deploying origami structures using geometrically misaligned crease patterns. *Proceedings of the Royal Society A*, 472(20150235).
- [Schenk and Guest, 2010] Schenk, M. and Guest, S. D. (2010). Origami folding: A structural engineering approach. In *Origami5, Proceedings of 5OSME*, pages 293–305. July 13-17, 2010, Singapore, CRC press.
- [Schenk and Guest, 2013] Schenk, M. and Guest, S. D. (2013). Geometry of miura-folded metamaterials. *PNAS*, 110(9):3276–3281.
- [Schenk et al., 2014] Schenk, M., Guest, S. D., and McShane, G. J. (2014). Novel stacked folded cores for blast-resistant sandwich beams. *International Journal of Solids and Structures*, 51:4196–5214.
- [Senturia, 2001] Senturia, S. D. (2001). *Microsystem Design*. Springer.
- [Seymour et al., 2018] Seymour, K., Burrow, D., Avila, A., Bateman, T., Morgan, D. C., Magleby, S. P., and Howell, L. L. (2018). Origami based deployable ballistic barrier. In *Origami 7*, volume 3, pages 763–778, Proceedings of the 7th International Meeting on Origami in Science, Mathematics and Education, Oxford, UK, Sept 5-7.
- [Shaar et al., 2015] Shaar, N. S., Barbastathis, G., and Livermore, C. (2015). Integrated folding, alignment, and latching for reconfigurable origami microelectromechanical systems. *Journal of Microelectromechanical Systems*, 24(4):1043–1051.
- [Silverberg et al., 2014] Silverberg, J. L., Evans, A. A., McLeod, L., Hayward, R. C., Hull, T., Santangelo, C. D., and Cohen, I. (2014). Using origami design principles to fold reprogrammable mechanical metamaterials. *Science*, 345(6197):647–650.
- [Silverberg et al., 2015] Silverberg, J. L., Na, J.-H., Evans, A. A., Liu, B., Hull, T. C., Santangelo, C. D., Lang, R. J., Hayward, R. C., and Cohen, I. (2015). Origami structures with a critical transition to bistability arising from hidden degrees of freedom. *Nature Materials*, 14:389–393.
- [Soleimani et al., 2021] Soleimani, H., Goudarzi, T., and Aghdam, M. M. (2021). Advanced structural modeling of a fold in origami/kirigami inspired structures. *Thin-Walled Structures*, 161(107406).
- [Song et al., 2012] Song, J., Chen, Y., and Lu, G. (2012). Axial crushing of thin-walled structures with origami patterns. *Thin-Walled Structures*, 54:65–71.
- [Sreetharan et al., 2012] Sreetharan, P. S., Whitney, J. P., Strauss, M. D., and Wood, R. J. (2012). Monolithic fabrication of millimeter-scale machines. *Journal of Micromechanics and micro-engineering*, 22(055027).

- [Stern et al., 2017] Stern, M., Pinson, M. B., and Murugan, A. (2017). The complexity of folding self-folding origami. *Physical Review X*, 7(041070).
- [Suh et al., 1999] Suh, J. W., Darling, R. B., Bohringer, K.-F., Donald, B. R., Baltes, H., and Kovacs, G. T. A. (1999). Cmos integrated ciliary actuator array as a general-purpose micromanipulation tool for small objects. *Journal of Microelectromechanical systems*, 8(4):483–496.
- [Suto and Tanimichi, 2021] Suto, K. and Tanimichi, K. (2021). Crane. <https://www.food4rhino.com/en/app/crane>.
- [Swaminathan et al., 2021] Swaminathan, R., Cai, C. J., Yuan, S., and Ren, H. (2021). Multi-physics simulation of magnetically actuated robotic origami worms. *IEEE Robotics and Automation Letters*, 6:4923 – 4930.
- [Tachi, 2009a] Tachi, T. (2009a). Generalization of rigid foldable quadrilateral mesh origami. *Journal of the International Association for Shell and Spatial Structures*, 50:173–179.
- [Tachi, 2009b] Tachi, T. (2009b). Rigid origami simulator. <https://tsg.ne.jp/TT/software/index.html>.
- [Tachi, 2009c] Tachi, T. (2009c). Simulation of rigid origami. In Lang, R. J., editor, *Origami 4*, pages 175–187. December 8-10 2015, Caltech, Pasadena, CA, CRC Press.
- [Tachi, 2010a] Tachi, T. (2010a). Freeform variations of origami. *Journal for Geometry and Graphics*, 14(2):203–215.
- [Tachi, 2010b] Tachi, T. (2010b). Geometric considerations for the design of rigid origami structures. In *Proceedings of the International Association for Shell and Spatial Structures (IASS) Symposium*. November 8-12 2010, Shanghai, China. International association for shell and spatial structures.
- [Tachi, 2010c] Tachi, T. (2010c). Origamizer. <https://tsg.ne.jp/TT/software/index.html>.
- [Tachi, 2010d] Tachi, T. (2010d). Origamizing polyhedral surfaces. *IEEE Transactions on Visualization and Computer Graphics*, 16:298–311.
- [Tachi, 2011] Tachi, T. (2011). Rigid-foldable thick origami. In *Origami 5*, pages 253–264.
- [Tachi, 2013] Tachi, T. (2013). Designing freeform origami tessellations by generalizing resch’s patterns. *Journal of Mechanical Design*, 135(111006).
- [Tachi, 2020] Tachi, T. (2020). Freeform origami. <https://tsg.ne.jp/TT/software/index.html>.
- [Thai et al., 2018] Thai, P. T., Savchenko, M., and Hagiwara, I. (2018). Finite element simulation of robotic origami folding. *Simulation Modelling Practice and Theory*, 54:65–71.
- [Tharwat, 2020] Tharwat, A. (2020). Classification assessment methods. *Applied Computing and Informatics*, 17:168–192.

- [Thota and Wang, 2018] Thota, M. and Wang, K. (2018). Tunable waveguiding in origami phononic structures. *Journal of Sound and Vibration*, 430:93–100.
- [Timoshenko, 1925] Timoshenko, S. (1925). Analysis of bi-metal thermostats. *J.O.S.A. & R.S.I.*, 11.
- [Timoshenko and Krieger, 1959] Timoshenko, S. P. and Krieger, S. W. (1959). *Theory of plates and shells*. Mc Graw Hill Education. Page 5, Eqn(3).
- [Todd et al., 2006] Todd, S. T., Jain, A., Qu, H., and Xie, H. (2006). A multi-degree-of-freedom micromirror utilizing inverted-series-connected bimorph actuators. *Journal of Optics A: Pure and Applied Optics*, 8:S352–S359.
- [Velvaluri et al., 2021] Velvaluri, P., Soor, A., Plucinsky, P., de Miranda, R. L., James, R. D., and Quandt, E. (2021). Origami-inspired thin-film shape memory alloy devices. *Scientific Reports*, 11(10988).
- [Vinyals et al., 2019] Vinyals, O., Babuschkin, I., Czarnecki, W. M., Mathieu, M., Dudzik, A., Chung, J., Choi, D. H., Powell, R., Ewalds, T., Georgiev, P., Oh, J., Horgan, D., Kroiss, M., Danihelka, I., Huang, A., Sifre, L., Cai, T., Agapiou, J. P., Jaderberg, M., Vezhnevets, A. S., Leblond, R., Pohlen, T., Dalibard, V., Budden, D., Sulsky, Y., Molloy, J., Paine, T. L., Gulcehre, C., Wang, Z., Pfaff, T., Wu, Y., Ring, R., Yogatama, D., Wünsch, D., McKinney, K., Smith, O., Schaul, T., Timothy Lillicrap, K. K., Hassabis, D., Apps, C., and Silver, D. (2019). Grandmaster level in starcraft ii using multi-agent reinforcement learning. *Nature*, 575:350–354.
- [Vorobiev, 2012] Vorobiev, O. (2012). Simple common plane contact algorithm. *International Journal for Numerical Methods in Engineering*, 90:243–268.
- [Waitukaitis et al., 2015] Waitukaitis, S., Menaut, R., ge Chen, B. G., and van Hecke, M. (2015). Origami multistability: From single vertices to metasheets. *Physical Review Letter*, 114(05503).
- [Wang and Zhou, 2017] Wang, B. and Zhou, C. (2017). The imperfection-sensitivity of origami crash boxes. *International Journal of Mechanical Sciences*, 121:58–66.
- [Wang et al., 2018] Wang, Z. J., Zhou, H., Khaliulin, V. I., and Shabalov, A. V. (2018). Six-ray folded configurations as the geometric basis of thin-walled element in engineering structures. *Thin-Walled Structures*, 130:435–448.
- [Wei and Dai, 2014] Wei, G. and Dai, J. S. (2014). Origami-inspired integrated planar-spherical overconstrained mechanisms. *Journal of Mechanical Design*, 136(051003).
- [Wei et al., 2013] Wei, Z. Y., Guo, Z. V., Gudte, L., Liang, H. Y., and Mahadevan, L. (2013). Geometric mechanics of periodic pleated origami. *Physical Review Letters*, 110(215501).
- [Wheeler and Culpeper, 2016] Wheeler, C. M. and Culpeper, M. L. (2016). Soft origami: Classification, constraint, and actuation of highly compliant origami structures. *Journal of Mechanisms and Robotics*, 8(051012-1).



- [Woo et al., 1993] Woo, A. C., Wang, H. T. G., Schuh, M. J., and Sanders, M. L. (1993). EM programmer’s notebook-benchmark radar targets for the validation of computational electromagnetics programs. *IEEE Antennas and Propagation Magazine*, 35(1):84–89.
- [Wood et al., 2008] Wood, R. J., Avadhanula, S., Sahai, R., Steltz, E., and Fearing, R. S. (2008). Microrobot design using fiber reinforced composites. *Journal of Mechanical Design*, 130(052304-1).
- [Wootton, 1981] Wootton, R. J. (1981). Support and deformability in insect wings. *Journal of Zoology*, 193:447–468.
- [Wu and You, 2010] Wu, W. and You, Z. (2010). Modelling rigid origami with quaternions. *Proceedings of the Royal Society A*, 466:2155–2174.
- [Wu and You, 2011] Wu, W. and You, Z. (2011). A solution for folding rigid tall shopping bags. *Proceedings of the Royal Society A*, 467:2561–2574.
- [Xi and Lien, 2015] Xi, Z. and Lien, J.-M. (2015). Folding and unfolding origami tessellation by reusing folding path. In *IEEE International Conference on Robotics and Automation (ICRA)*, Seattle, Washington, May 26-30.
- [Xia et al., 2021a] Xia, Y., Filipov, E., and Wang, K. W. (2021a). The deployment dynamics and multistability of tubular fluidic origami. In Han, J.-H., Wang, G., and Shahab, S., editors, *Active and Passive Smart Structures and Integrated Systems XV*, volume 11588, pages 98 – 108. International Society for Optics and Photonics, SPIE.
- [Xia et al., 2021b] Xia, Y., Kidambi, N., Filipov, E. T., and Wang, K. W. (2021b). Deployment dynamics of Miura origami sheets. submitted.
- [Xia and Wang, 2019] Xia, Y. and Wang, K.-W. (2019). Dynamics analysis of the deployment of Miura-origami sheets. In *International Design Engineering Technical Conferences and Computers and Information in Engineering Conference, August 18-21, Anaheim, CA, USA*, volume Volume 5B: 43rd Mechanisms and Robotics Conference.
- [Xiang et al., 2020] Xiang, X., Lu, G., and You, Z. (2020). Energy absorption of origami inspired structures and materials. *Thin-Walled Structures*, 157(107130).
- [Xiang et al., 2018] Xiang, X., You, Z., and Lu, G. (2018). Rectangular sandwich plates with Miura-ori folded core under quasi-static loadings. *Composite Structures*, 195:359–374.
- [Xu et al., 2016] Xu, T., Yoo, J. H., Babu, S., Roy, S., Lee, J.-B., and Lu, H. (2016). Characterization of the mechanical behavior of su-8 at microscale by viscoelastic analysis. *Journal of Micromechanics and Microengineering*, 26(105001).
- [Xu et al., 2019] Xu, T., Zhang, J., Salehizadeh, M., Onaizah, O., and Diller, E. (2019). Millimeter-scale flexible robots with programmable three-dimensional magnetization and motions. *Science Robotics*, 4(eaav4494).

- [Yang et al., 2016] Yang, K., Xu, S., Shen, J., Zhou, S., and Xie, Y. M. (2016). Energy absorption of thin-walled tubes with pre folded origami patterns: Numerical simulation and experimental verification. *Thin-Walled Structures*, 103:33–44.
- [Yang and Silverberg, 2017a] Yang, N. and Silverberg, J. (2017a). Decoupling local mechanics from large-scale structure in modular metamaterials. *PNAS*, 114(14).
- [Yang and Silverberg, 2017b] Yang, N. and Silverberg, J. L. (2017b). Decoupling local mechanics from large-scale structure in modular metamaterials. *PNAS*, 114(14):3590–3595.
- [Yang et al., 2020] Yang, X., Chang, L., and Perez-Arancibia, N. O. (2020). An 88-milligram insect-scale autonomous crawling robot driven by a catalytic artificial muscle. *Science Robotics*, 5(eaba0015).
- [Yasuda et al., 2020] Yasuda, H., koshiro Yamaguchi, Miyazawa, Y., Wiebe, R., Raney, J. R., and Yang, J. (2020). Data-driven prediction and analysis of chaotic origami dynamics. *Communications Physics*, 3(168).
- [Yasuda et al., 2017] Yasuda, H., Tachi, T., Lee, M., and Yang, J. (2017). Origami-based tunable truss structure for non-volatile mechanical memory operation. *Nature communications*, 18(962).
- [Yasuda and Yang, 2015] Yasuda, H. and Yang, J. (2015). Reentrant origami-based metamaterials with negative poisson’s ratio and bistability. *Physical Review Letters*, 114(185502).
- [Yasuda et al., 2013] Yasuda, H., Yein, T., Tachi, T., Miura, K., and Taya, M. (2013). Folding behaviour of Tachi-Miura polyhedron bellows. *Proceedings of the Royal Society A*, 469(20130351).
- [Yi and Liu, 1999] Yi, Y. W. and Liu, C. (1999). Magnetic actuation of hinged microstructures. *IEEE Journal of Microelectromechanical systems*, 8(1):10–17.
- [Yoon et al., 2014] Yoon, C., Xiao, R., Park, J., Cha, J., Nguyen, T. D., and Gracias, D. H. (2014). Functional stimuli responsive hydrogel devices by self-folding. *Smart Materials and Structures*, 23(094008).
- [Yu et al., 2019] Yu, Y., Chen, Y., and Paulino, G. H. (2019). On the Unfolding Process of Triangular Resch Patterns: A Finite Particle Method Investigation. In *International Design Engineering Technical Conferences and Computers and Information in Engineering Conference, August 18-21, Anaheim, CA, USA*, volume Volume 5B: 43rd Mechanisms and Robotics Conference.
- [Yu et al., 2011] Yu, Y., Paulino, G. H., and Luo, Y. (2011). Finite particle method for progressive failure simulation of truss structures. *Journal of Structural Engineering*, 137(10):1168–1181.
- [Yuan et al., 2020] Yuan, L., Dai, H., Song, J., Ma, J., and Chen, Y. (2020). The behavior of a functionally graded origami structure subjected to quasi-static compression. *Materials and Designs*, 189(108494).
- [Zaghloul and Bone, 2020] Zaghloul, A. and Bone, G. M. (2020). 3d shrinking for rapid fabrication of origami-inspired semi-soft pneumatic actuators. *IEEE Access*, 8:191330–191340.

- [Zhang, 2021] Zhang, H. (2021). Mechanics analysis of functional origamis applicable in biomedical robots. *IEEE/ASME Transactions on Mechatronics*.
- [Zhang et al., 2021] Zhang, H., Feng, H., Huang, J.-L., and Paik, J. (2021). Generalized modeling of origami folding joints. *Extreme Mechanics Letters*, 45(101213).
- [Zhang et al., 2019] Zhang, J., Karagiozova, D., You, Z., and Lu, G. (2019). Quasi-static large deformation compressive behaviour of origami-based metamaterials. *International Journal of Mechanical Sciences*, 153-154:194–207.
- [Zhang and Kawaguchi, 2021] Zhang, T. and Kawaguchi, K. (2021). Folding analysis for thick origami with kinematic frame models concerning gravity. *Automation in Construction*, 127(103691).
- [Zhang et al., 2018] Zhang, T., Kawaguchi, K., and Wu, M. (2018). A folding analysis method for origami based on the frame with kinematic indeterminacy. *International Journal of Mechanical Sciences*, 146-147:234–248.
- [Zhang et al., 2015] Zhang, X., Li, B., Li, X., and Xie, H. (2015). A robust fast electrothermal micromirror with symmetric bimorph actuators made of copper/tungsten. In *2015 Transducers - 2015 18th International Conference on Solid-State Sensors, Actuators and Microsystems (TRANSDUCERS)*, pages 912–915, Anchorage, Alaska, USA.
- [Zhao et al., 2018] Zhao, Y., Endo, Y., Kanamori, Y., and Mitani, J. (2018). Approximating 3d surfaces using generalized waterbomb tessellations. *Journal of Computational Design and Engineering*, 5:442–448.
- [Zheng et al., 2017] Zheng, Z., Zang, M., Chen, S., and Zhao, C. (2017). An improved dem-fem contact detection algorithm for the interaction simulations between particles and structures. *Powder Technology*, 305:308–322.
- [Zhong and Nilsson, 1989] Zhong, Z. H. and Nilsson, L. (1989). A contact searching algorithm for general contact problems. *Computers and Structures*, 33(1):197–209.
- [Zhu et al., 2019] Zhu, Y., Fei, F., Fan, S., Cao, L., Donda, K., and Assouar, B. (2019). Reconfigurable origami-inspired metamaterials for controllable sound manipulation. *Physical Review Applied*, 12(034029).
- [Zhu and Filipov, 2019a] Zhu, Y. and Filipov, E. (2019a). An efficient numerical approach for simulating contact in origami assemblages. *Proceedings of the Royal Society A*, 475(20190366).
- [Zhu and Filipov, 2019b] Zhu, Y. and Filipov, E. (2019b). Simulating compliant crease origami with a bar and hinge model. In *International Design Engineering Technical Conferences and Computers and Information in Engineering Conference, August 18-21, Anaheim, CA, USA*, number DETC2019-97119. August 16-19, 2019, Anaheim, CA, USA. ASME.
- [Zhu and Filipov, 2020] Zhu, Y. and Filipov, E. T. (2020). A bar and hinge model for simulating bistability in origami structures with compliant creases. *Journal of Mechanisms and Robotics*, 12(2): 021110(JMR-19-1425).

- [Zhu and Filipov, 2021a] Zhu, Y. and Filipov, E. T. (2021a). Rapid multi-physics simulation for electro-thermal origami systems. *International Journal of Mechanical Sciences*, 202-203(106537).
- [Zhu and Filipov, 2021b] Zhu, Y. and Filipov, E. T. (2021b). Sequentially working origami multi-physics simulator (swomps). <https://github.com/zzhuyii/OrigamiSimulator>.
- [Zhu and Filipov, 2021c] Zhu, Y. and Filipov, E. T. (2021c). Sequentially working origami multi-physics simulator (swomps): A versatile implementation. In *2021 International Design Engineering Technical Conferences & Computers and Information in Engineering Conference*, pages DETC2021-68042, online.
- [Zhu et al., 2020] Zhu, Y., Mayur, B., Oldham, K. R., and Filipov, E. T. (2020). Elastically and plastically foldable electro-thermal micro-origami for controllable and rapid shape morphing. *Advanced Functional Material*, 30(2003741).
- [Zimmermann et al., 2019] Zimmermann, L., Shea, K., and Stankovic, T. (2019). Conditions for rigid and flat foldability of degree-n vertices in origami. *Journal of Mechanisms and Robotics*, 12(011020).
- [Zou et al., 2001] Zou, J., Chen, J., Liu, C., and Schutt-Aine, J. E. (2001). Plastic deformation magnetic assembly of out-of-plane microstructures: Technology and application. *Journal of Microelectromechanical Systems*, 10(2):302-309.